

Design and Characterization of Chitosan-Based Nonwoven Fibrous Materials

A Thesis Submitted to the
College of Graduate and Postdoctoral Studies
In Partial Fulfillment of the Requirements
For the Degree of Doctor of Philosophy
In the Department of Chemistry
University of Saskatchewan
Saskatoon

By

Chen Xue

© Copyright Chen Xue, April, 2021. All rights reserved.

Unless otherwise noted, copyright of the material in this thesis belongs to the author

Permission to Use

In presenting this thesis in partial fulfillment of the requirements for a Postgraduate degree from the University of Saskatchewan, I agree that the Libraries of this University may make it freely available for inspection. I further agree that permission for copying of this thesis in any manner, in whole or in part, for scholarly purposes may be granted by Dr. L. D. Wilson who supervised my thesis work or, in his absence, by the Head of the Department of Chemistry or the Dean of the College in which my thesis work was done. It is understood that any copying or publication or use of this thesis or part of it for financial gain shall not be allowed without my written permission. It is also understood that due recognition shall be given to me and to the University of Saskatchewan in any scholarly use which may be made of any material in my thesis. Requests for permission to copy or to make other use of the material in this thesis in whole or part should be addressed to:

Head of the Department of Chemistry

University of Saskatchewan

110 Science Place

Saskatoon, Saskatchewan S7N 5C9 Canada

Dean

College of Graduate and Postdoctoral Studies

University of Saskatchewan

116 Thorvaldson Building, 110 Science Place

Saskatoon, Saskatchewan S7N 5C9 Canada

Acknowledgements

I would like to express my sincere appreciation to my supervisor, Prof. Lee D. Wilson, for the continuous support of my entire period of study and research, his inspiration, patience, enthusiasm, immense knowledge, and considerable effort to explain things clearly. Throughout the thesis-writing, he provided encouragement and sound advice. This thesis would not have been possible without him. I am also thankful to my supervisory committee for their sound advice, encouragement and constructive criticisms. Especially, I would like to thank Prof. Stephen Urquhart for providing a piece of essential equipment (High voltage DC power supply) for this thesis research. I am also thankful to Prof. Lim, Loong-Tak (University of Guelph, Guelph, Ontario) for graciously accepting to be my external examiner.

My sincere thanks also go to Drs. Sammynaiken, J. Maley, and Jianfeng (Peter) Zhu, and K. Thomas (Saskatchewan Structural Sciences Center (SSSC)) for their technical support. The Department of Chemistry is also acknowledged for allowing me to do research and further my scientific career. I am equally thankful to the entire faculty, staff and students of the department for their invaluable supports. Special thanks also go to the Natural Sciences and Engineering Research Council of Canada (Discovery Grant Number: RGPIN 2016-06197) for fully funding this research. I would like to especially thank the Saskatchewan Provincial Government for providing me with emergency financial aid during the lockdown due to the COVID-19 pandemic.

I am also thankful to my lab mates, Dr. Mohamed Mohamed, Dr. Abdalla Karoyo, Dr. Inimfon Udoetok, Dr. Leila Dehabadi, Dr. Asghar Dolatkah, Dr. Henry Agbovi, Savi Bhalkaran, Michael Danquah, Mohammad Mahaninia, Bahareh Vafakish, Dexu Kong, and Mostafa Solgi, for their diverse academic and non-academic support throughout my study.

Lastly, and most importantly, I would like to thank my parents for their long support during this PhD study.

Abstract

Chitosan-based nonwoven fibrous materials have found applications in many fields, especially in wastewater treatment, food packaging, wound dressing, and tissue engineering. Additive polymers, such as other biopolymers and synthetic polymers, are often used to improve the functional utility of chitosan-based fibrous materials. However, the interactions between chitosan and additive polymers are poorly understood since conventional characterization methods for solid-phase materials such as chitosan/biopolymers systems have some limitations, especially when overlapping spectral signatures are convoluted. Hence, the use of complementary methods and spectral deconvolution becomes important for the study of polymer interactions since it governs the structure and properties of such chitosan-based fibrous materials. The overall goal of this thesis research focuses on developing novel chitosan-based nonwoven micro-/nanofibrous materials with good water stability, various adsorption properties, and tunable surface features, along with an investigation of the formation of these materials. The overall goal can be divided into three objectives. In Chapter 4, carboxymethyl chitosan (chi)/alginate/poly(ethylene oxide) (PEO) self-assembled sponges (nonwoven microfibrinous materials) were prepared *via* freeze-drying. Their structurally modified forms were prepared *via* heat treatment (annealing). Original and thermally treated forms were characterized by a novel characterization method based on Raman spectral imaging. The results highlighted the multi-functional role of PEO and the value of Raman spectral imaging in understanding the interactions occurring for chitosan-based materials. In Chapter 5, various chi/hydroxypropyl- β -cyclodextrin (HP- β -CD) electrospun nanofibers were prepared and characterized by the Raman spectral imaging method (developed in Chapter 4) and other characterization methods. The results highlighted the formation of a supramolecular assembly (chi + HP- β -CD + solvent) and its importance to facilitate the electrospinning of chi/low molecular weight polymers systems. In Chapter 6, the chemically modified chitosan/low molecular weight (LMw) PEO electrospun nanofiber was prepared by forming the chi/LMw PEO assembly. A porous chitosan nanofiber was prepared through physical treatment. The results revealed that tunable porous surface features could be obtained using LMw PEO as a sacrificial template. Moreover, a dye uptake study with Methylene blue was conducted that revealed the porous fiber materials displayed enhanced uptake. The studies reported herein provide a greater understanding of the interactions between chitosan and additive polymers, which contribute to the design of novel chitosan-based materials with tunable surface features and various physicochemical properties.

Table of Contents

Permission to Use	i
Acknowledgements.....	ii
Abstract	iii
Table of Contents	iv
List of Tables.....	viii
List of Figures	ix
List of Schemes	xii
Abbreviations and Symbols.....	xiii
Abbreviations.....	xiii
Symbols	xv
CHAPTER 1	1
Introduction	1
1.1 Background.....	1
1.2 Knowledge gaps	2
1.3 Hypotheses	4
1.4 Objectives	5
1.5 Thesis organization	6
1.6 References	9
CHAPTER 2	16
Literature review	16
2.1 Chitosan and chitosan nonwoven fibrous materials	16
2.1.1 Chitosan	16
2.1.2 Chitosan nonwoven fibrous materials	18
2.2 Interactions in the polymer solution.....	21
2.2.1 Polymer-solvent interactions based on Flory-Huggins theory	22
2.2.2 Polymer-polymer interactions based on chain entanglements	23
2.2.3 Molecular interactions in the polymer solution	23
2.2.3.1 Hydrogen bonding	24
2.2.3.2 Hydrophobic effects.....	24
2.3 Freeze-drying method	25
2.4 Electrospinning method.....	28

2.4.1 Brief history of electrospinning	28
2.4.2 Basic theory of electrospinning	29
2.4.3 Factors regarding the electrospinnability of the system	32
2.5 Synthetic polymer in chitosan nonwoven fibrous materials.....	38
2.5.1 Background.....	38
2.5.2 Poly(ethylene oxide).....	39
2.6 Raman spectroscopy and Raman microimaging.....	41
2.6.1 Background of Raman spectroscopy	41
2.6.2 Data processing for obtaining Raman spectral imaging	44
2.7 References	46
CHAPTER 3	64
Experimental methods	64
3.1 Characterization methods	64
3.1.1 FT-IR	64
3.1.2 ¹³ C solid-state NMR spectroscopy	64
3.1.3 Differential scanning calorimetry (DSC)	64
3.1.4 Thermal gravimetric analysis (TGA)	65
3.1.5 Scanning electron microscopy (SEM)	65
3.1.7 Raman spectroscopy	65
3.1.8 Raman spectral imaging and Data processing	65
3.2 Experimental details of electrospinning and “in-house” electrospinning setup.....	66
CHAPTER 4	67
A structural study of self-assembled chitosan-based sponge materials	67
4.1 Introduction	68
4.2 Materials and Methods	70
4.2.1 Materials	70
4.2.2 Preparation of self-assembled chitosan-based sponge materials	71
4.2.2.1 Synthesis of carboxymethyl (cm-) modified chitosan (chi).....	71
4.2.2.2 Preparation 0.06% (w/v) 1:2 cm-chi/alg sponge (S-1)	71
4.2.2.3 Preparation 0.6% (w/v) 1:2 cm-chi/alg sponge (S-2)	71
4.2.2.4 Preparation cm-chi-alg/PEO 2:1 composite sponge (CP-1)	72
4.2.2.5 Preparation cm-chi-alg/PEO 5:1 composite sponge (CP-2)	72

4.2.2.6 Preparation of a physical mixture of cm-chi-alg/PEO	72
4.2.2.7 Preparation of physical treated sponge (TCP-1)	72
4.2.3 Characterization of prepared sponges	72
4.3 Results and Discussion	73
4.3.1 SEM images of self-assembled sponges	73
4.3.2 TGA results	74
4.3.3 Morphology and structure of the self-assembled (CP-1) and thermally annealed sponges (TCP-1)	76
4.3.4 Raman spectra and imaging results	78
4.3.5 Structure of self-assembled sponges before/after annealing	83
4.4 Conclusion	85
4.5 References	86
CHAPTER 5	92
A spectroscopic study of solid-phase chitosan/cyclodextrin-based electrospun fibers	92
5.1 Introduction	93
5.2 Materials and Methods	94
5.2.1. Materials	94
5.2.4 Characterization methods	96
5.3. Results and Discussion	96
5.3.1. SEM results	96
5.3.2. Determination of HP- β -CD content in the <i>as-spun</i> fibers	97
5.3.3. FT-IR results of <i>as-spun</i> fibers	98
5.3.4. TGA and DSC results of chi:HP- β -CD fiber	99
5.3.5. Raman spectroscopy results	100
5.3.6. Raman spectral imaging with dye probe (Rhodamine 6G)	102
5.3.7. Composition of chi:HP- β -CD electrospun fiber and its component interactions	105
5.4. Conclusion	106
5.5 References	107
CHAPTER 6	113
Preparation and characterization of grafted chitosan electrospun fibers	113
6.1 Introduction	114
6.2 Materials and Methods	115

6.2.1 Materials	115
6.2.2 Deacetylation of chitosan (Dachi)	116
6.2.3 Synthesis of salicylic acid grafted Dachi.....	116
6.2.4 Preparation of polymer solutions for electrospinning and corresponding electrospun nanofibers	116
6.2.5 Preparation of porous fibers via physical processes	117
6.3 Materials Characterization	117
6.4 Results and Discussion	118
6.4.1 Characterization of salicylic acid grafted Dachi (DachiSal)	118
6.4.2 SEM and surface component distribution of electrospun fibers.....	121
6.4.3 Characterization of prepared polymer solutions.....	123
6.4.4 Characterization of electrospun nanofibers	125
6.4.5 Morphology of DachiSal-2/PEO electrospun fiber treated with physical processing	127
6.4.6 <i>In-situ</i> MB dye uptake for various types of electrospun nanofibers.....	128
6.5 Conclusion.....	129
6.6 References	130
CHAPTER 7	136
Discussion, concluding remarks, and directions for future work.....	136
7.1 Integrated discussion of manuscript chapters	136
7.2 Conclusion.....	140
7.3 Future work	143
7.4 References	145
8 Appendix	153
8.1 Supplementary information	153
8.2 Copyright permissions	159

List of Tables

Table 5.1. Determination of HP- β -CD content in the as-spun chi:HP- β -CD fiber using ^1H NMR spectroscopy.....	98
--	----

List of Figures

Figure 2.1. Original chitosan and different types of carboxymethylated chitosan.	20
Figure 2.2. A schematic illustration of the formation of different polymer morphologies of the freeze-dried high molecular weight polymer dispersion.	28
Figure 2.3. A scheme of the basic electrospinning setup.	30
Figure 2.4. Categories of the molecular interaction-driven electrospinning. Reprinted (adapted) with permission from Ewaldz, E.; Brettmann, B. <i>Molecular Interactions in Electrospinning: From Polymer Mixtures to Supramolecular Assemblies</i> . ACS Appl. Polym. Mater. 2019, 1 (3), 298–308. ⁹² Copyright (2019) American Chemical Society.	37
Figure 2.5. (a) Synthesis of polyethylene oxide. (b) A schematic illustration of the <i>tgt</i> sequence of PEO in the crystalline state.	41
Figure 2.6. Raman and Rayleigh scattering of excitation at a frequency ν_0 . A molecular vibration in the sample is of frequency ν_j	43
Figure 4.1. Optical and SEM images of self-assembled sponge materials: A) S-1, and B) CP-1.	73
Figure 4.2. Photographs of various self-assembled sponges. From left to right, S-1 (0.06% w/v), S-2 (0.6% w/v), CP-1 (0.6% w/v), and CP-2 (0.75% w/v), respectively.	74
Figure 4.3. DTG plots of precursors and sponges: A) cm-chi, B) alg, C) PEO, D) Physical mixture (cm-chi, alg, and PEO), and E) CP-1.	75
Figure 4.4. A SEM image of a thermally treated sponge (TCP-1).	76
Figure 4.5. DSC profiles of biopolymer precursors, physical mixture (cm-chi, alg, and PEO), and self-assembled sponges (TCP-1, and CP-1). The left panel shows an expanded DSC trace for CP-1, PEO, TCP-1, and the physical mixture (cm-chi, alg, and PEO).	77
Figure 4.6. SEM images of CP-1 and TCP-1 before/after selective etching of PEO phase with deionized water. A) CP-1 and B) TCP-1 before solvent etching; C) CP-1 and D) TCP-1 after solvent etching.	78
Figure 4.7. Raman spectra (500 - 2000 cm^{-1}) of precursor components and self-assembled sponges: A) PEO, B) cm-chi, C) alg, D) S-1, E) physical mixture (cm-chi, alg, and PEO), F) CP-1 F), and G) TCP-1.	79
Figure 4.8. FT-IR spectra of precursors and sponge samples: A) cm-chi, B) alg, C) S-1, D) S-2, E) PEO, F) physical mixture (cm-chi, alg, and PEO), G) CP-1, and H) CP-2.	80
Figure 4.9. Raman spectral imaging results of CP-1 after etching with methylene blue (aq) and sample stack plots of Raman spectra centred at 450 cm^{-1} under static conditions ($\lambda_{\text{ex}} = 785\text{ nm}$). Raman images were constructed by use of spectral line intensity at variable Raman frequencies: A) cm-chi/alg region (427 cm^{-1}), B) MB region (447 cm^{-1}), C) cm-chi region (346 cm^{-1}), and D) PEO region (279 cm^{-1}), respectively.	82

Figure 4.10. Raman spectral imaging results of TCP-1 after etching with methylene blue (aq) and sample stack plots of Raman spectra centered at 450 cm^{-1} under static conditions ($\lambda_{\text{ex}} = 785\text{ nm}$). Raman images were constructed by use of spectral line intensity at variable Raman frequencies: A) cm-chi/alg region (427 cm^{-1}), B) MB region (447 cm^{-1}), C) cm-chi region (346 cm^{-1}), and D) PEO region (279 cm^{-1}), respectively..... 83

Figure 4.11. An illustrated view of the composition and structure of CP-1 and TCP-1. The red line represents PEO, red area represents PEO domains; blue line represents cm-chi and blue area represents cm-chi domains; yellow line represents alg, and yellow area represents alg domains.85

Figure 5.1. SEM images of chi/HP- β -CD fibers: A) chi:HP- β -CD 2:20 and B) chi:HP- β -CD 2:50. 97

Figure 5.2. FT-IR spectra of HP- β -CD (HPCD) and *as-spun* chi:HP- β -CD fiber (2:20 and 2:50, respectively) without normalization. The expanded region of the inset spectra is shown between 1250 and 900 cm^{-1} of the original spectra. 99

Figure 5.3. Thermal analysis results of *as-spun* chi: HP- β -CD fiber. A) DTG plots of HP- β -CD (HPCD) and chi:HP- β -CD 2:50 fiber (Chi:HPCD 2:50); and B) DSC profiles of chi, HP- β -CD (HPCD), physical mixture, and *as-spun* chi:HP- β -CD 2:50 fiber (Chi:HPCD 2:50). 100

Figure 5.4. Raman spectra of precursors and different chi:HP- β -CD fibers: A) HP- β -CD, B) pristine chi, C) *as-spun* chi:HP- β -CD 2:50 fiber, D) *as-spun* chi:HP- β -CD 2:20 fiber, E) chi:HP- β -CD 2:50 fiber after 3 days and F) chi:HP- β -CD 2:50 fiber after 3 months. The expanded region (Right side) covers the region between 770 and 990 cm^{-1} 102

Figure 5.5. Raman imaging results of dried chi:HP- β -CD 2:50 fiber after soaking with Rhodamine 6G in a benzene solution, where a sample Raman spectrum centered at 790 cm^{-1} was given under static conditions ($\lambda_{\text{ex}} = 785\text{ nm}$). The Raman image of the HP- β -CD area (A) was constructed by peak integration at 850 cm^{-1} . The Raman image of chi in area (B) was constructed by dividing the spectral intensity for Rhodamine 6G (610 cm^{-1}) against that for HP- β -CD (850 cm^{-1}) for each respective Raman spectrum, where a Raman spectrum is shown in panel C as an example..... 103

Figure 5.6. A combined Raman image from the spectral data for the chi region (Figure 5.5A) and the HP- β -CD region (Figure 5.5B). The sample spectrum was shown for different highlighted spectral regions: A) a chi rich domain, B) a chi/HP- β -CD mixed domain, and C) an HP- β -CD rich domain..... 104

Figure 6.1. Reaction scheme for the synthesis of salicylic acid grafted chi. **Panel I:** Solid-state ^{13}C CP-MAS NMR spectra of Dachichi (A), DachichiSal-1 (B), DachichiSal-2 (C), and ^{13}C MAS NMR spectrum of DachichiSal-2 (D). The inset graph is an expansion of the original spectra from 145 ppm to 175 ppm. Red region and blue region indicate carbonyl group (a) and carbonyl group (b), respectively. **Panel II:** FT-IR spectra of Dachichi, DachichiSal-1, and DachichiSal-2. The inset of the IR spectral region highlights 1800 to 1500 cm^{-1} spectrum. 120

Figure 6.2. SEM images and surface distributions of different electrospun fibers: Dachichi/PEO Panel (I), DachichiSal-1/PEO Panel (II), and DachichiSal-2/PEO Panel (III). Each panel contains the SEM and Raman images (a and b) generated by the Raman spectral intensity of the PEO peak (a) and Dachichi (b), and the Z score map (c) constructed by dividing the intensity of PEO peak (a) by

that of chi related peak (b). Colour scale for Z score map: white represents $z > 1.40$, red represents $0.30 < z < 1.40$, yellow represents $-0.30 < z < 0.30$, green represents $-1.40 < z < -0.30$, and black represents $z < -1.40$ 122

Figure 6.3. log-log plots of viscosity vs. shear rate of different total polymer concentration (1.2, 3, 3.6, 5.4, and 6 wt.%; where the ratio between chi and PEO remains at 2:1.) for various polymer solutions: Dachi/PEO (A), DachiSal-1/PEO (B), and DachiSal-2/PEO (C). Log-log Plot of specific viscosity (η_{sp}) at an 80 s^{-1} shear rate as a function of total polymer concentrations of electrospinning solutions (D). The slope, scaling value, is labeled beside the corresponding linear region. 124

Figure 6.4. (A) FT-IR spectra of PEO, Dachi, grafted Dachi, and grafted Dachi/PEO electrospun fibers; (B) Raman spectra of Dachi, grafted Dachi, and their electrospun fibers. 126

Figure 6.5. SEM images of DachiSal-2/PEO electrospun fiber after thermal treatment (A), DachiSal-2/PEO electrospun fiber **without** physical treatment after rinsing with water (B), and DachiSal-2/PEO electrospun fiber **with** physical treatment after rinsing with water (C). TEM images of DachiSal-2/PEO electrospun fiber **with** physical treatment after rinsing with water (D). 127

Figure 6.6. The Raman band intensity ratio variation at 1625 and 2382 cm^{-1} for various electrospun fibers imbibed in MB 90% D_2O /10% H_2O solution over time at ambient conditions. 129

Figure 7.1. Organization of the thesis research. 140

Figure A3.1. The picture of the “in-house” electrospinning apparatus. 153

Figure A4.1. DTG plots of precursor and fiber samples. A) cm-chi, B) alg, C) S-1, D) S-2, E) PEO, F) physical mixture (cm-chi, alg, PEO), G) CP-1, H) CP-2, and I) TCP-1. 154

Figure A4.2. A combined additive picture of methylene blue and cm-chitosan using Image-Pro® Plus 6.0. 155

Figure A5.1. ^1H NMR spectra of chi:HP- β -CD electrospun nanofibrous materials dissolved in 1% (w/w) THF/DMSO- d_6 solution for HP- β -CD content determination. **A)** chi:HP- β -CD 2:20 fiber and **B)** chi:HP- β -CD 2:50 fiber. 156

Figure A5.2. FT-IR spectrum (A) and DTG plot (B) of pristine chitosan. 157

List of Schemes

Scheme 4.1. Molecular structure of chi (i); cm-chi (ii) where R= -COCH₃ or H depending the degree of deacetylation; sodium alginate (iii); and PEO (iv). The terms m, n, p, x, y, and z are integer values that depend on the degree of polymerization of the respective polysaccharide. ... 70

Scheme 5.1. A schematic illustration of the electrospinning setup and molecular structure of the precursors: A) chi where R = -COCH₃ or H depending the degree of deacetylation, where n depends on the relative molecular weight of the biopolymer; B) HP-β-CD; and C) trifluoroacetic acid (TFA) is the solvent system. 95

Scheme 5.2. An illustrative view of the compositional change of a chi:HP-β-CD electrospun fiber over time, where the green arrow shows incremental temporal loss of trifluoroacetic acid (TFA). 106

Abbreviations and Symbols

Abbreviations

1D	One-dimensional
2D	Two-dimensional
3D	Three-dimensional
AC	Alternating Current
alg	Alginate
CCD	Charge Coupled Device
chi	Chitosan
cm	Carboxymethylated
CP-MAS	Cross Polarization with Magic Angle Spinning
CP-TOSS	Cross Polarization with Total Suppression of Spinning Sidebands
DA	Degree of Acetylation
Da	Deacetylation
DC	Direct Current
D-LAM	Disordered Longitudinal Acoustic Mode
DMF	Dimethylformamide
DRIFT	Diffuse Reflectance Infrared Fourier Transform
DSC	Differential Scanning Calorimetry
DTG	Differential Thermal Gravimetric Analysis
ESN	Electrospinning/Netting

FT-IR	Fourier Transform Infrared
G/M ratio	The ratio between guluronic acid and mannuronic acid in alginate
HFIP	1,1,1,3,3,3-hexafluoroisopropanol
HMw	High Molecular Weight
hydroxypropyl- β -cyclodextrin	HP- β -CD
KBr	Potassium Bromide
LMw	Low Molecular Weight
MAS	Magic Angle Spinning
MB	Methylene Blue
MOR	Morpholine
NFN	Nano-fiber/nets
NMR	Nuclear Magnetic Resonance
PAA	Poly(acrylic acid)
PAM	Polyacrylamide
PCL	Poly(ϵ -caprolactone)
PCs	Principal Components
PECs	Polyelectrolyte Complexes
PEG	Poly(ethylene glycol)
PEO	Poly(ethylene oxide)
PGA	Poly(galacturonic acid)
PLA	Poly(lactic acid)

PLGA	Poly(lactide-co-glycolide)
PMAA	Poly(methacrylic acid)
PS	Polystyrene
PVA	Poly(vinyl alcohol)
PVC	Poly(vinyl chloride)
PVP	Poly(N-vinyl pyrrolidone)
qNMR	Qualitative NMR
SEM	Scanning Electron Microscopy
TEM	Transmission Electron Microscopy
TFA	Trifluoroacetic acid
TGA	Thermal Gravimetric Analysis
THF	Tetrahydrofuran
XRD	X-ray diffraction
Symbols	
kDa	kilo-Dalton
pK_a	Dissociation constant
$\Delta\psi(\alpha)$	Difference in electrostatic potential
α	Degree of dissociation
k_B	Boltzmann constant
T	Absolute temperature
e	electron charge
pK_o	Intrinsic dissociation

χ		Polymer-solvent interaction parameter
χ_{12}		Flory-Huggins thermodynamic interaction parameter
M		Molecular weight
M_c		Critical molecular weight
M_e		Entanglement molecular weight for polymer melts
C		Polymer solution concentration
C^*		Critical entanglement concentration
$(M_e)_{soln}$		Entanglement molecular weight for polymer solutions
ϕ_p		Polymer volume fraction
P_e		Electrostatic pressure
ε		Dielectric constant
E		Intensity of the electric field
P_c		Capillary pressure
γ		Surface tension
r		Mean radius of curvature of the surface
V_c		Critical voltage
H		Distance between the tip of the spinneret and the collector
L		Length of the spinneret
R		Outer radius of the spinneret

$(n_e)_{soln}$		Solution entanglement number
M_w		Weight-average molecular weight
η_{sp}		Specific viscosity
η_{soln}		Viscosity of the polymer solution
η_{solv}		Viscosity of the solvent
c_e		Entanglement concentration
h		Planck's constant
ν_k		Classical frequency of the molecular motion
ν_ν		Raman frequency as the result of inelastic scattering
$\bar{\nu}_\nu$		Raman wavenumber
c		Velocity of light
λ_ν		Wavelength of light

CHAPTER 1

Introduction

1.1 Background

Nonwoven fibrous materials can be described as highly porous structures with interlocked continuous pore volume, which have drawn increasing attention because of their high surface areas, interconnective pore structures, and diverse morphologies.¹⁻⁵ Synthetic polymers and biopolymers have been used to prepare nonwoven fibrous materials. Since the 1990s, due to environmental concerns of synthetic polymers, nonwoven fibrous materials using biopolymers as raw materials have multiplied because biopolymers are biodegradable and obtained from renewable natural sources, including cotton, wood, hemp, flax, fungi, bacteria, tunicate, crustacean shells, silkworm, algae, *etc.*⁶⁻¹³ Chitosan (chi)-based materials are among the most interesting nonwoven micro-/nano- biopolymer fibrous materials because of chitosan's abundance, versatility, and antimicrobial properties. Chi-based fibrous materials have been used in many different fields, especially in wastewater treatment¹⁴, food packaging^{2,9}, wound dressing¹⁵⁻²¹, and tissue engineering^{22,23}, since chi has many unique properties, which will be further discussed in Chapter 2.

Unlike synthetic polymers, thermal processes like melt blowing are not suitable for preparing biopolymer fibrous materials because biopolymers can be degraded at a high temperature.² Therefore, non-thermal methods, such as electrospinning, solution blowing, wet spinning, and freeze-drying, are often used to produce nonwoven micro-/nano- biopolymer fibrous materials.² For chi-based nonwoven micro-/nano- fibrous materials, electrospinning and freeze-drying, are usually applied in the literature. Meanwhile, additive polymers, such as synthetic polymers or other biopolymers, are employed in chi-based fibrous materials for many purposes: to accommodate different mechanical properties; to tune the morphology and the physicochemical properties of chi-based materials for various applications; or to facilitate the fiber formation for materials prepared by electrospinning.^{2,9,15,24-28} This thesis will focus on two chi systems obtained by these two methods. The first system is prepared by a freeze-drying method, which is chi/sodium alginate (alg)/poly(ethylene oxide) (PEO) sponges (nonwoven microfibrinous materials). The second one is prepared by the electrospinning method, including two examples:

chitosan/hydroxypropyl- β -cyclodextrin (chi/HP- β -CD) electrospun nanofibrous materials; and the other one is chi/PEO electrospun nanofibrous materials.

1.2 Knowledge gaps

However, four major knowledge gaps are hindering the material design of such fibrous materials. Because aqueous media is involved in most of the applications of chi-based fibrous materials, uncontrolled dissolution is a significant challenge for these fibrous materials.^{29,30} The occurrence of uncontrolled dissolution leads to unsatisfactory performance due to a constituent component's exfoliation (or loss). Further modification (chemical and physical) of chi-based materials can be applied to resolve this issue. All the modification approaches depend on an understanding of the interaction between chi and the additive polymer. The first knowledge gap is that the nature of the interactions between chi and the additive polymer is poorly understood as conventional characterization methods have limitations regarding the deconvolution of critical spectral signatures to identify solid-state products containing structurally similar components. Historically, many reported literature studies on the interaction between chi and the additive polymer focused on solution-based characterization methods such as solution-based NMR spectroscopy.^{31–33} A question remains as to whether solution-based methods are relevant to the solid fibrous material's structure, although solution-based methods provide great insight into each component's interaction in the solution. Polymer-polymer interactions for solid fibrous materials may be distinct from those in the solution for two reasons: one is that solvent molecules intervene in polymer-polymer interactions; the other one is that new interactions are established for solid materials during the freeze-drying and electrospinning process.^{34–36}

Moreover, some solid-based characterization methods such as FT-IR spectroscopy and differential scanning calorimetry (DSC) may limit the level of detailed structural insight for chi-based materials. FT-IR spectra of chi overlap with other structurally similar spectral signatures of components (other biopolymers) in 4000–400 cm^{-1} , making the interaction between components challenging to interpret. As for DSC, the bound water in chi may skew the DSC results, weakening the ability to obtain meaningful structural information for chi-based materials by DSC.^{37,38} X-ray diffraction (XRD) provides limited structural information for amorphous biopolymer composites, while microscopy methods such as scanning electron microscopy (SEM) merely afford the characterization of the surface morphology of materials but no spectral information. It is noted that

it is difficult to directly connect spectral information (chemical and physical interactions among each component) with the morphology of materials, limiting the understanding of the solid fibrous materials' structure. Therefore, Raman spectral imaging has been widely used to study complex biological samples and composite nanofibrous materials, where the relationship between the morphology of the samples and their spectral information can be correlated.^{39–43} The change of the samples' morphology could be related to spectral variations among the samples, which provides more in-depth knowledge about the contribution of constituent molecular components of the sample to its morphology. Different dye solutions can be used to distinguish structurally similar biopolymer constituents due to their different biopolymer-dye interactions, such as electrostatic interactions, ion-dipole interactions or hydrogen bonding.^{39,44–47}

The second knowledge gap is that the underlying interaction for promoting the electrospinning of chi/HP- β -CD electrospun fibrous materials is not well understood. According to the study by Burns et al. on chi/HP- β -CD electrospun fibrous materials³¹, the mixture of different ratios of chi and HP- β -CD was reported to be electrospinnable in trifluoroacetic acid (TFA). This study also suggests that hydrogen bonding is not an essential factor in the chi/HP- β -CD system's electrospinning process, in contrast to the pure HP- β -CD system where hydrogen bonding among HP- β -CD molecules plays a vital role in the electrospinning process.^{33,48,49} However, due to the study by Burns et al. focusing on the solution-based characterization method (NMR spectroscopy) and the conventional characterization method (FT-IR), the potential interaction between each component leading to the formation of such electrospun fiber has not been fully revealed, which prevents the development of such electrospun materials.

Surface porous morphology has been introduced to electrospun microfiber using high volatility solvents⁵⁰ or controlling the environment's humidity during electrospinning.⁵¹ A post-treatment method has also been used to create porous surface morphology on the PEO blended electrospun microfiber. During the post-treatment, the porous surface morphology originates from removing recrystallized PEO domains by water after the thermal treatment of PEO blended electrospun microfiber.^{52,53} The third knowledge gap is that this post-treatment method has not been used for the electrospun nanofiber because melted PEO domains in the electrospun nanofibrous material coalesce during recrystallization prohibits the application of this method for the electrospun nanofiber.⁵² The coalescence of melted PEO domains could be limited using

relatively low molecular weight PEO as the additive polymer in the electrospinning process. Low molecular weight PEO possesses shorter polymer chains than high molecular weight species leading to the isolated PEO domain in the nanofiber.⁵⁴ Therefore, this post-treatment method could be applied chi/PEO electrospun nanofibrous materials, which in turn increases the utility of PEO in the chi/PEO system as PEO usually serves only one role as a fiber formation aide in the chi/PEO electrospun fibrous material and is preferably removed after the formation of such electrospun fibers.^{27,55}

The fourth knowledge gap is that only high molecular weight PEO has been used in current chi/PEO systems in the literature. For the chi/PEO system, PEO with a molecular weight above 400 kDa (HMw PEO) in the literature has been employed to obtain electrospun fibers, whereas PEO with a molecular weight \approx 100 kDa (LMw PEO) and below is generally considered inadequate to aide in the formation of electrospun fibers. The difficulty with LMw PEO relates to the weak PEO-PEO chain entanglement, which prevents the formation of electrospun fibers, in contrast to the strong PEO-PEO chain entanglement of HMw PEO.^{56,57} This knowledge gap restricts the material design of chi-based electrospun fibers. Supramolecular interactions as an essential solution to facilitate the electrospinning of low molecular weight polymers has recently been recognized (detailed discussion in section 2.4.3, Chapter 2).⁵⁸

1.3 Hypotheses

Hypothesis #1: Enhancement of the interactions among all constituents for chi-based nonwoven fibrous composites will occur in the thermal treatment, leading to improved water stability. The insight into these structural changes could be studied using Raman spectral imaging with suitable dye probes (corresponding to the first knowledge gap).

Hypothesis #2: A multicomponent (Chi-TFA-HP- β -CD) assembly will exist in the chi/HP- β -CD eletrospun nanofiber, attributed to the electrospinning of the chi/HP- β -CD system. The use of solid-state characterization methods, including Raman spectral imaging with suitable dye probes, could be used to investigate the structure of the assembly in the chi/HP- β -CD system (corresponding to the second knowledge gap).

Hypothesis #3: Physical processes will create porous features on the surface of the chi/LMw PEO electrospun nanofiber (corresponding to the third knowledge gap).

Hypothesis #4: A supramolecular assembly between chemically modified chi and LMw PEO will facilitate the electrospinning of chi/LMw PEO system (corresponding to the fourth knowledge gap).

1.4 Objectives

The overall goal of this thesis research focuses on developing novel chi-based nonwoven micro-/nanofibrous materials with good water stability, various adsorption properties, and tunable surface features, along with an investigation of the formation of these materials. The overall goal can be divided into three objectives. Each objective corresponds to a specific hypothesis mentioned in Section 1.3.

Objective #1: The structure of chi-based self-assembled sponges (nonwoven microfibrillar materials) prepared *via* freeze-drying and their thermally treated forms is investigated using a novel characterization method based on Raman spectral imaging to understand the role of the additive polymer and the interaction between chi and the additive polymer in the materials. This objective relates to Hypothesis #1 and has three short-term goals:

- i) preparation of carboxymethyl chi/alginate/PEO self-assembled sponges *via* freeze-drying;
- ii) preparation of their structurally modified forms *via* heat treatment (annealing);
- iii) a structural study of composites at variable composition is carried out using Raman spectral imaging in conjunction with suitable dye probes.

Objective #2: The interactions leading to the formation of the chi/HP- β -CD electrospun fiber are investigated using solid-state characterization methods, including Raman spectral imaging with a suitable dye probe. This objective relates to Hypothesis #2 and has two short-term goals:

- i) preparation of chi/HP- β -CD electrospun fibers at variable mass ratios (mass ratios between chi and HP- β -CD in nonaqueous media (TFA as a solvent);
- ii) the characterization of the electrospun fibers in the solid-state using thermal analysis and spectroscopic (FT-IR and Raman) methods and Raman spectral imaging assisted by the use of a rhodamine dye probe.

Objective #3: The structure of the chemically modified chi/LMw PEO electrospun nanofiber and its porous nanofiber prepared by utilizing a LMw PEO additive are investigated, which relates to Hypothesis #3 and #4. This objective can be divided into four short-term goals:

- i) The first short-term goal relates to the synthesis of salicylic acid grafted chi and the preparation of electrospun fibers from blends of grafted chi with LMw PEO (Mw \approx 100 kDa).
- ii) The second short-term goal is to carry out a structural characterization study of the electrospun fibers to ascertain the interactions between the grafted chi and PEO.
- iii) The third short-term goal is to prepare a porous chi fiber using a physical method in which the grafted chi/PEO electrospun fiber is treated thermally, followed by the controlled removal of PEO with the solvent.
- iv) The fourth short-term goal is to investigate different uptake properties of electrospun chi fibers prepared in this study towards methylene blue (MB) to demonstrate the effects of salicylic acid and the addition of porous features on chi-based materials.

1.5 Thesis organization

Chapter 2 is the literature review section for this thesis, which provides relevant background information. Chapter 3 is the experimental methods. Chapters 4-6 contain formatted, edited articles (including both published articles and manuscripts in preparation). Chapter 7 is an integrated discussion of manuscript chapters (Chapters 4-6), conclusion, and proposed future work. The published articles and manuscript in preparation are outlined below:

1. Xue, C.; Wilson, L. D. A Structural Study of Self-Assembled Chitosan-Based Sponge Materials. *Carbohydr. Polym.* **2019**, 206, 685–693.
<https://doi.org/10.1016/j.carbpol.2018.10.111>.
2. Xue, C.; Wilson, L. D. A Spectroscopic Study of Solid-Phase Chitosan/Cyclodextrin-Based Electrospun Fibers. *Fibers* **2019**, 7 (5). <https://doi.org/10.3390/FIB7050048>.
3. Xue, C.; Wilson, L. D. Preparation and Characterization of Grafted Chitosan Composite Porous Electrospun Fibers. *Carbohydr. Polym.* **2021**. (under review).

A summary of the research work and a description of each author's contributions are presented at the beginning of each chapter. Besides, the justification for the completion of the general objective of the Ph.D. thesis is also included. A summary of each chapter is given below.

Chapter 2 is the literature review, and it discusses the concepts used in the thesis. Firstly, chi and its properties are discussed. Secondly, chi nonwoven fibrous materials and their applications are introduced in terms of preparation procedures: the methods used for the solubilization of chi; the examples of chi nonwoven fibrous materials prepared by electrospinning and freeze-drying; the post-treatment for enhancing the stability of chi nonwoven fibrous materials in aqueous materials. Moreover, the freeze-drying method's background is introduced, followed by an overview of the conditions during freeze-drying, which controls the freeze-dried product's morphology. The background of electrospinning, including various conditions in the electrospinning process, is discussed by highlighting different approaches to facilitate electrospun fibers formation. Furthermore, the purpose of using synthetic polymers as additive polymers in chi nonwoven materials is described, where PEO and its related properties are the main focus of this section. Finally, Raman spectroscopy and its applications are briefly discussed, followed by Raman spectral imaging, including data processes for Raman spectral imaging and its applications.

Chapter 3 is the experimental methods and section. The details of characterization methods and the details of an "in-house" electrospinning setup used in the thesis are summarized to avoid repeating the experimental methods that would otherwise appear within the manuscript chapters (Chapters 4-6).

Chapter 4, relating to Objective #1, focused on the preparation of freeze-dried chi-based sponges (nonwoven microfibrinous materials) with and without annealing to compare their structural and physicochemical properties that highlighted the utility of Raman spectral imaging in conjunction with a suitable dye probe as an effective and facile method to reveal structural features for chi-based microfibrinous materials before and after thermal annealing. The multi-functional role of PEO, such as a sacrificial template and a protective barrier in the materials, was evaluated using solvent etching. The treated materials' improved stability reveals their potential utility for applications such as wounding dressing and tissue engineering in aqueous media. Raman spectral imaging with suitable dye probes as a powerful characterization tool was used in Chapter 5 to

study the structure of chi-based electrospun nanofibrous materials. PEO as the sacrificial template for creating porous morphology supports the works done in Chapter 6.

Chapter 5 corresponds to Objective #2. In this study, two chi/HP- β -CD nanofibers (mass ratio between chi and HP- β -CD = 2:20 and 2:50) were prepared from a mixture of chi and HP- β -CD using TFA as a solvent by electrospinning. The Raman spectral imaging mentioned in Chapter 4 and other complementary characterization methods, including thermal analyses (thermal gravimetric analysis (TGA) and differential scanning calorimetry (DSC)) and spectroscopic methods (Raman/IR), were used to evaluate the structure and composition of the fiber assemblies in the solid-state. This study highlighted the multi-functional role of TFA as a solvent, an electrostatically bound pendant group to chi, and a guest molecule binding with HP- β -CD. The experimental results also inferred the formation of a ternary supramolecular assembly based on unique host-guest interactions. This work contributes further insight on the formation and stability of such ternary (chi + HP- β -CD + TFA) electrospun fibers and their potential utility as “smart” fiber coatings for advanced applications. The potential application of supramolecular assembly between chi and an additive polymer in the electrospinning process supports the works done in Chapter 6.

Chapter 6 relates to Objective #3. Chi electrospun fibers have been found in medical applications and food packaging materials despite the technical challenges in their preparation. PEO is an additive polymer that is commonly used to facilitate the electrospun fiber formation of chi because it offers PEO-PEO chain entanglement to aid such electrospun fibers formation. Therefore, PEO with a molecular weight greater than 400 kDa is employed to ensure chi electrospun fiber formation. LMw PEO (Mw less than 100 kDa) can be employed to create porous surface features on chi nanofibrous materials, but the chi/LMw PEO system is not suitable for electrospinning. Therefore, an alternative method that utilizes LMw PEO is required. Herein, chi grafted with salicylic acid was prepared to afford improved electrospun fiber formation with LMw PEO (Mw \approx 100 kDa). Unmodified (pristine) chi did not yield electrospun fibers with LMw PEO under the conditions reported in this study. The investigation of the interactions between unmodified or grafted chi with PEO revealed that supramolecular assemblies were formed between grafted chi and PEO, contributing to chi electrospun fiber formation. The supramolecular assembly could offer an alternative approach for the design of chi electrospun fibers. Moreover, tunable

porous surface features could be designed for electrospun chi fibers *via* physical processing that employs PEO as a sacrificial template, as reported herein.

Chapter 7 provides an overview of the thesis research results and discusses how Chapters 4-6 connect with the various objectives and the thesis research's overall goal. Chapter 7 concludes this thesis, outlines the advancement of novel chi-based nonwoven micro-/nano- fibrous materials mentioned in the thesis, and suggestions for future research.

1.6 References

- (1) Burger, C.; Hsiao, B. S.; Chu, B. Nanofibrous Materials And Their Applications. *Annu. Rev. Mater. Res.* **2006**, *36* (1), 333–368.
<https://doi.org/10.1146/annurev.matsci.36.011205.123537>.
- (2) Kumar, A.; Sinha-Ray, S. A Review on Biopolymer-Based Fibers via Electrospinning and Solution Blowing and Their Applications. *Fibers* **2018**, *6* (3), 1–53.
<https://doi.org/10.3390/fib6030045>.
- (3) Teo, W. E.; Ramakrishna, S. A Review on Electrospinning Design and Nanofibre Assemblies. *Nanotechnology* **2006**, *17* (14), R89–R106. <https://doi.org/10.1088/0957-4484/17/14/R01>.
- (4) Kim, M. Y.; Lee, J. Chitosan Fibrous 3D Networks Prepared by Freeze Drying. *Carbohydr. Polym.* **2011**, *84* (4), 1329–1336.
<https://doi.org/10.1016/j.carbpol.2011.01.029>.
- (5) Ding, J.; Zhang, J.; Li, J.; Li, D.; Xiao, C.; Xiao, H.; Yang, H.; Zhuang, X.; Chen, X. Electrospun Polymer Biomaterials. *Prog. Polym. Sci.* **2019**, *90*, 1–34.
<https://doi.org/10.1016/j.progpolymsci.2019.01.002>.
- (6) Hearle, J. W. S. Fiber Production. In *Materials Science And Engineering-Volume II*; Rawlings, R. D., Ed.; Encyclopedia of Life Support Systems; Physical Sciences, Eng; EOLSS Publishers Company Limited: Oxford, 2009; p 296.
- (7) John, M. J.; Thomas, S. Biofibres and Biocomposites. *Carbohydr. Polym.* **2008**, *71* (3), 343–364. <https://doi.org/10.1016/j.carbpol.2007.05.040>.

- (8) Faruk, O.; Bledzki, A. K.; Fink, H. P.; Sain, M. Biocomposites Reinforced with Natural Fibers: 2000-2010. *Prog. Polym. Sci.* **2012**, *37* (11), 1552–1596. <https://doi.org/10.1016/j.progpolymsci.2012.04.003>.
- (9) Sampath, U. G. T. M.; Ching, Y. C.; Chuah, C. H.; Sabariah, J. J.; Lin, P. C. Fabrication of Porous Materials from Natural/Synthetic Biopolymers and Their Composites. *Materials (Basel)*. **2016**, *9* (12), 1–32. <https://doi.org/10.3390/ma9120991>.
- (10) Eichhorn, S. J.; Dufresne, A.; Aranguren, M.; Marcovich, N. E.; Capadona, J. R.; Rowan, S. J.; Weder, C.; Thielemans, W.; Roman, M.; Renneckar, S.; Gindl, W.; Veigel, S.; Keckes, J.; Yano, H.; Abe, K.; Nogi, M.; Nakagaito, A. N.; Mangalam, A.; Simonsen, J.; Benight, A. S.; Bismarck, A.; Berglund, L. A.; Peijs, T. Review: Current International Research into Cellulose Nanofibres and Nanocomposites. *J. Mater. Sci.* **2010**, *45* (1), 1–33. <https://doi.org/10.1007/s10853-009-3874-0>.
- (11) Bledzki, A. .; Gassan, J. Composites Reinforced with Cellulose. *Prog. Polym. Sci* **1999**, *24*, 221–274.
- (12) Pandey, V.; Haider, T.; Jain, P.; Gupta, P. N.; Soni, V. Silk as a Leading-Edge Biological Macromolecule for Improved Drug Delivery. *J. Drug Deliv. Sci. Technol.* **2020**, *55*, 101294. <https://doi.org/10.1016/j.jddst.2019.101294>.
- (13) Zhang, T.-W.; Tian, T.; Shen, B.; Song, Y.-H.; Yao, H.-B. Recent Advances on Biopolymer Fiber Based Membranes for Lithium-Ion Battery Separators. *Compos. Commun.* **2019**, *14*, 7–14. <https://doi.org/10.1016/j.coco.2019.05.003>.
- (14) Elsabee, M. Z.; Naguib, H. F.; Morsi, R. E. Chitosan Based Nanofibers, Review. *Mater. Sci. Eng. C* **2012**, *32* (7), 1711–1726. <https://doi.org/10.1016/j.msec.2012.05.009>.
- (15) Naseri-Nosar, M.; Ziora, Z. M. Wound Dressings from Naturally-Occurring Polymers: A Review on Homopolysaccharide-Based Composites. *Carbohydr. Polym.* **2018**, *189*, 379–398. <https://doi.org/10.1016/j.carbpol.2018.02.003>.
- (16) Sarhan, W. A.; Azzazy, H. M. E. High Concentration Honey Chitosan Electrospun Nanofibers: Biocompatibility and Antibacterial Effects. *Carbohydr. Polym.* **2015**, *122*, 135–143. <https://doi.org/10.1016/j.carbpol.2014.12.051>.

- (17) Zhou, Y.; Yang, D.; Chen, X.; Xu, Q.; Lu, F.; Nie, J. Electrospun Water-Soluble Carboxyethyl Chitosan/Poly(Vinyl Alcohol) Nanofibrous Membrane as Potential Wound Dressing for Skin Regeneration. *Biomacromolecules* **2008**, *9* (1), 349–354. <https://doi.org/10.1021/bm7009015>.
- (18) Chen, J. P.; Chang, G. Y.; Chen, J. K. Electrospun Collagen/Chitosan Nanofibrous Membrane as Wound Dressing. *Colloids Surfaces A Physicochem. Eng. Asp.* **2008**, *313–314*, 183–188. <https://doi.org/10.1016/j.colsurfa.2007.04.129>.
- (19) Ding, F.; Deng, H.; Du, Y.; Shi, X.; Wang, Q. Emerging Chitin and Chitosan Nanofibrous Materials for Biomedical Applications. *Nanoscale* **2014**, *6* (16), 9477–9493. <https://doi.org/10.1039/C4NR02814G>.
- (20) Chen, R. N.; Wang, G. M.; Chen, C. H.; Ho, H. O.; Sheu, M. T. Development of N,O-(Carboxymethyl)Chitosan/Collagen Matrixes as a Wound Dressing. *Biomacromolecules* **2006**, *7* (4), 1058–1064. <https://doi.org/10.1021/bm050754b>.
- (21) Kalantari, K.; Afifi, A. M.; Jahangirian, H.; Webster, T. J. Biomedical Applications of Chitosan Electrospun Nanofibers as a Green Polymer – Review. *Carbohydr. Polym.* **2019**, *207*, 588–600. <https://doi.org/10.1016/j.carbpol.2018.12.011>.
- (22) Chen, Z.; Mo, X.; Qing, F. Electrospinning of Collagen-Chitosan Complex. *Mater. Lett.* **2007**, *61* (16), 3490–3494. <https://doi.org/10.1016/j.matlet.2006.11.104>.
- (23) Pellá, M. C. G.; Lima-Tenório, M. K.; Tenório-Neto, E. T.; Guilherme, M. R.; Muniz, E. C.; Rubira, A. F. Chitosan-Based Hydrogels: From Preparation to Biomedical Applications. *Carbohydr. Polym.* **2018**, *196*, 233–245. <https://doi.org/10.1016/j.carbpol.2018.05.033>.
- (24) Muzzarelli, C.; Muzzarelli, R. A. A. Natural and Artificial Chitosan-Inorganic Composites. *J. Inorg. Biochem.* **2002**, *92* (2), 89–94. [https://doi.org/10.1016/S0162-0134\(02\)00486-5](https://doi.org/10.1016/S0162-0134(02)00486-5).
- (25) Muzzarelli, R. A. A.; Morganti, P.; Morganti, G.; Palombo, P.; Palombo, M.; Biagini, G.; Belmonte, M. M.; Giantomassi, F.; Orlandi, F.; Muzzarelli, C. Chitin Nanofibrils/Chitosan Glycolate Composites as Wound Medicaments. *Carbohydr. Polym.* **2007**, *70* (3), 274–

284. <https://doi.org/10.1016/j.carbpol.2007.04.008>.
- (26) Zhang, H.; Li, S.; White, C. J. B.; Ning, X.; Nie, H.; Zhu, L. Studies on Electrospun Nylon-6/Chitosan Complex Nanofiber Interactions. *Electrochim. Acta* **2009**, *54* (24), 5739–5745. <https://doi.org/10.1016/j.electacta.2009.05.021>.
- (27) Zhao, X.; Chen, S.; Lin, Z.; Du, C. Reactive Electrospinning of Composite Nanofibers of Carboxymethyl Chitosan Cross-Linked by Alginate Dialdehyde with the Aid of Polyethylene Oxide. *Carbohydr. Polym.* **2016**, *148*, 98–106. <https://doi.org/10.1016/j.carbpol.2016.04.051>.
- (28) Yihan, W.; Minato, W. Nanofiber Fabrication Techniques and Its Applicability to Chitosan. *Prog. Chem.* **2014**, *26* (11), 1821–1831. <https://doi.org/10.7536/PC140636>.
- (29) Croisier, F.; Jérôme, C. Chitosan-Based Biomaterials for Tissue Engineering. *Eur. Polym. J.* **2013**, *49* (4), 780–792. <https://doi.org/10.1016/j.eurpolymj.2012.12.009>.
- (30) Sun, W.; Chen, G.; Wang, F.; Qin, Y.; Wang, Z.; Nie, J.; Ma, G. Polyelectrolyte-Complex Multilayer Membrane with Gradient Porous Structure Based on Natural Polymers for Wound Care. *Carbohydr. Polym.* **2018**, *181*, 183–190. <https://doi.org/10.1016/J.CARBPOL.2017.10.068>.
- (31) Burns, N. A.; Burroughs, M. C.; Gracz, H.; Pritchard, C. Q.; Brozena, A. H.; Willoughby, J.; Khan, S. A. Cyclodextrin Facilitated Electrospun Chitosan Nanofibers. *RSC Adv.* **2015**, *5* (10), 7131–7137. <https://doi.org/10.1039/c4ra09662b>.
- (32) Mengistu Lemma, S.; Bossard, F.; Rinaudo, M. Preparation of Pure and Stable Chitosan Nanofibers by Electrospinning in the Presence of Poly(Ethylene Oxide). *Int. J. Mol. Sci.* **2016**, *17* (11), 1790. <https://doi.org/10.3390/ijms17111790>.
- (33) Topuz, F.; Uyar, T. Influence of Hydrogen-Bonding Additives on Electrospinning of Cyclodextrin Nanofibers. *ACS Omega* **2018**, *3* (12), 18311–18322. <https://doi.org/10.1021/acsomega.8b02662>.
- (34) Shenoy, S. L.; Bates, W. D.; Frisch, H. L.; Wnek, G. E. Role of Chain Entanglements on Fiber Formation during Electrospinning of Polymer Solutions: Good Solvent, Non-

- Specific Polymer-Polymer Interaction Limit. *Polymer (Guildf)*. **2005**, *46* (10), 3372–3384. <https://doi.org/10.1016/j.polymer.2005.03.011>.
- (35) Han, J.; Zhou, C.; Wu, Y.; Liu, F.; Wu, Q. Self-Assembling Behavior of Cellulose Nanoparticles during Freeze-Drying: Effect of Suspension Concentration, Particle Size, Crystal Structure, and Surface Charge. *Biomacromolecules* **2013**, *14* (5), 1529–1540. <https://doi.org/10.1021/bm4001734>.
- (36) Jiang, C.; Wang, Z.; Zhang, X.; Zhu, X.; Nie, J.; Ma, G. Crosslinked Polyelectrolyte Complex Fiber Membrane Based on Chitosan-Sodium Alginate by Freeze-Drying. *RSC Adv.* **2014**, *40* (78), 41551–41560. <https://doi.org/10.1039/c4ra04208e>.
- (37) Sakurai, K. Glass Transition Temperature of Chitosan and Miscibility of Chitosan/Poly(N-Vinyl Pyrrolidone) Blends. *Polymer (Guildf)*. **2000**, *41* (19), 7051–7056. [https://doi.org/10.1016/S0032-3861\(00\)00067-7](https://doi.org/10.1016/S0032-3861(00)00067-7).
- (38) Dong, Y.; Ruan, Y.; Wang, H.; Zhao, Y.; Bi, D. Studies on Glass Transition Temperature of Chitosan with Four Techniques. *J. Appl. Polym. Sci.* **2004**, *93* (4), 1553–1558. <https://doi.org/10.1002/app.20630>.
- (39) Bocklitz, T. W.; Guo, S.; Ryabchykov, O.; Vogler, N.; Popp, J. Raman Based Molecular Imaging and Analytics: A Magic Bullet for Biomedical Applications!? *Anal. Chem.* **2016**, *88* (1), 133–151. <https://doi.org/10.1021/acs.analchem.5b04665>.
- (40) Ando, M.; Hamaguchi, H. Molecular Component Distribution Imaging of Living Cells by Multivariate Curve Resolution Analysis of Space-Resolved Raman Spectra. *J. Biomed. Opt.* **2014**, *19* (1). <https://doi.org/10.1117/1.JBO.19.1.011016>.
- (41) Chylinska, M.; Szymanska-Chargot, M.; Zdunek, A. Imaging of Polysaccharides in the Tomato Cell Wall with Raman Microspectroscopy. *Plant Methods* **2014**, *10*. <https://doi.org/10.1186/1746-4811-10-14>.
- (42) Szymanska-Chargot, M.; Chylinska, M.; Pieczywek, P. M.; Roesch, P.; Schmitt, M.; Popp, J.; Zdunek, A. Raman Imaging of Changes in the Polysaccharides Distribution in the Cell Wall during Apple Fruit Development and Senescence. *Planta* **2016**, *243* (4), 935–945. <https://doi.org/10.1007/s00425-015-2456-4>.

- (43) Smith, G. P. S.; McLaughlin, A. W.; Clarkson, A. N.; Gordon, K. C.; Walker, G. F. Raman Microscopic Imaging of Electrospun Fibers Made from a Polycaprolactone and Polyethylene Oxide Blend. *Vib. Spectrosc.* **2017**, *92*, 27–34. <https://doi.org/10.1016/j.vibspec.2017.05.002>.
- (44) Humphrey, C. D.; Pittman, F. E. A Simple Methylene Blue-Azure II-Basic Fuchsin Stain for Epoxy-Embedded Tissue Sections. *Stain Technol.* **1974**, *49* (1), 9–14. <https://doi.org/10.3109/10520297409116929>.
- (45) Mahaninia, M. H.; Wilson, L. D. Modular Cross-Linked Chitosan Beads with Calcium Doping for Enhanced Adsorptive Uptake of Organophosphate Anions. *Ind. Eng. Chem. Res.* **2016**, *55* (45), 11706–11715. <https://doi.org/10.1021/acs.iecr.6b02814>.
- (46) Kwon, J. H.; Wilson, L. D.; Sammynaiken, R. Synthesis and Characterization of Magnetite and Activated Carbon Binary Composites. *Synth. Met.* **2014**, *197*, 8–17. <https://doi.org/10.1016/J.SYNTHMET.2014.08.010>.
- (47) Dehabadi, L.; Karoyo, A. H.; Wilson, L. D. Spectroscopic and Thermodynamic Study of Biopolymer Adsorption Phenomena in Heterogeneous Solid–Liquid Systems. *ACS Omega* **2018**, *3* (11), 15370–15379. <https://doi.org/10.1021/acsomega.8b01663>.
- (48) Celebioglu, A.; Uyar, T. Cyclodextrin Nanofibers by Electrospinning. *Chem. Commun.* **2010**, *46* (37), 6903–6905. <https://doi.org/10.1039/c0cc01484b>.
- (49) Celebioglu, A.; Uyar, T. Electrospinning of Polymer-Free Nanofibers from Cyclodextrin Inclusion Complexes. *Langmuir* **2011**, *27* (10), 6218–6226. <https://doi.org/10.1021/la1050223>.
- (50) Megelski, S.; Stephens, J. S.; Bruce Chase, D.; Rabolt, J. F. Micro- and Nanostructured Surface Morphology on Electrospun Polymer Fibers. *Macromolecules* **2002**, *35* (22), 8456–8466. <https://doi.org/10.1021/ma020444a>.
- (51) Casper, C. L.; Stephens, J. S.; Tassi, N. G.; Chase, D. B.; Rabolt, J. F. Controlling Surface Morphology of Electrospun Polystyrene Fibers: Effect of Humidity and Molecular Weight in the Electrospinning Process. *Macromolecules* **2004**, *37* (2), 573–578. <https://doi.org/10.1021/ma0351975>.

- (52) Samanta, P.; Thangapandian, V.; Singh, S.; Srivastava, R.; Nandan, B.; Liu, C. L.; Chen, H. L. Crystallization Behaviour of Poly(Ethylene Oxide) under Confinement in the Electrospun Nanofibers of Polystyrene/Poly(Ethylene Oxide) Blends. *Soft Matter* **2016**, *12* (23), 5110–5120. <https://doi.org/10.1039/c6sm00648e>.
- (53) Zhong, G.; Wang, K.; Zhang, L.; Li, Z. M.; Fong, H.; Zhu, L. Nanodroplet Formation and Exclusive Homogenously Nucleated Crystallization in Confined Electrospun Immiscible Polymer Blend Fibers of Polystyrene and Poly(Ethylene Oxide). *Polymer (Guildf)*. **2011**, *52* (24), 5397–5402. <https://doi.org/10.1016/j.polymer.2011.09.045>.
- (54) Lu, C.; Pelton, R. Factors Influencing the Size of PEO Complexes with a Tyrosine-Rich Polypeptide. *Langmuir* **2004**, *20* (10), 3962–3968. <https://doi.org/10.1021/la036032s>.
- (55) Dodero, A.; Brunengo, E.; Alloisio, M.; Sionkowska, A.; Vicini, S.; Castellano, M. Chitosan-Based Electrospun Membranes: Effects of Solution Viscosity, Coagulant and Crosslinker. *Carbohydr. Polym.* **2020**, *235*, 115976. <https://doi.org/10.1016/j.carbpol.2020.115976>.
- (56) Saquing, C. D.; Tang, C.; Monian, B.; Bonino, C. A.; Manasco, J. L.; Alsberg, E.; Khan, S. A. Alginate-Polyethylene Oxide Blend Nanofibers and the Role of the Carrier Polymer in Electrospinning. *Ind. Eng. Chem. Res.* **2013**, *52* (26), 8692–8704. <https://doi.org/10.1021/ie302385b>.
- (57) Klossner, R. R.; Queen, H. A.; Coughlin, A. J.; Krause, W. E. Correlation of Chitosan's Rheological Properties and Its Ability to Electrospin. *Biomacromolecules* **2008**, *9* (10), 2947–2953. <https://doi.org/10.1021/bm800738u>.
- (58) Ewaldz, E.; Brettmann, B. Molecular Interactions in Electrospinning: From Polymer Mixtures to Supramolecular Assemblies. *ACS Appl. Polym. Mater.* **2019**, *1* (3), 298–308. <https://doi.org/10.1021/acsapm.8b00073>.

CHAPTER 2

Literature review

2.1 Chitosan and chitosan nonwoven fibrous materials

2.1.1 Chitosan

Chitosan (chi), β -(1,4)-aminoglucopyranose containing randomly distributed N-acetylglucosamine and glucosamine residues (*cf.* Fig. 2.1), is a copolymer made from deacetylation of chitin, which is the second most abundant biopolymer in nature next to cellulose and is mainly found in invertebrates, fungi, and yeasts.¹ Chitin is mainly found in invertebrates, fungi, and yeasts.¹ Chi can be made from chitin by enzymatic or chemical processes.² The enzymatic process represents a controlled, non-degradable process to hydrolyze N-acetamide bonds in chitin utilizing chitin deacetylases, leading to well-defined chi such as chi oligomers.² The chemical process is a favorable method to produce chi for commercial usage due to the low cost and mass production ability.² Chi is a non-toxic, biodegradable, biocompatible material with many interesting chemical and physical properties and attractive biological functionalities, such as antimicrobial, antioxidant, antitumor activities, *etc.*² The degree of acetylation (DA) of chi is lower than 40% and soluble in acidic media, making chi easier to manipulate using solution-based methods than cellulose.³ Moreover, chi behaves as a cationic polyelectrolyte with a dissociation constant (pK_a) value of ~ 6.3 because the presence of the free amine groups on its structure can undergo protonation in acidic media.⁴ The occurrence of protonation of the glucosamine groups provides chi with the potential to form polyelectrolyte complexes. Chi also has been reported to dissolve in several organic solvents/solvent mixtures, such as trifluoroacetic acid (TFA), 1,1,1,3,3,3-hexafluoroisopropanol (HFIP), chloroform, glycine chloride, aqueous acetic acid/dimethylformamide, aqueous acetic acid/dimethyl sulfoxide, lithium hydroxide/urea, HFIP/formic acid, and tetrahydrofuran/dimethylformamide.⁵ However, the solubility of chi in these solvents or solvent mixtures is limited and strongly depends on the DA and molar mass of the chi. In addition, the free amine groups on C-2 (*cf.* Fig. 2.1) affords chi the ability to undergo various chemical modifications, which will be discussed later. Chi has good water swelling ability, which is beneficial for wound dressing. These advantages of chi over other biopolymers make chi a versatile precursor for materials design and development.

Chemical and physical properties of chi, such as crystallinity, solubility (in acidic medium) and reactivity, depend on several structural features of the chi molecule. These features include the average molecular weight, DA of the chi materials, and the local and global distribution of N-acetyl-glucosamine units along the chain.¹ For example, the DA of chi and the local and global distribution of N-acetyl-glucosamine units along the chi chain contribute to inter- or intra-molecular interactions (in terms of hydrogen bonding). In turn, the bonding arrangement determines the structural arrangement of chitosan and the crystalline nature of chi.⁶ Furthermore, the crystallinity of chi relates to the accessibility of the hydroxyl and amine groups of chi, which determines the chemical reactivity of chi, the hydration properties of chi in aqueous media, and the ability to form complexes with cationic species.⁷ The solubility of chi in acidic media can be evaluated from its pKa value, Where the pKa value of chi can be calculated using Katchalsky's equation, as given in equation (2.1).^{4,8}

$$pKa = pH + \log\left(\frac{1-\alpha}{\alpha}\right) = pKo - \frac{e\Delta\psi(\alpha)}{k_B T} \quad (2.1)$$

Here, $\Delta\psi(\alpha)$ is the difference in electrostatic potential between the surface of chi and the reference state at a distance from the axis in the rod-like model, where α is the degree of dissociation, k_B is the Boltzmann constant, T is the absolute temperature, and e is the electron charge. The intrinsic dissociation constant of the ionizable groups, pKo , can be obtained by extrapolating the pKa value to $\alpha = 1$, where the polymer becomes uncharged (or completely deionized). This value (pKo) is ~6.5, which is independent of the degree of dissociation; however, the pKa value is highly dependent on the degree of dissociation.⁴ The degree of dissociation relates to the accessibility of amine groups of chi, which in turn depends on the DA of chi and the distribution of N-acetyl-glucosamine units along the chi chain.^{6,8} Chi in acidic medium displays a semi-rigid behavior depicted by a persistence length, which is marginally determined by the DA of the sample.² The source of chitin used as the precursor and the method employed for the deacetylation of chitin in the chemical process can influence the physicochemical properties of chi.² The chitin precursor used can be α -, β -, or γ -chitin. Different unit cell arrangements clearly differentiate α - and β -, but γ -chitin is considered to be a mixture or distortion of α - and β -forms.^{7,9} According to Hajji et al.¹⁰, chi prepared from β -chitin has a lower DA than α -chitin but a higher degree of degradation because β -chitin has higher reactivity than α -chitin. Chi prepared from α -chitin demonstrated a slightly higher crystallinity than that prepared from β -chitin.¹⁰ Methods of

deacetylation of chitin in the chemical process are either homogenous or heterogeneous. For the heterogeneous method, chitin is immersed in a hot concentrated NaOH solution for several hours, and then chi is obtained as an insoluble settlement with DA up to ~1% to 15%.² For the homogeneous method, chitin is dispersed in concentrated NaOH (with a mass ratio between NaOH, H₂O, and chitin being 10 : 15 : 1) at 25 °C for three hours or more, then the dispersion is cooled in crushed ice at 0 °C.² The heterogeneous method leads to an irregular distribution of N-acetylglucosamine units along the chi chain, whereas the homogeneous method results in a uniform distribution.¹¹ The deacetylation methods may also affect DA, molar mass, and viscosity in the solution.²

2.1.2 Chitosan nonwoven fibrous materials

As described above, chi is a versatile platform for materials design. Various forms of chi have been developed for different applications. For example, beads, microspheres, nanoparticles, and coatings have been used for drug delivery, enzyme immobilization, gene delivery, surface modification, and textile finishes. Films have been used for dialysis membranes and antimicrobial membranes. Powders of chi have been used directly as adsorbents for water and various form of water contaminants (heavy metals and dyes). Chi solutions have been involved in floc-coagulants, cosmetics, bacteriostatic agents, anticoagulants and antitumor agents. Chi gels have been applied for implants, coatings, and tissue engineering. Chi tablets and capsules have been used for disintegrating agents and delivery vehicles. Chi nonwoven micro- or nanofibrous materials, the main targets of this thesis, have drawn increasing attention in food packaging, medical textiles, suture, bone regeneration, tissue engineering, wound dressing, drug delivery, enzyme entrapment, and artificial skin.⁵ As mentioned in Chapter 1, common methods to prepare nonwoven micro-/nanofibrous materials are either freeze-drying or electrospinning. For both methods, the first step of the material preparation is to solubilize chi. Although chi is soluble in acidic conditions or somewhat soluble in organic solvents or organic solvent mixtures as discussed in Section 2.1.1, chi is further chemically modified to make it soluble in a neutral aqueous medium and increase the solubility of chi in organic solvents as a result of adapting to different application requirements. Common approaches are grafting chi with various chemicals and polymers, such as carboxymethylation, quaternization, and PEGylation.⁵ Most of the modification methods utilize

the hydroxyl group on C6 (sometimes with a side reaction at the hydroxyl group on C3) and the amine group on C2 of chi. Carboxymethylation is the common method to make chi soluble in the neutral aqueous medium. Some of the approaches used to synthesize carboxymethylated (cm) chi are shown in Figure 2.1. It is worth noting that the difference between O- and N-carboxymethylated chi in the inter- or intra-molecular interaction leads to distinct reactivities and solution behaviors, which is the same for other chemical modifications.¹² Apart from carboxymethylation, quaternization of chi is also used. Quaternary ammonium groups are introduced to chi, leading to the enhancement of the solubility of chi at neutral and high pH aqueous environment.¹³ PEGylation is another important method to increase the solubility of chi in aqueous media.¹⁴ For both carboxymethylation and quaternization, ionic groups charged at neutral and high pH aqueous medium are attached to chi. However, in PEGylation, a non-ionic hydrophilic polymer, poly(ethylene glycol) (PEG), is grafted to chi. During PEGylation, PEG with an appropriate end group is firstly synthesized, then attached to the chi. To increase chi solubility in organic solvents or change the hydrophilic-hydrophobic balance of chi, acylation, alkylation, and benzylation can be performed.⁵

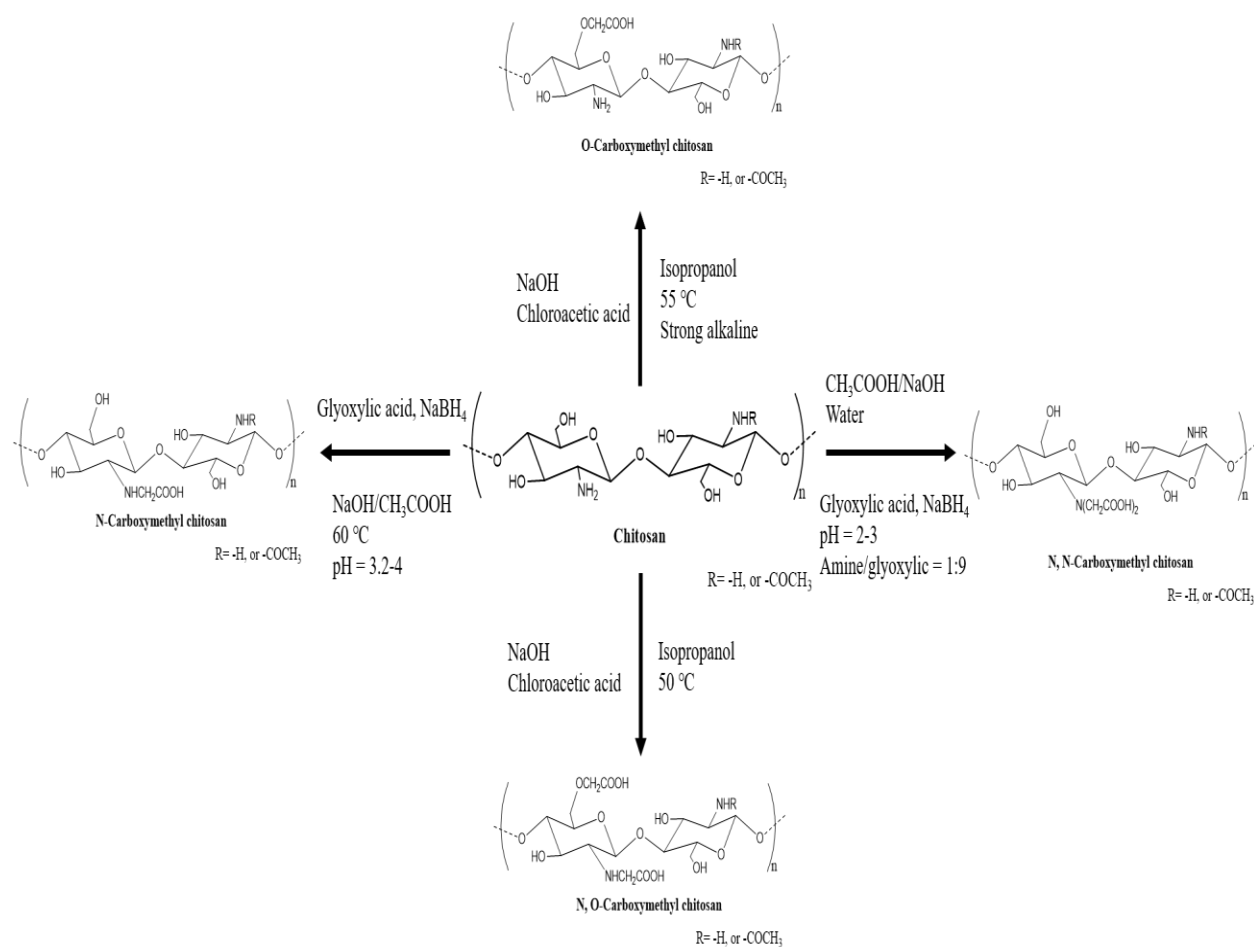


Figure 2.1. Original chitosan and different types of carboxymethylated chitosan.

During the preparation of nonwoven fibrous materials by electrospinning, the chi or its modified form is initially dissolved in a proper solvent. After that, the solution properties, such as polymer concentration, viscosity, surface tension, dielectric constant, conductivity, *etc*, are adjusted to achieve the desired strength of intermolecular interactions suitable for electrospinning. Thereafter, the resulting solution is converted into a solid fibrous material through electrospinning. Some examples of chi-based electrospun fibers are hexanoyl chi, PEGylated chi, cm-chi blended with other water-soluble synthetic polymers (PEO, polyacrylamide (PAM), poly(acrylic acid) (PAA), poly(vinyl alcohol) (PVA))¹⁵, chi/PVA¹⁶, chi/poly(lactide-co-glycolide) (PLGA)/PVA¹⁷, chi/PEO^{18–22}, chi/collagen²³, chi/agarose, chi/zein, chi/nylon-6, *etc*¹⁵.

For fibrous materials prepared by freeze-drying, the first step is to form polyelectrolyte complexes (PECs) in the solution. These PECs are then assembled into solid fibrous materials by the freeze-drying method. Some examples are chi/acetate²⁴, chi/alginate²⁵, chi/hyaluronate²⁶, chi/poly(galacturonic acid) (PGA)²⁷, and so on. It is worth noting that even though various forms of chi (e.g., chi films, powders, tablets, capsules, *etc.*) can be prepared by freeze-drying, the formation of a dispersion of PECs in the solution prior to freeze-drying is a sufficient condition to produce chi-based micro- or nanofibrous materials, which relates to the mechanism of freeze-drying and will be discussed later in this chapter.

Once chi-based nonwoven fibrous materials are obtained, post-treatment is sometimes required to increase the stability of the materials in an aqueous medium. There are two categories for post-treatment of chi fibrous materials: chemical and physical methods.⁴ In the case of chemical methods, cross-linking through a covalent bond is typically used to reduce the number of free hydrophilic groups in the chi (amino group or hydroxy group), increasing the stability of chi in water. Some commonly used cross-linking agents are epichlorohydrin²⁸ or glutaraldehyde²⁹. Although a study conducted by Zhao et al.³⁰ has shown that the chemical cross-linking does not change the biocompatibility of chi, the safety of chemically cross-linked chi is still of concern due to the presence of the unreacted or partially reacted cytotoxic cross-linking agent in the product. For physical methods, the chi-based material is cross-linked *via* electrostatic interactions by multivalent anions, like oxalic acid³¹, citric acid^{32–34}, or tripolyphosphate^{35,36}. Another physical method often used is thermal treatment.^{37,38} Physical methods are favorable for preparing materials for applications such as wound dressing, tissue engineering, and food packaging because there are no questionable or harmful organic chemicals used in the process.

2.2 Interactions in the polymer solution

As mentioned in Section 2.1.2, it is necessary to prepare the chi solution or chi-based polymer blends before producing chi nonwoven fibrous materials. Various interactions occurring in the chi solution or chi blend (a mixture of chi and a synthetic polymer in a common solvent) determine the product's morphologies and physicochemical properties. Therefore, some common interactions in the polymer solution are discussed hereafter.

2.2.1 Polymer-solvent interactions based on Flory-Huggins theory

Flory and Huggins independently introduced a lattice model for calculating the enthalpy and entropy of mixing polymers in solution media. The assumptions used in this theory are monodisperse polymer chains (same molar mass), uniformity of concentrated polymer solutions, very flexible polymer chains or free-joint polymer chains (no bond angle), no volume change on mixing, and no specific interactions between polymer repeat units and solvent.³⁹ A polymer-solvent interaction parameter, χ , can be found based on Flory-Huggins theory. When $\chi = 0$, it is called a theta-solvent (θ -solvent) in which the solvent-polymer segment interactions and the interaction between the polymer segment are equally favored. As the solvent does not induce chain expansion, the polymer shows unperturbed chain dimensions. Hence, the conformational characteristic of the polymer can be studied in its dilute solution under θ -solvent conditions. On the other hand, in a good solvent ($\chi < 0.5$), the polymer-solvent interaction is energetically favored, and the polymer chain exhibits full expansion leading to a larger “end-to-end” distance of the polymer chain than that of the polymer chain in the θ -solvent. When $\chi > 0.5$, it represents a poor solvent where solvent-polymer interaction is energetically less favored than polymer-polymer interaction leading to a contracted polymer chain conformation in this solvent.

The concepts of the Flory-Huggins theory have been extended to the understanding of polymer/polymer miscibility for polymer blends. The Flory-Huggins thermodynamic interaction parameter χ_{12} depicts the interaction in free energy of mixing and is used to measure the excess enthalpic and entropic contributions to potentially favorable mixing. The more negative the parameter, the stronger the interaction.²¹ Because the chi polymer chain in the solution displays stiffness and the concentration of chi solutions used in the examples mentioned in Section 2.1.2 are not dilute, chi solutions may not satisfy Flory-Huggins polymer-solvent interactions parameter. However, chi blends’ miscibility can be understood with this theory as synthetic polymers used in chi blends follow the assumptions. For example, chi/poly(N-vinyl pyrrolidone) (PVP) and chi/PVA result in miscible blends, but chi/PEO is miscible to ~30% of PEO.^{21,40,41} For chi blends, the morphology of microscopic domains from immiscible components will affect the ability to form nonwoven fibrous materials, even the products’ physicochemical properties.

2.2.2 Polymer-polymer interactions based on chain entanglements

The terminology, chain entanglements, are brought from polymer melts (or rubbery-like materials) into polymer solutions to describe polymer-polymer interactions in non-diluted polymer solutions. The most critical assumption of chain entanglements is that the materials behave as an ideal rubber with only entropic forces on stretching. In other words, chain entanglements are the physical interlocking of polymer chains acting similarly as chemical and physical cross-links, resulting from chain overlap above a certain concentration.⁴² However, chain entanglements differ from chemical and physical cross-links in a way that polymer chains, owing to the assumption, can move past one another, affecting viscoelastic behavior but have no specific interactions (no internal energy contributions).⁴³ In a polymer melt, chain entanglements can be expressed with the number of entanglements (or entanglement density), which increases with polymer chain length or molecular weight, M . The number of entanglements in the polymer melt can relate to the ratio of M_c/M_e , where M_c represents the critical molecular weight corresponding to one entanglement per chain and M_e represents the entanglement molecular weight corresponding to the average molecular weight between entanglement junctions (or couples). In a polymer solution, when the polymer solution concentration (C) is below the critical value (C^*), there are no chain entanglements in a dilute solution due to no chain overlap. When $C = C^*$, the chain overlap takes place, and the number of chain entanglements is proportional to C . The relation between the entanglement molecular weight in the solution ($(M_e)_{soln}$) and the melt (M_e) can be described as the equation (2.2):

$$(M_e)_{soln} = M_e/\phi_p \quad (2.2)$$

where ϕ_p is the polymer volume fraction. Therefore, the strength of polymer-polymer interactions in the polymer solution ($C \geq C^*$) can be evaluated using the number of entanglements.⁴²

2.2.3 Molecular interactions in the polymer solution

As mentioned above, chain entanglements relate to non-specific polymer-polymer interactions. However, in the context of chi solutions and blends, molecular interactions can not be ignored.

2.2.3.1 Hydrogen bonding

Hydrogen bonding is a special type of dipole-dipole attractive force which occurs between two species owing to a through-space interaction such as $X-H\cdots Y$, where X and Y are polar atoms, X-H represents a hydrogen donor (X is more electronegative than H), and Y represents a hydrogen acceptor containing a lone-pair electron.⁴⁴ Hydrogen bonding is energetically weaker than ionic and covalent bonds but stronger than dipole-dipole and dispersion forces. Chi and modified chi (*cf.* Section 2.1.2) possess many groups contributing to hydrogen bonding, such as -OH, -NH₂, and -C=O, making hydrogen bonding the most vital molecular interaction for chi solutions and chi blends.

2.2.3.2 Hydrophobic effects

Hydrophobic effects are a long-range attractive force that occurs due to two hydrophobic surfaces trying to eliminate water molecules between them.^{45–47} Polar and ionic compounds can readily dissolve in water due to the polar nature of water. However, the introduction of nonpolar (hydrophobic) compounds into water or polar solvent leads to hydrophobic effects. Hydrophobic effects are the tendency of nonpolar molecules to self-associate instead of dissolving individually in water.⁴⁵ Hydrophobic effects are the driving force for the formation of host-guest inclusion complexes for cyclodextrins, aggregation or formation of micelles by amphiphilic molecules, and removal of non-polar molecules from the aqueous environment.^{45–47} Hydrophobic forces were found to be much greater than van der Waals forces at large distances, and increase with increased hydrophobicity of the surface. Hydrophobic effects could affect solution behaviors of chi solutions and blends attributed to the hydrophobic parts of chi, although chi is considered hydrophilic due to the -OH and -NH groups on the surface. Furthermore, after chemical modification of chi mentioned in Section 2.1.2, because the hydrophilic-hydrophobic balance of modified chi differs from original chi, hydrophobic effects could lead to the formation of organized microstructures in chi blends.

2.3 Freeze-drying method

Freeze-drying, also known as lyophilization or cryodesiccation, is a dehydration process where water in the product is frozen then removed by subliming the ice to vapor. There are three stages in the freeze-drying process: freezing, primary drying, and secondary drying. During the freezing stage, the sample's temperature is reduced until the initiation of the nucleation of ice crystal, which is followed by ice crystal growth.⁴⁸ This leads to the separation of most of the water (in the form of ice crystal) from a concentrated solute phase, usually containing a small amount of water.⁴⁸ During primary drying, the crystalline ice formed during freezing is removed by sublimation.^{48,49} Therefore, the chamber pressure is reduced well below the vapor pressure of ice, and the shelf temperature is raised to supply the heat removed by ice sublimation.⁴⁸ At the end of the primary drying, the sample can still contain about 20% of unfrozen water in the concentrated solute phase, which is then desorbed during the secondary drying stage, usually at elevated temperature and low pressure, to finally attain the desired low moisture content.⁴⁸

The freezing stage plays an essential role in the freeze-drying method. Many studies have shown that the freezing stage dramatically impacts the quality and the morphology of the final freeze-dried product.^{25,49–54} Generally, freezing can be defined as the process of ice crystallization from supercooled water (it is a type of water remaining as a liquid at the temperature below its equilibrium freezing point).⁴⁹ Supercooling is a non-equilibrium, meta-stable state, of which the energy is close to the activation energy of the nucleation process. The formation of ice crystals starts from the nucleation. Ice-like clusters, resembling the molecular structure of ice crystal, are formed by water molecules in the supercooled water through prolonged hydrogen bonds due to density fluctuations from Brownian motion.⁴⁹ The probability of forming these energetically unfavorable clusters increases as the temperature decreases.⁴⁹ Ice crystal growth is initiated when the critical mass of these clusters (nuclei) is met.⁴⁹ There are two types of nucleation, which are homogenous and heterogeneous nucleation. Heterogeneous nucleation is observed during the freeze-drying process, which suggests that ice-like clusters are formed by adsorbing layers of water on “foreign impurities” such as the container's surface, particulate contaminants present in the water, and large molecules.⁵⁵ Ice crystal growth is controlled by the heat released from the addition of water molecules to the ice-water interface and the cooling rate to which the sample is exposed. Because merely a portion of the heat released by the ice formation (15 cal/g of the 79 cal/g of heat

given off by the ice formation) can be absorbed by the supercooled water, the rest of the heat needs to be removed by further cooling.⁴⁹ The ice morphology is based on two factors: the degree of supercooling and the freezing mechanism.⁴⁹ The degree of supercooling depends on the solution properties and process conditions. It is defined as the difference between the equilibrium ice formation temperature and the actual temperature at which the ice crystal first forms.^{48,49} High degree of supercooling results in a higher number of small ice crystals because of the number of ice nuclei formed, where a fast freezing rate at the ice-water interface leads to small ice crystals. However, at a lower degree of supercooling, a lower number of large ice crystals were observed.⁵⁶

There are two basic freezing mechanisms involved in the freeze-drying process: global supercooling and directional solidification. During the occurrence of global supercooling (like shelf-ramped freezing), the whole liquid volume has a similar level of supercooling, and solidification occurs through the already nucleated volume, which leads to spherulitic ice crystals.⁴⁹ For directional solidification, it occurs when a small volume is supercooled, which is the case for high cooling rates, like with liquid nitrogen sample immersion. During high cooling rates, the nucleation and the development of the ice-water interface occur almost simultaneously; and the ice-water interface moves further into non-nucleated solution leading to directional lamellar morphologies with connected pores.^{49,52,54,56} As ice crystals grow in the freezing stage, the phase separation takes place between most of the water (in the form of the ice crystal) and a concentrated solute phase. As a result, the space among ice crystals is occupied by the concentrated solute phase.⁵² If this separation does not happen, a mixture of the sample is formed with a greatly reduced vapor pressure, which cannot be freeze-dried.⁴⁹ The concentrated solute phase may undergo eutectic crystallization or vitrification depending on the properties of the solutes, which results in a mixture of small crystals of ice and solute or a mixture of amorphous solutes and amorphous (unfrozen) water, respectively.⁴⁹ Other behaviors, like liquid-liquid phase separation (further phase separation of the multicomponent system in the concentrated solute phase), crystallization of amorphous solids, or amorphization from crystalline solids, may also take place, which profoundly affects the physicochemical properties of the freeze-dried product. Following the completion of freezing, the concentrated solute phase adopts the morphology of ice crystal acting as a “template”. Upon removal of the “template” in the second and third stages of the freeze-drying process, the freeze-dried product with the corresponding morphology can be obtained.^{52,54}

It is reported that nonwoven fibrous materials such as sponges and foams can be prepared through freeze-drying.^{24–27,50,51,54,57,58} Despite the differences in the starting materials and some preparation procedures among these studies, there are two common features in the preparation of nonwoven fibrous materials: freezing with high cooling rates and the use of a diluted dispersion of high molecular weight polymers as the starting material like cellulose, chi, alginate, poly(lactic acid) (PLA), PLGA, gelatin, *etc.*^{24–27,50,51,54,57–59} As discussed above, freezing with high cooling rates results in the directional solidification of the sample leading to directional lamellar structure of ice crystal with connected pores. The dispersed polymers in the concentrated solute phase are rearranged into the fibrous structure or the lamella structure according to the initial dispersion concentration.^{25,51} Moreover, the use of high molecular weight polymers ensures that the microstructure created by “the ice template” remains unchanged during the second and third drying process. A schematic illustration of the formation of different morphologies of the freeze-dried high molecular weight polymer is shown in Figure 2.2. In the context of chi-based nonwoven fibrous materials, such materials can be prepared by the freeze-drying process, following the same mechanism. A stable diluted dispersion of chi-based materials can be achieved in the solution by forming polyelectrolyte complexes, as mentioned in Section 2.1.2, then is frozen with high cooling rates, like with liquid nitrogen immersion (or the ultra-low-temperature freezer) and dried.^{24–27} Therefore, the formation of a dispersion of PECs in the solution is crucial for the preparation of chi-based nonwoven nano- or micro-fibrous materials.

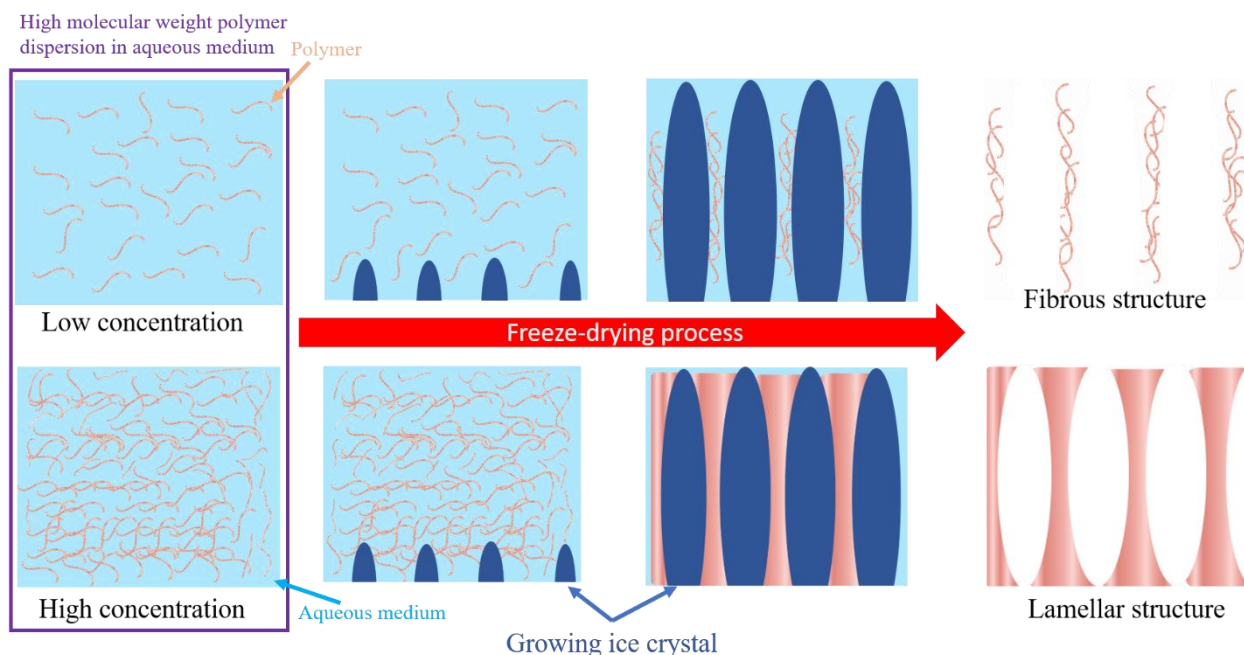


Figure 2.2. A schematic illustration of the formation of different polymer morphologies of the freeze-dried high molecular weight polymer dispersion.

2.4 Electrospinning method

2.4.1 Brief history of electrospinning

Electrospinning provides a facile method to produce ultrathin fibers with diameters down to the nanometer scale. Electrospinning may be considered a variant of the electrostatic spraying (or electrospray) process, both of which depend on using a high voltage to eject liquid jets.⁶⁰ The significant differences between electrospinning and electrospraying are the viscosity and viscoelasticity of the liquid involved and thus the behavior of the jet.⁶¹ During electrospinning, the continuous jet results in fibers, whereas the jet breaks into droplets leading to the formation of particles during electrospraying. The earliest concept of electrospinning could be found in 1887. Charles V. Boys reported that fibers could be drawn from a viscoelastic liquid (e.g., beeswax and collodion) under an external electric field.⁶² A prototype of the electrospinning setup was patented in 1902.⁶¹ In the late 1930s, the improvement of the electrospinning setup was made by Anton Formhals that aimed to commercialize electrospinning.⁶¹ In the same period, the first example of electrospun nanofibers, “Petryanov filters”, was realized in the Soviet Union to capture aerosol

particles.⁶¹ Afterward, for 60 years, academia or industry has not paid much attention to electrospinning, resulting from the limitation on characterization tools to measure fibers with sub-micron diameters accurately.⁶¹ The tide turned in the late 1990s. Several research groups, notably those led by Darrell Reneker and Gregory Rutledge^{63–70}, brought this “ancient technique” into the laboratory to produce nanofibers from various organic polymers as electron microscopes that can resolve nanoscale features became available for researchers.⁶¹ Thus, the term “electrospinning” was widely accepted and used in the literature to describe this technique. Since the beginning of the 21st century, because of its remarkable simplicity, versatility, and potential uses, the electrospinning method has been considered to be the method of choice for producing fibrous materials with nanoscale diameters.⁶¹

2.4.2 Basic theory of electrospinning

In 1887, Charles V. Boys used an insulated dish connected to an electrical supply.⁶² Currently, a basic electrospinning setup consists of a high-voltage power supply, a spinneret, and a collector (a grounded conductor). It is not much different from the first apparatus. A scheme of the basic electrospinning setup is shown in Figure 2.3. The high-voltage power supply can either be direct current (DC) or alternating current (AC). The spinneret, containing the polymer solution, is equipped with a blunt-tip needle, and a syringe pump controls the polymer solution's flow rate. Many advanced electrospinning setups have been developed to regulate the alignment of electrospun nanofibers⁶¹, to control the structure of electrospun nanofibers (coaxial setup for core-sheath and hollow nanofibers⁷¹), or to increase the throughput of electrospun nanofibers (multi-needle electrospinning setup⁷²).

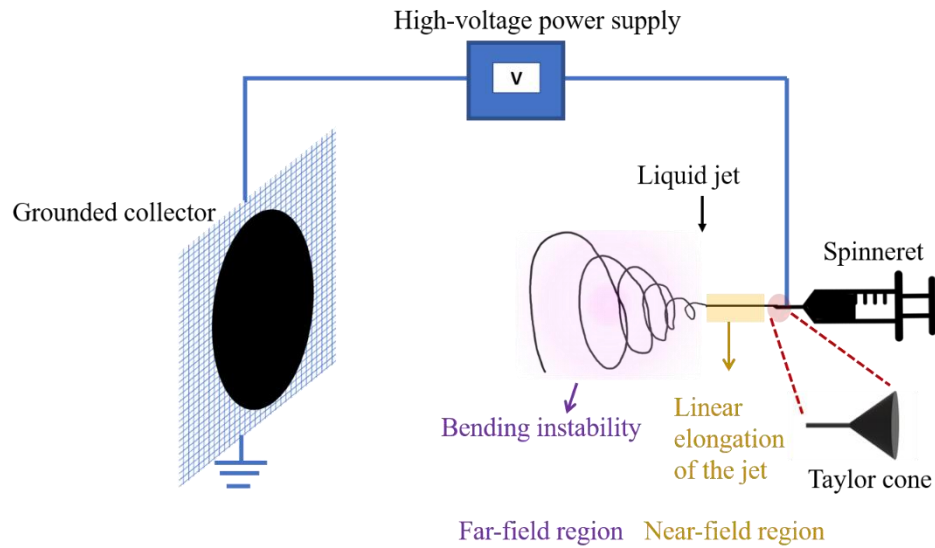


Figure 2.3. A scheme of the basic electrospinning setup.

Nevertheless, the electrospinning process generally can be divided into four successive steps: 1) charging a pendant droplet to form a cone-shaped jet in an electric field; 2) elongating the charged jet; 3) stretching and thinning the charged jet under the electric field leading to the growth of bending instability (also called whipping instability); 4) solidification and collection of the jet as solid fibers on a grounded collector. The first step is the formation of a cone-shaped jet in an electric field. During electrospinning, the polymer solution is ejected from the spinneret to form a pendant droplet due to surface tension. The droplet is then electrified in the presence of the external electric field, which results in the deformation of the electrified droplet into a conical shape due to the electrostatic repulsion among the surface charges that feature the same sign. Thus, a charged jet is ejected from the tip of the conical shape. According to Plateau-Rayleigh instability, the deformation of the droplet into the conical shape in an external electric field was first mathematically explained by Geoffrey Taylor between 1964 and 1969.^{73,74} This conical shape is now known as “Taylor cone”. By assuming the liquid in the droplet as a perfect conductor⁷³, the electrostatic pressure (P_e) caused by the external electric field is applied on the surface of the droplet, which can be described by equation (2.3)

$$P_e = \varepsilon E^2 / 2 \quad (2.3)$$

where ε is the dielectric constant of the medium surrounding the droplet and E is the intensity of the electric field. The capillary pressure (P_c) due to the surface tension can be calculated using the Young-Laplace equation in the following form (2.4):

$$P_c = 2\gamma/r \quad (2.4)$$

where γ is the surface tension and r is the mean radius of curvature of the surface, which approximately equals to the inner radius of the spinneret.^{75,76} As the electric field is increased to a threshold, a critical voltage (V_c), P_e will surpass P_c , which suggests that the strength of the electrostatic repulsion will surmount the surface tension. As a result, the droplet will deform into a conical shape.⁷³ In this case, V_c can be determined with the use of the following equation (2.5):⁷⁴

$$V_c^2 = \frac{4H^2}{l^2} \left(\ln \left(\frac{2l}{R} \right) - 1.5 \right) (1.3\pi R\gamma)(0.09) \quad (2.5)$$

where H is the distance between the tip of the spinneret and the collector, l is the length of the spinneret, and R is the outer radius of the spinneret. The units of H , l , and R are all in centimeters, while the unit of γ is dyn/cm and the unit of the voltage is kV. The factor 1.3 is derived from $2 \cos 49.3^\circ$ when assuming that the cone has a semi-vertical angle close to a possible equilibrium value of 49.3° . Properties of the liquid also affect the critical voltage required to deform the droplet into a conical shape. When a viscous liquid such as a polymer solution is used to form a Taylor cone, the electrostatic repulsion threshold generated by the voltage needs to be greater than the sum of the surface tension and the viscoelastic force of the liquid. The Taylor cone can be kept in shape if there is enough supply of liquid to compensate the ejected amount during an electrospinning process.⁶¹

The second and third steps of electrospinning are usually studied together. After being ejected from the tip of the Taylor cone, an electrically charged jet is elongated straightly in the direction of the electric field as it travels toward the collector with acceleration.⁷⁷ This linear elongated segment of the jet is named the near-field region, as shown in Figure 2.3. The electric force is dominant in this region.⁷⁸ The acceleration is gradually reduced by the surface tension and viscoelastic force in the jet.⁷⁹ Meanwhile, because the jet is continuously elongated, its diameter in the straight segment decreases as it moves away from the tip. In this region, The Rayleigh instability should be overcome by the viscoelastic properties of the fluid to prevent the jet from

breaking into droplets.⁸⁰ When the acceleration is reduced to zero or a constant, any small perturbation, such as the electrostatic repulsion generated by the surface charges located on the jet, can disturb this straight movement, resulting in the indication's instability of the far-field region.⁷⁸ In the far-field region, there are three different types of instabilities: Rayleigh instability (axisymmetric), axisymmetric instability occurring at a stronger electric field, and bending instability (whipping, non-axisymmetric).^{65–68,70} Rayleigh instability leads to the potential breakup of the jet into the droplets, governed by the surface tension. Rayleigh instability can be suppressed at a strong electric field according to equation (2.5). For bending instability, it describes that the aerodynamic instability coordinates the “lateral electrostatic force”, perpendicular to the electric field, to generate the wave-like perturbations onto the jet.⁷⁹ Consequently, the jet is compelled to bend by the lateral force created by the electrostatic repulsion among the surface charges in a strong electric field to form a coil, as shown in Figure 2.3.⁷⁹ According to both experimental observations and electrohydrodynamic theories, different models have been developed to describe the behavior of the charged jet to understand the electrospinning process.⁶¹ Based on these models, these three instabilities are controlled by the physicochemical properties of the liquid and the electrospinning parameters. The final step of electrospinning is solidification and the collection of the jet as solid fibers. Solidification of the jet occurs during the second and the third step, where the solvent is evaporated. A slow solidification will result in fibers with a thinner diameter.⁶¹ Solidified fibers are collected on the grounded collector leading to nonwoven fibrous materials. The morphologies of the products are mostly determined by bending instability (the third step of electrospinning).⁶¹ In order to obtain electrospun nanofibers, bending or stretching of the jet resulting from the rapid growth of bending instability is essential.⁶¹

2.4.3 Factors regarding the electrospinnability of the system

As discussed above, the critical processing parameters of the electrospinning setup are the voltage applied to the spinneret, the flow rate of the liquid, and the working distance between the tip of the spinneret and the collector. In general, the voltage applied to the spinneret determines the strength of the electric field. The flow rate of the liquid typically relates to the diameter of the fiber. A long enough working distance is required to achieve fully extended solid fibers. However, there is a complicated interplay among all the processing parameters, making the optimization of the electrospinning process difficult. Besides, the physicochemical properties of the polymer

solution can also affect the electrospinning process significantly, such as the molecular weight of the polymer, viscosity, viscoelasticity, surface tension, dielectric constant, *etc.* In particular, the ability for the polymer solution to overcome the Rayleigh instability occurring in the second step of the electrospinning process is the crucial factor to prevent the jet from breaking up into the droplet leading to the fiber formation. For a polymer melt or a single component polymer solution system, this ability has been correlated to chain entanglements using the “solution entanglement number” by Shenoy et al., which is a semi-empirical methodology with an important assumption that chain entanglements are solely responsible for both the increase of the solution viscosity and the cause of the elastic network under the influence of an elongational strain.⁸¹ The solution entanglement number, $(n_e)_{soln}$, is defined as the ratio of the weight-average molecular weight (M_w) to the entanglement molecular weight in solution ($(M_e)_{soln}$).⁸¹ The corresponding mathematical expression is given in equation (2.6):

$$(n_e)_{soln} = \frac{M_w}{(M_e)_{soln}} = \frac{\phi M_w}{M_e} \quad (2.6)$$

where M_e is the entanglement molecular weight in the melt and ϕ is the polymer volume fraction. Generally, M_e are a function of chain topology or geometry and ϕ relates to the dilution effect due to the presence of a solvent. Shenoy et al.⁸¹ demonstrated that stable fiber formation for a neutral polymer in a good solvent occurs when $(n_e)_{soln} = 3.5$ (or the number of entanglements per chain is greater than 2.5) depending on the polymer molecular weight, concentration, and solvent quality. This solution entanglement number suggests that the polymer with high molecular weight has large number of entanglements per chain, resulting in better electrospinnability. Many systems have displayed a similar threshold of the number of entanglements per chain (> 2.5).^{82–85} However, because of the underlying assumption of this approach, it is valid only for the single polymer system in a good solvent where polymer-polymer interactions are negligible.⁴² Under a similar assumption, four solution regimes have been predicted for linear neutral polymers in a good solvent using a slope transition when plotting the log of specific viscosity (η_{sp}) as a function of log of polymer concentration (c), including the dilute regime ($\eta_{sp} \sim c^{1.0}$), the semi-dilute unentangled regime ($\eta_{sp} \sim c^{1.25}$), the semi-dilute entangled regime ($\eta_{sp} \sim c^{4.8}$), and the concentrated regime ($\eta_{sp} \sim c^{3.6}$).⁸³ The specific viscosity is expressed by equation (2.7).

$$\eta_{sp} = (\eta_{soln} - \eta_{solv})/\eta_{solv} \quad (2.7)$$

Here, η_{soln} is the viscosity of the polymer solution and η_{solv} is the viscosity of the solvent. The slope for each regime is also called the scaling value, which represents the contribution of the polymer concentration to the viscosity in a specific regime. The entanglement concentration (c_e) is defined as the polymer concentration at the transition from the semi-dilute unentangled to the semi-dilute entangled regimes.^{86,87} The entanglement concentration has been used to envisage the electrospinnability of the polymer solution and the corresponding morphology of the electrospun nanofibers.⁸³ It is found that beaded nanofibers formed at $c = c_e$, while defects and droplets disappear at $c = 2 - 2.5 c_e$.⁸³ Rubinstein⁸⁸ and Dobrynin⁸⁹ expands the theory to the salt-free linear polyelectrolyte solution, predicting that the semi-dilute unentangled regime ($\eta_{sp} \sim c^{0.5}$), the semi-dilute entangled regime ($\eta_{sp} \sim c^{1.5}$), and the concentrated regimes ($\eta_{sp} \sim c^{3.75}$). It was found that a uniform electrospun fiber can be prepared from the salt-free polyelectrolyte solution at $c = 8 - 10 c_e$.⁹⁰

For the systems in which the polymer-polymer interactions cannot be neglected, the ability to maintain the jet during electrospinning can be provided by physical molecular interactions between polymer units or other molecules in the spinning solutions as polymer entanglements.^{81,91} These physical molecular interactions include hydrogen bonding, electrostatic interactions, and hydrophobic effects.⁹² This means that the fiber formation can take place without high molecular weight polymers or at lower concentrations leading to advanced electrospinning formulations. The molecular interaction-driven electrospinning can be divided into three categories: polymer-polymer interactions, polymer-small molecule interactions, and supramolecular interactions, as shown in Figure 2.4. In the context of this thesis, two categories, polymer-polymer interactions and supramolecular interactions, are discussed. For polymer-polymer interactions, the first sub-category is polymer self-interactions. Shenoy et al. demonstrated that PVA solution prepared in a good solvent could experience self-interactions at a certain temperature.⁸¹ When PVA was heated to 80 °C, where the polymer is mostly dissolved, but polymer aggregates (small crystallites) were present, the onset of fiber formation occurred at a point where there were no chain entanglements as $(n_e)_{soln} < 1$. If the polymer is first heated to 92 °C, where the aggregates are fully dissolved, then the onset of fiber formation happens at the predicted as $(n_e)_{soln} > 2$ for other high molecular weight polymers. The existence of small aggregates clearly stabilized the jet instead of chain entanglements during electrospinning. Self-interactions can also be induced by the “poor solvent”

for the polymer. Poly(vinyl chloride) (PVC) dissolved in tetrahydrofuran (THF), a good solvent that displayed $(n_e)_{soln} > 2$ for fiber formation while PVC dissolved in morpholine (MOR), a poor solvent, had $(n_e)_{soln} < 1$.⁸¹ The second sub-category is polymer blends. In this case, chi-based electrospun nanofibrous materials are good examples. As discussed in Section 2.1, chi is a polyelectrolyte with different rheological properties and electrospinning behaviors compared with neutral polymers. The stiffness of chi polymer chains in the solution showed a weaker relationship between viscosity and concentration than neutral polymers in dilute and semi-dilute regimes.^{89,90,93} However, because of the repulsion between charges, electrospinning of charged polymers requires higher concentrations, with $(n_e)_{soln} > 8$ compared to > 2.5 for neutral polymers.⁹⁰ Furthermore, depending on the DA of chi, it may undergo gelation at a high concentration⁹⁴, preventing chi from electrospinning at higher concentration values. Therefore, chi was blended with other high molecular weight polymers, like PEO, PVA, collagen, *etc.*, to achieve the stable jet during electrospinning and facilitate the formation of chi-based electrospun nanofibrous materials. For example, the addition of high molecular weight (HMw, greater than 400 kDa) PEO to the chi solution is a promising material to promote chi electrospun nanofibrous formation materials.^{18–22,95,96} Moreover, HMw PEO can act as a plasticizer for chi as flexible PEO chains which can occupy the void space among the rigid chi chains to reduce the inter- and intra- molecular interactions of chi chains that result in the prevention of the gelation of chi and reduction of the viscosity of the blends.^{95,96} Collagen and PVA can also be used as additive polymers blended with chi.^{16,23} Blending of chi with collagen or PVA favours hydrogen bonding between the polymer subunits, leading to increased molecular interactions and stable jet formation during electrospinning.^{16,23} Other hypotheses have been proposed for chi/collagen blends to explain for the improved electrospinning performance, which includes the enhancement of molecular interactions through chi wrapping with collagen in a triple helix or the two polymers undergo ionic complex formation.⁹²

For supramolecular interactions, the first sub-category is cyclodextrin-related interactions. Pure HP- β -CD system⁹⁷ has been known to form an electrospun fiber despite the relatively low molecular weight of HP- β -CD because of the tendency to form supramolecular assemblies through hydrogen bonding. The role of hydrogen bonding in the system was studied by the addition of urea, as urea is known to disturb hydrogen bonding.⁹⁷ As a result, the viscosity of the solution decreased

significantly, and the solution was no longer spinnable.⁹⁷ Further rheological study was conducted focusing on HP- β -CD in dimethylformamide (DMF) by Zhang et al.⁹⁸ Based on the dependence of the specific viscosity on the concentration of the HP- β -CD, a transition from the unentangled ($\eta_{sp} \sim c^{11.0}$) and entangled regimes ($\eta_{sp} \sim c^{15.5}$) was shown, and the scaling values for both regimes were higher than those for neutral polymers in a good solvent, ($\eta_{sp} \sim c^{1.25}$) and ($\eta_{sp} \sim c^{4.8}$), respectively. However, the scaling value for HP- β -CD entangled regime was in agreement with the concentrated regime ($\eta_{sp} \sim c^{14.0}$) of the surfactants.⁹⁸ This suggests that the HP- β -CD solution has similar behavior to that of wormlike micelles, which contributes to the electrospinnability.⁹⁸ An alternative mechanism for electrospinning of HP- β -CD in pure aqueous solutions was proposed by Manasco et al.⁹⁹ According to their study⁹⁹, the jet during electrospinning was stabilized by the water-HP- β -CD assemblies formed through the strong hydrogen bonding, which was supported by the fact that there was almost 0% free water in 60% (w/w) HP- β -CD solution (an electrospinnable concentration). This study also demonstrated that HP- β -CD solutions in water had high viscosity but not high elasticity. This result is in contrast to the previous report that high elasticity is a condition for electrospinning solutions without polymer entanglements.⁸⁴

The second sub-category is that small-molecule systems, which tend to assemble into supramolecular assemblies *via* noncovalent bonding, have been studied for electrospinning, such as benzo-21-crown-7 (B21C7) binding with secondary dialkylammonium salts in chloroform, pillar[5]arene binding with a tertiary ammonium salt, *etc.*^{100–105} Especially, 40 - 55 wt % solutions of tannic acid in a water/ethanol solvent mixture can be electrospun due to the aggregations of tannic acid formed by hydrogen bonding between tannic acid molecules.¹⁰⁵ In this study, the electrospinnable concentration was in the concentrated regime with a scaling value, $\eta_{sp} \sim c^9$,¹⁰⁵ which indicates the appearance of strong molecular interactions. The third sub-category is that amphiphilic molecule systems such as phospholipids and surfactants, which tend to construct self-assembled supramolecular structures due to the balance of their hydrophobic and hydrophilic groups, demonstrate their ability to undergo electrospinning.^{106–109} The phospholipid lecithin (derived from soybeans), with the scaling values for the semi-dilute unentangled regime ($\eta_{sp} \sim c^{2.4}$) and semi-dilute entangled regime ($\eta_{sp} \sim c^{8.4}$), can be electrospun at high concentrations because the formation of wormlike micelles provides sufficient molecular interactions to stabilize the jet during electrospinning. As the concentration increased, it was reported that the

entanglement could take place among the wormlike micelles leading to better stabilization of the jet during electrospinning.¹⁰⁷ Gemini surfactants, like N,N'-didodecyl-N,N,N',N'-tetramethyl-N,N'-ethanedioldiammonium dibromide (12-2-12) in water/methanol, can also be electrospun at high concentration due to the increase of molecular interactions through the formation of the globular micelles in methanol/water.¹⁰⁶

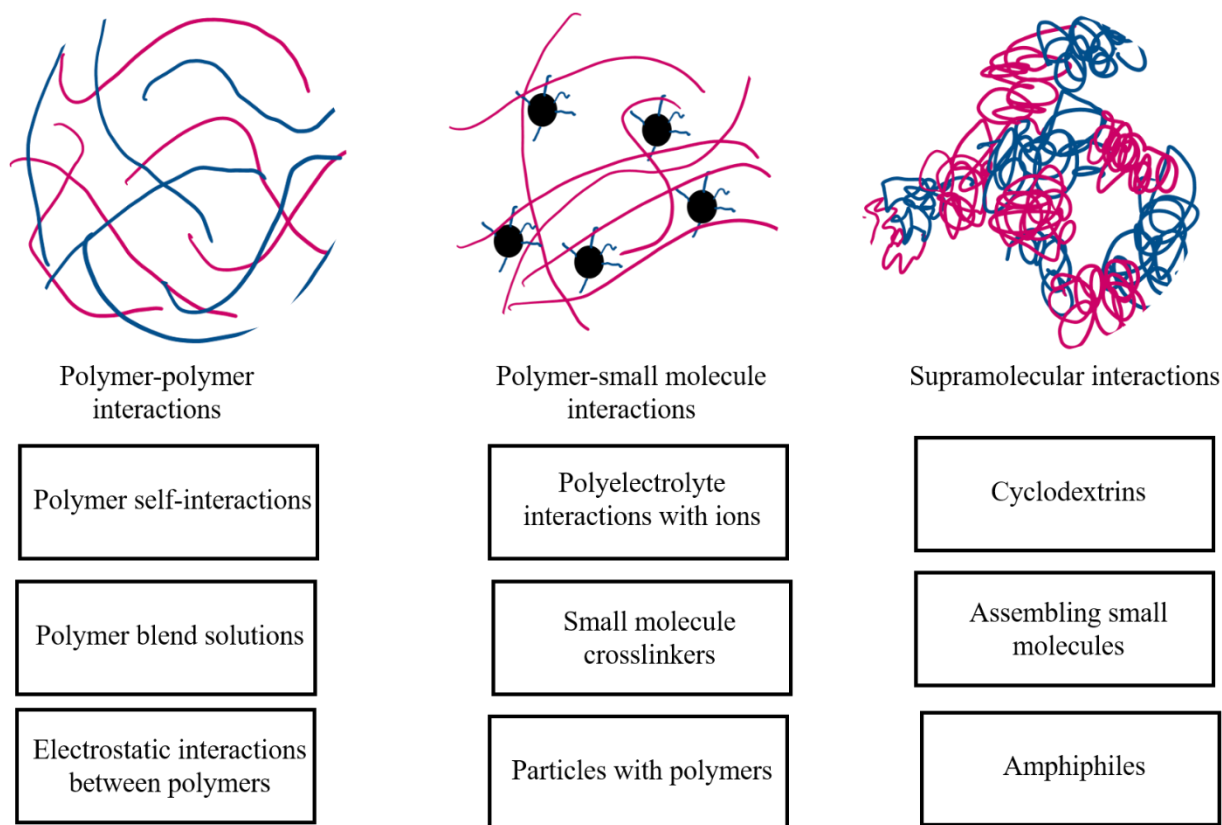


Figure 2.4. Categories of the molecular interaction-driven electrospinning. Reprinted (adapted) with permission from Ewaldz, E.; Brettmann, B. *Molecular Interactions in Electrospinning: From Polymer Mixtures to Supramolecular Assemblies*. *ACS Appl. Polym. Mater.* **2019**, 1 (3), 298–308.⁹² Copyright (2019) American Chemical Society.

Overall, it is worth noting that, because of the underlying assumption of the chain entanglement, the entanglement concentration and the scaling value acquired from the polymer system of interest cannot be applied to foresee the electrospinnability of the system and the morphology of the corresponding electrospun nanofiber for many systems, as mentioned above.^{98,105–107,110–112} Nevertheless, the entanglement concentration and the scaling value,

especially the scaling value compared with the theoretical value of the linear neutral or polyelectrolyte polymer system^{98,105–107,110–112}, can provide valuable information on the microstructure of the interested polymer solution.

2.5 Synthetic polymer in chitosan nonwoven fibrous materials

2.5.1 Background

Synthetic polymers, as additives, are widely used in the preparation of chi nonwoven fibrous materials to optimize chemical, structural, mechanical, morphological, and biological properties. The application of these additive polymers helps overcome the disadvantages prevalent in chi as a biopolymer, including hydrophilicity, crystallinity, and brittleness.¹¹³ Hydrophilicity of chi can lead to poor moisture barrier properties, which is important for food packaging.¹¹⁴ Moreover, although it leads to the loss of constituents in an aqueous medium, resulting in poor stability of the product in an aqueous environment, hydrophilicity can be beneficial for biomedical applications as it contributes to good water swelling property.^{113,114} Therefore, the materials for biomedical applications need to reach a balance between hydrophilicity and hydrophobicity, which can be accomplished through chemical modifications of chi and/or post-treatment methods, as mentioned in Section 2.1.2 as well as with the addition of the synthetic polymer. Crystallinity and brittleness of chi can also be addressed with the use of additive polymers. The crystallinity of chi can provide barrier properties to gasses (O₂ and CO₂), which is useful for food packaging to extend the shelf life of food products, while the semi-crystalline nature of chi leads to the brittleness of chi-based materials.^{113,114} A compromise can be made through the formation of multilayer composites or post-treatment methods.^{113,114} Meanwhile, for chi nonwoven fibrous materials, the applications, such as active food packaging and biomedical applications, share some common properties, including biodegradability, biocompatibility, and ductility.^{113–115} These properties can be fulfilled using water-soluble, biocompatible, and biodegradable synthetic polymers such as PEO^{18–22}, PVA^{15,16}, PAM⁵, PLGA¹⁷, poly(ϵ -caprolactone) (PCL)⁵, poly(vinyl pyrrolidone) (PVP)^{116,117}. Simultaneously, new functionalities, including sensitivity to photooxidation¹¹⁶, high ion exchange ability¹¹⁷, and conductivity¹¹⁸, can be cooperated into chi with synthetic polymers.¹¹⁹ Because chi can be easily dissolved in the dilute acidic aqueous solution but have limited solubility in other solvents to prepare chi nonwoven fibrous materials from polymer blends, chi and synthetic polymers need to be dissolved in the same solvent. Therefore, the first condition to select synthetic

polymers as additives for chi-based materials is water solubility. Miscibility of chi and the synthetic polymer determines the blend's fluid property, which affects the component distribution, the morphology, and the physicochemical property of the corresponding product (i.e., crystallinity).^{21,40} The additive polymer can be utilized in the freeze-drying process and the electrospinning process to control the morphology and tune the physicochemical property of chi nonwoven fibrous materials. For instance, during freeze-drying, a compact lamellar structure may be formed due to strong molecular interactions among PECs. In order to obtain a fibrous structure, the synthetic polymer with a flexible backbone can be used as a space-filler to attenuate the interactions among PECs by weakening the electrostatic interactions or hydrogen bonding, which leads to the formation of the fibrous structure.^{41,119} During electrospinning, the benefit of using the synthetic polymer was discussed in Section 2.4. Briefly, the electrospinning of chi-based systems can be facilitated by the addition of synthetic polymers in two ways: enhancing chain entanglements in chi/synthetic polymers blends or inducing molecular interactions between chi and synthetic polymers.

2.5.2 Poly(ethylene oxide)

Among all the synthetic polymers mentioned previously, PEO has been used extensively as the additive polymer to prepare chi nonwoven fibrous materials due to its viscoelasticity, flexible backbone, and good solubility in water.¹⁸⁻²² PEO is synthesized through the ring-opening polymerization of ethylene oxide, as shown in Figure 2.5a. PEO is a semi-crystalline material that contains about 70-85% crystallinity and an amorphous elastomeric phase at room temperature.¹²⁰ PEO in the crystal state displays a helical conformation with a conformational assignment to the internal rotations, which follows a *trans-gauche-trans* (*tgt*) sequence, as shown in Figure 2.5b.¹²¹ In aqueous solution, PEO shows hydrophilicity by forming hydrogen bonding with water molecules through oxygen atoms on the polymer. Meanwhile, ethylene groups on the polymer repel water molecules leading to the hydrophobicity of PEO. The good water solubility of PEO is attributed to a layer of water molecules surrounding the PEO chain.¹²² Based on the frequency shifts and band shapes of D-LAM (Disordered Longitudinal Acoustic Mode) band in Raman spectra, it indicates that a more ordered conformation of PEO chain closer to the *tgt* sequence in the crystal state present in aqueous solution is compared to the random coil conformation of PEO chain in the molten state.¹²¹ PEO can also form supramolecular assemblies with other polymers in

water. One example is that PEO can form PEO-polymer complexes with poly(carboxylic acid), like PAA and poly(methacrylic acid) (PMAA), through establishing hydrogen bonding between oxygen atoms on PEO and carboxylic groups on poly(carboxylic acid).^{123,124} Due to hydrophobic interactions between -CH₃ on PMAA and -CH₂-CH₂- on PEO, it is easier for PMAA to form complexes with PEO than PAA.¹²⁵ A recent study demonstrated that hydrogen bonding between PEO and PAA in the water solution could be induced through an external force (or the deformation of PEO/PAA blends), resulting in the change of the network of PEO/PAA complexes.¹²⁶ The other example is that PEO can form complexes with various aromatic compounds such as phenol-formaldehyde resin (PFR), tannic acid, poly(vinyl phenol), and β -naphthalene sulfonate.^{127–131} The complex formation between phenolic compounds and PEO results from the intermolecular hydrogen bonding and hydrophobic interactions between -CH₂-CH₂- on PEO and aromatic groups.^{128,130} The complexation between PEO and aromatic compounds depends on the molecular weight of PEO and the aromatic compound.^{127,131,132} For a given arene molecule, for high molecular weight PEO, a single PEO chain with high molecular weight acts as a coupling or physical crosslinking agent that can form complexes with multiple aromatic compounds. On the other hand, one PEO chain can bind with a single aromatic compound when PEO has low molecular weight.¹³¹

Besides properties discussed above, PEO also exhibits confined crystallization, especially in electrospun nanofibrous materials of immiscible polymer blends with PEO as the minority component.^{133–136} Confined crystallization of the polymer occurs when polymer chains are placed into nanosized domains (at least on dimension in the order of 1-100 nm) called confined space. During confined crystallization, a polymer may form the nanostructure in the confined space because of the geometric limitation and the distortion of the phase transition's kinetic pathway of the polymer.¹³⁷ In the case of electrospun nanofibrous materials of immiscible polymer blends with PEO as the minority component, PEO will form a dispersed phase in the nanofibrous materials because of its semi-crystallinity. However, because of the limitation of both the diameter and the shape of nanofibers, phase separation between PEO and the other constituent has a limited length-scale, leading to restricted PEO domains during crystallization. For example, in thermally-treated polystyrene (PS)/PEO electrospun fibers, removing PEO from the electrospun fibers led to small-sized porous features on the surface of the fiber.¹³⁴ At a temperature near the glass transition

temperature of PS during the thermal treatment, porous features' size reduced due to PEO domains that underwent breakup caused by the Plateau-Rayleigh instability. When the temperature was much higher than the glass transition temperature of PS, the porous features' size increased as the mobility of PS matrix increased, leading to the coalescence of the PEO domains.¹³⁴ Therefore, the final shape and size of the created porous features were determined by balancing the coalescence and breakup of PEO domains during crystallization.¹³⁷ Confined crystallization of PEO can be utilized to create porous features on the surface of electrospun fibers easily and rapidly, although the downside of this approach is that the porous features created are highly polydisperse.

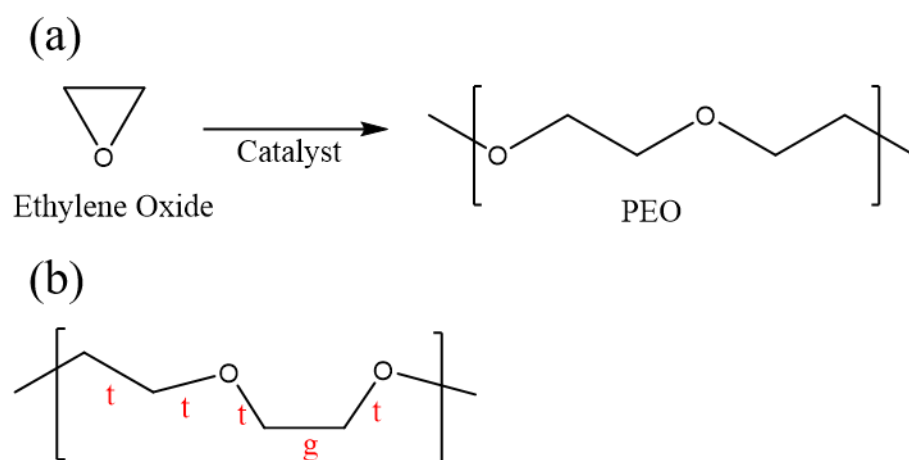


Figure 2.5. (a) Synthesis of polyethylene oxide. (b) A schematic illustration of the *tgt* sequence of PEO in the crystalline state.

2.6 Raman spectroscopy and Raman microimaging

2.6.1 Background of Raman spectroscopy

Raman spectroscopy is a spectral technique typically used to determine vibrational modes and some low-frequency modes of systems (i.e. rotational) based on the Raman effect.¹³⁸ The Raman effect is a phenomenon that results from the interaction of vibrational and/or rotational motions of molecules with electromagnetic radiation. In other words, the Raman effect results from the interaction of light and matter. When light and matter interact, the scattered light can be categorized as elastic (Rayleigh scattering) or inelastic (Raman scattering). The Rayleigh scattering possesses the same frequency as the incident light, while the Raman scattering is detected at different frequencies, which constitutes the Raman spectrum of the sample. In 1928,

when Sir Chandrasekhara Venkata Raman observed the inelastic scattering of light that bears his name, where only simple instrumentation was available, including a focused, filtered beam of sunlight, a large volume of a neat liquid as the sample, and the human eye as a detector. After the initial discovery, the spectroscopic application of the Raman effect had not made much progress until the invention of the laser (the ideal source for Raman spectroscopy). In 1966, Delhaye and Migeon pointed out that Raman scattered light's intensity should not decrease with decreasing sample volume leading to the invention of Raman microspectroscopy. Two different Raman Microspectrometer systems were described in 1974. One of the systems was commercialized and capable of Raman imaging (mapping) and single-point analysis.¹³⁸

According to quantum theory, a molecular motion can have only certain discrete energy states. A change in the state leads to the gain or loss of one or more quanta of energy, which can be expressed according to equation (2.8)

$$\Delta E = h\nu_k \quad (2.8)$$

where h represents Planck's constant ($6.62608 \times 10^{-34} \text{ Js}$) and ν_k is the classical frequency of the molecular motion. The interaction of a molecule with electromagnetic radiation can thus be examined with an energy-transfer mechanism. For instance, during the simplest absorption process, the gain of a quantum of energy by the molecule leads to the annihilation of a photon (a quantum of light); whereas, during spontaneous emission, the loss of a quantum of energy by the molecule corresponds to the creation of a photon. In the light-matter interaction system, scattering processes are composed of at least two quanta acting simultaneously. When a quantum of electromagnetic energy is created for elastic scattering, an identical one is simultaneously annihilated. Thus, the molecule is unchanged under elastic scattering. For inelastic scattering, the two photons are not identical. Thus, a net change in the state of the molecule occurs. When the frequency of the scattered light observed is lower than that of the incident light as the created photon is less energetic than the annihilated one, this is referred to as Stokes Raman scattering. On the other hand, when the Raman frequency is higher than that of the incident light (the laser), this is called anti-Stokes Raman scattering. The scattering processes mentioned above are demonstrated in Figure 2.6. The laser excitation at the frequency ν_0 reappears as the relatively strong Rayleigh line. The weaker Raman frequencies are the consequence of inelastic scattering by a molecular vibration of frequency ν_v . In general, the intensity of the Rayleigh line is 1000 times weaker than that of the

incident excitation, while the Raman scattering is at least 1000 times weaker than that of the Rayleigh line. In practice, the Raman frequencies can be expressed in relation to that of the excitation. Thus, the origin of the abscissa scale in Figure 2.6 is placed at the position of the excitation frequency, which gives the position of the Raman frequencies at $\pm\nu_v$. Moreover, the frequency value in the Raman spectrum is usually represented in wavenumber units of cm^{-1} , which is calculated by $\bar{\nu}_v = \nu_v/c = 1/\lambda_v$, where c corresponds to the velocity of light and λ_v is the corresponding wavelength. The intensity of the Raman effect relates to the polarizability of electrons in a molecule. The vibrational Raman spectra of amorphous materials yield broad features compared to those of the crystalline solids. Furthermore, impurities, vacancies, or other imperfections in the crystal lattice lead to broadening the corresponding Raman bands.¹³⁸ Nowadays, a primary dispersive Raman instrument consists of a laser source with a high excitation intensity, the interference filter to suppress the Rayleigh scattering, a diffraction grating to disperse the Raman scattering, and the charge-coupled-device (CCD) capable of simultaneous detection of a certain wavenumber region.

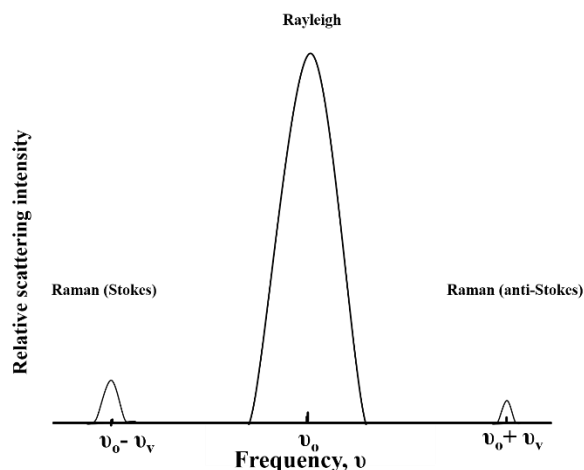


Figure 2.6. Raman and Rayleigh scattering of excitation at a frequency ν_0 . A molecular vibration in the sample is of frequency ν_v .

Both Raman and IR spectroscopies are used to detect the vibrational information of a molecule. However, there are many differences between these two techniques. The most crucial difference is that selection rules are distinct. The vibration is Raman-active if the size, shape, or orientation changes during the normal vibration regarding the polarization of electron clouds in a

molecule while the vibration is IR-active when there is a change in the dipole moment in a molecule.¹³⁹ The latter one is that the intensity of some vibrations is inherently different. For example, the stretching vibrations of the C-S bonds are strong in Raman, while the stretching of the carbonyl groups yields strong intensity in IR. Bending vibrations are generally weaker than stretching vibration in Raman spectra. Moreover, the bond stretching in plane is stronger than that of stretching out of plane, which means that the “ring breathing” in cyclic molecules displays relatively strong Raman bands. Raman spectroscopy has several advantages over IR spectroscopy. One major advantage of Raman spectroscopy is that the quantity of the sample required is small. Compared with conventional IR, Raman spectroscopy only demands a small quantity of the sample for the measurement since the laser beam typically has a small diameter. Another advantage is that there is no major interference of water in Raman spectroscopy as water is a weak Raman scatter, whereas IR suffers from the strong absorption of water.¹³⁹ The low scattering cross-section of water represents an advantage that makes Raman spectroscopy a powerful tool to study the biological system¹⁴⁰ or composite fibrous materials related to the bulk molecular properties of fibrous materials.^{141,142} As well, studies of the time-dependent change of the bulk molecular properties and their interactions with the solvent.^{143,144} However, some disadvantage of Raman includes fluorescence of some compound generated by the laser beam and the “burning” and/or photodecomposition of the sample due to the intense laser power.¹³⁹ Several approaches have been developed to attenuate or avoid fluorescence contributions, including excitation in the near-infrared, enhancement of the Raman signal, and temporal gating to isolate the Raman signal from the fluorescence.^{138,145}

2.6.2 Data processing for obtaining Raman spectral imaging

Raman spectral imaging is an imaging technique that maps the spatial location of one constituent of an inhomogeneous sample based on the Raman scattered photons generated from a characteristic Raman line of the specific compound.¹⁴⁶ Raman spectral imaging has been used for biological studies such as component distribution imaging of living cell^{147–149} and tissue imaging and diagnostics¹⁴⁰ or the determination of the component distribution of the composite fibrous materials.^{150–154} Raman spectral imaging methods can be categorized into two groups: direct-imaging techniques and series-imaging techniques. Direct-imaging techniques relate to the immediate creation of a complete two-dimensional (2D) image at a given wavelength, which

corresponds to a molecular compound within the fully illuminated specimen. For direct imaging, there is no need for extra data processing to produce an image, but image quality can be improved using additional data treatment. On the other hand, series-imaging techniques require image reconstruction, which is achieved either by a laser-scanning method, where the sample is scanned by a finely focused laser beam, or by an encoding method where the image of the sample is encoded with a mask illuminated by an expanded laser beam. A set of 2D images of the sample at various wavelengths can be visualized and manipulated only after the collected data is processed. There are several methods to accomplish laser-scanning methods, including point illumination, line illumination, etc.¹⁴⁶ For the case of point illumination, the laser spot is scanned over the sample sequentially in a raster pattern (or the sample is moved equivalently under the microscope objective). At each resolved position of the sample, a spectrum is collected. Since the Raman signal is weak, a complete set of spatial/spectral Raman data is time-consuming. On the other hand, in the line illumination method, the laser is focused on a narrow line to illuminate the sample. After that, the spectra are collected simultaneously from multiple positions on the sample to generate a large data set. Line illumination results in a significant reduction of data collection time, compared to point illumination. Additionally, the line illumination method may result in better spectral resolution (without signal reduction) and Rayleigh line rejection. Once the data are collected, the spectra are processed, as described above. The first step of data processing involves the removal of the Rayleigh line. Several mathematical methods have been applied to remove the Rayleigh line. For example, polynomial and median filters can be used when the Rayleigh line is sharper than the real Raman bands and the unaffected neighboring pixels. Eradicating the Rayleigh line is very important for Raman spectral imaging because the residue of the Rayleigh line has a great influence on the later data process.¹⁵⁵ The second step is baseline correction, which is another critical step as the baseline intensity may be so high that it could hinder real Raman bands.¹⁴⁰ This step needs to proceed with caution as Emry et al. indicated that an unreasonable baseline correction may introduce errors and lead to artefacts.¹⁵⁶ The final step in data processing is reducing the noise. For a set of data containing a large number of spectra (the data set collected for the Raman spectral imaging), the noise can be reduced by utilizing principal component analysis (PCA), which is an unsupervised data transformation procedure of complex data sets leading to reducing the dimensionality and retaining the most significant information for further analysis.¹⁵⁷ After the data

processing, Raman 2D spectral imaging could be constructed based on the desired Raman spectral information.

2.7 References

- (1) de Oliveira, A. M.; Franco, T. T.; Oliveira Junior, E. N. De. Physicochemical Characterization of Thermally Treated Chitosans and Chitosans Obtained by Alkaline Deacetylation. *Int. J. Polym. Sci.* **2014**, *2014*, 1–9. <https://doi.org/10.1155/2014/853572>.
- (2) Younes, I.; Rinaudo, M. Chitin and Chitosan Preparation from Marine Sources. Structure, Properties and Applications. *Mar. Drugs* **2015**, *13* (3), 1133–1174. <https://doi.org/10.3390/md13031133>.
- (3) Kumar, M. N. V. R.; Muzzarelli, R. A. A.; Muzzarelli, C.; Sashiwa, H.; Domb, A. J. Chitosan Chemistry and Pharmaceutical Perspectives. *Chem. Rev.* **2004**, *104* (12), 6017–6084. <https://doi.org/10.1021/cr030441b>.
- (4) Pillai, C. K. S. S.; Paul, W.; Sharma, C. P. Chitin and Chitosan Polymers: Chemistry, Solubility and Fiber Formation. *Prog. Polym. Sci.* **2009**, *34* (7), 641–678. <https://doi.org/10.1016/j.progpolymsci.2009.04.001>.
- (5) Sakkara, S.; Santosh, M. S.; Reddy, N. Chitosan Fibers. In *Handbook of Fibrous Materials*; Wiley: Weinheim, Germany, 2020; pp 125–156. <https://doi.org/10.1002/9783527342587.ch5>.
- (6) Rinaudo, M.; Domard, A. Solution Properties of Chitosan. In *Chitin and Chitosan*; Skjak-Braek, G., Anthonsen, T., Sandford, P. A., Eds.; Springer Netherlands: Dordrecht, The Netherlands, 1989; pp 71–86.
- (7) Jaworska, M.; Sakurai, K.; Gaudon, P.; Guibal, E. Influence of Chitosan Characteristics on Polymer Properties. I: Crystallographic Properties. *Polym. Int.* **2003**, *52* (2), 198–205. <https://doi.org/10.1002/pi.1159>.
- (8) Wang, Q. Z.; Chen, X. G.; Liu, N.; Wang, S. X.; Liu, C. S.; Meng, X. H.; Liu, C. G. Protonation Constants of Chitosan with Different Molecular Weight and Degree of Deacetylation. *Carbohydr. Polym.* **2006**, *65* (2), 194–201. <https://doi.org/10.1016/j.carbpol.2006.01.001>.

- (9) Barikani, M.; Oliaei, E.; Seddiqi, H.; Honarkar, H. Preparation and Application of Chitin and Its Derivatives: A Review. *Iran. Polym. J.* **2014**, *23* (4), 307–326.
<https://doi.org/10.1007/s13726-014-0225-z>.
- (10) Hajji, S.; Younes, I.; Ghorbel-Bellaaj, O.; Hajji, R.; Rinaudo, M.; Nasri, M.; Jellouli, K. Structural Differences between Chitin and Chitosan Extracted from Three Different Marine Sources. *Int. J. Biol. Macromol.* **2014**, *65*, 298–306.
<https://doi.org/10.1016/j.ijbiomac.2014.01.045>.
- (11) Aiba, S. Studies on Chitosan: 3. Evidence for the Presence of Random and Block Copolymer Structures in Partially N-Acetylated Chitosans. *Int. J. Biol. Macromol.* **1991**, *13* (1), 40–44. [https://doi.org/10.1016/0141-8130\(91\)90008-I](https://doi.org/10.1016/0141-8130(91)90008-I).
- (12) Upadhyaya, L.; Singh, J.; Agarwal, V.; Tewari, R. P. Biomedical Applications of Carboxymethyl Chitosans. *Carbohydr. Polym.* **2013**, *91* (1), 452–466.
<https://doi.org/10.1016/j.carbpol.2012.07.076>.
- (13) Tan, H.; Ma, R.; Lin, C.; Liu, Z.; Tang, T. Quaternized Chitosan as an Antimicrobial Agent: Antimicrobial Activity, Mechanism of Action and Biomedical Applications in Orthopedics. *Int. J. Mol. Sci.* **2013**, *14* (1), 1854–1869.
<https://doi.org/10.3390/ijms14011854>.
- (14) Casettari, L.; Vllasaliu, D.; Castagnino, E.; Stolnik, S.; Howdle, S.; Illum, L. PEGylated Chitosan Derivatives: Synthesis, Characterizations and Pharmaceutical Applications. *Prog. Polym. Sci.* **2012**, *37* (5), 659–685.
<https://doi.org/10.1016/j.progpolymsci.2011.10.001>.
- (15) Elsabee, M. Z.; Naguib, H. F.; Morsi, R. E. Chitosan Based Nanofibers, Review. *Mater. Sci. Eng. C* **2012**, *32* (7), 1711–1726. <https://doi.org/10.1016/j.msec.2012.05.009>.
- (16) Jia, Y. T.; Gong, J.; Gu, X. H.; Kim, H. Y.; Dong, J.; Shen, X. Y. Fabrication and Characterization of Poly (Vinyl Alcohol)/Chitosan Blend Nanofibers Produced by Electrospinning Method. *Carbohydr. Polym.* **2007**, *67* (3), 403–409.
<https://doi.org/10.1016/j.carbpol.2006.06.010>.
- (17) Duan, B.; Yuan, X.; Zhu, Y.; Zhang, Y.; Li, X.; Zhang, Y.; Yao, K. A Nanofibrous

- Composite Membrane of PLGA–Chitosan/PVA Prepared by Electrospinning. *Eur. Polym. J.* **2006**, 42 (9), 2013–2022. <https://doi.org/10.1016/j.eurpolymj.2006.04.021>.
- (18) Ma, G.; Liu, Y.; Peng, C.; Fang, D.; He, B.; Nie, J. Paclitaxel Loaded Electrospun Porous Nanofibers as Mat Potential Application for Chemotherapy against Prostate Cancer. *Carbohydr. Polym.* **2011**, 86 (2), 505–512. <https://doi.org/10.1016/j.carbpol.2011.04.082>.
- (19) Rieger, K. A.; Birch, N. P.; Schiffman, J. D. Electrospinning Chitosan/Poly(Ethylene Oxide) Solutions with Essential Oils: Correlating Solution Rheology to Nanofiber Formation. *Carbohydr. Polym.* **2016**, 139, 131–138. <https://doi.org/10.1016/j.carbpol.2015.11.073>.
- (20) Klossner, R. R.; Queen, H. A.; Coughlin, A. J.; Krause, W. E. Correlation of Chitosan's Rheological Properties and Its Ability to Electrospin. *Biomacromolecules* **2008**, 9 (10), 2947–2953. <https://doi.org/10.1021/bm800738u>.
- (21) Mucha, M.; Pieklna, J.; Wiczorek, A. Characterisation and Morphology of Biodegradable Chitosan / Synthetic Polymer Blends. *Macromol. Symp.* **1999**, 144 (1), 391–412. <https://doi.org/10.1002/masy.19991440137>.
- (22) Seo, H.; Matsumoto, H.; Hara, S.; Minagawa, M.; Tanioka, A.; Yako, H.; Yamagata, Y.; Inoue, K. Preparation of Polysaccharide Nanofiber Fabrics by Electrospray Deposition: Additive Effects of Poly(Ethylene Oxide). *Polym. J.* **2005**, 37 (6), 391–398. <https://doi.org/10.1295/polymj.37.391>.
- (23) Chen, Z.; Mo, X.; He, C.; Wang, H. Intermolecular Interactions in Electrospun Collagen–Chitosan Complex Nanofibers. *Carbohydr. Polym.* **2008**, 72 (3), 410–418. <https://doi.org/10.1016/j.carbpol.2007.09.018>.
- (24) Zhao, J.; Han, W.; Chen, H.; Tu, M.; Zeng, R.; Shi, Y.; Cha, Z.; Zhou, C. Preparation, Structure and Crystallinity of Chitosan Nano-Fibers by a Solid-Liquid Phase Separation Technique. *Carbohydr. Polym.* **2011**, 83 (4), 1541–1546. <https://doi.org/10.1016/j.carbpol.2010.10.009>.
- (25) Jiang, C.; Wang, Z.; Zhang, X.; Zhu, X.; Nie, J.; Ma, G. Crosslinked Polyelectrolyte Complex Fiber Membrane Based on Chitosan-Sodium Alginate by Freeze-Drying. *RSC*

- Adv.* **2014**, *40* (78), 41551–41560. <https://doi.org/10.1039/c4ra04208e>.
- (26) Ma, G.; Wang, Z.; Chen, J.; Yin, R.; Chen, B.; Nie, J. Freeze-Dried Chitosan–Sodium Hyaluronate Polyelectrolyte Complex Fibers as Tissue Engineering Scaffolds. *New J. Chem.* **2014**, *38* (3), 1211. <https://doi.org/10.1039/c3nj00701d>.
 - (27) Verma, D.; Katti, K. S.; Katti, D. R. Polyelectrolyte-Complex Nanostructured Fibrous Scaffolds for Tissue Engineering. *Mater. Sci. Eng. C* **2009**, *29* (7), 2079–2084. <https://doi.org/10.1016/j.msec.2009.04.006>.
 - (28) Wei, Y. C.; Hudson, S. M.; Mayer, J. M.; Kaplan, D. L. The Crosslinking of Chitosan Fibers. *J. Polym. Sci. Part A Polym. Chem.* **1992**, *30* (10), 2187–2193. <https://doi.org/10.1002/pola.1992.080301013>.
 - (29) Monteiro, O. A. C.; Airoidi, C. Some Studies of Crosslinking Chitosan-Glutaraldehyde Interaction in a Homogeneous System. *Int. J. Biol. Macromol.* **1999**, *26* (2–3), 119–128. [https://doi.org/10.1016/S0141-8130\(99\)00068-9](https://doi.org/10.1016/S0141-8130(99)00068-9).
 - (30) Zhao, X.; Chen, S.; Lin, Z.; Du, C. Reactive Electrospinning of Composite Nanofibers of Carboxymethyl Chitosan Cross-Linked by Alginate Dialdehyde with the Aid of Polyethylene Oxide. *Carbohydr. Polym.* **2016**, *148*, 98–106. <https://doi.org/10.1016/j.carbpol.2016.04.051>.
 - (31) Hirano, S.; Yamaguchi, R.; Fukui, N.; Iwata, M. A Chitosan Oxalate Gel: Its Conversion to an N-Acetylchitosan Gel via a Chitosan Gel. *Carbohydr. Res.* **1990**, *201* (1), 145–149. [https://doi.org/10.1016/0008-6215\(90\)84231-I](https://doi.org/10.1016/0008-6215(90)84231-I).
 - (32) Shen, X.; Tong, H.; Jiang, T.; Zhu, Z.; Wan, P.; Hu, J. Homogeneous Chitosan/Carbonate Apatite/Citric Acid Nanocomposites Prepared through a Novel in Situ Precipitation Method. *Compos. Sci. Technol.* **2007**, *67* (11–12), 2238–2245. <https://doi.org/10.1016/j.compscitech.2007.01.034>.
 - (33) Yokoyama, A.; Yamamoto, S.; Kawasaki, T.; Kohgo, T.; Nakasu, M. Development of Calcium Phosphate Cement Using Chitosan and Citric Acid for Bone Substitute Materials. *Biomaterials* **2002**, *23* (4), 1091–1101. [https://doi.org/10.1016/S0142-9612\(01\)00221-6](https://doi.org/10.1016/S0142-9612(01)00221-6).

- (34) Gawish, S. M.; Abo El-Ola, S. M.; Ramadan, A. M.; Abou El-Kheir, A. A. Citric Acid Used as a Crosslinking Agent for the Grafting of Chitosan onto Woolen Fabric. *J. Appl. Polym. Sci.* **2012**, *123* (6), 3345–3353. <https://doi.org/10.1002/app.33873>.
- (35) Desai, K. G. H.; Park, H. J. Encapsulation of Vitamin C in Tripolyphosphate Cross-Linked Chitosan Microspheres by Spray Drying. *J. Microencapsul.* **2005**, *22* (2), 179–192. <https://doi.org/10.1080/02652040400026533>.
- (36) Katas, H.; Alpar, H. O. Development and Characterisation of Chitosan Nanoparticles for SiRNA Delivery. *J. Control. Release* **2006**, *115* (2), 216–225. <https://doi.org/10.1016/j.jconrel.2006.07.021>.
- (37) Du, J.; Hsieh, Y.-L. Nanofibrous Membranes from Aqueous Electrospinning of Carboxymethyl Chitosan. *Nanotechnology* **2008**, *19* (12), 125707. <https://doi.org/10.1088/0957-4484/19/12/125707>.
- (38) Miraftab, M.; Saifullah, A. N.; Cay, A. Physical Stabilisation of Electrospun Poly(Vinyl Alcohol) Nanofibres: Comparative Study on Methanol and Heat-Based Crosslinking. *J. Mater. Sci.* **2015**, *50* (4), 1943–1957. <https://doi.org/10.1007/s10853-014-8759-1>.
- (39) Sadiku-Agboola, O.; Sadiku, E. R. Theoretical Modeling of Nanostructured Formation in Polymer Blends. In *Nanostructured Polymer Blends*; Elsevier, 2014; pp 33–99. <https://doi.org/10.1016/B978-1-4557-3159-6.00003-1>.
- (40) Sakurai, K. Glass Transition Temperature of Chitosan and Miscibility of Chitosan/Poly(N-Vinyl Pyrrolidone) Blends. *Polymer (Guildf)*. **2000**, *41* (19), 7051–7056. [https://doi.org/10.1016/S0032-3861\(00\)00067-7](https://doi.org/10.1016/S0032-3861(00)00067-7).
- (41) Kolhe, P.; Kannan, R. M. Improvement in Ductility of Chitosan through Blending and Copolymerization with PEG: FTIR Investigation of Molecular Interactions. *Biomacromolecules* **2003**, *4* (1), 173–180. <https://doi.org/10.1021/bm025689+>.
- (42) Shenoy, S. L.; Bates, W. D.; Frisch, H. L.; Wnek, G. E. Role of Chain Entanglements on Fiber Formation during Electrospinning of Polymer Solutions: Good Solvent, Non-Specific Polymer-Polymer Interaction Limit. *Polymer (Guildf)*. **2005**, *46* (10), 3372–3384. <https://doi.org/10.1016/j.polymer.2005.03.011>.

- (43) Porter, R. S.; Johnson, J. F. The Entanglement Concept in Polymer Systems. *Chem. Rev.* **1966**, 66 (1), 1–27. <https://doi.org/10.1021/cr60239a001>.
- (44) Arunan, E.; Desiraju, G. R.; Klein, R. A.; Sadlej, J.; Scheiner, S.; Alkorta, I.; Clary, D. C.; Crabtree, R. H.; Dannenberg, J. J.; Hobza, P.; Kjaergaard, H. G.; Legon, A. C.; Mennucci, B.; Nesbitt, D. J. Defining the Hydrogen Bond: An Account (IUPAC Technical Report). *Pure Appl. Chem.* **2011**, 83 (8), 1619–1636. <https://doi.org/10.1351/PAC-REP-10-01-01>.
- (45) Blokzijl, W.; Engberts, J. B. F. N. Hydrophobic Effects. Opinions and Facts. *Angewandte Chemie International Edition.* **1993**, 32(11), 1545–1579. <https://doi.org/10.1002/anie.199315451>.
- (46) Widom, B.; Bhimalapuram, P.; Koga, K. The Hydrophobic Effect. *Phys. Chem. Chem. Phys.* **2003**, 5 (15), 3085. <https://doi.org/10.1039/b304038k>.
- (47) Southall, N. T.; Dill, K. A.; Haymet, A. D. J. A View of the Hydrophobic Effect. *J. Phys. Chem. B* **2002**, 106 (3), 521–533. <https://doi.org/10.1021/jp015514e>.
- (48) Tang, X. (Charlie); Pikal, M. J. Design of Freeze-Drying Processes for Pharmaceuticals: Practical Advice. *Pharm. Res.* **2004**, 21 (2), 191–200. <https://doi.org/10.1023/B:PHAM.0000016234.73023.75>.
- (49) Kasper, J. C.; Friess, W. The Freezing Step in Lyophilization: Physico-Chemical Fundamentals, Freezing Methods and Consequences on Process Performance and Quality Attributes of Biopharmaceuticals. *Eur. J. Pharm. Biopharm.* **2011**, 78 (2), 248–263. <https://doi.org/10.1016/j.ejpb.2011.03.010>.
- (50) Kim, M. Y.; Lee, J. Chitosan Fibrous 3D Networks Prepared by Freeze Drying. *Carbohydr. Polym.* **2011**, 84 (4), 1329–1336. <https://doi.org/10.1016/j.carbpol.2011.01.029>.
- (51) Han, J.; Zhou, C.; Wu, Y.; Liu, F.; Wu, Q. Self-Assembling Behavior of Cellulose Nanoparticles during Freeze-Drying: Effect of Suspension Concentration, Particle Size, Crystal Structure, and Surface Charge. *Biomacromolecules* **2013**, 14 (5), 1529–1540. <https://doi.org/10.1021/bm4001734>.

- (52) Deville, S. Freezing as a Path to Build Complex Composites. *Science* (80-.). **2006**, *311* (5760), 515–518. <https://doi.org/10.1126/science.1120937>.
- (53) Huang, S.; Yu, Z.; Qi, C.; Zhang, Y. Chitosan/Organic Rectorite Nanocomposites Rapidly Synthesized by Microwave Irradiation: Effects of Chitosan Molecular Weight. *Rsc Adv.* **2015**, *5* (104), 85272–85279. <https://doi.org/10.1039/c5ra13939b>.
- (54) Lee, J.; Deng, Y. The Morphology and Mechanical Properties of Layer Structured Cellulose Microfibril Foams from Ice-Templating Methods. *Soft Matter* **2011**, *7* (13), 6034. <https://doi.org/10.1039/c1sm05388d>.
- (55) Wilson, P. .; Heneghan, A. .; Haymet, A. D. . Ice Nucleation in Nature: Supercooling Point (SCP) Measurements and the Role of Heterogeneous Nucleation. *Cryobiology* **2003**, *46* (1), 88–98. [https://doi.org/10.1016/S0011-2240\(02\)00182-7](https://doi.org/10.1016/S0011-2240(02)00182-7).
- (56) Searles, J. A.; Carpenter, J. F.; Randolph, T. W. The Ice Nucleation Temperature Determines the Primary Drying Rate of Lyophilization for Samples Frozen on a Temperature-controlled Shelf. *J. Pharm. Sci.* **2001**, *90* (7), 860–871. <https://doi.org/10.1002/jps.1039>.
- (57) Qian, L.; Zhang, H. Controlled Freezing and Freeze Drying: A Versatile Route for Porous and Micro-/Nano-Structured Materials. *J. Chem. Technol. Biotechnol.* **2011**, *86* (2), 172–184. <https://doi.org/10.1002/jctb.2495>.
- (58) Ma, P. X.; Zhang, R. Synthetic Nano-Scale Fibrous Extracellular Matrix. *J. Biomed. Mater. Res.* **1999**, *46* (1), 60–72. [https://doi.org/10.1002/\(SICI\)1097-4636\(199907\)46:1<60::AID-JBM7>3.0.CO;2-H](https://doi.org/10.1002/(SICI)1097-4636(199907)46:1<60::AID-JBM7>3.0.CO;2-H).
- (59) Chen, W.; Ma, J.; Zhu, L.; Morsi, Y.; El-Hamshary, H.; Al-Deyab, S. S.; Mo, X. Superelastic, Superabsorbent and 3D Nanofiber-Assembled Scaffold for Tissue Engineering. *Colloids Surfaces B Biointerfaces* **2016**, *142*, 165–172. <https://doi.org/10.1016/j.colsurfb.2016.02.050>.
- (60) Li, D.; Xia, Y. N. Electrospinning of Nanofibers: Reinventing the Wheel? *Adv. Mater.* **2004**, *16* (14), 1151–1170. <https://doi.org/10.1002/adma.200400719>.

- (61) Xue, J.; Wu, T.; Dai, Y.; Xia, Y. Electrospinning and Electrospun Nanofibers: Methods, Materials, and Applications. *Chem. Rev.* **2019**, *119* (8), 5298–5415. <https://doi.org/10.1021/acs.chemrev.8b00593>.
- (62) Boys, C. V. On the Production, Properties, and Some Suggested Uses of the Finest Threads. *Proc. Phys. Soc. London* **1887**, *9* (1), 8–19. <https://doi.org/10.1088/1478-7814/9/1/303>.
- (63) Yarin, A. L.; Koombhongse, S.; Reneker, D. H. Taylor Cone and Jetting from Liquid Droplets in Electrospinning of Nanofibers. *J. Appl. Phys.* **2001**, *90* (9), 4836–4846. <https://doi.org/10.1063/1.1408260>.
- (64) Fong, H.; Chun, I.; Reneker, D. Beaded Nanofibers Formed during Electrospinning. *Polymer (Guildf)*. **1999**, *40* (16), 4585–4592. [https://doi.org/10.1016/S0032-3861\(99\)00068-3](https://doi.org/10.1016/S0032-3861(99)00068-3).
- (65) Yarin, A. L.; Koombhongse, S.; Reneker, D. H. Bending Instability in Electrospinning of Nanofibers. *J. Appl. Phys.* **2001**, *89* (5), 3018–3026. <https://doi.org/10.1063/1.1333035>.
- (66) Reneker, D. H.; Yarin, A. L.; Fong, H.; Koombhongse, S. Bending Instability of Electrically Charged Liquid Jets of Polymer Solutions in Electrospinning. *J. Appl. Phys.* **2000**, *87* (9), 4531–4547. <https://doi.org/10.1063/1.373532>.
- (67) Shin, Y. M.; Hohman, M. M.; Brenner, M. P.; Rutledge, G. C. Electrospinning: A Whipping Fluid Jet Generates Submicron Polymer Fibers. *Appl. Phys. Lett.* **2001**, *78* (8), 1149–1151. <https://doi.org/10.1063/1.1345798>.
- (68) Shin, Y. M. M.; Hohman, M. M. M.; Brenner, M. P. P.; Rutledge, G. C. C. Experimental Characterization of Electrospinning: The Electrically Forced Jet and Instabilities. *Polymer (Guildf)*. **2001**, *42* (25), 09955–09967. [https://doi.org/10.1016/S0032-3861\(01\)00540-7](https://doi.org/10.1016/S0032-3861(01)00540-7).
- (69) Hohman, M. M.; Shin, M.; Rutledge, G.; Brenner, M. P. Electrospinning and Electrically Forced Jets. I. Stability Theory. *Phys. Fluids* **2001**, *13* (8), 2201–2220. <https://doi.org/10.1063/1.1383791>.
- (70) Hohman, M. M.; Shin, M.; Rutledge, G.; Brenner, M. P. Electrospinning and Electrically

- Forced Jets. II. Applications. *Phys. Fluids* **2001**, *13* (8), 2221–2236.
<https://doi.org/10.1063/1.1384013>.
- (71) Loscertales, I. G. Micro/Nano Encapsulation via Electrified Coaxial Liquid Jets. *Science* (80-.). **2002**, *295* (5560), 1695–1698. <https://doi.org/10.1126/science.1067595>.
 - (72) Ding, B.; Kimura, E.; Sato, T.; Fujita, S.; Shiratori, S. Fabrication of Blend Biodegradable Nanofibrous Nonwoven Mats via Multi-Jet Electrospinning. *Polymer (Guildf)*. **2004**, *45* (6), 1895–1902. <https://doi.org/10.1016/j.polymer.2004.01.026>.
 - (73) Taylor, G. Disintegration of Water Drops in an Electric Field. *Proc. R. Soc. London. Ser. A. Math. Phys. Sci.* **1964**, *280* (1382), 383–397. <https://doi.org/10.1098/rspa.1964.0151>.
 - (74) Taylor, G. Electrically Driven Jets. *Proc. R. Soc. London. A. Math. Phys. Sci.* **1969**, *313* (1515), 453–475. <https://doi.org/10.1098/rspa.1969.0205>.
 - (75) Young, T. An Essay on the Cohesion of Fluids. *Philos. Trans. R. Soc. London* **1805**, *95*, 65–87.
 - (76) Finn, R. Capillary Surface Interactions. *Not. AMS* **1999**, *46*, 770–781.
 - (77) Collins, R. T.; Jones, J. J.; Harris, M. T.; Basaran, O. A. Electrohydrodynamic Tip Streaming and Emission of Charged Drops from Liquid Cones. *Nat. Phys.* **2008**, *4* (2), 149–154. <https://doi.org/10.1038/nphys807>.
 - (78) He, J.-H.; Wu, Y.; Zuo, W.-W. Critical Length of Straight Jet in Electrospinning. *Polymer (Guildf)*. **2005**, *46* (26), 12637–12640. <https://doi.org/10.1016/j.polymer.2005.10.130>.
 - (79) Reneker, D. H.; Yarin, A. L. Electrospinning Jets and Polymer Nanofibers. *Polymer*. May 2008, pp 2387–2425. <https://doi.org/10.1016/j.polymer.2008.02.002>.
 - (80) Duft, D.; Achtzehn, T.; Müller, R.; Huber, B. A.; Leisner, T. Rayleigh Jets from Levitated Microdroplets. *Nature* **2003**, *421* (6919), 128–128. <https://doi.org/10.1038/421128a>.
 - (81) Shenoy, S. L.; Bates, W. D.; Wnek, G. Correlations between Electrospinnability and Physical Gelation. *Polymer (Guildf)*. **2005**, *46* (21), 8990–9004.
<https://doi.org/10.1016/j.polymer.2005.06.053>.

- (82) Kong, L.; Ziegler, G. R. Role of Molecular Entanglements in Starch Fiber Formation by Electrospinning. *Biomacromolecules* **2012**, *13* (8), 2247–2253.
<https://doi.org/10.1021/bm300396j>.
- (83) McKee, M. G.; Wilkes, G. L.; Colby, R. H.; Long, T. E. Correlations of Solution Rheology with Electrospun Fiber Formation of Linear and Branched Polyesters. *Macromolecules* **2004**, *37* (5), 1760–1767. <https://doi.org/10.1021/ma035689h>.
- (84) Yu, J. H.; Fridrikh, S. V.; Rutledge, G. C. The Role of Elasticity in the Formation of Electrospun Fibers. *Polymer (Guildf)*. **2006**, *47* (13), 4789–4797.
<https://doi.org/10.1016/j.polymer.2006.04.050>.
- (85) Ewaldz, E.; Patel, R.; Banerjee, M.; Brettmann, B. K. Material Selection in Electrospinning Microparticles. *Polymer (Guildf)*. **2018**, *153*, 529–537.
<https://doi.org/10.1016/j.polymer.2018.08.015>.
- (86) Krause, W. E.; Bellomo, E. G.; Colby, R. H. Rheology of Sodium Hyaluronate under Physiological Conditions. *Biomacromolecules* **2001**, *2* (1), 65–69.
<https://doi.org/10.1021/bm0055798>.
- (87) Colby, R. H.; Fetters, L. J.; Funk, W. G.; Graessley, W. W. Effects of Concentration and Thermodynamic Interaction on the Viscoelastic Properties of Polymer Solutions. *Macromolecules* **1991**, *24* (13), 3873–3882. <https://doi.org/10.1021/ma00013a021>.
- (88) Rubinstein, M.; Colby, R. H.; Dobrynin, A. V. Dynamics of Semidilute Polyelectrolyte Solutions. *Phys. Rev. Lett.* **1994**, *73* (20), 2776–2779.
<https://doi.org/10.1103/PhysRevLett.73.2776>.
- (89) Dobrynin, A. V.; Colby, R. H.; Rubinstein, M. Scaling Theory of Polyelectrolyte Solutions. *Macromolecules* **1995**, *28* (6), 1859–1871.
<https://doi.org/10.1021/ma00110a021>.
- (90) McKee, M. G.; Hunley, M. T.; Layman, J. M.; Long, T. E. Solution Rheological Behavior and Electrospinning of Cationic Polyelectrolytes. *Macromolecules* **2006**, *39* (2), 575–583.
<https://doi.org/10.1021/ma051786u>.

- (91) Zhong, W.; Li, F.; Chen, L.; Chen, Y.; Wei, Y. A Novel Approach to Electrospinning of Pristine and Aligned MEH-PPV Using Binary Solvents. *J. Mater. Chem.* **2012**, *22* (12), 5523. <https://doi.org/10.1039/c2jm15970h>.
- (92) Ewaldz, E.; Brettmann, B. Molecular Interactions in Electrospinning: From Polymer Mixtures to Supramolecular Assemblies. *ACS Appl. Polym. Mater.* **2019**, *1* (3), 298–308. <https://doi.org/10.1021/acsapm.8b00073>.
- (93) Chen, S.-P.; Archer, L. A. Relaxation Dynamics of Salt-Free Polyelectrolyte Solutions Using Flow Birefringence and Rheometry. *J. Polym. Sci. Part B Polym. Phys.* **1999**, *37* (8), 825–835. [https://doi.org/10.1002/\(SICI\)1099-0488\(19990415\)37:8<825::AID-POLB8>3.0.CO;2-H](https://doi.org/10.1002/(SICI)1099-0488(19990415)37:8<825::AID-POLB8>3.0.CO;2-H).
- (94) Montembault, A.; Viton, C.; Domard, A. Rheometric Study of the Gelation of Chitosan in Aqueous Solution without Cross-Linking Agent. *Biomacromolecules* **2005**, *6* (2), 653–662. <https://doi.org/10.1021/bm049593m>.
- (95) Pakravan, M.; Heuzey, M.-C.; Ajji, A. A Fundamental Study of Chitosan/PEO Electrospinning. *Polymer (Guildf)*. **2011**, *52* (21), 4813–4824. <https://doi.org/10.1016/j.polymer.2011.08.034>.
- (96) Bhattarai, N.; Edmondson, D.; Veisheh, O.; Matsen, F. A.; Zhang, M. Q. Electrospun Chitosan-Based Nanofibers and Their Cellular Compatibility. *Biomaterials* **2005**, *26* (31), 6176–6184. <https://doi.org/10.1016/j.biomaterials.2005.03.027>.
- (97) Celebioglu, A.; Uyar, T. Cyclodextrin Nanofibers by Electrospinning. *Chem. Commun.* **2010**, *46* (37), 6903–6905. <https://doi.org/10.1039/c0cc01484b>.
- (98) Zhang, W.; Chen, M.; Zha, B.; Diao, G. Correlation of Polymer-like Solution Behaviors with Electrospun Fiber Formation of Hydroxypropyl- β -Cyclodextrin and the Adsorption Study on the Fiber. *Phys. Chem. Chem. Phys.* **2012**, *14* (27), 9729. <https://doi.org/10.1039/c2cp41092c>.
- (99) Manasco, J. L.; Saquing, C. D.; Tang, C.; Khan, S. A. Cyclodextrin Fibers via Polymer-Free Electrospinning. *Rsc Adv.* **2012**, *2* (9), 3778–3784. <https://doi.org/10.1039/c2ra00004k>.

- (100) Chung, K.-T.; Wong, T. Y.; Wei, C.-I.; Huang, Y.-W.; Lin, Y. Tannins and Human Health: A Review. *Crit. Rev. Food Sci. Nutr.* **1998**, *38* (6), 421–464.
- (101) Yan, X.; Zhou, M.; Chen, J.; Chi, X.; Dong, S.; Zhang, M.; Ding, X.; Yu, Y.; Shao, S.; Huang, F. Supramolecular Polymer Nanofibers via Electrospinning of a Heteroditopic Monomer. *Chem. Commun.* **2011**, *47* (25), 7086–7088.
<https://doi.org/10.1039/c1cc11790d>.
- (102) Xu, J.-F.; Chen, Y.-Z.; Wu, D.; Wu, L.-Z.; Tung, C.-H.; Yang, Q.-Z. Photoresponsive Hydrogen-Bonded Supramolecular Polymers Based on a Stiff Stilbene Unit. *Angew. Chemie Int. Ed.* **2013**, *52* (37), 9738–9742. <https://doi.org/10.1002/anie.201303496>.
- (103) Wang, K.; Wang, C.-Y.; Wang, Y.; Li, H.; Bao, C.-Y.; Liu, J.-Y.; Zhang, S. X.-A.; Yang, Y.-W. Electrospun Nanofibers and Multi-Responsive Supramolecular Assemblies Constructed from a Pillar[5]Arene-Based Receptor. *Chem. Commun.* **2013**, *49* (89), 10528–10530. <https://doi.org/10.1039/c3cc46477f>.
- (104) Chen, D.; Zhan, J.; Zhang, M.; Zhang, J.; Tao, J.; Tang, D.; Shen, A.; Qiu, H.; Yin, S. A Fluorescent Supramolecular Polymer with Aggregation Induced Emission (AIE) Properties Formed by Crown Ether-Based Host–Guest Interactions. *Polym. Chem.* **2015**, *6* (1), 25–29. <https://doi.org/10.1039/C4PY01206B>.
- (105) Allais, M.; Mailley, D.; Hébraud, P.; Ihiwakrim, D.; Ball, V.; Meyer, F.; Hébraud, A.; Schlatter, G. Polymer-Free Electrospinning of Tannic Acid and Cross-Linking in Water for Hybrid Supramolecular Nanofibres. *Nanoscale* **2018**, *10* (19), 9164–9173.
<https://doi.org/10.1039/C8NR01067F>.
- (106) Cashion, M. P.; Li, X.; Geng, Y.; Hunley, M. T.; Long, T. E. Gemini Surfactant Electrospun Membranes. *Langmuir* **2010**, *26* (2), 678–683.
<https://doi.org/10.1021/la902287b>.
- (107) Hunley, M. T.; McKee, M. G.; Long, T. E. Submicron Functional Fibrous Scaffolds Based on Electrospun Phospholipids. *J. Mater. Chem.* **2007**, *17* (7), 605–608.
<https://doi.org/10.1039/B613474B>.
- (108) Hemp, S. T.; Hudson, A. G.; Allen, M. H.; Pole, S. S.; Moore, R. B.; Long, T. E. Solution

- Properties and Electrospinning of Phosphonium Gemini Surfactants. *Soft Matter* **2014**, *10* (22), 3970–3977. <https://doi.org/10.1039/C4SM00271G>.
- (109) Tayi, A. S.; Pashuck, E. T.; Newcomb, C. J.; McClendon, M. T.; Stupp, S. I. Electrospinning Bioactive Supramolecular Polymers from Water. *Biomacromolecules* **2014**, *15* (4), 1323–1327. <https://doi.org/10.1021/bm401877s>.
- (110) Gupta, D.; Jassal, M.; Agrawal, A. K. Solution Properties and Electrospinning of Poly(Galacturonic Acid) Nanofibers. *Carbohydr. Polym.* **2019**, *212*, 102–111. <https://doi.org/10.1016/j.carbpol.2019.02.023>.
- (111) McKee, M. G.; Elkins, C. L.; Long, T. E. Influence of Self-Complementary Hydrogen Bonding on Solution Rheology/Electrospinning Relationships. *Polymer (Guildf)*. **2004**, *45* (26), 8705–8715. <https://doi.org/10.1016/j.polymer.2004.10.049>.
- (112) Burns, N. A.; Burroughs, M. C.; Gracz, H.; Pritchard, C. Q.; Brozena, A. H.; Willoughby, J.; Khan, S. A. Cyclodextrin Facilitated Electrospun Chitosan Nanofibers. *RSC Adv.* **2015**, *5* (10), 7131–7137. <https://doi.org/10.1039/c4ra09662b>.
- (113) Youssef, A. M.; El-Sayed, S. M. Bionanocomposites Materials for Food Packaging Applications: Concepts and Future Outlook. *Carbohydr. Polym.* **2018**, *193* (February), 19–27. <https://doi.org/10.1016/j.carbpol.2018.03.088>.
- (114) Elsabee, M. Z.; Abdou, E. S. Chitosan Based Edible Films and Coatings: A Review. *Mater. Sci. Eng. C* **2013**, *33* (4), 1819–1841. <https://doi.org/10.1016/j.msec.2013.01.010>.
- (115) Ahmed, S.; Annu; Ali, A.; Sheikh, J. A Review on Chitosan Centred Scaffolds and Their Applications in Tissue Engineering. *Int. J. Biol. Macromol.* **2018**, *116*, 849–862. <https://doi.org/10.1016/j.ijbiomac.2018.04.176>.
- (116) Sionkowska, A.; Wisniewski, M.; Skopinska, J.; Vicini, S.; Marsano, E. The Influence of UV Irradiation on the Mechanical Properties of Chitosan/Poly(Vinyl Pyrrolidone) Blends. *Polym. Degrad. Stab.* **2005**, *88* (2), 261–267. <https://doi.org/10.1016/j.polymdegradstab.2004.08.018>.
- (117) Smitha, B.; Sridhar, S.; Khan, A. A. Chitosan–Poly(Vinyl Pyrrolidone) Blends as

- Membranes for Direct Methanol Fuel Cell Applications. *J. Power Sources* **2006**, *159* (2), 846–854. <https://doi.org/10.1016/j.jpowsour.2005.12.032>.
- (118) Gan, D.; Han, L.; Wang, M.; Xing, W.; Xu, T.; Zhang, H.; Wang, K.; Fang, L.; Lu, X. Conductive and Tough Hydrogels Based on Biopolymer Molecular Templates for Controlling in Situ Formation of Polypyrrole Nanorods. *ACS Appl. Mater. Interfaces* **2018**, *10* (42), 36218–36228. <https://doi.org/10.1021/acsami.8b10280>.
- (119) Sionkowska, A. Current Research on the Blends of Natural and Synthetic Polymers as New Biomaterials: Review. *Prog. Polym. Sci.* **2011**, *36* (9), 1254–1276. <https://doi.org/10.1016/j.progpolymsci.2011.05.003>.
- (120) Arya, A.; Sharma, A. L. Insights into the Use of Polyethylene Oxide in Energy Storage/Conversion Devices: A Critical Review. *J. Phys. D. Appl. Phys.* **2017**, *50* (44), 443002. <https://doi.org/10.1088/1361-6463/aa8675>.
- (121) Branca, C.; Faraone, A.; Magazú, S.; Maisano, G.; Migliardo, P.; Villari, V. PolyEthylene Oxide: A Review of Experimental Findings by Spectroscopic Techniques. *J. Mol. Liq.* **2000**, *87* (1), 21–68. [https://doi.org/10.1016/S0167-7322\(00\)00129-X](https://doi.org/10.1016/S0167-7322(00)00129-X).
- (122) Hammouda, B.; Ho, D. L.; Kline, S. Insight into Clustering in Poly(Ethylene Oxide) Solutions. *Macromolecules* **2004**, *37* (18), 6932–6937. <https://doi.org/10.1021/ma049623d>.
- (123) Ikawa, T.; Abe, K.; Honda, K.; Tsuchida, E. Interpolymer Complex between Poly(Ethylene Oxide) and Poly(Carboxylic Acid). *J. Polym. Sci. Polym. Chem. Ed.* **1975**, *13* (7), 1505–1514. <https://doi.org/10.1002/pol.1975.170130703>.
- (124) Iliopoulos, I.; Audebert, R. Complexation of Acrylic Acid Copolymers with Polybases: Importance of Cooperative Effects. *Macromolecules* **1991**, *24* (9), 2566–2575. <https://doi.org/10.1021/ma00009a066>.
- (125) Miyoshi, T.; Takegoshi, K.; Hikichi, K. High-Resolution Solid-State ^{13}C Nuclear Magnetic Resonance Study of a Polymer Complex: Poly(Methacrylic Acid)/Poly(Ethylene Oxide). *Polymer (Guildf)*. **1996**, *37* (1), 11–18. [https://doi.org/10.1016/0032-3861\(96\)81594-1](https://doi.org/10.1016/0032-3861(96)81594-1).

- (126) Van Kesteren, S.; Nikolaeva, T.; Van As, H.; Dijksman, J. A. Direct Evidence of Stress-Induced Chain Proximity in a Macromolecular Complex. *Phys. Rev. Mater.* **2020**, *4* (5), 1–13. <https://doi.org/10.1103/PhysRevMaterials.4.055603>.
- (127) Stack, K. R.; Dunn, L. A.; Roberts, N. K. Study of the Interaction between Poly(Ethylene Oxide) and Phenol-Formaldehyde Resin. *Colloids and Surfaces* **1991**, *61* (C), 205–218. [https://doi.org/10.1016/0166-6622\(91\)80310-K](https://doi.org/10.1016/0166-6622(91)80310-K).
- (128) Cong, R.; Bain, A. D.; Pelton, R. An NMR Investigation of the Interaction of Polyethylene Oxide with Water-Soluble Poly(Vinyl Phenol-Co-Potassium Styrene Sulfonate). *J. Polym. Sci. Part B Polym. Phys.* **2000**, *38* (10), 1276–1284. [https://doi.org/10.1002/\(SICI\)1099-0488\(20000515\)38:10<1276::AID-POLB20>3.0.CO;2-6](https://doi.org/10.1002/(SICI)1099-0488(20000515)38:10<1276::AID-POLB20>3.0.CO;2-6).
- (129) Zhang, X.; Takegoshi, K.; Hikichi, K. Composition Dependence of the Miscibility and Phase Structure of Amorphous/Crystalline Polymer Blends As Studied by High-Resolution Solid-State ¹³C NMR Spectroscopy. *Macromolecules* **1992**, *25* (9), 2336–2340. <https://doi.org/10.1021/ma00035a009>.
- (130) Pickelmann, J.; Plank, J. A Mechanistic Study Explaining the Synergistic Viscosity Increase Obtained from Polyethylene Oxide (PEO) and β -Naphthalene Sulfonate (BNS) in Shotcrete. *Cem. Concr. Res.* **2012**, *42* (11), 1409–1416. <https://doi.org/10.1016/j.cemconres.2012.08.003>.
- (131) Lu, C.; Pelton, R. Factors Influencing the Size of PEO Complexes with a Tyrosine-Rich Polypeptide. *Langmuir* **2004**, *20* (10), 3962–3968. <https://doi.org/10.1021/la036032s>.
- (132) Cong, R.; Pelton, R.; Russo, P.; Doucet, G. Factors Affecting the Size of Aqueous Poly(Vinylphenol-Co-Potassium Styrenesulfonate)/Poly(Ethylene Oxide) Complexes. *Macromolecules* **2003**, *36* (1), 204–209. <https://doi.org/10.1021/ma020965y>.
- (133) Rufino, T. D. C.; Felisberti, M. I. Confined PEO Crystallisation in Immiscible PEO/PLLA Blends. *RSC Adv.* **2016**, *6* (37), 30937–30950. <https://doi.org/10.1039/C6RA02406H>.
- (134) Samanta, P.; Thangapandian, V.; Singh, S.; Srivastava, R.; Nandan, B.; Liu, C. L.; Chen, H. L. Crystallization Behaviour of Poly(Ethylene Oxide) under Confinement in the

- Electrospun Nanofibers of Polystyrene/Poly(Ethylene Oxide) Blends. *Soft Matter* **2016**, *12* (23), 5110–5120. <https://doi.org/10.1039/c6sm00648e>.
- (135) Kupka, V.; Dvůřáková, E.; Manakhov, A.; Michlíček, M.; Petruš, J.; Vojtová, L.; Zajíčková, L. Well-Blended PCL/PEO Electrospun Nanofibers with Functional Properties Enhanced by Plasma Processing. *Polymers (Basel)*. **2020**, *12* (6), 1403. <https://doi.org/10.3390/polym12061403>.
- (136) Zhong, G.; Wang, K.; Zhang, L.; Li, Z. M.; Fong, H.; Zhu, L. Nanodroplet Formation and Exclusive Homogenously Nucleated Crystallization in Confined Electrospun Immiscible Polymer Blend Fibers of Polystyrene and Poly(Ethylene Oxide). *Polymer (Guildf)*. **2011**, *52* (24), 5397–5402. <https://doi.org/10.1016/j.polymer.2011.09.045>.
- (137) Samanta, P.; Liu, C.-L.; Nandan, B.; Chen, H.-L. Crystallization of Polymers in Confined Space. In *Crystallization in Multiphase Polymer Systems*; Elsevier, 2018; pp 367–431. <https://doi.org/10.1016/B978-0-12-809453-2.00013-X>.
- (138) Turrell, G. The Raman Effect. In *Raman Microscopy*; Turrell, G., Corset, J., Eds.; Academic Press: London, 1996; pp 1–25. <https://doi.org/10.1016/B978-0-12-189690-4.X5018-2>.
- (139) Ferraro, J. R.; Nakamoto, K.; Brown, C. W. Chapter 1 - Basic Theory. In *Introductory Raman spectroscopy*; Ferraro, J. R., Nakamoto, K., Brown, C. W. B. T.-I. R. S. (Second E., Eds.; Academic Press: San Diego, 2003; pp 1–94. <https://doi.org/https://doi.org/10.1016/B978-012254105-6/50004-4>.
- (140) Bocklitz, T. W.; Guo, S.; Ryabchykov, O.; Vogler, N.; Popp, J. Raman Based Molecular Imaging and Analytics: A Magic Bullet for Biomedical Applications!? *Anal. Chem.* **2016**, *88* (1), 133–151. <https://doi.org/10.1021/acs.analchem.5b04665>.
- (141) Ayutsede, J.; Gandhi, M.; Sukigara, S.; Micklus, M.; Chen, H.-E.; Ko, F. Regeneration of Bombyx Mori Silk by Electrospinning. Part 3: Characterization of Electrospun Nonwoven Mat. *Polymer (Guildf)*. **2005**, *46* (5), 1625–1634. <https://doi.org/10.1016/j.polymer.2004.11.029>.
- (142) Wang, C.; Li, Y.; Ding, G.; Xie, X.; Jiang, M. Preparation and Characterization of

- Graphene Oxide/Poly(Vinyl Alcohol) Composite Nanofibers via Electrospinning. *J. Appl. Polym. Sci.* **2013**, *127* (4), 3026–3032. <https://doi.org/10.1002/app.37656>.
- (143) Pavoni, E.; Tsukada, M.; Taddei, P. Influence of Grafting with Acrylate Compounds on the Conformational Rearrangements of Silk Fibroin upon Electrospinning and Treatment with Aqueous Methanol. *J. Raman Spectrosc.* **2016**, *47* (11), 1367–1374. <https://doi.org/10.1002/jrs.4974>.
- (144) Lee, K.-H.; Snively, C. M.; Givens, S.; Chase, D. B.; Rabolt, J. F. Time-Dependent Transformation of an Electrospun Isotactic Poly(1-Butene) Fibrous Membrane. *Macromolecules* **2007**, *40* (7), 2590–2595. <https://doi.org/10.1021/ma062074m>.
- (145) Wei, D.; Chen, S.; Liu, Q. Review of Fluorescence Suppression Techniques in Raman Spectroscopy. *Appl. Spectrosc. Rev.* **2015**, *50* (5), 387–406. <https://doi.org/10.1080/05704928.2014.999936>.
- (146) Barbillat, J. 4 - Raman Imaging. In *Raman Microscopy*; Turrell, G., Corset, J. B. T.-R. M., Eds.; Academic Press: London, 1996; pp 175–200. <https://doi.org/https://doi.org/10.1016/B978-012189690-4/50024-7>.
- (147) Ando, M.; Hamaguchi, H. Molecular Component Distribution Imaging of Living Cells by Multivariate Curve Resolution Analysis of Space-Resolved Raman Spectra. *J. Biomed. Opt.* **2014**, *19* (1). <https://doi.org/10.1117/1.JBO.19.1.011016>.
- (148) Szymanska-Chargot, M.; Chylinska, M.; Pieczywek, P. M.; Roesch, P.; Schmitt, M.; Popp, J.; Zdunek, A. Raman Imaging of Changes in the Polysaccharides Distribution in the Cell Wall during Apple Fruit Development and Senescence. *Planta* **2016**, *243* (4), 935–945. <https://doi.org/10.1007/s00425-015-2456-4>.
- (149) Chylinska, M.; Szymanska-Chargot, M.; Zdunek, A. Imaging of Polysaccharides in the Tomato Cell Wall with Raman Microspectroscopy. *Plant Methods* **2014**, *10*. <https://doi.org/10.1186/1746-4811-10-14>.
- (150) Smith, G. P. S.; McLaughlin, A. W.; Clarkson, A. N.; Gordon, K. C.; Walker, G. F. Raman Microscopic Imaging of Electrospun Fibers Made from a Polycaprolactone and Polyethylene Oxide Blend. *Vib. Spectrosc.* **2017**, *92*, 27–34.

<https://doi.org/10.1016/j.vibspec.2017.05.002>.

- (151) Sóti, P. L.; Nagy, Z. K.; Serneels, G.; Vajna, B.; Farkas, A.; Van der Gucht, F.; Fekete, P.; Vigh, T.; Wagner, I.; Balogh, A.; Pataki, H.; Mező, G.; Marosi, G. Preparation and Comparison of Spray Dried and Electrospun Bioresorbable Drug Delivery Systems. *Eur. Polym. J.* **2015**, *68*, 671–679. <https://doi.org/10.1016/j.eurpolymj.2015.03.035>.
- (152) Nagy, Z. K.; Balogh, A.; Vajna, B.; Farkas, A.; Patyi, G.; Kramarics, Á.; Marosi, G. Comparison of Electrospun and Extruded Soluplus®-Based Solid Dosage Forms of Improved Dissolution. *J. Pharm. Sci.* **2012**, *101* (1), 322–332. <https://doi.org/10.1002/jps.22731>.
- (153) Kotzianová, A.; Řebíček, J.; Pokorný, M.; Hrbáč, J.; Velebný, V. Raman Spectroscopy Analysis of Biodegradable Electrospun Nanofibers Prepared from Polymer Blends. *Monatshefte für Chemie - Chem. Mon.* **2016**, *147* (5), 919–923. <https://doi.org/10.1007/s00706-015-1639-9>.
- (154) Büttiker, R.; Ebert, J.; Hinderling, C.; Adlhart, C. Membranes for Specific Adsorption: Immobilizing Molecularly Imprinted Polymer Microspheres Using Electrospun Nanofibers. *Chim. Int. J. Chem.* **2011**, *65* (3), 182–186. <https://doi.org/10.2533/chimia.2011.182>.
- (155) Šašić, S.; Prusnick, T. Raman Chemical Imaging of Intact Non-Flat Tablets in Regular and High-Confocal Mode. *Anal. Methods* **2020**, *12* (4), 471–482. <https://doi.org/10.1039/C9AY02340B>.
- (156) Emry, J. R.; Olcott Marshall, A.; Marshall, C. P. Evaluating the Effects of Autofluorescence during Raman Hyperspectral Imaging. *Geostand. Geoanalytical Res.* **2016**, *40* (1), 29–47. <https://doi.org/10.1111/j.1751-908X.2015.00354.x>.
- (157) Gautam, R.; Vanga, S.; Ariese, F.; Umapathy, S. Review of Multidimensional Data Processing Approaches for Raman and Infrared Spectroscopy. *EPJ Tech. Instrum.* **2015**, *2* (1), 8. <https://doi.org/10.1140/epjti/s40485-015-0018-6>.

CHAPTER 3

Experimental methods

3.1 Characterization methods

The purpose of this chapter is to summarize common characterization methods along with experimental details of electrospinning and “in-house” electrospinning setup used in this thesis research to avoid repetition of the experimental methods that would otherwise appear within the manuscript chapters (Chapters 4-6).

3.1.1 FT-IR

Diffuse reflectance FT-IR spectra were obtained with a Bio-RADFTS-40 (Massachusetts, USA) instrument. Solid samples were prepared by mixing samples (~5 mg) and pure spectroscopic grade KBr (~50 mg) by grinding in a mortar and pestle. The DRIFT (Diffuse Reflectance Infrared Fourier Transform) spectra were recorded at 295 K with a resolution of 4 cm⁻¹ operating in the range of 400-4000 cm⁻¹ in reflectance mode (Kubelka-Munk intensity units). Multiple scans were averaged and corrected against a background matrix spectrum of pure KBr.

3.1.2 ¹³C solid-state NMR spectroscopy

¹³C solid-state NMR spectra were obtained with a Bruker AVANCE III HD spectrometer equipped with a 4 mm DOTY CP-MAS (cross-polarization with magic angle spinning) solids probe operating at 125.77 MHz (¹H spectral frequency at 500.23 MHz). The ¹³C CP-TOSS (Cross-polarization with total suppression of spinning sidebands) spectra were obtained at a spinning speed of 7.5 kHz, a 1H 90° pulse of 5 μs, variable contact time (2 ms) with a ramp pulse on the 1H channel, and 20k accumulated scans with a recycle delay of 2 s for all samples. ¹³C MAS NMR spectra were obtained at a spinning speed of 10 kHz with 10k accumulated scans, and a recycle delay of 20s.

3.1.3 Differential scanning calorimetry (DSC)

DSC profiles of solid samples were acquired using a TA Q20 thermal analyzer (TA Instruments, New Castle, DE, USA) over a temperature range of 40-190 °C. The scan rate was set at 10 °C/min, and dry nitrogen gas was used to regulate the sample temperature and gas purging of the compartment (flow rate at 50 mL/min). Solid samples were analyzed in hermetically sealed aluminum pans with variable sample weight (1.55 mg to 3.20 mg).

3.1.4 Thermal gravimetric analysis (TGA)

The thermogram profiles of samples (~15 mg) were reported as weight loss profiles against temperature with a Q50 (TA instruments; New Castle, USA) thermogravimetric analyzer. A heating rate ($5^{\circ}\text{C min}^{-1}$) up to a maximum temperature (500°C) with an N_2 (carrier gas) atmosphere was employed. The thermal stability of materials was evaluated using first derivative plots (DTG plots) expressed as weight %/ $^{\circ}\text{C}$ vs. temperature ($^{\circ}\text{C}$).

3.1.5 Scanning electron microscopy (SEM)

SEM images were obtained with a JSM-6010LV at variable magnification with 508 dpi resolution. The samples were mounted onto the sample stub with the use of conductive carbon tape.

3.1.7 Raman spectroscopy

A Renishaw InVia Reflex Raman microscope (785 nm solid-state diode laser with a 1200 lines/mm grating system) (Renishaw plc, New Mills, UK) was used to collect Raman spectra with a Pelletier cooled CCD (charge coupled device) detector (400×576 pixels). The instrument wavelength was calibrated at 520 cm^{-1} using an internal Si (110) sample.

3.1.8 Raman spectral imaging and Data processing

Raman spectral measurements were carried out using a Renishaw InVia Reflex Raman microscope (Renishaw plc, New Mills, UK) using a 785 nm solid-state diode laser (500 mW) with a grating system having 1200 lines/mm. The microscope was focused onto the sample using a Leica objective with a magnification of $50\times$ (numerical aperture = 0.50) long working distance, where the backscattered Raman signals were collected with a Pelletier cooled CCD detector (400×576 pixels). High-resolution Raman Spectral imaging ($1.1 \times 1.1\text{ }\mu\text{m}$ pixel size) was acquired using Streamline™ mode within the instrument software (Renishaw Wire™ V3.4) using various exposure time and a static scan mode centered at a specific Raman frequency. A total $66 \times 49^*$ spectra were collected in a uniform $72 \times 52^*\text{ }\mu\text{m}$ grid (*numbers may be varied according to each project).

Data processing was carried out using the instrument software (Renishaw Wire™ V3.4). Cosmic rays (Rayleigh lines) were removed by replacement with the nearest neighbour. Principal components (PCs) were calculated, and pseudo-colour principal component score maps were then

gathered. After any remaining cosmic rays were removed, PCs were recalculated. Then, the signal-to-noise ratio of the collected spectra was increased with the use of recalculated PCs. Raman images were constructed by collecting intensity data (relative to baseline) at specific Raman frequency values. The baseline of spectra for Raman imaging was linearized and normalized to zero intensity to remove any baseline effects (sloping) and baseline offset effects caused by laser focus or other experimental artifacts using the method provided by Renishaw Wire™ V3.4 prior to the creation of Raman images. Each spectral component of interest was mapped individually by using a corresponding peak maximum from the spectrum. The colour intensity of the pixels on the image was determined by the relative intensity of the respective spectral band to baseline as required. Samples were treated using specific dye solutions to differentiate each component of samples before Raman imaging and air-dried onto an Au-coated Si wafer, where sample imaging was collected after 24 h of dye-treatment. The instrument calibration was verified using an internal Si (110) sample measured at 520 cm^{-1} .

3.2 Experimental details of electrospinning and “in-house” electrospinning setup

Electrospinning Solutions (2.5 mL) were placed into a 10 mL syringe with a metal needle (Inner Diameter = 0.508 mm) that was operated by a Cole-Palmer 78-0100c syringe pump (Cole-Palmer, Montreal, QC, Canada). The distance between the needle tip and a grounded collector plate (copper plate covered with Alumina foil) was set to 11.5 cm. The flow rate was controlled at 0.1 mL h^{-1} , where a high voltage was produced by a high voltage DC (direct current) power supply (Spellman CZE 1000R) (Spellman, Hauppauge, NY, USA) and was applied between the needle tip and collector plate during electrospinning. The voltage was slowly adjusted from 7 to 15 kV to achieve a stable Taylor cone. The resulting fiber product was accumulated onto a foil-covered, electrically grounded collector plate. The “in-house” electrospinning apparatus is shown in Figure A3.1 in Appendix.

CHAPTER 4

A structural study of self-assembled chitosan-based sponge materials

Xue, C.; Wilson, L. D. A Structural Study of Self-Assembled Chitosan-Based Sponge Materials. *Carbohydr. Polym.* **2019**, 206, 685–693. <https://doi.org/10.1016/j.carbpol.2018.10.111>.¹

Author's contribution

Chen Xue performed all the experimental work (i.e., data analysis, data curation, visualization, formal analysis, etc.) and wrote the first draft of the manuscript. Chen Xue made further revisions to the final draft stage with the supervisor. Dr. L. D. Wilson was responsible for the supervision of the project, editorial guidance for revision of the manuscript drafts, and corresponding authorship.

Description

The original published paper was reformatted to integrate Chapter 4 into a coherent thesis and to meet the formatting guideline of the College of Graduate and Postdoctoral Studies (CGPS) at the University of Saskatchewan. Specifically, the introduction and conclusion section of the original paper was revised to avoid repetition. The general details of routine characterization methods are introduced in Chapter 3, the experimental section is modified accordingly, where specific details are included, as required. The reference style of the original paper is changed to the CGPS thesis' style. Some of the supplementary information in the original paper is included in the methods and discussion section. Other supplementary information and the Copyright permission forms are included in the Appendix.

This research contributed significantly to the overall goal of the thesis in three aspects. Firstly, self-assembled chi-based sponges as chi-based nonwoven microfibrinous materials were prepared *via* freeze-drying, and its structurally modified form was prepared by thermal-annealing. Secondly, the utility of Raman spectral imaging with suitable dye probes was demonstrated in this work by revealing structural features for chi nonwoven microfibrinous composite materials before and after thermal annealing. The first and second aspects satisfied Objective #1 of this thesis. Besides, Raman spectral imaging with dye probes mentioned in the second aspect was employed

in Chapter 5. The final aspect is that it is found that PEO could work as the sacrificial template to generate porous morphology, which supports Hypothesis #3.

4.1 Introduction

Sponge-like composite materials (nonwoven fibrous composite materials) formed by the self-assembly of biopolymers have found many applications in wound dressings^{2–5}, tissue engineering⁶, and wastewater treatment^{7,8} due to their high porosity and tunable mechanical and physicochemical properties. Among all the various materials, as discussed in Chapter 2, chi (*cf.* Scheme 4.1) is a linear cationic biopolymer composed of β -linked glucosamine and N-acetyl-glucosamine units that offer versatile synthetic utility to yield modified forms of chi.⁹ Chi-based nonwoven fibrous composite materials have gained increasing attention because of their unique biocompatibility, biodegradability, and low toxicity comparing to other biomaterial composites.^{2–5,10–12} To achieve various mechanical properties for different purposes, additive components such as poly(ethylene oxide) (PEO), poly(vinyl alcohol) (PVA), *etc.*, are used to formulate biopolymer composites.⁷ Suitable elasticity of chi fibrous materials is crucial for their applications in wound dressings and wastewater treatment.¹³ The component addition of PEO to biopolymer composites contributes to changes in the hydrophilicity and mechanical properties due to the well-known plasticizer effect of PEO in biopolymer composites.^{5,7,14,15}

Freeze drying offers a potential preparation method for the design of biocompatible and multi-component sponges that contain biopolymer precursors.^{6,16} In a previous study¹⁷, self-assembled colloidal particles with tunable physicochemical properties were formed between carboxymethylated chi (cm-chi) and alg *via* electrostatic interactions. The resulting colloidal particles can be transformed into self-assembled sponges in the presence of PEO upon freeze-drying, where the resulting composites possess tunable mechanical and physicochemical properties for diverse applications.

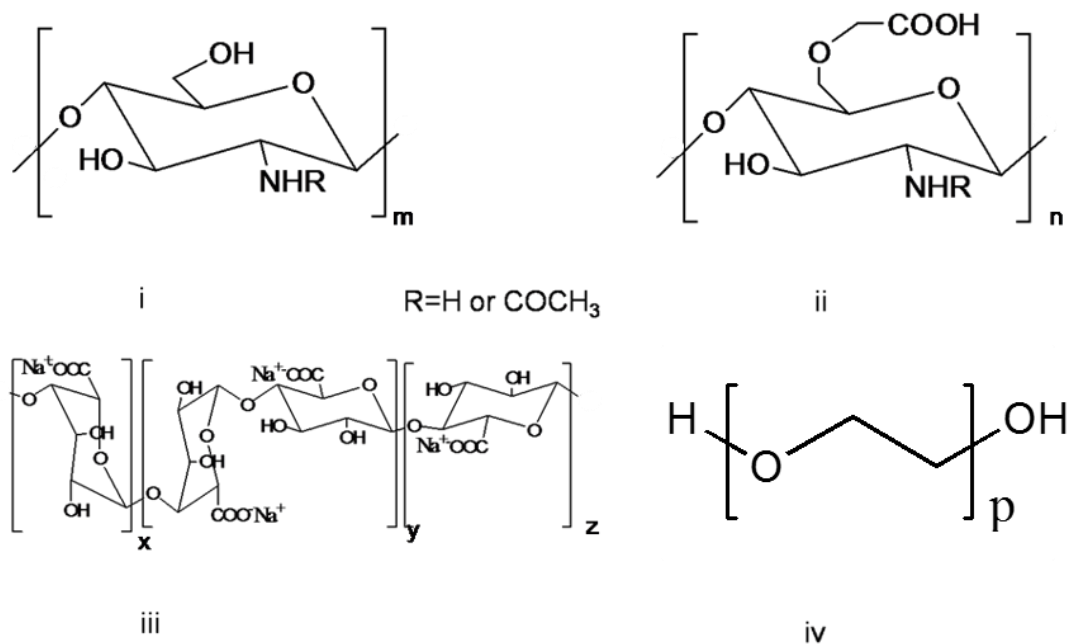
As discussed in Chapter 1, a potential limiting feature of PEO-biopolymer composites relates to their uncontrolled dissolution in aqueous media^{2,5} due to their hydrophilic character. Uncontrolled dissolution limits the practical application of such PEO-based composites, where strategies to overcome dissolution may include chemical treatment *via* cross-linking and heat

treatment *via* annealing¹⁸. The potential concern over the toxicity and biocompatibility of various chemical additives has led to the preferred use of physical methods such as heat treatment. The routine use of characterization methods such as FT-IR spectroscopy and thermal analysis (TGA and DSC) may limit the level of detailed structural insight for polysaccharide materials and their composites, especially before and after heat treatment. X-ray diffraction (XRD) provides limited structural information in dealing with amorphous biopolymers, while microscopy methods such as scanning electron microscopy (SEM) afford the characterization of materials' morphology. In the case of chi-based materials subjected to heat treatment, it is difficult to ascertain the role of thermal effects *a priori* on the structure of such multi-component systems. This knowledge gap underscores the need to develop alternate characterization methods that yield further structural insight on the *structure-function* properties of such complex materials.

As mentioned in Chapter 2, Raman spectral imaging has been reported to study complex biological samples such as cells or tissues. Spectral maps contain compositional information, spatial distribution, and the arrangement of constituents that can be visualized by this spectral construction technique.¹⁹ The use of secondary components such as dye probes can be employed to distinguish between chemically similar composites that vary in morphology and/or the surface accessibility of various functional groups, as reported for chi-polyaniline materials.²⁰ The use of dye probes as an indirect method relies on the role of adsorption between the target material (adsorbent) to be imaged and the bound dye probe (adsorbate).^{19,21,22} Recent reports have shown that materials with variable morphology and surface accessibility can be studied according to their uptake properties with suitable dyes (phenolphthalein, fluorescein, and methylene blue) that possess variable ionization.²²⁻²⁴ According to the role of specific target-dye interactions, chemically similar components and their composites can be differentiated.^{20,22}

The purpose of this chapter is to fulfill Objective #1 of this thesis (*cf.* Section 1.4) through three short-term goals: preparation of cm-chi/alg/PEO self-assembled sponges (nonwoven microfibrinous materials) *via* freeze-drying and their structurally modified forms *via* heat treatment (annealing) as well as a structural study of composites at variable composition prepared above using Raman spectral imaging in conjunction with a suitable dye probe. In detail, the first short-term goal is that cm-chi/alg and cm-chi/alg/PEO self-assembled sponges were obtained *via* freeze-drying. The second short-term goal is that structurally modified forms of cm-chi/alg/PEO sponges

were obtained by heat treatment (annealing). The third short-term goal is that a structural study of composites at variable composition prepared above was conducted using Raman spectral imaging in conjunction with suitable dye probes. This method is anticipated to complement standard structural tools such as SEM, thermal analysis (DSC and TGA) and FT-IR spectroscopy to gain insight on the structural and morphological changes of cm-chi/alg/PEO sponges before/after annealing.



Scheme 4.1. Molecular structure of chi (i); cm-chi (ii) where R= -COCH₃ or H depending the degree of deacetylation; sodium alginate (iii); and PEO (iv). The terms m, n, p, x, y, and z are integer values that depend on the degree of polymerization of the respective polysaccharide.

4.2 Materials and Methods

4.2.1 Materials

Hydrochloric acid (HCl), sodium chloride (NaCl), and sodium hydroxide (NaOH) were obtained from EMD (Edmonton, Canada). Low molecular weight (LMW) chi was obtained from Sigma-Aldrich Canada Ltd. (Oakville, ON.) with 75-80% deacetylation, Brookfield viscosity 20 cPs, with a range of molecular weights (50-190 kDa). Alg was obtained from Sigma-Aldrich Canada Ltd. (Oakville, ON.), where its molecular weight was specified between 12-40 kDa. The

G/M ratio of alginate was estimated as 1.22 by a FT-IR spectral method reported by Filippov and Kohn.²⁵ Poly(ethylene oxide) (PEO) was obtained from BDH Inc. (Toronto, Canada) with an average molecular weight at 3.11 kDa with a melting point at 60 °C. All materials were used as received unless specified otherwise.

4.2.2 Preparation of self-assembled chitosan-based sponge materials

4.2.2.1 Synthesis of carboxymethyl (cm-) modified chitosan (chi)

cm-chi was synthesized according to an adapted procedure reported by Chen and Park.²⁶ Chi (1 g) was stirred in 15 mL Millipore water with NaOH (3 g) at 295 K for 12 h. Millipore water was completely removed using a rotoevaporator ca. 50 °C. Isopropanol (15 mL) was added to the chi mixture and monochloroacetic acid (1.5 g) was dissolved in 2 mL isopropanol with drop-wise addition to the mixture at 60 °C with stirring for over 30 min. After 8 h, the product was collected and washed with ethanol (ca. 100 mL) along with filtration through a Whatman no. 2 filter paper (pore size: 8 µm) under vacuum. The sodium salt of cm-chi was dialysed in 1 L of Millipore water for 48 h to remove residual NaOH and the product was finally dried for 12 h in a vacuum oven at 50 °C.

4.2.2.2 Preparation 0.06% (w/v) 1:2 cm-chi/alg sponge (S-1)

cm-chi (0.08 g) was dissolved in 50 mL of 0.2% (v/v) HCl (aq). Alg (0.16 g) was dissolved in Millipore water (350 mL). The cm-chi solution was added to the alg solution drop-wise over 6 h with stirring. The solution was adjusted to pH 6.5 with aqueous NaOH. Then, the sample was freeze-dried for 48 h. For all freeze-dried samples prepared in this project, the vials containing respective solutions were immersed into liquid nitrogen to freeze samples before they were placed in the freeze-dryer.

4.2.2.3 Preparation 0.6% (w/v) 1:2 cm-chi/alg sponge (S-2)

cm-chi (0.04 g) was dissolved in 5 mL of 0.2% (v/v) HCl (aq). Alg (0.08 g) was dissolved in Millipore water (15 mL). The chi solution was added to the alg solution drop-wise over 6 h with stirring. The solution was adjusted to pH 6.5 with aqueous NaOH and the sample was subsequently freeze-dried for 48 h.

4.2.2.4 Preparation cm-chi-alg/PEO 2:1 composite sponge (CP-1)

cm-chi (0.04 g) was dissolved in 5 mL of 0.2% (v/v) HCl (aq). PEO (0.06 g) and alg (0.08 g) were dissolved in Millipore water (15 mL). The cm-chi solution was added to the mixed solution drop-wise over 6 h with stirring. The solution was adjusted to pH 6.5 with aqueous NaOH and was subsequently freeze-dried for 48 h.

4.2.2.5 Preparation cm-chi-alg/PEO 5:1 composite sponge (CP-2)

cm-chi (0.05 g) was dissolved in 5 mL of 0.2% (v/v) HCl (aq). PEO (0.03 g) and alg (0.10 g) were dissolved in Millipore water (15 mL). The cm-chi solution was added to the mixture solution drop-wise over 6 h with stirring. The solution was adjusted to pH 6.5 with aqueous NaOH and subsequently freeze-dried for 48 h.

4.2.2.6 Preparation of a physical mixture of cm-chi-alg/PEO

cm-chi (0.04 g), PEO (0.06 g) and alg (0.08 g) were thoroughly mixed in a mortar and pestle for 15 mins and stored in glass screw cap vials.

4.2.2.7 Preparation of physical treated sponge (TCP-1)

A thin film of CP-1 was placed in a 5 mL glass test tube, where it was subject to heating and cooling in the oil bath in the temperature range from 20 °C to 130 °C at a rate of 2 °C min⁻¹ under argon at a flow rate 10 mL min⁻¹.

4.2.3 Characterization of prepared sponges

DSC profiles (*cf.* Section 3.1.3), DTG plots (*cf.* Section 3.1.4). FT-IR (*cf.* Section 3.1.1), and Raman spectra (*cf.* Section 3.1.7) of the cm-chi, alg, PEO, physical mixture, S-1, S-2, CP-1, CP-2 and TCP-1 were acquired. SEM images (*cf.* Section 3.1.5) of samples were obtained at variable magnification (1000×, 3000×, and 5000×). Raman spectral imaging and data processing (*cf.* Section 3.1.8) was done as described in Chapter 3. In detail, Raman spectral imaging was performed using a 60s exposure time and a static scan mode centered at 450 cm⁻¹ (leads to an effective spectral range of 243-659 cm⁻¹) for various samples. A total 66 × 49 spectra were collected in a uniform 72 × 52 μm grid. Then, Raman images were constructed by the relative intensity of the respective spectral band (427 cm⁻¹, 447 cm⁻¹, 346 cm⁻¹, and 279 cm⁻¹) to baseline as required. A methylene blue (MB) solution (~0.1 μM, ambient pH) was used as a dye probe in this study.

4.3 Results and Discussion

4.3.1 SEM images of self-assembled sponges

Optical photographs and SEM images of S-1 and CP-1 (*cf.* Section 4.2.2 for acronym definitions) are shown in Figure 4.1. The images in Fig. 4.1 for S-1 and CP-1 are composed of fibrous and sheet-like domains that reveal their heterogeneous nature. Moreover, the fibrous part of CP-1 has a rough surface with grooves, while S-1 displays a relatively smooth surface topography. The sponge materials have a denser appearance with more efficient packing as the concentration of cm-chi/alg increases from 0.06% (w/v) to 0.6% (w/v) in Figure 4.2. For S-2, the denser appearance is attributed to the formation of the lamellar structure during freeze-drying because of its higher colloidal suspension concentration, as discussed in Section 2.3. In Fig. 4.2, CP-1 appears more loosely packed than S-2, which indicates that the addition of PEO leads to a reduction in the sponge density.

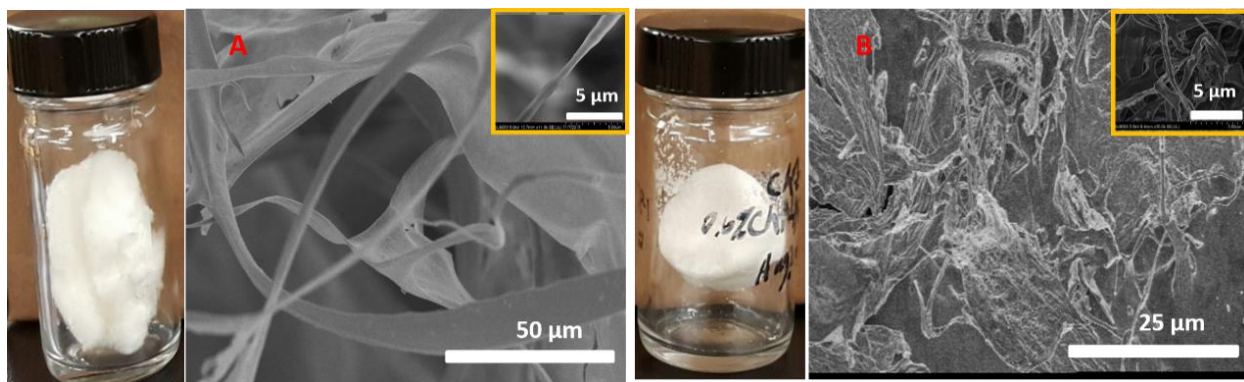


Figure 4.1. Optical and SEM images of self-assembled sponge materials: A) S-1, and B) CP-1.

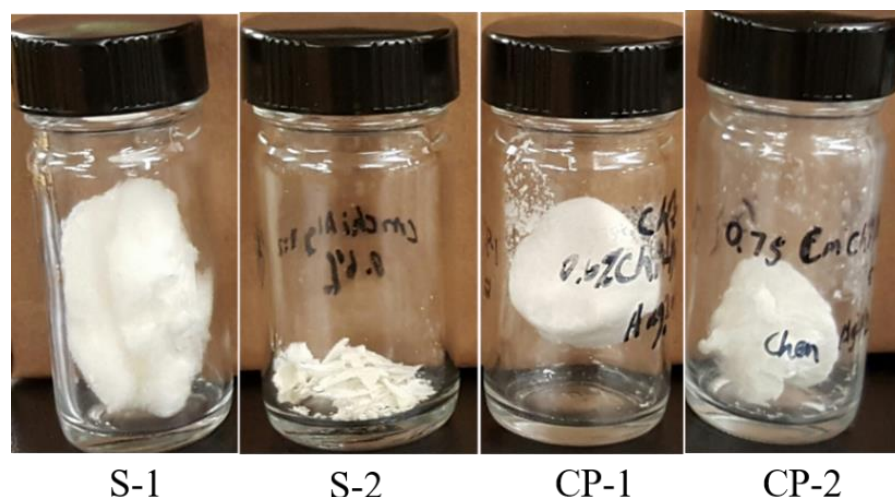


Figure 4.2. Photographs of various self-assembled sponges. From left to right, S-1 (0.06% w/v), S-2 (0.6% w/v), CP-1 (0.6% w/v), and CP-2 (0.75% w/v), respectively.

4.3.2 TGA results

The effect of PEO and other components in the sponge materials was studied using TGA since it has been shown in other studies that interactions among polymer constituents in multicomponent mixtures and composites can be estimated by this method.^{27,28} TGA was used to study the interactions among the respective components (cm-chi, alg, and PEO), and the relative thermal stability was determined based on the trends in the TGA profiles that follow their respective physical and chemical modification. A previous report on cross-linked chi materials indicated that variable TGA profiles result for chi with variable cross-linker content, as evidenced by the differential TGA (DTG) plots that revealed distinguishable weight loss profiles for cross-linked chi.²⁹ The DTG results for cm-chi, alg, PEO, physical mixture of components, and CP-1 are illustrated in Figure 4.3A-E. A thermal event corresponding to the decomposition of chi is observed at 300 °C.²⁹ In Fig. 4.3A, the thermal event for the decomposition of cm-chi is shifted to a lower temperature (271 °C). Another report³⁰ revealed that the maximum temperature stability for sodium alginate is ca. 245 °C agrees by the TGA results in Fig. 4.3B. In the case of cross-linked chi²⁹, the TGA results reveal lower onset temperatures relative to unmodified chi. By comparison, parallel trends in TGA profiles were observed for the chi composite materials herein, as shown in Fig.4.3E and Fig. A4.1(A-H) (*cf.* supplementary information in Appendix). The reduced thermal stability for the composites was attributed to decreased crystallinity due to defects

in the intermolecular H-bonding network for the amine and hydroxyl groups of chi. Analogous effects were observed for cross-linking of chi, where reduced thermal stability was attributed to *pillaring effects* that ultimately attenuate hydrogen bonding interactions between adjacent biopolymers.²⁸ Likewise, modification of pristine chi by carboxymethylation and fiber formation *via* electrostatic interactions (between protonated cm-chi and alg) is inferred to alter the degree of inter-chain H-bonding due to reduced availability of H-bond donor and acceptor groups. The reduced onset temperature for the DTG profiles of the self-assembled sponges is consistent with an overall lowering of the lattice energy of such polymers that resemble chi materials.^{31–33} Overlapping thermal events between 200 and 300 °C are evident in Fig. 4.3E and Fig. A4.1(C-H) (*cf.* Appendix). The addition of PEO to cm-chi/alg results in an additional overlap of the thermal events that reside between 200 and 300 °C, along with a weight loss event due to the presence of PEO in CP-1 is noted at 360 °C instead of 400 °C (pure PEO). The TGA results provide supporting evidence of an association between PEO and cm-chi/alg. The formation of polymer complexes is further supported by comparing the DTG profile of the self-assembled composites with a physical mixture (*cf.* Fig. 4.3D) of the single component polymers (cm-chi, alg, and PEO).

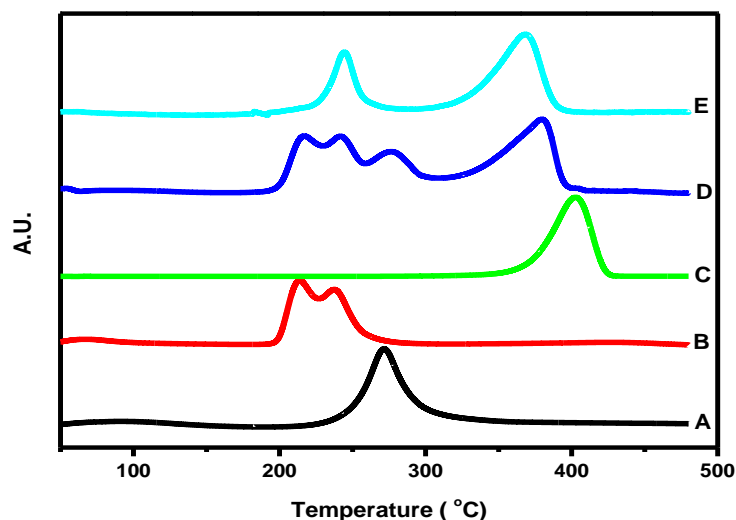


Figure 4.3. DTG plots of precursors and sponges: A) cm-chi, B) alg, C) PEO, D) Physical mixture (cm-chi, alg, and PEO), and E) CP-1.

4.3.3 Morphology and structure of the self-assembled (CP-1) and thermally annealed sponges (TCP-1)

SEM images of the annealed sponges are shown in Figure 4.4. By comparison with the original, untreated sponge (*cf.* Fig. 4.1B), the formation of *island-like* features is noted on the thermally annealed sponges' surface. These *island-like* features on the fiber surface display a combined appearance of indented and pendant structures. These features are formed due to re-crystallization of the PEO fraction with different dimensions during annealing. The heterogeneous distribution of PEO in the composite with amorphous constituents is described in Section 2.5.3. As a result, PEO forms a dispersed phase between cm-chi and alg in the composite. The DSC results of the precursors, physical mixture, CP-1, and TCP-1 are illustrated in Figure 4.5, where an endotherm occurs at 58.7 °C, corresponding to the melting of PEO (Fig. 4.5A). This thermal event becomes broader as PEO mixes or forms a composite with other biopolymer components, as seen in Fig. 4.5. Furthermore, the melting point of PEO shifts to 55.0 °C and 54.0 °C for the case of CP-1 and TCP-1, respectively. This effect relates to alteration of the degree of intermolecular association and the level of PEO crystallization upon mixing, in agreement with another report.³⁴



Figure 4.4. A SEM image of a thermally treated sponge (TCP-1).

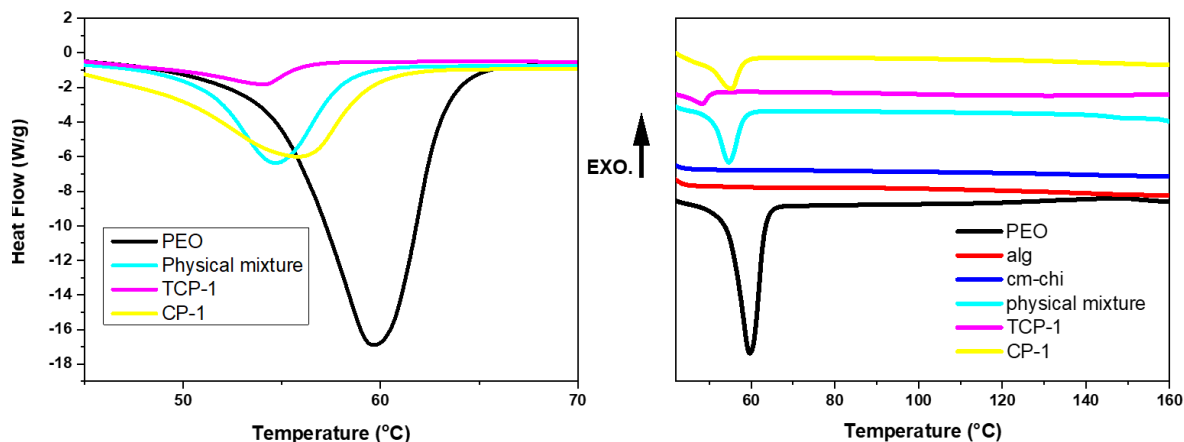


Figure 4.5. DSC profiles of biopolymer precursors, physical mixture (cm-chi, alg, and PEO), and self-assembled sponges (TCP-1, and CP-1). The left panel shows an expanded DSC trace for CP-1, PEO, TCP-1, and the physical mixture (cm-chi, alg, and PEO).

Etching of the PEO phase was carried out with deionized water at ambient conditions to investigate the structure of the fibrous sponge before and after annealing. Etching with deionized water serves as a solvent-based “scalpel” to excise polar components from the multi-component system (cm-chi/alg/PEO). Herein, it will be shown that the morphology and structural features can be further resolved using microscopy and spectroscopy upon selective removal of the PEO phase. The SEM images of CP-1 and TCP-1, before and after solvent etching, are shown in Figure 4.6. A comparison of the morphology of CP-1 with that of TCP-1 after etching reveals that CP-1 undergoes swelling that reveals in a change of material morphology from *sponge-like* to *film-like* product. By comparison, TCP-1 retains much of its original surface features and gains additional surface pore features. This morphology change of TCP-1 may be due to removing the PEO phase *via* washing with the deionized water because of its hydrophilic nature, in agreement with other independent results³⁴ that provide porous features upon removal of PEO with deionized water.

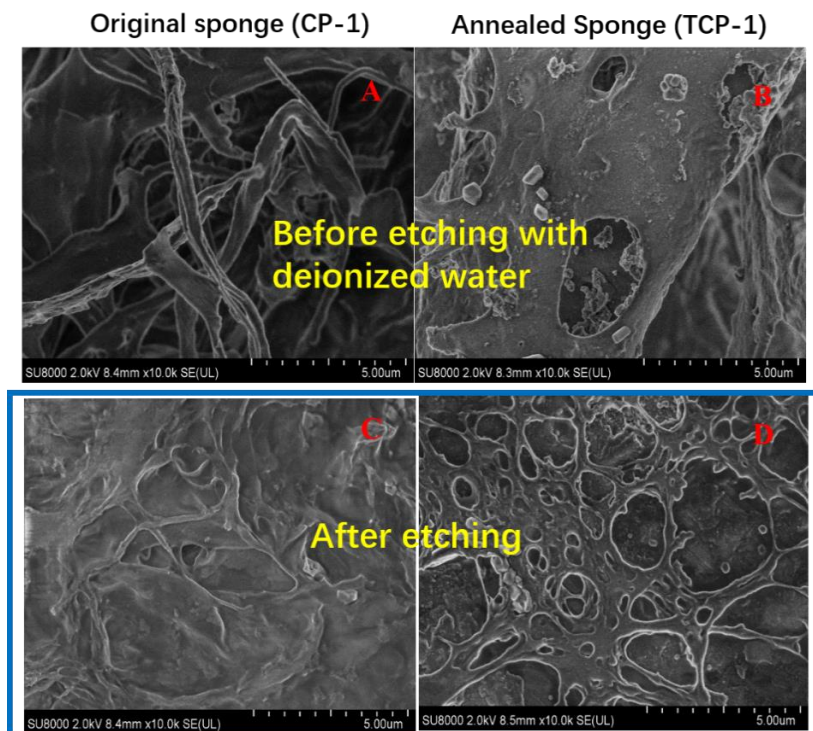


Figure 4.6. SEM images of CP-1 and TCP-1 before/after selective etching of PEO phase with deionized water. A) CP-1 and B) TCP-1 before solvent etching; C) CP-1 and D) TCP-1 after solvent etching.

4.3.4 Raman spectra and imaging results

The change in morphology of CP-1 and TCP-1 sample upon exposure to water is discussed in Section 4.3.3. Raman spectral results are presented to complement the SEM images to gain further insight on the composite structure for these sponge materials as Raman spectroscopy provides information on the chemical fingerprint of the respective components within such mixtures.¹⁹ Raman spectra of the biopolymer precursors and the self-assembled sponges are shown in Figure 4.7. The vibrational bands between 750 cm^{-1} and 1000 cm^{-1} from Fig. 4.7B-G correspond to the ring-breathing mode of a polysaccharide³⁵, where it corresponds to C-O-C bending for PEO in Fig. 4.7A³⁶. Sodium alginate displays Raman bands at 809 , 886 , and 952 cm^{-1} assigned to the ring breathing of sodium alginate (Fig. 4.7C), in agreement with the different types of monomer units (*cf.* Scheme 4.1). The band at 891 cm^{-1} for cm-chi (Fig. 4.7B) relates to its ring-breathing mode. The spectral intensity change from 1000 cm^{-1} to 750 cm^{-1} corresponds to the interaction between the PEO chain and the monosaccharide unit because the C-O-C torsional angle has a

profound impact on the spectral intensity in this region.³⁷ The Raman spectra of S-1 and CP-1 is shown in Fig. 4.7D and 4.7F, respectively. The spectral differences at 809, 886, 891, and 952 cm^{-1} for S-1 and CP-1 are trivial compared to the physical mixture shown in Fig. 4.7E. However, electrostatic interactions between protonated amino groups of chi with carboxylate groups of alg are supported by the FT-IR spectra in Fig. 4.8A-H. The vibrational band at 1510-1520 cm^{-1} corresponds to the N-H bending vibration of the protonated amine group of chi undergoes a spectral shift to 1527 cm^{-1} .^{29,38,39} The observed FT-IR shift results from the electrostatic interaction between chi and the respective counter-ion species. The Raman spectra of TCP-1 in Fig. 4.7G reveal that the vibrational fingerprint band in the range shows large differences relative to the physical mixture and CP-1 (*cf.* Fig. 4.7E & 4.7F). The spectral band for PEO is enhanced, whereas the ring breathing of the polysaccharide moiety undergoes attenuation upon annealing. This attenuation of the ring breathing band indicates that the polymer units of cm-chi and alg undergo complex formation due to favourable H-bonding and structural rearrangement of each polymer segment upon annealing.

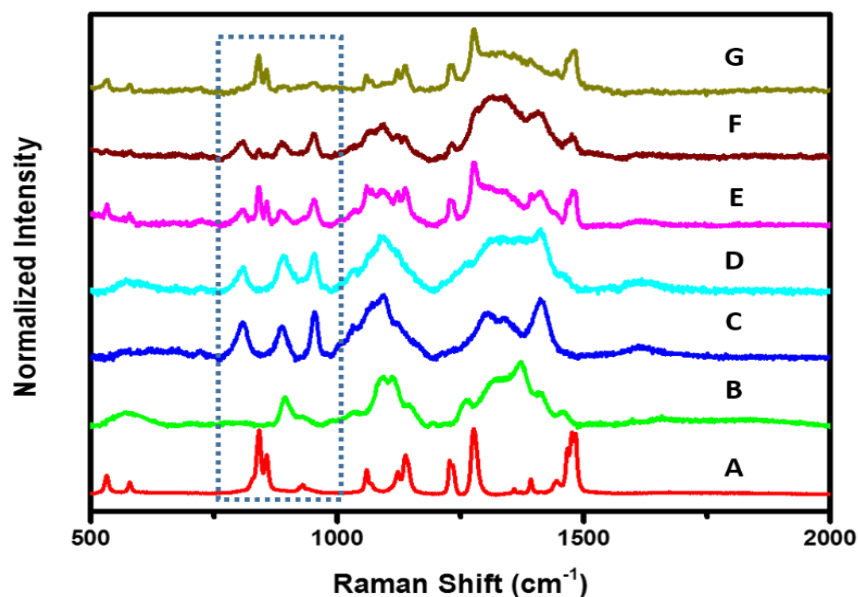


Figure 4.7. Raman spectra (500 - 2000 cm^{-1}) of precursor components and self-assembled sponges: A) PEO, B) cm-chi, C) alg, D) S-1, E) physical mixture (cm-chi, alg, and PEO), F) CP-1 F), and G) TCP-1.

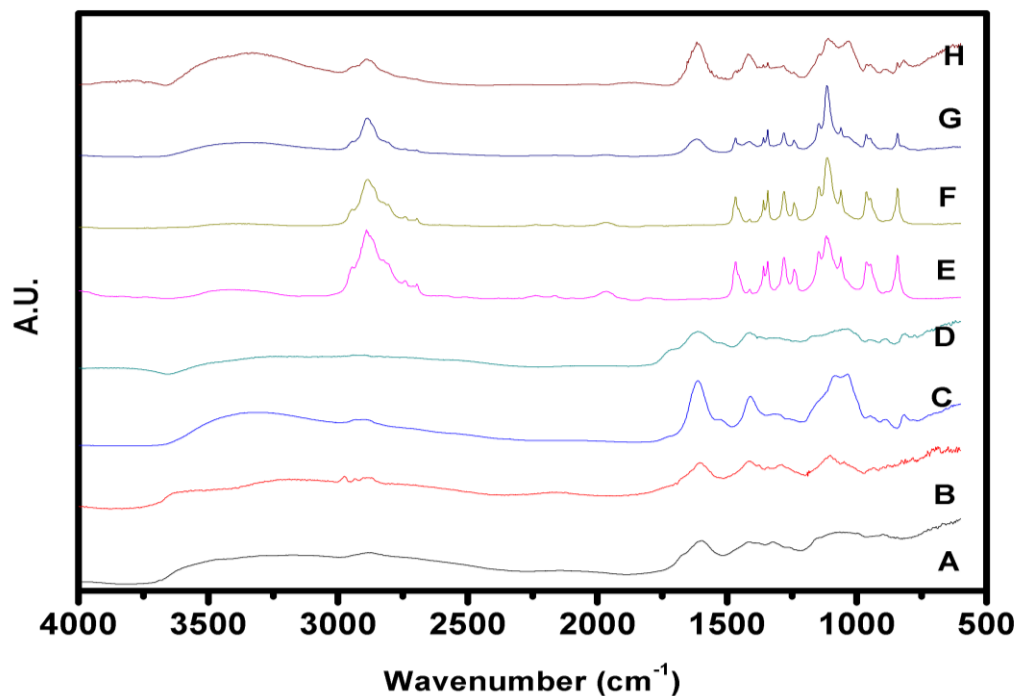


Figure 4.8. FT-IR spectra of precursors and sponge samples: A) cm-chi, B) alg, C) S-1, D) S-2, E) PEO, F) physical mixture (cm-chi, alg, and PEO), G) CP-1, and H) CP-2.

To further illustrate the structural variation of original (as-prepared) and annealed sponges, Raman spectral imaging was applied to ascertain the role of specific functional groups of the respective biopolymer components with the structure of the resulting composite material. The presence of surface accessible, functional groups in the composite can be identified by studying the relative affinity of adsorption using a dye-based probe.¹⁹ Herein, self-assembled sponges were exposed to a solution containing MB before obtaining Raman spectra, where evidence of dye adsorption onto **CP-1** can be deduced from the results in Figure 4.9 and Figure A4.2 (*cf.* Appendix). Panel A (Fig. 4.9) shows the Raman image obtained at 427 cm^{-1} that corresponds to the C-C-C and C-O-C bending for cm-chi and alg.^{35,40} Panel B and C (Fig. 4.9) are related to the spectral image at 447 cm^{-1} for MB⁴¹ and at 346 cm^{-1} due to C-C-O bending of cm-chi⁴⁰, while panel D corresponds to Raman imaging of PEO at 279 cm^{-1} . Due to the structural similarity of cm-chi and alg, there is no characteristic fingerprint between 200 and 600 cm^{-1} for alginate. MB is a cationic dye with a favourable binding affinity toward anionic sites as those localized on the surface of alg. The Raman images of MB (*cf.* Fig.4.9B) and cm-chi (*cf.* Fig. 4.9C) were combined into an additive picture (*cf.*

Figure A4.2 in the Appendix) using Image-Pro® Plus 6.0. This additive picture is similar to the image constructed using Raman fingerprints of cm-chi/alg in Figure 4.9A, which suggests that MB locates at the anionic domains of alginate, in line with its known favourable adsorption properties for polymers which contain carboxylate groups.³¹ As a result of etching with the dye solution, the Raman imaging results reveal that cm-chi and alg undergo phase separation to form isolated domains. In Fig. 4.9D, a portion of PEO remains in this region after etching with water and the remaining fraction of PEO also forms a separate domain. The change in morphology that occurs for **CP-1** is discernible according to the variation in the SEM images from Fig. 4.6A to 4.6C is not due to the sole effect of biopolymer swelling but also involves phase separation of the polymer components after water etching. The Raman spectral imaging results indicate that the structure of the original sponge assembly is loosely packed before etching, which accounts for the uncontrolled dissolution of composites that are formed by physical association. The same method was applied to **TCP-1** where its Raman image is shown in Figure 4.10. Small pores were noted, in agreement with SEM results (Fig. 4.6). A comparison of Fig. 4.9 and 4.10 reveals the co-location of three polymer components occurs in overlapping domains: alg (*cf.* Fig. 4.10B), cm-chi (*cf.* Fig. 4.10C), and PEO (*cf.* Fig. 4.10D). The results reveal that cm-chi/alg does not undergo significant phase separation after etching with the dye solution. This reveals that annealing improves the structural stability of the composite toward dissolution in water due to the supramolecular association of cm-chi, sodium alginate, and PEO.

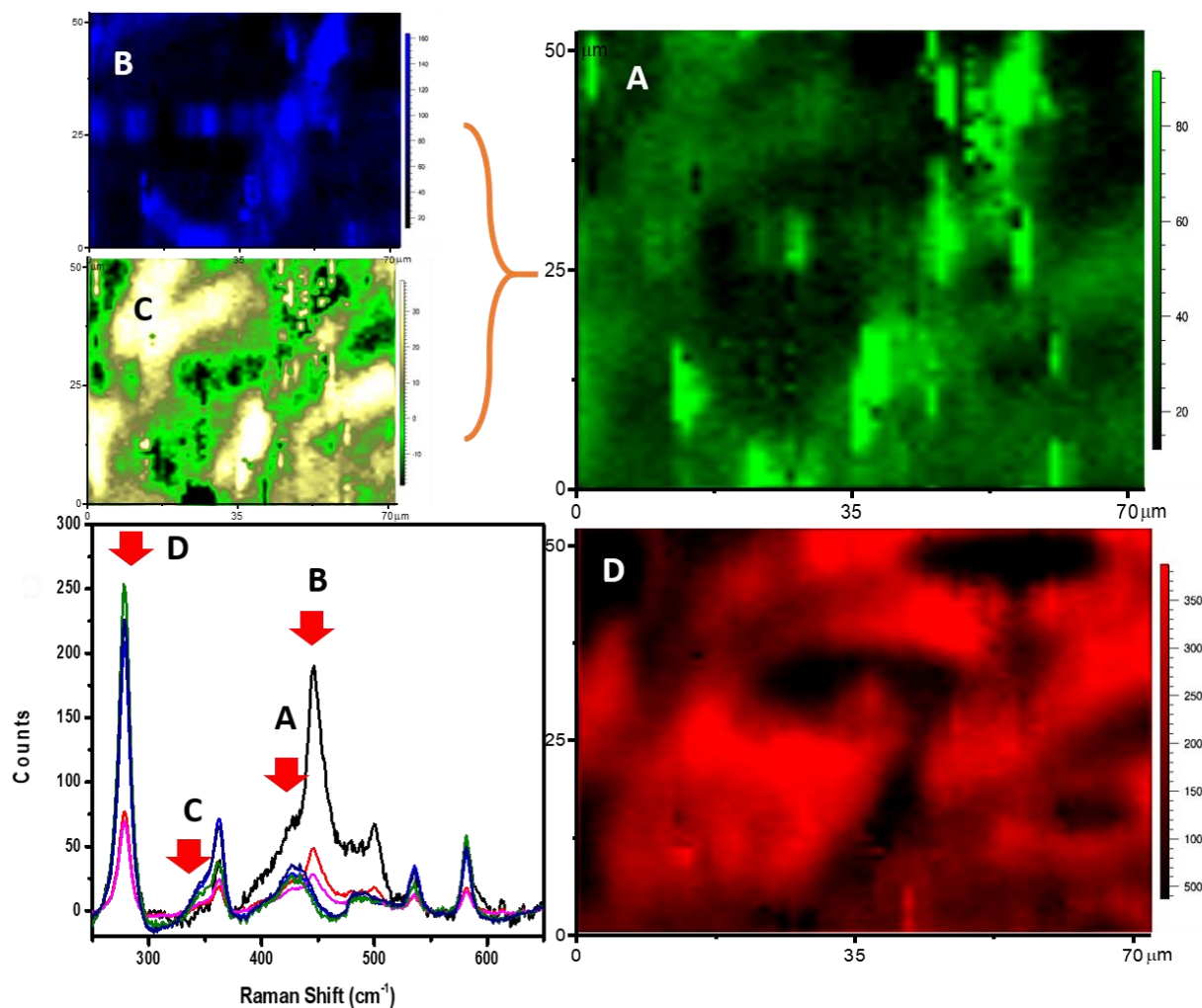


Figure 4.9. Raman spectral imaging results of CP-1 after etching with methylene blue (aq) and sample stack plots of Raman spectra centred at 450 cm⁻¹ under static conditions ($\lambda_{ex} = 785$ nm). Raman images were constructed by use of spectral line intensity at variable Raman frequencies: A) cm-chi/alg region (427 cm⁻¹), B) MB region (447 cm⁻¹), C) cm-chi region (346 cm⁻¹), and D) PEO region (279 cm⁻¹), respectively.

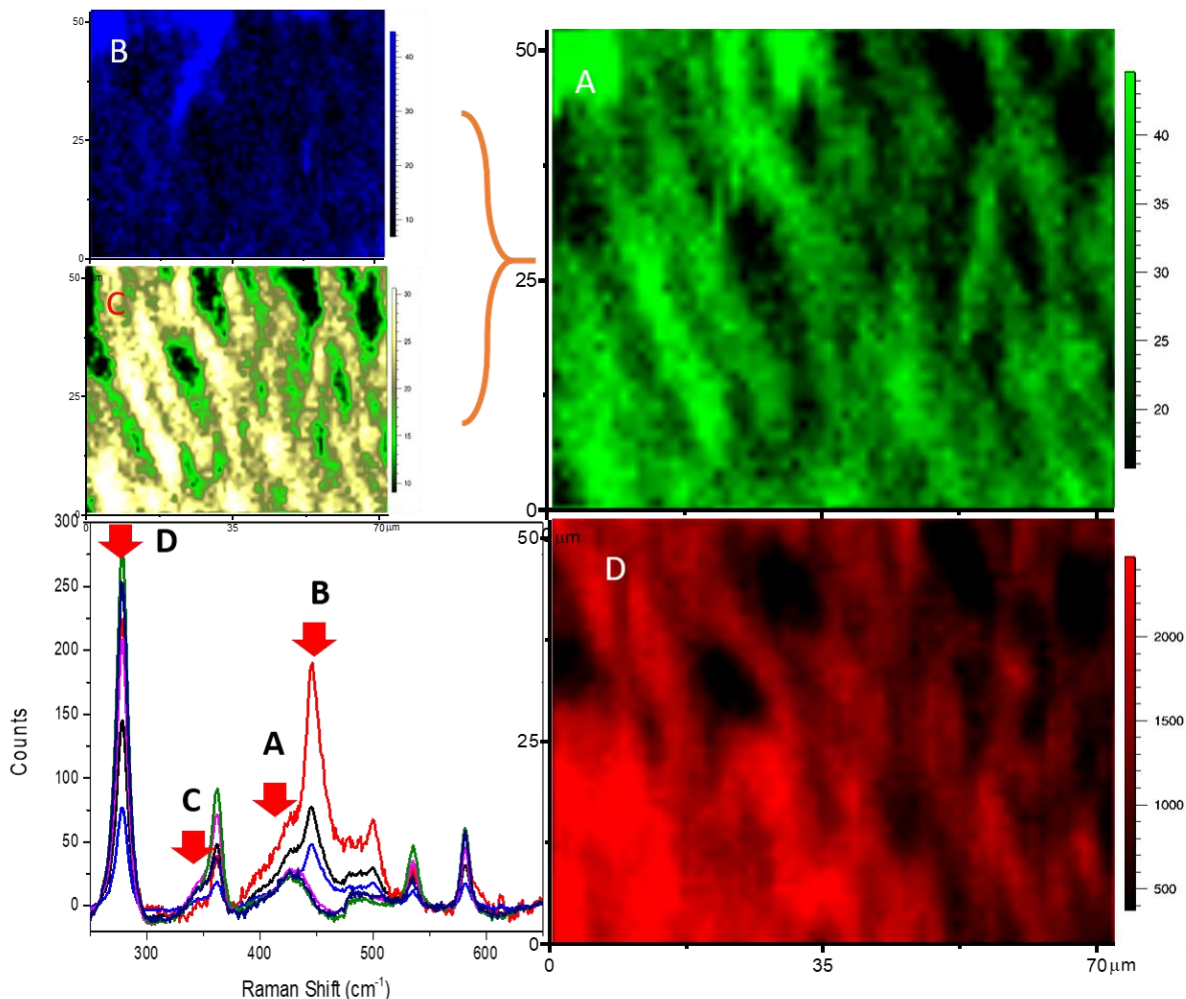


Figure 4.10. Raman spectral imaging results of TCP-1 after etching with methylene blue (aq) and sample stack plots of Raman spectra centered at 450 cm^{-1} under static conditions ($\lambda_{ex} = 785\text{ nm}$). Raman images were constructed by use of spectral line intensity at variable Raman frequencies: A) cm-chi/alg region (427 cm^{-1}), B) MB region (447 cm^{-1}), C) cm-chi region (346 cm^{-1}), and D) PEO region (279 cm^{-1}), respectively.

4.3.5 Structure of self-assembled sponges before/after annealing

Based on the previous results, a structural mechanism of self-assembly for a multi-component sponge before and after annealing is proposed in Figure 4.11. Original self-assembly of the sponge may be described as a “sandwich-like” arrangement with a loosely packed structure. The biopolymer building blocks (cm-chi and alg) are assembled *via* electrostatic interactions according to the FT-IR spectra in Fig. 4.8. PEO associates with cm-chi and alg *via* hydrogen

bonding.⁴² Therefore, the void space among the polymer chains is occupied by PEO and results in a greater separation of the biopolymer chains. The supramolecular assembly of PEO is also supported by TGA results (Fig. 4.3), DSC (Fig.4.5), and Raman spectra (Fig. 4.7). Zhao et al.¹⁵ reported that PEO was used to suppress electrostatic interactions between cationic and anionic polysaccharides. A consequence of weak interactions between cm-chi and alg for CP-1 leads to phase separation upon exposure of the composite to water because of its high dielectric constant (Fig. 4.9). During annealing, reordering of the resulting polysaccharide complex occurs upon melting and re-crystallizing PEO by reducing the distance between the biopolymer chains and strengthening the polysaccharide assembly upon annealing. PEO crystallization occurs at the polysaccharide surface or within the void space between the polymer chains (Fig. 4.4), revealing two different roles for PEO in the etching process.^{34,43,44} Firstly, PEO may serve as a sacrificial template to create additional pore structure since water etching (*cf.* Fig. 4.10) results in pore formation, in agreement with Fig. 4.6. Secondly, PEO may serve as a protective barrier on the cm-chi/alg fiber surface to shield the hydrophilic surface sites of the composite material from solvent etching effects.

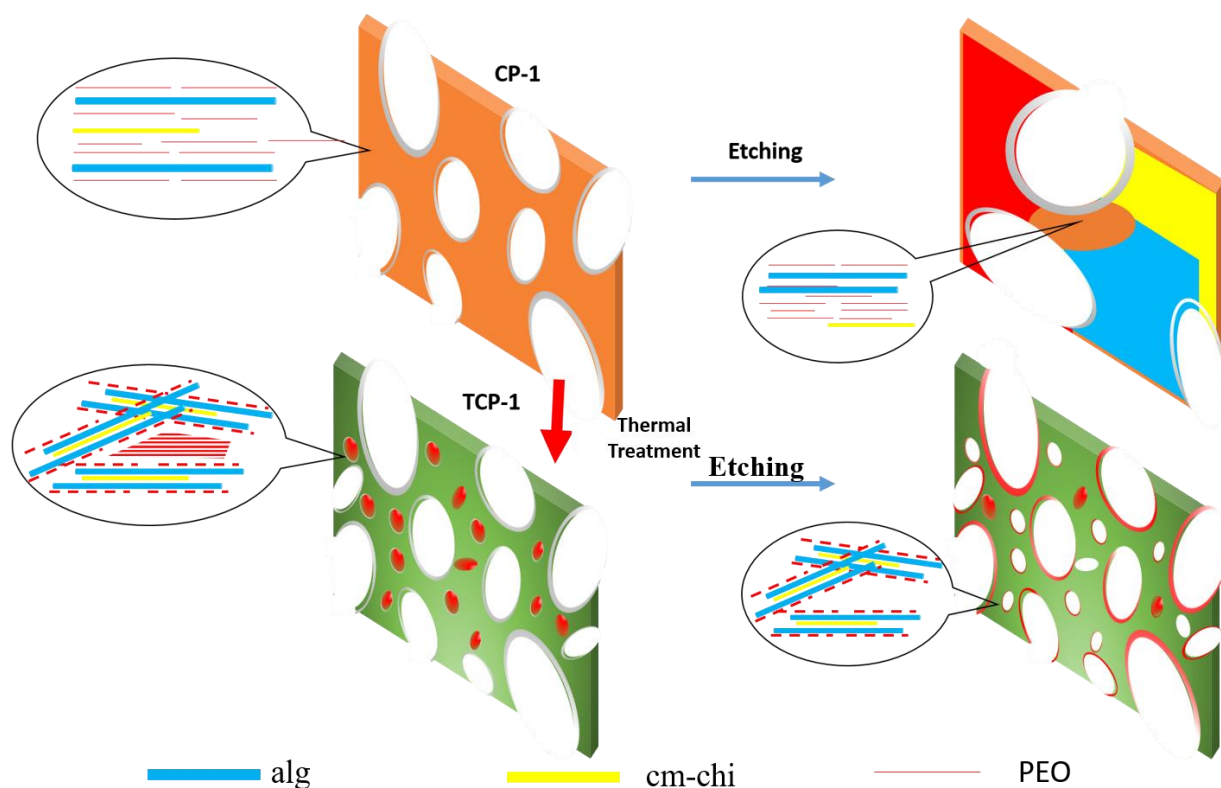


Figure 4.11. An illustrated view of the composition and structure of CP-1 and TCP-1. The red line represents PEO, red area represents PEO domains; blue line represents cm-chi and blue area represents cm-chi domains; yellow line represents alg, and yellow area represents alg domains.

4.4 Conclusion

Chi self-assembled sponges (nonwoven microfibrinous materials) were successfully prepared by freeze-drying, and the structural features were characterized by various spectral methods. In particular, Raman spectral imaging with a suitable dye probe was developed to study the composition and structure of biopolymer composites before/after thermal annealing. Prior to annealing, the composite displayed a phase-separated “sandwich” structure, while the annealing of cm-chi and alg with PEO led to the strengthening of the cohesive interactions between cm-chi and alg. Meanwhile, PEO forms *island-like* features on the biopolymer fiber surface. PEO may serve a dual function upon annealing, where it may either serve as a sacrificial template to create a porous morphology or as a protective layer to prevent water intrusion upon exposure to solvent.

The Raman spectral methods reported herein will contribute to a greater understanding of the *structure-function* properties of chi-based composites electrospun fibrous materials in Chapter 5 and other biopolymer composites for a wide range of emerging applications in the formulation of biomedical devices, nutraceuticals, pharmaceuticals, and cosmetics. Furthermore, the ideology of PEO being a sacrificial template to create a porous morphology on the surface of the fiber, which was demonstrated herein, has been applied in Chapter 6 to help address Objective #3.

4.5 References

- (1) Xue, C.; Wilson, L. D. A Structural Study of Self-Assembled Chitosan-Based Sponge Materials. *Carbohydr. Polym.* **2019**, *206*, 685–693. <https://doi.org/10.1016/j.carbpol.2018.10.111>.
- (2) Croisier, F.; Jérôme, C. Chitosan-Based Biomaterials for Tissue Engineering. *Eur. Polym. J.* **2013**, *49* (4), 780–792. <https://doi.org/10.1016/j.eurpolymj.2012.12.009>.
- (3) Naseri-Nosar, M.; Ziora, Z. M. Wound Dressings from Naturally-Occurring Polymers: A Review on Homopolysaccharide-Based Composites. *Carbohydr. Polym.* **2018**, *189*, 379–398. <https://doi.org/10.1016/j.carbpol.2018.02.003>.
- (4) Rogina, A.; Rico, P.; Gallego Ferrer, G.; Ivanković, M.; Ivanković, H. Effect of in Situ Formed Hydroxyapatite on Microstructure of Freeze-Gelled Chitosan-Based Biocomposite Scaffolds. *Eur. Polym. J.* **2015**, *68*, 278–287. <https://doi.org/10.1016/J.EURPOLYMJ.2015.05.004>.
- (5) Sun, W.; Chen, G.; Wang, F.; Qin, Y.; Wang, Z.; Nie, J.; Ma, G. Polyelectrolyte-Complex Multilayer Membrane with Gradient Porous Structure Based on Natural Polymers for Wound Care. *Carbohydr. Polym.* **2018**, *181*, 183–190. <https://doi.org/10.1016/J.CARBPOL.2017.10.068>.
- (6) Jiang, C.; Wang, Z.; Zhang, X.; Zhu, X.; Nie, J.; Ma, G. Crosslinked Polyelectrolyte Complex Fiber Membrane Based on Chitosan-Sodium Alginate by Freeze-Drying. *RSC Adv.* **2014**, *40* (78), 41551–41560. <https://doi.org/10.1039/c4ra04208e>.
- (7) Rogovina, S.; Aleksanyan, K.; Vladimirov, L.; Prut, E.; Ivanushkina, N.; Berlin, A. Development of Novel Biodegradable Polysaccharide-Based Composites and

- Investigation of Their Structure and Properties. *J. Polym. Environ.* **2018**, 26 (4), 1727–1736. <https://doi.org/10.1007/s10924-017-1069-3>.
- (8) Xu, L.; Chen, Y.; Liu, N.; Zhang, W.; Yang, Y.; Cao, Y.; Lin, X.; Wei, Y.; Feng, L. Breathing Demulsification: A Three-Dimensional (3D) Free-Standing Superhydrophilic Sponge. *ACS Appl. Mater. Interfaces* **2015**, 7 (40), 22264–22271. <https://doi.org/10.1021/acsami.5b07530>.
 - (9) Younes, I.; Rinaudo, M. Chitin and Chitosan Preparation from Marine Sources. Structure, Properties and Applications. *Mar. Drugs* **2015**, 13 (3), 1133–1174. <https://doi.org/10.3390/md13031133>.
 - (10) Albanna, M. Z.; Bou-Akl, T. H.; Blowytsky, O.; Walters, H. L.; Matthew, H. W. T. Chitosan Fibers with Improved Biological and Mechanical Properties for Tissue Engineering Applications. *J. Mech. Behav. Biomed. Mater.* **2013**, 20, 217–226. <https://doi.org/10.1016/j.jmbbm.2012.09.012>.
 - (11) Elsabee, M. Z.; Naguib, H. F.; Morsi, R. E. Chitosan Based Nanofibers, Review. *Mater. Sci. Eng. C* **2012**, 32 (7), 1711–1726. <https://doi.org/10.1016/j.msec.2012.05.009>.
 - (12) Knaul, J. Z.; Hudson, S. M.; Creber, K. A. M. Improved Mechanical Properties of Chitosan Fibers. *J. Appl. Polym. Sci.* **1999**, 72 (13), 1721–1732. <https://doi.org/AID-APP8>3.0.CO;2-V>.
 - (13) Prateepchanachai, S.; Thakhiew, W.; Devahastin, S.; Soponronnarit, S. Mechanical Properties Improvement of Chitosan Films via the Use of Plasticizer, Charge Modifying Agent and Film Solution Homogenization. *Carbohydr. Polym.* **2017**, 174, 253–261. <https://doi.org/10.1016/J.CARBPOL.2017.06.069>.
 - (14) Çaykara, T.; Demirci, S.; Eroğlu, M. S.; Güven, O. Poly(Ethylene Oxide) and Its Blends with Sodium Alginate. *Polymer (Guildf)*. **2005**, 46 (24), 10750–10757. <https://doi.org/10.1016/j.polymer.2005.09.041>.
 - (15) Zhao, X.; Chen, S.; Lin, Z.; Du, C. Reactive Electrospinning of Composite Nanofibers of Carboxymethyl Chitosan Cross-Linked by Alginate Dialdehyde with the Aid of Polyethylene Oxide. *Carbohydr. Polym.* **2016**, 148, 98–106.

<https://doi.org/dx.doi.org/10.1016/j.carbpol.2016.04.051>.

- (16) Duan, G.; Jiang, S.; Jérôme, V.; Wendorff, J. H.; Fathi, A.; Uhm, J.; Altstädt, V.; Herling, M.; Breu, J.; Freitag, R.; Agarwal, S.; Greiner, A. Ultralight, Soft Polymer Sponges by Self-Assembly of Short Electrospun Fibers in Colloidal Dispersions. *Adv. Funct. Mater.* **2015**, 25 (19), 2850–2856. <https://doi.org/10.1002/adfm.201500001>.
- (17) Xue, C.; Wilson, L. D. Design and Characterization of Chitosan-Based Composite Particles with Tunable Interfacial Properties. *Carbohydr. Polym.* **2015**, 132, 369–377. <https://doi.org/10.1016/j.carbpol.2015.06.058>.
- (18) Miraftab, M.; Saifullah, A. N.; Cay, A. Physical Stabilisation of Electrospun Poly(Vinyl Alcohol) Nanofibres: Comparative Study on Methanol and Heat-Based Crosslinking. *J. Mater. Sci.* **2015**, 50 (4), 1943–1957. <https://doi.org/10.1007/s10853-014-8759-1>.
- (19) Bocklitz, T. W.; Guo, S.; Ryabchykov, O.; Vogler, N.; Popp, J. Raman Based Molecular Imaging and Analytics: A Magic Bullet for Biomedical Applications!? *Anal. Chem.* **2016**, 88 (1), 133–151. <https://doi.org/10.1021/acs.analchem.5b04665>.
- (20) Dolatkah, A.; Wilson, L. D. Salt-Responsive Fe₃O₄ Nanocomposites and Phase Behavior in Water. *Langmuir* **2018**, 34 (1), 341–350. <https://doi.org/10.1021/acs.langmuir.7b03613>.
- (21) Humphrey, C. D.; Pittman, F. E. A Simple Methylene Blue-Azure II-Basic Fuchsin Stain for Epoxy-Embedded Tissue Sections. *Stain Technol.* **1974**, 49 (1), 9–14. <https://doi.org/10.3109/10520297409116929>.
- (22) Mahaninia, M. H.; Wilson, L. D. Modular Cross-Linked Chitosan Beads with Calcium Doping for Enhanced Adsorptive Uptake of Organophosphate Anions. *Ind. Eng. Chem. Res.* **2016**, 55 (45), 11706–11715. <https://doi.org/10.1021/acs.iecr.6b02814>.
- (23) Mohamed, M. H.; Wilson, L. D.; Headley, J. V. Tuning the Physicochemical Properties of β -Cyclodextrin Based Polyurethanes via Cross-Linking Conditions. *Microporous Mesoporous Mater.* **2015**, 214 (0), 23–31. <https://doi.org/10.1016/j.micromeso.2015.04.029>.

- (24) Mohamed, M. H.; Wilson, L. D. Kinetic Uptake Studies of Powdered Materials in Solution. *Nanomaterials* **2015**, 5 (2), 969–980. <https://doi.org/10.3390/nano5020969>.
- (25) Filippov, M. P.; Kohn, R. Determination of Composition of Alginates by Infrared Spectroscopic Method. *Chem. Zvesti* **1974**, 28 (6), 817–819.
- (26) Chen, X. G.; Park, H. J. Chemical Characteristics of O-Carboxymethyl Chitosans Related to the Preparation Conditions. *Carbohydr. Polym.* **2003**, 53 (4), 355–359. [https://doi.org/10.1016/S0144-8617\(03\)00051-1](https://doi.org/10.1016/S0144-8617(03)00051-1).
- (27) Mohamed, M. H.; Wilson, L. D.; Headley, J. V. Design and Characterization of Novel β -Cyclodextrin Based Copolymer Materials. *Carbohydr. Res.* **2011**, 346 (2), 219–229. <https://doi.org/10.1016/J.CARRES.2010.11.022>.
- (28) Mohamed, M. H.; Udoetok, I. A.; Wilson, L. D.; Headley, J. V. Fractionation of Carboxylate Anions from Aqueous Solution Using Chitosan Cross-Linked Sorbent Materials. *RSC Adv.* **2015**, 5 (100), 82065–82077. <https://doi.org/10.1039/C5RA13981C>.
- (29) Wilson, L. D.; Xue, C. Macromolecular Sorbent Materials for Urea Capture. *J. Appl. Polym. Sci.* **2013**, 128 (1), 667–675. <https://doi.org/10.1002/app.38247>.
- (30) Zohuriaan, M. J.; Shokrolahi, F. Thermal Studies on Natural and Modified Gums. *Polym. Test.* **2004**, 23 (5), 575–579. <https://doi.org/10.1016/j.polymertesting.2003.11.001>.
- (31) Guo, R.; Wilson, L. D. Synthetically Engineered Chitosan-Based Materials and Their Sorption Properties with Methylene Blue in Aqueous Solution. *J. Colloid Interface Sci.* **2012**, 388, 225–234. <https://doi.org/10.1016/j.jcis.2012.08.010>.
- (32) Hritcu, D.; Popa, M. I.; Popa, N.; Badescu, V.; Balan, V. Preparation and Characterization of Magnetic Chitosan Nanospheres. *Turkish J. Chem.* **2009**, 33 (6), 785–796. <https://doi.org/10.3906/kim-0812-42>.
- (33) Lin, H.-Y.; Yeh, C.-T. Alginate-Crosslinked Chitosan Scaffolds as Pentoxifylline Delivery Carriers. *J. Mater. Sci. Med.* **2010**, 21 (5), 1611–1620. <https://doi.org/10.1007/s10856-010-4028-2>.
- (34) Samanta, P.; Thangapandian, V.; Singh, S.; Srivastava, R.; Nandan, B.; Liu, C. L.; Chen,

- H. L. Crystallization Behaviour of Poly(Ethylene Oxide) under Confinement in the Electrospun Nanofibers of Polystyrene/Poly(Ethylene Oxide) Blends. *Soft Matter* **2016**, *12* (23), 5110–5120. <https://doi.org/10.1039/c6sm00648e>.
- (35) Campos-Vallette, M. M.; Chandía, N. P.; Clavijo, E.; Leal, D.; Matsuhira, B.; Osorio-Román, I. O.; Torres, S. Characterization of Sodium Alginate and Its Block Fractions by Surface-Enhanced Raman Spectroscopy. *J. Raman Spectrosc.* **2010**, *41* (7), 758–763. <https://doi.org/10.1002/jrs.2517>.
- (36) Maxfield, J.; Shepherd, I. W. Conformation of Poly(Ethylene Oxide) in the Solid State, Melt and Solution Measured by Raman Scattering. *Polymer (Guildf)*. **1975**, *16* (7), 505–509. [https://doi.org/10.1016/0032-3861\(75\)90008-7](https://doi.org/10.1016/0032-3861(75)90008-7).
- (37) Frech, R.; Chintapalli, S.; Bruce, P. G.; Vincent, C. A. Crystalline and Amorphous Phases in the Poly(Ethylene Oxide)–LiCF₃SO₃ System. *Macromolecules* **1999**, *32* (3), 808–813. <https://doi.org/10.1021/ma9812682>.
- (38) Kasaai, M. The Use of Various Types of NMR and IR Spectroscopy for Structural Characterization of Chitin and Chitosan. In *Chitin, Chitosan, Oligosaccharides and Their Derivatives*; CRC Press, 2010; pp 149–170. <https://doi.org/10.1201/EBK1439816035-c12>.
- (39) Shigemasa, Y.; Matsuura, H.; Sashiwa, H.; Saimoto, H. Evaluation of Different Absorbance Ratios from Infrared Spectroscopy for Analyzing the Degree of Deacetylation in Chitin. *Int. J. Biol. Macromol.* **1996**, *18* (3), 237–242. [https://doi.org/10.1016/0141-8130\(95\)01079-3](https://doi.org/10.1016/0141-8130(95)01079-3).
- (40) Zajac, A.; Hanuza, J.; Wandas, M.; Dymińska, L. Determination of N-Acetylation Degree in Chitosan Using Raman Spectroscopy. *Spectrochim. Acta Part A Mol. Biomol. Spectrosc.* **2015**, *134*, 114–120. <https://doi.org/10.1016/j.saa.2014.06.071>.
- (41) Nicolai, S. H. A.; Rubim, J. C. Surface-Enhanced Resonance Raman (SERR) Spectra of Methylene Blue Adsorbed on a Silver Electrode. *Langmuir* **2003**, *19* (10), 4291–4294. <https://doi.org/10.1021/la034076v>.
- (42) Kubo, S.; Kadla, J. F. Poly(Ethylene Oxide)/Organosolv Lignin Blends: Relationship between Thermal Properties, Chemical Structure, and Blend Behavior. *Macromolecules*

- 2004**, 37 (18), 6904–6911. <https://doi.org/10.1021/ma0490552>.
- (43) Taden, A.; Landfester, K. Crystallization of Poly(Ethylene Oxide) Confined in Miniemulsion Droplets. *Macromolecules* **2003**, 36 (11), 4037–4041. <https://doi.org/10.1021/ma034052v>.
- (44) Yao, Y.; Sakai, T.; Steinhart, M.; Butt, H. J.; Floudas, G. Effect of Poly(Ethylene Oxide) Architecture on the Bulk and Confined Crystallization within Nanoporous Alumina. *Macromolecules* **2016**, 49 (16), 5945–5954. <https://doi.org/10.1021/acs.macromol.6b01406>.

CHAPTER 5

A spectroscopic study of solid-phase chitosan/cyclodextrin-based electrospun fibers

Xue, C.; Wilson, L. D. A Spectroscopic Study of Solid-Phase Chitosan/Cyclodextrin-Based Electrospun Fibers. *Fibers* **2019**, 7 (5). <https://doi.org/10.3390/FIB7050048>.

Author's contribution

Chen Xue performed all the experimental work (i.e., data analysis, data curation, visualization, formal analysis, etc.) and wrote the first draft of the manuscript. Chen Xue made further revisions to the final draft stage with the supervisor. Dr. L. D. Wilson was responsible for the supervision of the project, editorial guidance for revision of the manuscript drafts, and corresponding authorship.

Description

The original published paper was reformatted to meet the requirements of the College of Graduate and Postdoctoral Studies (CGPS) at the University of Saskatchewan, along with formulating the published work into a comprehensive thesis document. Specifically, the introduction and conclusion section of the original paper was revised to avoid unnecessary repetition. As general details of routine characterization methods are introduced in Chapter 3, the experimental section is modified accordingly in which only specific details are included. The reference style of the original paper was changed to the CGPS thesis' style. The supplementary information for the published study is included in the Appendix.

This research accomplished Objective #2 of this thesis, contributing to the overall goal in two aspects. The first aspect is that chi-based electrospun nanofibrous materials were prepared. The other one is that the role of the supramolecular ternary assembly (chi + HP- β -CD + trifluoroacetic acid) role in forming chi-based electrospun fibers was elucidated through several complementary characterization methods. The latter includes FT-IR, Raman spectroscopy, and Raman spectral imaging with a dye probe to support Hypothesis #4 as described in Section 1.3.

5.1 Introduction

According to the degree of ionization of glucosamine groups of chi, the antimicrobial and adsorption properties can be altered by variable pH levels.¹⁻⁴ Diverse chi applications have been found in many fields that exploit its pH-dependent binding properties, as evidenced in wastewater treatment, food preservation, and biomedical devices.^{1,2,5-11} To attain additional performance in these applications, research has also focused on the design of different morphological forms of chi that include nanofibrous systems, owing to the high surface area of these biomaterials.^{7,9-16} Among the various approaches for the design of fibrous and nanofibrous materials as outlined in Chapters 1 and 2, where electrospinning methods represent a commonly accepted method.^{9-11,17-20} While chi is soluble in acidic aqueous solution, technical difficulties related to the electrospinning of uniform fibers arise due to repulsive interactions between the cationic sites of the biopolymer glucosamine sub-units that attenuate chain entanglement effects.^{14-17,21} The judicious choice of additive components offers a solution to offset such charge repulsion effects during electrospinning.^{14,22-27} For example, Burns et al. reported the use of trifluoroacetic acid (TFA) and hydroxypropyl β -cyclodextrin (HP- β -CD) as additives to assist in the electrospinning of chi nanofibers.²⁸ The potential of HP- β -CD to form noncovalent host-guest complexes with various molecular species, in conjunction with the polyelectrolyte nature of chi, may further enhance the utility of such nanofibrous materials as advanced coatings for diverse applications.^{28,29} Notwithstanding the complexation properties of HP- β -CD, the molecular level details that account for the uniform formation of chi fibers *via* this pathway are not well understood. While Burns et al.²⁸ allude to the possibility that inclusion complex formation occurs between chi and HP- β -CD, further research is required to gain insight on the molecular basis of the improvement of fiber formation in this ternary (HP- β -CD + chi + TFA) system to advance the field of chi nanofibrous materials. As demonstrated in Chapter 4, Raman spectral imaging with a suitable dye probe is a useful tool to decipher complex multi-component systems' structures. Therefore, the insight on improvements to the electrospun fiber formation process through such ternary systems can be addressed using this strategy.

The purpose of this thesis chapter is to accomplish Objective #2 by two short-term goals. The first short-term goal is to prepare chi/HP- β -CD nanofibrous materials at variable mass ratios *via* electrospinning in nonaqueous media (TFA) using an “in-house” electrospinning apparatus.

The second short-term goal is that the composition and structure of the electrospun fibrous materials in the solid-state was studied using thermal analysis and spectroscopic (FT-IR and Raman) methods, along with Raman spectral imaging with a suitable dye probe. Raman spectral imaging being assisted by a rhodamine dye probe was employed to gain further structural information on the chi nanofibrous composite materials reported herein. This study's results are foreseen to help develop electrospinning formulations for chi systems by taking advantage of such ternary component systems.

5.2 Materials and Methods

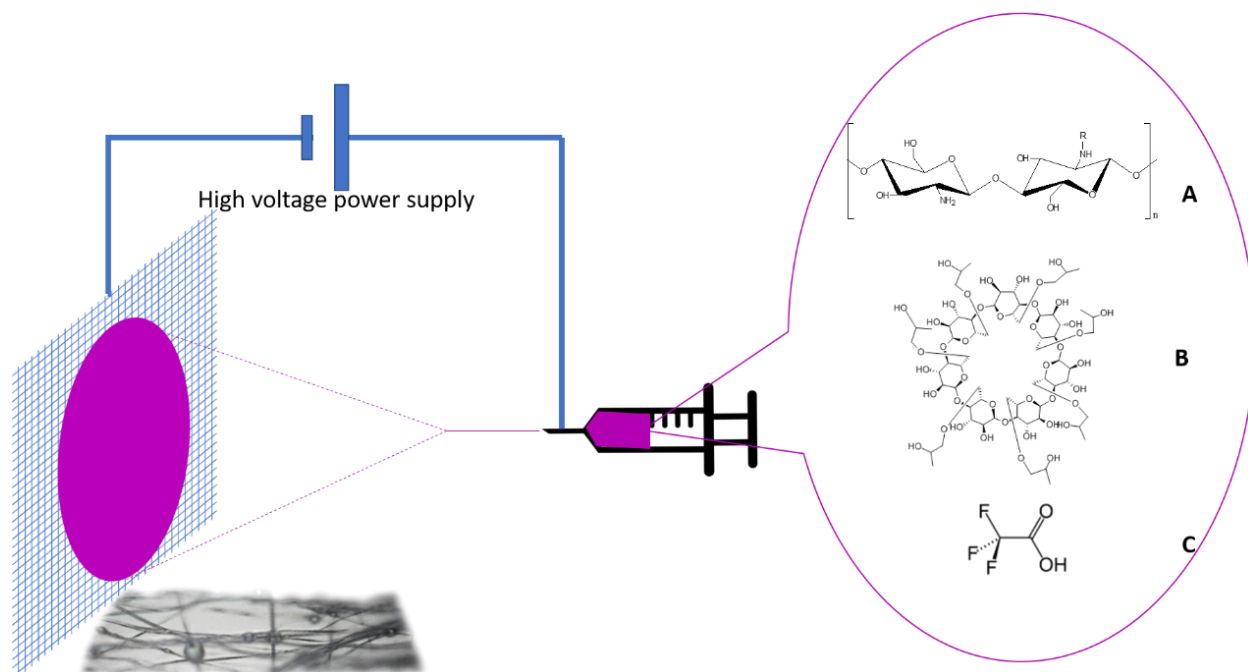
5.2.1. Materials

Research grade 6-O-hydroxypropyl β -cyclodextrin (HP- β -CD) with a degree of substitution (DS) = 4.6 was purchased from CYCLOLAB, Ltd. (Budapest, Hungary) and was used as received. Rhodamine 6G was purchased from Allied Chemical (Morristown, New Jersey, NJ, USA) and used as received. Low molecular weight (LMW) chi (chi, 75-80% deacetylation and molecular weights in the range of 50–190 kDa, according to Brookfield viscosity 20 cPs), deuterated dimethyl sulfoxide (DMSO- d_6 , 99.9%), tetrahydrofuran (THF) and trifluoroacetic acid (TFA) was obtained from Sigma-Aldrich Canada Ltd. (Oakville, ON, Canada).

5.2.2. Preparation of chi/HP- β -CD electrospun nanofibrous materials

All solutions used for electrospinning were formulated according to Burns et al.²⁸, where the designated mass of chi and HP- β -CD (wt.%) was added to neat TFA and allowed to mix overnight with stirring (100 rpm) at 23 °C. All solutions were kept at 4 °C and consumed within 72 h.

The resulting solutions were used to prepare chi/HP- β -CD electrospun nanofibrous materials according to Section 3.2 described further in Chapter 3. Chi/HP- β -CD electrospun nanofibrous materials with two different mass ratios (chi : HP- β -CD = 2:20 and 2:50) were prepared; chi:HP- β -CD 2:20 and chi:HP- β -CD 2:50. The electrospinning apparatus and molecular structures of the precursors and the solvent are shown in Scheme 5.1.



Scheme 5.1. A schematic illustration of the electrospinning setup and molecular structure of the precursors: A) chi where R = -COCH₃ or H depending the degree of deacetylation, where n depends on the relative molecular weight of the biopolymer; B) HP-β-CD; and C) trifluoroacetic acid (TFA) is the solvent system.

5.2.3. ¹H NMR spectroscopy in solution

The HP-β-CD content of the fiber samples was estimated using a qualitative NMR (qNMR) method adapted from a previous report. A 1% (w/w) THF/DMSO-*d*₆ solution was prepared by adding a desired amount of THF to DMSO-*d*₆ to which ca. 5 mg of the *as-spun* fiber was dissolved with ~600 mg of solvent (THF/DMSO- *d*₆) in a 5 mm NMR tube. ¹H NMR spectra were obtained using a wide-bore (89 mm) 11.7 T (500 MHz) Oxford superconducting magnet system (Bruker BioSpin Corp., Billerica, MA, USA) equipped with a 5 mm Pa Tx1 probe and a recycle delay of 10 s. THF served as an internal quantitative standard for estimation of HP-β-CD content of a fiber sample.

5.2.4 Characterization methods

DSC profiles (*cf.* Section 3.1.3), DTG plots (*cf.* Section 3.1.4), FT-IR (*cf.* Section 3.1.1), and Raman spectra (*cf.* Section 3.1.7) of chi, HP- β -CD, the physical mixture (chi and HP- β -CD), chi/HP- β -CD electrospun fibrous materials were acquired. SEM images (*cf.* Section 3.1.5) of samples were obtained at variable magnification (1000 \times , 3000 \times , and 5000 \times). Raman spectral imaging and data processing (*cf.* Section 3.1.8) for chi:HP- β -CD 2:50 electrospun fibrous materials was done as described in Chapter 3. In detail, Raman spectral imaging was performed using a 12s exposure time and a static scan mode centered at 790 cm^{-1} , where such conditions lead to an effective spectral range of 596-985 cm^{-1} for various samples. A total 92×70 spectra were collected in a uniform $101 \times 77 \mu\text{m}$ grid. Then, the Raman images were constructed by the relative intensity of the respective spectral band (610 cm^{-1} and 850 cm^{-1}) to baseline as required. The results from dividing the band intensity at 610 cm^{-1} by the band at 850 cm^{-1} were used to construct the Raman image for the highlighted chi region. A Rhodamine 6G dye in a benzene solution ($\sim 0.1 \mu\text{M}$) was used as a dye probe in this project.

5.3. Results and Discussion

As indicated in the introduction section above, the role of additives (TFA, HP- β -CD) for the assisted electrospinning of chi is not well known. Therefore, structural characterization of the nanofibrous materials was carried out to gain an improved understanding of the structure and composition of these composite materials, as described in following sections below.

5.3.1. SEM results

SEM images of chi:HP- β -CD 2:50 fiber are shown in Figure 5.1. A mixture of products that possess nodule-shaped elements and fiber-like morphology was observed in Figures 5.1A-B, showing the resulting materials for both ratios (2:20 and 2:50) with a heterogeneous composition in terms of morphology. It was noted that the chi:HP- β -CD 2:50 fiber contained fewer nodule-shape elements and had a large fiber diameter when compared with the chi:HP- β -CD 2:20 fiber. These general observations coincide with those reported in the previous study by Burns et al.²⁸

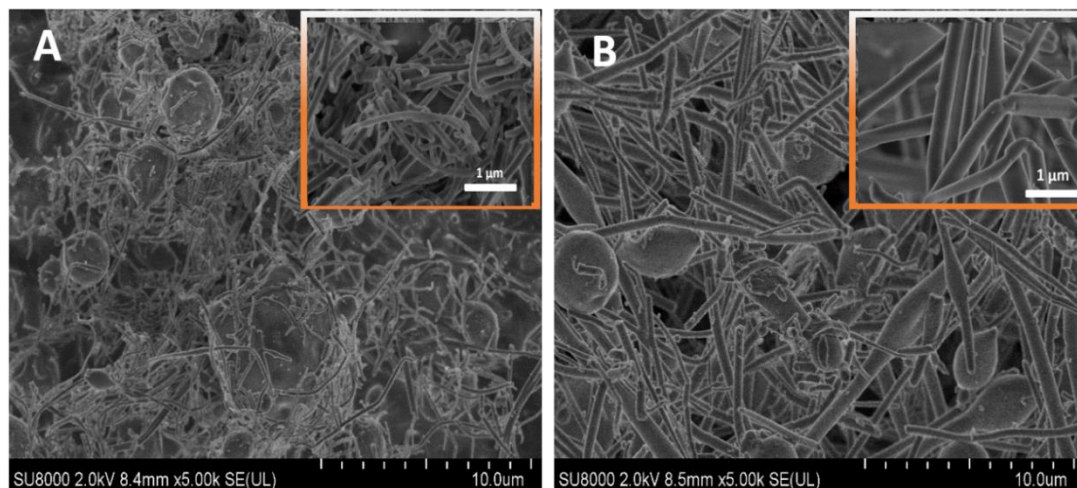


Figure 5.1. SEM images of chi/HP- β -CD fibers: A) chi:HP- β -CD 2:20 and B) chi:HP- β -CD 2:50.

5.3.2. Determination of HP- β -CD content in the *as-spun* fibers

To assess the composition of the chi:HP- β -CD electrospun fibers, the HP- β -CD content in the *as-spun* fibers was examined using ^1H NMR spectroscopy. The composition of HP- β -CD (wt. %) in the *as-spun* fibers was calculated based on the integration of a $-\text{CH}_3$ group of HP- β -CD ($\delta = 0.99$ ppm) relative to the internal standard THF ($\delta = 1.60$ ppm). The ^1H NMR spectra are shown in Figure A5.1 of the Appendix. A quantitative determination of a known amount of HP- β -CD was evaluated in a test sampling trial to verify the accuracy of the method. The results are summarized in Table 5.1, where the measured content (wt. %) of HP- β -CD in the *as-spun* fiber sample was drastically lower than that of the predicted value (the theoretical composition according to mass ratios in the prepared solution). The chi: HP- β -CD 2:20 fiber had ~50% difference, and the chi:HP- β -CD 2:50 fiber had ~20% difference compared with the respective theoretical values based on wt. % content. This difference in wt. % suggests that solvent effects may contribute to the *as-spun* fiber's weight, which yields a reduced composition (wt. %) of HP- β -CD. This difference also infers more solvent residue (TFA) in the 2:20 fiber than the 2:50 fiber.

Table 5.1. Determination of HP- β -CD content in the as-spun chi:HP- β -CD fiber using ^1H NMR spectroscopy.

Material	Experimental HP- β -CD Content	Theoretical Value *
HP- β -CD	100% \pm 6.9% (4.47 mg) ²	100% (4.80 mg) ¹
chi: HP- β -CD 2:20 Fiber	~40%	~91%
chi: HP- β -CD 2:50 Fiber	~75%	~96%

*Theoretical value was calculated based on mass ratios between chi and HP- β -CD in the prepared solution, assuming that all the solvent was evaporated from fibers. ¹Values in parentheses refer to the actual sample weight used for the qNMR calibration. ²Values in parentheses refer to the determined HP- β -CD weight for the qNMR calibration.

5.3.3. FT-IR results of *as-spun* fibers

The chi:HP- β -CD fibers were further characterized by FT-IR to identify the composition of the *as-spun* fiber. The FT-IR spectra of *as-spun* fibers are presented in Figure 5.2 without normalization. FT-IR spectrum of pristine chi was shown in Figure A5.2(A) in Appendix. The IR band at 1786 cm^{-1} relates to a free $-\text{COOH}$ group in TFA.^{30–33} The intensity of this band for chi:HP- β -CD 2:20 was higher than the value estimated for chi:HP- β -CD 2:50. This increased band intensity further indicates higher TFA content in the 2:20 fiber than the 2:50 fiber system, in agreement with the results in Table 5.1. The $-\text{COO}^-$ band at 1679 cm^{-1} corresponded to that of the trifluoroacetate ion³⁰, whereas the band at 1526 cm^{-1} was assigned to the protonated amine ($-\text{NH}_3^+$) group of chi^{34–36}. These signatures indicate that electrostatic interactions are likely to occur between the $-\text{COO}^-$ group from TFA with the cation sites ($-\text{NH}_3^+$) of chi within the fiber composite. The band at 1221 cm^{-1} and the shoulder at 1183 cm^{-1} was assigned to the vibrational signature of C–F for TFA.^{31–33,36} The two spectral signatures disappear in the 2:50 fiber but were evident for the 2:20 fiber. The spectral variation between samples is the result of interference of free TFA in the 2:20 fiber, as it contains more TFA over the 2:50 fiber, according to the qNMR results in Section 5.3.2 and the IR band intensity results of the free $-\text{COOH}$ group (1786 cm^{-1}) of TFA^{30–33}.

Hence, the attenuation of two signatures at 1221 and 1183 cm^{-1} in the 2:50 fiber can infer that the $-\text{CF}_3$ group of TFA is bound by the annular region of the HP- β -CD host to form a stable complex. Wilson and Verrall²⁹ have reported an analogous inclusion mode for β -cyclodextrin-guest complexes formed between volatile organics such as halothane with a trifluoromethyl moiety for a range of β -CD/halothane systems (*cf.* Scheme 2 in Ref. 29).

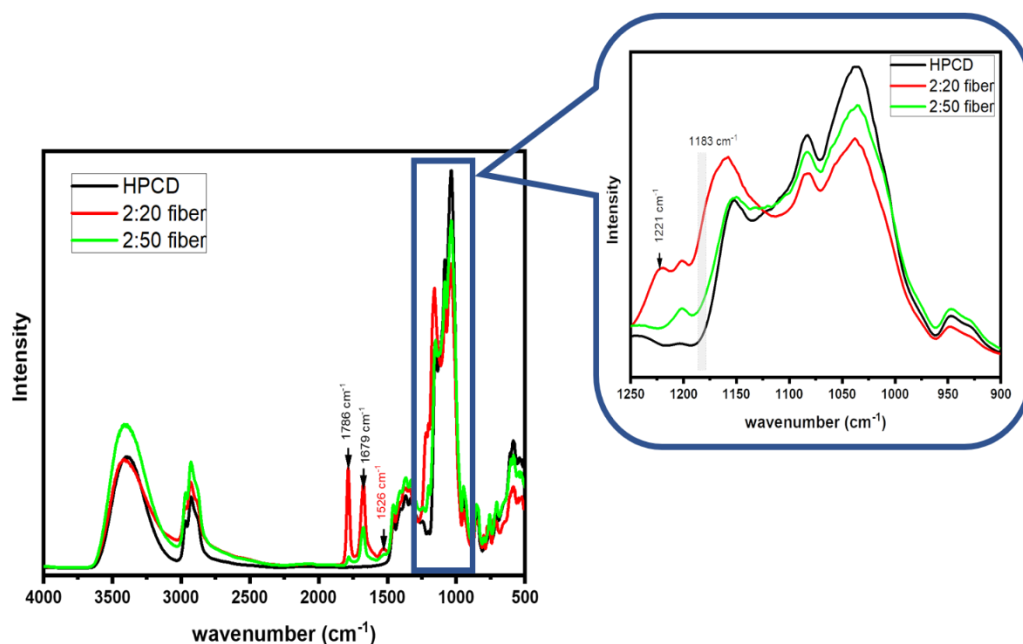


Figure 5.2. FT-IR spectra of HP- β -CD (HPCD) and *as-spun* chi:HP- β -CD fiber (2:20 and 2:50, respectively) without normalization. The expanded region of the inset spectra is shown between 1250 and 900 cm^{-1} of the original spectra.

5.3.4. TGA and DSC results of chi:HP- β -CD fiber

The *as-spun* chi:HP- β -CD 2:50 fiber was characterized by TGA and DSC, where the 2:20 *as-spun* fiber was not measured because it contained a higher level of free TFA, which was done in order to avoid potential damage to the instrument. TGA results are shown in the form of a DTG plot of chi in Figure A5.2(B) of the Appendix. The DTG plots of HP- β -CD and chi:HP- β -CD 2:50 are shown in Figure 5.3A, where a thermal event for HP- β -CD at ~ 350 $^{\circ}\text{C}$ showed no apparent

temperature shift, as compared with that of the fiber prepared at the 2:50 ratio. The 2:50 fiber displayed a new thermal event at ~ 260 °C that corresponds to the decomposition of a trifluoroacetate salt.³⁷ This indicates that the major fraction of TFA in 2:50 fiber is in the form of a trifluoroacetate salt ($\text{CF}_3\text{COO}^-/\text{NH}_3^+$), where the NH_3^+ groups are the cationic glucosamine sites of chi. This trend is consistent with the FT-IR results reported herein (*cf.* Figure 5.2). According to the DSC results in Figure 5.3, evidence of mixing occurs between chi and HP- β -CD. However, because of the greater mass content of HP- β -CD in the binary system (chi + HP- β -CD), the thermal analysis (TGA and DSC) results for the chi:HP- β -CD fiber may be obscured, precluding further detailed compositional analysis of the fiber material.

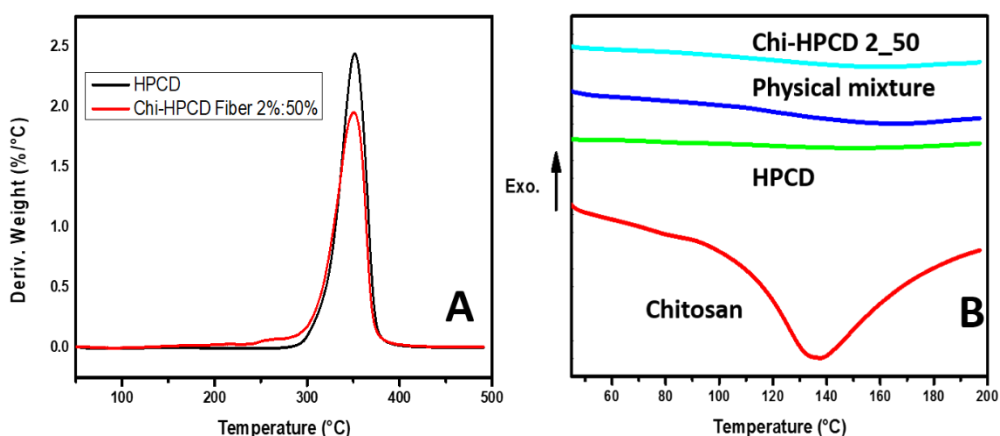


Figure 5.3. Thermal analysis results of *as-spun* chi: HP- β -CD fiber. A) DTG plots of HP- β -CD (HPCD) and chi:HP- β -CD 2:50 fiber (Chi:HPCD 2:50); and B) DSC profiles of chi, HP- β -CD (HPCD), physical mixture, and *as-spun* chi:HP- β -CD 2:50 fiber (Chi:HPCD 2:50).

5.3.5. Raman spectroscopy results

The Raman spectra of HP- β -CD, pristine chi, *as-spun* chi:HP- β -CD fibers, and chi: HP- β -CD fibers at three days and three months after preparation are illustrated in Figure 5.4. The band at 730 cm^{-1} and 1788 cm^{-1} was assigned to the deformation of COO^- and the stretching of the carbonyl group in trifluoroacetate anion, respectively.³⁸ The relative intensity of this band to other spectral signatures revealed a gradual decrease between the *as-spun* fiber (Figure 5.4C) to an aged fiber after three days (Figure 5.4E), then to a further aged fiber after three months (Figure 5.4F). This reduction of the band intensity demonstrates that TFA content in the fiber decreases slowly

over time. A noticeable fact is that signatures related to the $-\text{CF}_3$ group (1143, 1202, 601 and 521 cm^{-1})³⁸ were not clearly observed in the Raman spectra, in contrast to the $-\text{COO}^-$ group of TFA, which suggests that the $-\text{CF}_3$ group may form an inclusion complex with HP- β -CD due to the favourable size-fit compatibility between the cavity of β -CD and the $-\text{CF}_3$ group in line with Ref. 29. The FT-IR results support this conclusion, as evidenced by the disappearance of bands at 1221 and 1183 cm^{-1} in Figure 5.2. Expansions of the original Raman spectra in the range of 770 and 990 cm^{-1} are similarly shown in Figure 5.4. The Raman signatures over this spectral range relate to the variation of the C–O–C torsional angle since it is sensitive to its local conformations.^{34,39} For HP- β -CD, the band at 850 and 925 cm^{-1} was related to ring-breathing modes of HP- β -CD, while the band at 948 cm^{-1} related to the skeletal vibrations for the α -1,4 linkages of HP- β -CD.⁴⁰ A comparison was made among precursors (i.e, HP- β -CD and chi) and different chi:HP- β -CD fiber types. New bands were observed at 827, 864, 884, and 918 cm^{-1} . By comparison, the band at 950 cm^{-1} , compared with the spectrum of HP- β -CD in Figure 5.4A, displayed minimum change. Among the new spectral bands observed, none were associated with the signatures of the CF_3COO^- anion compared with the results reported by Robinson and Taylor’s Raman spectral study of the trifluoroacetate ion.³⁸ These bands showed maximum relative intensity for the *as-spun* chi:HP- β -CD 2:50 fiber spectrum (Figure 5.4C) and minimum relative intensity in the spectrum of chi:HP- β -CD 2:50 fiber after three months (Figure 5.4F). Therefore, new spectral bands at 827, 864, 884, and 918 cm^{-1} may be related to conformational changes of the glucopyranose unit of HP- β -CD that result from the interfacial host-guest complex²⁹ formed between the $-\text{CF}_3$ group of TFA and HP- β -CD. The attenuation of the relative intensity of these spectral bands may be ascribed to the attenuated formation of such complexes between TFA and HP- β -CD, as the trifluoroacetate ion content of the fiber decreased. Similar Raman spectral changes have been reported elsewhere^{41,42}. Furthermore, the spectral band shapes centered at 850 and 925 cm^{-1} for the chi:HP- β -CD 2:50 fiber after three months in the spectrum (Figure 5.4F) was similar to HP- β -CD (Figure 5.4A), but revealed broader Raman spectral features. By comparison, the spectral band at 948 cm^{-1} showed little difference between HP- β -CD (Figure 5.4A) and the chi:HP- β -CD fibers (Figure 5.4C–F). This effect may suggest that the $-\text{CF}_3$ group of TFA was bound to the interfacial region of HP- β -CD since there was limited host-guest interaction with the α -1,4 linkage domain of HP- β -CD. The compositional difference between chi and HP- β -CD precluded a diagnostic spectral analysis to

assess the details of the host–guest interaction between chi and HP- β -CD due to the presence of excess HP- β -CD in the system.

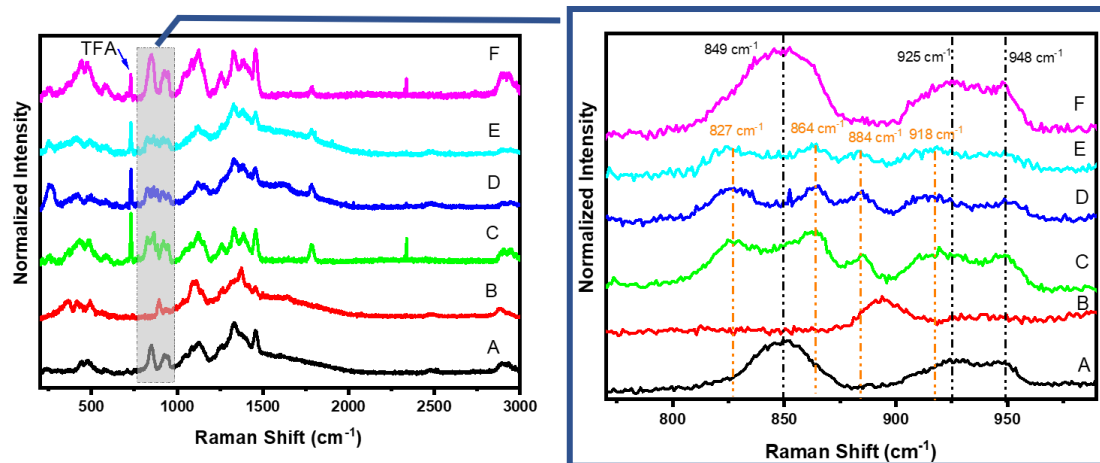


Figure 5.4. Raman spectra of precursors and different chi:HP- β -CD fibers: A) HP- β -CD, B) pristine chi, C) *as-spun* chi:HP- β -CD 2:50 fiber, D) *as-spun* chi:HP- β -CD 2:20 fiber, E) chi:HP- β -CD 2:50 fiber after 3 days and F) chi:HP- β -CD 2:50 fiber after 3 months. The expanded region (Right side) covers the region between 770 and 990 cm^{-1} .

5.3.6. Raman spectral imaging with dye probe (Rhodamine 6G)

The TFA content was minimized for the chi:HP- β -CD 2:50 fiber by exposing the fibers to the open atmosphere under adequate ventilation at ambient conditions to assess the interaction between chi and HP- β -CD. This setup favored the volatilization of excess TFA that may influence the sensitivity of the fiber characterization by reducing contributions of high spectral intensity that arise from TFA. The combined use of Raman spectral imaging with a suitable dye probe afforded a spectral method that highlighted the chi fiber domains that enable the spectral characterization of the regions of interest. Rhodamine 6G was chosen as the dye probe for this study because of the reported favorable binding of chi⁴³ relative to HP- β -CD with the Rhodamine 6G dye^{44,45}. Benzene was used as the solvent to avoid the dissolution of fiber components and to maintain the integrity of the electrospun fiber system as it is a poor solvent for such polysaccharide systems (chi:HP- β -CD). The characteristic Raman signature at 610 and 850 cm^{-1} corresponded to the C–C–C ring in-

plane bending for Rhodamine 6G^{46,47} and the respective ring breathing band for the HP- β -CD glucopyranose unit⁴⁰ that was used to construct the Raman images.

Raman spectral imaging results in the presence of the Rhodamine 6G dye probe are shown in Figure 5.5. The Raman image of the HP- β -CD area generated using the Raman signal at 850 cm^{-1} for the fiber is shown in Figure 5.5A. From this Raman image, fibrous materials with a heterogeneous morphology of beads and fibers concur with the SEM results, as shown in Figure 5.1. The Raman spectral imaging of the chi fraction was generated using the Raman band at 610 cm^{-1} , as shown in Figure 5.5B. It appears that chi adopts a *bundle-type* structure in various sample loci. Upon comparing Figure 5.5A-B, the spectral region for the chi domains was not congruently matched with the spectral region of HP- β -CD and may indicate that the composition of the electrospun fiber was heterogeneous in nature. Such heterogeneities likely take place during the electrospinning process. Despite the efforts made to remove TFA from the fiber, the persistence of Raman signatures of TFA was noted at $\sim 730 \text{ cm}^{-1}$ but with reduced spectral intensity.

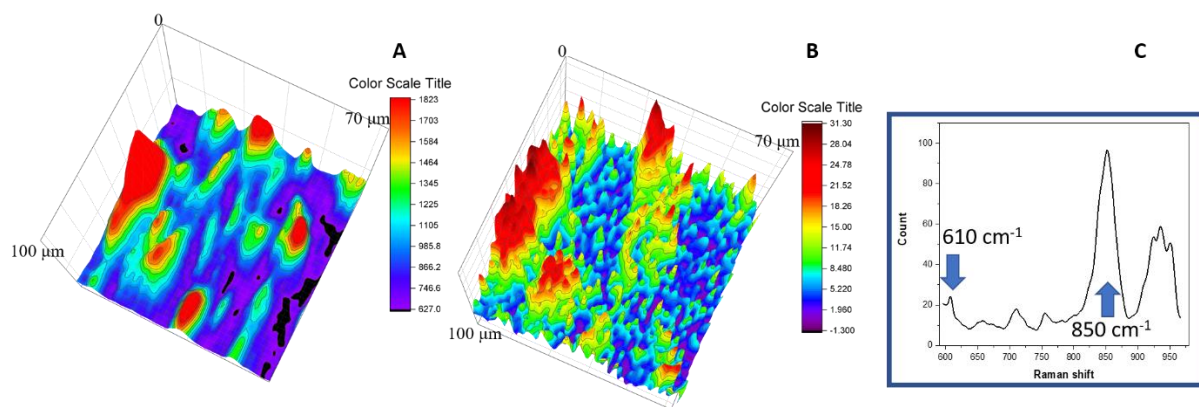


Figure 5.5. Raman imaging results of dried chi:HP- β -CD 2:50 fiber after soaking with Rhodamine 6G in a benzene solution, where a sample Raman spectrum centered at 790 cm^{-1} was given under static conditions ($\lambda_{\text{ex}} = 785 \text{ nm}$). The Raman image of the HP- β -CD area (A) was constructed by peak integration at 850 cm^{-1} . The Raman image of chi in area (B) was constructed by dividing the spectral intensity for Rhodamine 6G (610 cm^{-1}) against that for HP- β -CD (850 cm^{-1}) for each respective Raman spectrum, where a Raman spectrum is shown in panel C as an example.

Figure 5.5A-B was combined into one additive image, as shown in Figure 5.6 to emphasize different structural domains of the fiber: a chi rich area, a chi/HP- β -CD mixed area, and a HP- β -CD rich area. In the spectrum for the chi rich domain (Figure 5.6A), a Raman signature related to the ring breathing mode of chi was noted at 895 cm^{-1} . This band had no apparent spectral change compared to the Raman spectrum of pristine chi (Figure 5.4B). Moreover, the shape of the spectral band at ~ 850 and $\sim 930\text{ cm}^{-1}$ for all samples (Figure 5.6A–C) was nearly identical, suggesting that HP- β -CD has no direct intermolecular interactions with the chi polysaccharide chain of the fiber. Moreover, the TFA/HP- β -CD peak intensity ratios between TFA ($\sim 730\text{ cm}^{-1}$) and HP- β -CD ($\sim 850\text{ cm}^{-1}$) were obtained for the chi rich area, the mixed area, and the HP- β -CD rich area based on Figure 5.6A-C. The highest TFA/HP- β -CD ratio was observed in the mixed area, while the lowest TFA/HP- β -CD ratio was found in the HP- β -CD rich area. This finding may suggest that chi/TFA/HP- β -CD forms a stable complex in the final electrospun fiber.

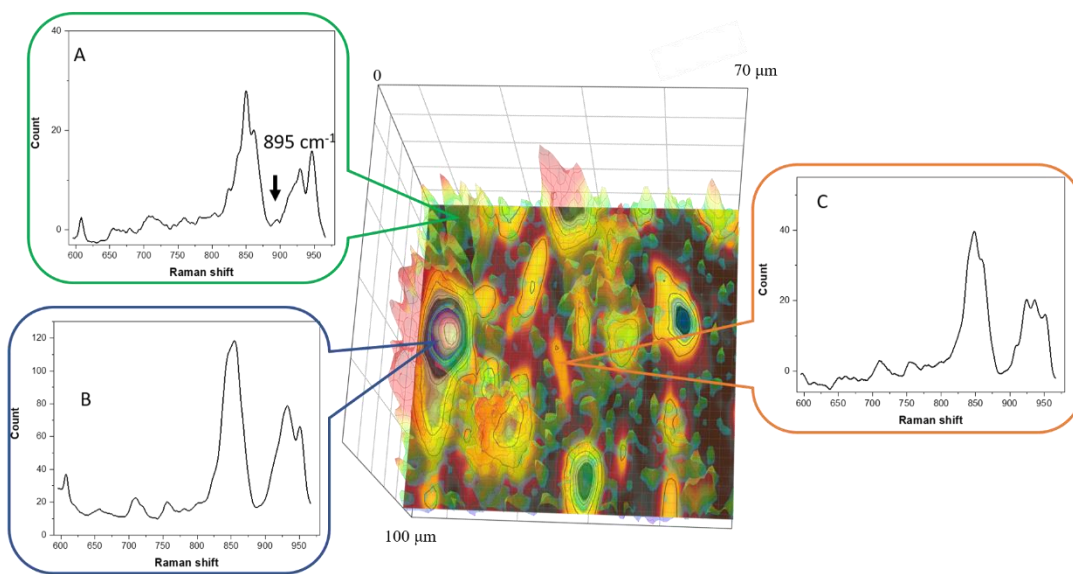
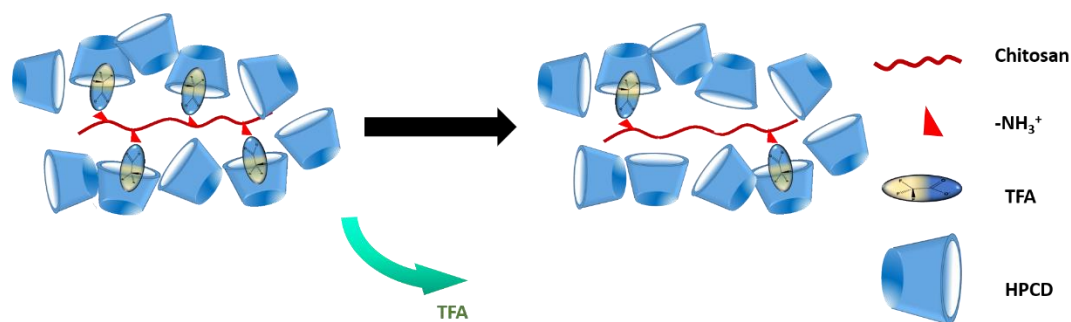


Figure 5.6. A combined Raman image from the spectral data for the chi region (Figure 5.5A) and the HP- β -CD region (Figure 5.5B). The sample spectrum was shown for different highlighted spectral regions: A) a chi rich domain, B) a chi/HP- β -CD mixed domain, and C) an HP- β -CD rich domain.

5.3.7. Composition of chi:HP- β -CD electrospun fiber and its component interactions

An illustration of the compositional change of the chi:HP- β -CD electrospun fiber over time is shown in Scheme 5.2. According to the FT-IR and Raman spectral results, TFA exists in the chi:HP- β -CD electrospun fiber as a third component that undergoes slow release from the fiber composite over time that leads to compositional and/or structural changes of the fiber. Electrostatic interactions were likely to occur between the COO^- group from the TFA and NH_3^+ group from chi under such conditions. A host-guest complex is inferred between the CF_3 group in TFA and HP- β -CD, as described above. According to FT-IR spectra, this is supported by the disappearance of the C-F band at 1221 and 1183 cm^{-1} . Secondly, this is confirmed by the reduction of the relative intensity of CF_3 signatures in the Raman spectra. Thirdly, further verification is judged by the Raman spectral modifications of the ring breathing region of HP- β -CD for the chi:HP- β -CD fiber. Thus, the majority of remaining TFA in the fiber may have served as a “connector unit” between chi and HP- β -CD, where the COO^- group of TFA is associated with the NH_3^+ group of chi *via* ion-ion interactions, while the CF_3 group of TFA forms an interfacial complex with HP- β -CD.²⁹ To afford this type of host-guest complex, the wider annular region that contained the secondary hydroxyl groups of HP- β -CD is implicated since the narrow annular region contained C6-hydroxyl and C6-hydroxypropyl substituents that may have resulted in steric effects. Upon ion-ion binding of TFA with the charged amine sites (NH_3^+) of chi, repulsive electrostatic forces between chi polymer chains become attenuated. As well, the presence of bound TFA onto chi with subsequent binding by HP- β -CD may have afforded additional charge screening effects that lead to improved electrospinning performance of the system, as illustrated in Scheme 5.2. Based on the Raman spectral imaging results, compositional heterogeneity of chi:HP- β -CD electrospun fiber was depicted, where no evidence of a direct or well-defined host-guest interaction between chi and HP- β -CD for the fiber system is supported by the Raman spectral results. In turn, this is consistent with the likely formation of a “facial complex”, as reported for the case of a weakly bound β -CD/halothane complex with a reported 1:1 binding constant (ca. $K_{1:1} = 10^2 \text{ M}^{-1}$) in aqueous media.²⁹



Scheme 5.2. An illustrative view of the compositional change of a chi:HP- β -CD electrospun fiber over time, where the green arrow shows incremental temporal loss of trifluoroacetic acid (TFA).

5.4. Conclusion

Chi:HP- β -CD 2:20 and 2:50 fiber were produced *via* electrospinning of mixtures of HP- β -CD and chi using TFA as a solvent. The composition of chi:HP- β -CD fibers was determined using thermal analysis and complementary spectral methods. TFA was found to be a constituent in the chi:HP- β -CD fiber assembly. The heterogeneous morphology and composition of this electrospun fiber composite were revealed using SEM and Raman spectral imaging with a dye-based probe method described in Chapter 4. Interactions among the components were also characterized using complementary methods, such as IR/Raman spectroscopy. TFA appears to have multifunctional properties as a solvent during the electrospinning process: TFA protonates chi and stabilizes host-guest interactions with HP- β -CD. Hence, the presence of lateral binding sites along the chi backbone (*cf.* Scheme 5.2) due to electrostatically bound TFA are found to play a crucial role in the effective dispersion of chi and the reduction of repulsive forces during electrospinning between chi polymer chains that favor fiber formation. There was no clear evidence of direct interactions between the glucosamine moiety of chi and HP- β -CD in the solid-state according to Raman spectral imaging with the dye probe method. The combined complementary results herein account for the fiber formation process as the role of weak host-guest supramolecular interactions that arise from the formation of an interfacial association complex.

In turn, the ideology that the supramolecular assembly can be employed to facilitate the formation of chi electrospun nanofibrous materials, as discussed in this chapter, will pave the way to achieve Objective #3 of the thesis research (Chapter 6). Moreover, such controlled-release

supramolecular disassembly will contribute to the development of “smart coatings” that may utilize diverse types of chi polyelectrolyte complexes.

5.5 References

- (1) Kumar, M. N. V. R.; Muzzarelli, R. A. A.; Muzzarelli, C.; Sashiwa, H.; Domb, A. J. Chitosan Chemistry and Pharmaceutical Perspectives. *Chem. Rev.* **2004**, *104* (12), 6017–6084. <https://doi.org/10.1021/cr030441b>.
- (2) Kumar, M. N. V. R. A Review of Chitin and Chitosan Applications. *React. Funct. Polym.* **2000**, *46* (1), 1–27.
- (3) Dash, M.; Chiellini, F.; Ottenbrite, R. M.; Chiellini, E. Chitosan-A Versatile Semi-Synthetic Polymer in Biomedical Applications. *Prog. Polym. Sci.* **2011**, *36* (8), 981–1014. <https://doi.org/10.1016/j.progpolymsci.2011.02.001>.
- (4) Crini, G.; Badot, P.-M. Application of Chitosan, a Natural Aminopolysaccharide, for Dye Removal from Aqueous Solutions by Adsorption Processes Using Batch Studies: A Review of Recent Literature. *Prog. Polym. Sci.* **2008**, *33* (4), 399–447. <https://doi.org/10.1016/j.progpolymsci.2007.11.001>.
- (5) Naseri-Nosar, M.; Ziora, Z. M. Wound Dressings from Naturally-Occurring Polymers: A Review on Homopolysaccharide-Based Composites. *Carbohydr. Polym.* **2018**, *189*, 379–398. <https://doi.org/10.1016/j.carbpol.2018.02.003>.
- (6) Verma, D.; Katti, K. S.; Katti, D. R. Polyelectrolyte-Complex Nanostructured Fibrous Scaffolds for Tissue Engineering. *Mater. Sci. Eng. C* **2009**, *29* (7), 2079–2084. <https://doi.org/10.1016/j.msec.2009.04.006>.
- (7) Li, L.; Hsieh, Y. L. Chitosan Bicomponent Nanofibers and Nanoporous Fibers. *Carbohydr. Res.* **2006**, *341* (3), 374–381. <https://doi.org/10.1016/j.carres.2005.11.028>.
- (8) Muzzarelli, R. A. A.; Mehtedi, M. El; Mattioli-Belmonte, M. Emerging Biomedical Applications of Nano-Chitins and Nano-Chitosans Obtained via Advanced Eco-Friendly Technologies from Marine Resources. *Mar. Drugs* **2014**, *12* (11), 5468–5502.

<https://doi.org/10.3390/md12115468>.

- (9) Karimian, A.; Parsian, H.; Majidinia, M.; Rahimi, M.; Mir, S. M.; Samadi Kafil, H.; Shafiei-Irannejad, V.; Kheyrollah, M.; Ostadi, H.; Yousefi, B. Nanocrystalline Cellulose: Preparation, Physicochemical Properties, and Applications in Drug Delivery Systems. *Int. J. Biol. Macromol.* **2019**, *133*, 850–859. <https://doi.org/10.1016/j.ijbiomac.2019.04.117>.
- (10) Aranday-Garcia, R.; Saimoto, H.; Shirai, K.; Ifuku, S. Chitin Biological Extraction from Shrimp Wastes and Its Fibrillation for Elastic Nanofiber Sheets Preparation. *Carbohydr. Polym.* **2019**, *213*, 112–120. <https://doi.org/10.1016/j.carbpol.2019.02.083>.
- (11) Jamshidifard, S.; Koushkbaghi, S.; Hosseini, S.; Rezaei, S.; Karamipour, A.; Jafari rad, A.; Irani, M. Incorporation of UiO-66-NH₂ MOF into the PAN/Chitosan Nanofibers for Adsorption and Membrane Filtration of Pb(II), Cd(II) and Cr(VI) Ions from Aqueous Solutions. *J. Hazard. Mater.* **2019**, *368*, 10–20. <https://doi.org/10.1016/j.jhazmat.2019.01.024>.
- (12) Bhattarai, N.; Edmondson, D.; Veis, O.; Matsen, F. A.; Zhang, M. Q. Electrospun Chitosan-Based Nanofibers and Their Cellular Compatibility. *Biomaterials* **2005**, *26* (31), 6176–6184. <https://doi.org/10.1016/j.biomaterials.2005.03.027>.
- (13) Jayakumar, R.; Prabakaran, M.; Nair, S. V.; Tamura, H. Novel Chitin and Chitosan Nanofibers in Biomedical Applications. *Biotechnol. Adv.* **2010**, *28* (1), 142–150. <https://doi.org/10.1016/j.biotechadv.2009.11.001>.
- (14) Min, B.-M.; Lee, S. W.; Lim, J. N.; You, Y.; Lee, T. S.; Kang, P. H.; Park, W. H. Chitin and Chitosan Nanofibers: Electrospinning of Chitin and Deacetylation of Chitin Nanofibers. *Polymer (Guildf)*. **2004**, *45* (21), 7137–7142. <https://doi.org/10.1016/j.polymer.2004.08.048>.
- (15) Li, L.; Li, Y.; Cao, L.; Yang, C. Enhanced Chromium (VI) Adsorption Using Nanosized Chitosan Fibers Tailored by Electrospinning. *Carbohydr. Polym.* **2015**, *125*, 206–213. <https://doi.org/10.1016/j.carbpol.2015.02.037>.
- (16) Habiba, U.; Siddique, T. A.; Talebian, S.; Lee, J. J. L.; Salleh, A.; Ang, B. C.; Afifi, A. M. Effect of Deacetylation on Property of Electrospun Chitosan/PVA Nanofibrous Membrane

- and Removal of Methyl Orange, Fe(III) and Cr(VI) Ions. *Carbohydr. Polym.* **2017**, *177*, 32–39. <https://doi.org/10.1016/J.CARBPOL.2017.08.115>.
- (17) Yihan, W.; Minato, W. Nanofiber Fabrication Techniques and Its Applicability to Chitosan. *Prog. Chem.* **2014**, *26* (11), 1821–1831. <https://doi.org/10.7536/PC140636>.
 - (18) Megelski, S.; Stephens, J. S.; Bruce Chase, D.; Rabolt, J. F. Micro- and Nanostructured Surface Morphology on Electrospun Polymer Fibers. *Macromolecules* **2002**, *35* (22), 8456–8466. <https://doi.org/10.1021/ma020444a>.
 - (19) Casasola, R.; Thomas, N. L.; Trybala, A.; Georgiadou, S. Electrospun Poly Lactic Acid (PLA) Fibres: Effect of Different Solvent Systems on Fibre Morphology and Diameter. *Polymer (Guildf)*. **2014**, *55* (18), 4728–4737. <https://doi.org/10.1016/j.polymer.2014.06.032>.
 - (20) Khil, M. S.; Cha, D. I.; Kim, H. Y.; Kim, I. S.; Bhattarai, N. Electrospun Nanofibrous Polyurethane Membrane as Wound Dressing. *J. Biomed. Mater. Res. Part B-Applied Biomater.* **2003**, *67B* (2), 675–679. <https://doi.org/10.1002/jbm.b.10058>.
 - (21) Zhao, X.; Chen, S.; Lin, Z.; Du, C. Reactive Electrospinning of Composite Nanofibers of Carboxymethyl Chitosan Cross-Linked by Alginate Dialdehyde with the Aid of Polyethylene Oxide. *Carbohydr. Polym.* **2016**, *148*, 98–106. <https://doi.org/10.1016/j.carbpol.2016.04.051>.
 - (22) Elsabee, M. Z.; Naguib, H. F.; Morsi, R. E. Chitosan Based Nanofibers, Review. *Mater. Sci. Eng. C* **2012**, *32* (7), 1711–1726. <https://doi.org/10.1016/j.msec.2012.05.009>.
 - (23) Chang, J.-J.; Lee, Y.-H.; Wu, M.-H.; Yang, M.-C.; Chien, C.-T. Preparation of Electrospun Alginate Fibers with Chitosan Sheath. *Carbohydr. Polym.* **2012**, *87* (3), 2357–2361. <https://doi.org/10.1016/j.carbpol.2011.10.054>.
 - (24) Ma, G.; Liu, Y.; Peng, C.; Fang, D.; He, B.; Nie, J. Paclitaxel Loaded Electrospun Porous Nanofibers as Mat Potential Application for Chemotherapy against Prostate Cancer. *Carbohydr. Polym.* **2011**, *86* (2), 505–512. <https://doi.org/10.1016/j.carbpol.2011.04.082>.
 - (25) Haider, S.; Al-Zeghayer, Y.; Ali, F. A. A.; Haider, A.; Mahmood, A.; Al-Masry, W. A.;

- Imran, M.; Aijaz, M. O. Highly Aligned Narrow Diameter Chitosan Electrospun Nanofibers. *J. Polym. Res.* **2013**, *20* (4), 105. <https://doi.org/10.1007/s10965-013-0105-9>.
- (26) Wu, C.; Su, H.; Tang, S.; Bumgardner, J. D. The Stabilization of Electrospun Chitosan Nanofibers by Reversible Acylation. *Cellulose* **2014**, *21* (4), 2549–2556. <https://doi.org/10.1007/s10570-014-0306-3>.
- (27) Jia, Y. T.; Gong, J.; Gu, X. H.; Kim, H. Y.; Dong, J.; Shen, X. Y. Fabrication and Characterization of Poly (Vinyl Alcohol)/Chitosan Blend Nanofibers Produced by Electrospinning Method. *Carbohydr. Polym.* **2007**, *67* (3), 403–409. <https://doi.org/10.1016/j.carbpol.2006.06.010>.
- (28) Burns, N. A.; Burroughs, M. C.; Gracz, H.; Pritchard, C. Q.; Brozena, A. H.; Willoughby, J.; Khan, S. A. Cyclodextrin Facilitated Electrospun Chitosan Nanofibers. *RSC Adv.* **2015**, *5* (10), 7131–7137. <https://doi.org/10.1039/c4ra09662b>.
- (29) Wilson, L. D.; Verrall, R. E. A Volumetric and NMR Study of Cyclodextrin-Inhalation Anesthetic Complexes in Aqueous Solutions. *Can. J. Chem.* **2015**, *93* (8), 815–821. <https://doi.org/10.1139/cjc-2014-0549>.
- (30) Skrepleva, I. Y.; Voloshenko, G. I.; Librovich, N. B.; Maiorov, V. D.; Vishnetskaya, M. V.; Mel'nikov, M. Y. Infrared Spectroscopic Studies on Interactions in Trifluoroacetic Acid-Sulfur Dioxide Systems. *Moscow Univ. Chem. Bull.* **2011**, *66* (4), 232–234. <https://doi.org/10.3103/S0027131411040080>.
- (31) Valenti, L. E.; Paci, M. B.; De Pauli, C. P.; Giacomelli, C. E. Infrared Study of Trifluoroacetic Acid Unpurified Synthetic Peptides in Aqueous Solution: Trifluoroacetic Acid Removal and Band Assignment. *Anal. Biochem.* **2011**, *410* (1), 118–123. <https://doi.org/10.1016/j.ab.2010.11.006>.
- (32) Fuson, N.; Josien, M. L.; Jones, E. A.; Lawson, J. R. Infrared and Raman Spectroscopy Studies of Light and Heavy Trifluoroacetic Acids. *J. Chem. Phys.* **1952**, *20* (10), 1627–1634. <https://doi.org/10.1063/1.1700229>.
- (33) Redington, R. L.; Lin, K. C. Infrared Spectra of Trifluoroacetic Acid and Trifluoroacetic Anhydride. *Spectrochim. Acta Part A Mol. Spectrosc.* **1971**, *27* (12), 2445–2460.

[https://doi.org/10.1016/0584-8539\(71\)80143-5](https://doi.org/10.1016/0584-8539(71)80143-5).

- (34) Xue, C.; Wilson, L. D. A Structural Study of Self-Assembled Chitosan-Based Sponge Materials. *Carbohydr. Polym.* **2019**, *206*, 685–693.
<https://doi.org/10.1016/j.carbpol.2018.10.111>.
- (35) Sun, W.; Chen, G.; Wang, F.; Qin, Y.; Wang, Z.; Nie, J.; Ma, G. Polyelectrolyte-Complex Multilayer Membrane with Gradient Porous Structure Based on Natural Polymers for Wound Care. *Carbohydr. Polym.* **2018**, *181*, 183–190.
<https://doi.org/10.1016/J.CARBPOL.2017.10.068>.
- (36) Kasaai, M. The Use of Various Types of NMR and IR Spectroscopy for Structural Characterization of Chitin and Chitosan. In *Chitin, Chitosan, Oligosaccharides and Their Derivatives*; CRC Press, 2010; pp 149–170. <https://doi.org/10.1201/EBK1439816035-c12>.
- (37) Mosiadz, M.; Juda, K. L.; Hopkins, S. C.; Soloduch, J.; Glowacki, B. A. An In-Depth in Situ IR Study of the Thermal Decomposition of Yttrium Trifluoroacetate Hydrate. *J. Therm. Anal. Calorim.* **2012**, *107* (2), 681–691. <https://doi.org/10.1007/s10973-011-1772-6>.
- (38) Robinson, R. E.; Taylor, R. C. Raman Spectrum and Vibrational Assignments for the Trifluoroacetate Ion. *Spectrochim. Acta* **1962**, *18* (4), 1093–1095.
[https://doi.org/10.1016/S0371-1951\(62\)80225-2](https://doi.org/10.1016/S0371-1951(62)80225-2).
- (39) Frech, R.; Chintapalli, S.; Bruce, P. G.; Vincent, C. A. Crystalline and Amorphous Phases in the Poly(Ethylene Oxide)–LiCF₃SO₃ System. *Macromolecules* **1999**, *32* (3), 808–813.
<https://doi.org/10.1021/ma9812682>.
- (40) Egyed, O. Spectroscopic Studies on β -Cyclodextrin. *Anal. Chim. Acta* **1990**, *240* (2), 225–227. [https://doi.org/10.1016/0924-2031\(90\)80041-2](https://doi.org/10.1016/0924-2031(90)80041-2).
- (41) Li, W.; Lu, B.; Chen, F.; Yang, F.; Wang, Z. Host-Guest Complex of Cypermethrin with β -Cyclodextrin: A Spectroscopy and Theoretical Investigation. *J. Mol. Struct.* **2011**, *990* (1–3), 244–252. <https://doi.org/10.1016/j.molstruc.2011.01.053>.
- (42) De Oliveira, V. E.; Almeida, E. W. C.; Castro, H. V.; Edwards, H. G. M.; Dos Santos, H.

- F.; De Oliveira, L. F. C. Carotenoids and β -Cyclodextrin Inclusion Complexes: Raman Spectroscopy and Theoretical Investigation. *J. Phys. Chem. A* **2011**, *115* (30), 8511–8519. <https://doi.org/10.1021/jp2028142>.
- (43) Vanamudan, A.; Pamidimukkala, P. Chitosan, Nanoclay and Chitosan-Nanoclay Composite as Adsorbents for Rhodamine-6G and the Resulting Optical Properties. *Int. J. Biol. Macromol.* **2015**, *74*, 127–135. <https://doi.org/10.1016/j.ijbiomac.2014.11.009>.
- (44) Serra-Gómez, R.; Tardajos, G.; González-Benito, J.; González-Gaitano, G. Rhodamine Solid Complexes as Fluorescence Probes to Monitor the Dispersion of Cyclodextrins in Polymeric Nanocomposites. *Dye. Pigment.* **2012**, *94* (3), 427–436. <https://doi.org/10.1016/j.dyepig.2012.02.009>.
- (45) Bakkialakshmi, S.; Menaka, T. A Study of the Interaction between Rhodamine 6g and Hydroxy Propyl β -Cyclodextrin by Steady State Fluorescence. *Spectrochim. Acta - Part A Mol. Biomol. Spectrosc.* **2011**, *81* (1), 8–13. <https://doi.org/10.1016/j.saa.2011.04.082>.
- (46) Dieringer, J. A.; Wustholz, K. L.; Masiello, D. J.; Camden, J. P.; Kleinman, S. L.; Schatz, G. C.; Van Duyne, R. P. Surface-Enhanced Raman Excitation Spectroscopy of a Single Rhodamine 6G Molecule. *J. Am. Chem. Soc.* **2009**, *131* (2), 849–854. <https://doi.org/10.1021/ja8080154>.
- (47) Black, P. N.; He, X. N.; Zhou, Y. S.; Mahjouri-Samani, M.; Mitchell, M.; Gao, Y.; Allen, J.; Lu, Y. F.; Xiong, W.; Jiang, L. Surface-Enhanced Raman Spectroscopy Using Gold-Coated Horizontally Aligned Carbon Nanotubes. *Nanotechnology* **2012**, *23* (20), 205702. <https://doi.org/10.1088/0957-4484/23/20/205702>.

CHAPTER 6

Preparation and characterization of grafted chitosan electrospun fibers

Xue, C.; Wilson, L. D. Preparation and Characterization of Grafted Chitosan Composite Porous Electrospun Fibers. *Carbohydr. Polym.* **2021**. (under review).

Author's contribution

Chen Xue performed all the experimental work (i.e., data analysis, data curation, visualization, formal analysis, etc.), wrote the first draft of the manuscript, and made further revisions with the supervisor to reach the final draft stage. Dr. L.D. Wilson was responsible for the project supervision, editorial guidance for revising the manuscript drafts, and role as the corresponding author.

Description

The original manuscript was reformatted to meet the requirements of the College of Graduate and Postdoctoral Studies (CGPS) at the University of Saskatchewan, along with formulating the published work into a comprehensive thesis document. Specifically, the introduction and conclusion section of the original manuscript was revised to avoid unnecessary repetition. As general details of routine characterization methods are introduced in Chapter 3, the experimental section is modified accordingly in which only specific details are included. The reference style of the original paper was changed to the CGPS thesis' style. The supplementary information for this manuscript is included in Appendix.

This research builds upon the results from previous chapters (i.e., the results from Chapters 4 and 5 provided support for Hypothesis #3 and Hypothesis #4, respectively), targeting on fulfilling Objective #3 of the thesis as mentioned in Section 1.4 in four aspects. Firstly, grafted chi was synthesized, followed by the preparation of novel grafted chi electrospun fibers with LMw PEO. Secondly, a structural characterization study of the electrospun fibers was conducted to understand the interactions between the grafted chi and LMw PEO. Thirdly, porous chi nanofibrous materials were prepared through physical processes. Lastly, the dye uptake properties of prepared electrospun nanofibrous materials are discussed in this chapter.

6.1 Introduction

As mentioned in Chapter 1, the development of unique chi electrospun nanofibrous materials for water treatment and biomedical applications is of great interest because of their high porosity and high surface area.¹⁻⁴ Despite the advantages of biopolymer-based electrospun nanofibers, chi in its native form is a challenging biomaterial for electrospinning due to its polycationic nature. As discussed in Chapter 2, the protonated form of chi displays strong electrostatic repulsion between polymer chains, which results in significantly reduced chain entanglement for effective electrospinning.⁵⁻⁸ Therefore, PEO was used to assist the production of chi electrospun nanofibers. Since many applications of chi electrospun nanofibers usually involve aqueous media, the uncontrolled dissolution of the water-soluble component such as PEO negatively impacts the materials' performance and integrity. In order to overcome this challenge, PEO is removed in a controlled manner after the formation of such electrospun fibers.^{2,3}

Previous studies revealed that PEO might function as a sacrificial template to create porous features on the fiber surface *via* the post-treatment method introduced in Chapter 1⁹⁻¹¹, which was also supported by the result from Chapter 4. The concept of PEO as a sacrificial template is extended to the chi/PEO electrospun fiber system to prepare a porous chi electrospun fiber when PEO could form a dispersed phase in the chi electrospun nanofiber. As discussed in Chapter 1, a relatively low molecular weight PEO ($M_w \leq 100$ kDa) might be necessary for forming a dispersed phase in the nanofiber.¹²

Generally, PEO with a molecular weight above 400 kDa (HMw PEO) has been employed as an additive to aid in the formation of chi electrospun fibers, whereas PEO with a molecular weight below 400 kDa (LMw PEO) is considered unsuitable to aid in the formation of such fibers. The difficulty with LMw PEO relates to the weak PEO-PEO chain entanglement, which prevents the formation of electrospun fibers, in contrast to the greater PEO-PEO chain entanglement of HMw PEO.^{8,13} Hence, there is a limitation on the use of low molecular weight PEO as an additive to promote the chi electrospun nanofiber formation. The importance of supramolecular interactions to facilitate the electrospinning of low molecular weight polymers has recently been recognized.¹⁴ This approach may be worthy of further investigation to develop a chi/LMw PEO electrospun fiber system by establishing the supramolecular interactions between chi and PEO. Such supramolecular interactions can be achieved indirectly by grafting chi with small arene units because, as mentioned

in Section 2.5.2, PEO can form supramolecular complexes with aromatic compounds by hydrogen bonding and CH- π interactions.^{15–17} Consequently, chi and LMw PEO could form supramolecular assembly through grafted arene units. Salicylic acid is a potential moiety for grafting onto chi since grafted salicylic acid alters the solubility profile of chi and may impart additional effects to the nanofibers for fiber-based wound dressings such as anti-inflammatory properties.¹⁸ Moreover, controlled-release of salicylic acid for seed coating materials that consist of chi-based nanofibers could provide cold weather acclimatization effects for certain crops.¹⁹

The purpose of this research is to complete Objective #3 through four short-term goals. The first short-term goal relates to the synthesis of salicylic acid grafted chi and the preparation of electrospun fibers from solutions of grafted chi with LMw PEO ($M_w \approx 100$ kDa). The second short-term goal is to carry out a structural characterization study of the electrospun fibers to ascertain the interactions between the grafted chi and PEO. The third short-term goal is to prepare a porous chi fiber using a physical method in which the grafted chi/PEO electrospun fiber is treated thermally, followed by the controlled removal of PEO with the solvent. The fourth short-term goal is to investigate different uptake properties of chi electrospun fibers prepared in this study towards methylene blue (MB) to demonstrate the effects of salicylic acid and the addition of porous features on chi-based materials. This study will address the above objectives, where the use of salicylic acid grafted chi represents a *first example* of a report for such a chi-based fiber system in the literature. The use of PEO as a sacrificial template is shown to yield microporous fibers that build upon previous work for self-assembled fiber systems. These innovative contributions are envisaged to expand the field of application for chi-based electrospun fibers that span diverse applications relevant to adsorption-desorption phenomena from advanced water treatment to biomedical devices that employ controlled-release systems.

6.2 Materials and Methods

6.2.1 Materials

Low molecular weight (LMW) chi was obtained from Sigma-Aldrich Canada Ltd. (Oakville, ON.) with 75–80% deacetylation, Brookfield viscosity 20 cPs, with a range of molecular weights (50–190 kDa). Polyethylene oxide (PEO) with $M_w \approx 100,000$ was acquired from Sigma-Aldrich Canada Ltd. (Oakville, ON.). Acetic acid, ammonia, iso-propanol, NaOH, NaCl, salicylic acid, and NaHCO_3 were obtained from EMD (Edmonton, Canada). Deuterium oxide (D_2O , 99%)

was obtained from Cambridge Isotope Laboratories Inc. All other chemicals were purchased from Sigma-Aldrich (Oakville, ON, Canada) and were used as received. All aqueous solutions were prepared by using distilled and deionized water.

6.2.2 Deacetylation of chitosan (Dachi)

Chi (5 g) was dispersed in 40 mL of NaOH solution (1.25 M). The mixture was heated at 90 °C with continuous stirring for 2 h. Then, the resulting mixture was left to dry in an oven at 60 °C overnight. The product was thoroughly washed with distilled water until pH of the filtrate was neutral (pH = 7). The final product was dried in an oven at 60 °C for 48 h and stored until further use. The estimated degree of deacetylation (ca. 95%) was obtained by ¹H NMR spectral analysis.²⁰ The viscosity-average molecular weight of Dachi (120 kDa) was determined with the use of the Mark-Houwink equation, $[\eta] = K \overline{M}_\eta^\alpha$, where $K = 1.81 \times 10^{-6}$ L/g and $\alpha = 0.93$, based on estimates of the intrinsic viscosity $[\eta]$ measured in 0.2 M NaCl and 0.1 M acetic acid solution at 25 °C.^{21,22}

6.2.3 Synthesis of salicylic acid grafted Dachi

The experimental procedure for the synthesis of grafted chi was adapted and modified based on reports by Khalafi-Nezhad et al. and Hussain et al.^{23–25} 1 g of Dachi and a requisite amount of salicylic acid (Sal, 0.25 equiv. and 0.5 equiv. relative to a mole of glucosamine unit in Dachi) and 4-toluenesulfonyl chloride were well mixed in a 10 mL beaker. Triethyl amine (4 equiv.) was added to the mixture. The mixture was continuously stirred for 1 h. The resulting mixture was suspended in 3% w/w NaHCO₃ solution (200 mL) and stirred overnight. The settled product was collected by vacuum filtration and washed thoroughly with deionized and distilled water (400 mL). Then, the product was washed with diethyl ether (50 mL). Finally, the product was dried in an oven at 60 °C for further use. The products are referred to as DachiSal-1 and DachiSal-2 that corresponds to the amount of salicylic acid used (0.25 equiv. and 0.5 equiv. per mole of glucosamine unit in Dachi, respectively).

6.2.4 Preparation of polymer solutions for electrospinning and corresponding electrospun nanofibers

0.24 g of Dachi and DachiSal (-1 and -2, respectively) and 0.12 g of PEO was dissolved in 4 mL of 3.8% v/v acetic acid/50% v/v iso-propanol/deionized and distilled water.

Chi-based electrospun nanofibrous materials were formed using prepared polymer solutions, as described in Section 3.2. After electrospinning, the resulting fibers were placed in a chamber filled with ammonia vapor to neutralize the protonated amine groups of chi.

6.2.5 Preparation of porous fibers *via* physical processes

DachiSal-2/PEO electrospun fiber was gradually heated from room temperature (22 °C) to 120 °C under N₂ gas, followed by slow cooling down to 70 °C in 1 h. The heated electrospun fiber was placed in the liquid N₂ for 30 mins. Subsequently, the treated fiber was imbibed in acetonitrile for 48 h under quiescent conditions to remove polyethylene oxide. Then, the fiber was air-dried under ambient conditions.

6.3 Materials Characterization

The viscosity of the polymer solutions prepared at variable total polymer concentration was determined using a rheometer (AR G2, TA Instruments, Montreal, QC, Canada) equipped with a parallel-plate geometry (40 mm, 500 μ m gap) as a function of shear rate in the range 0.01–100 s⁻¹ at 25 °C. The solutions were delivered by the syringe pump, as described in Section 3.2, and the shear rate generated in the syringe was estimated to be 80 s⁻¹, according to the Poiseuille equation.²⁶ Therefore, the solution (η) viscosity at a 80 s⁻¹ shear rate was used to calculate specific viscosity (η_{sp}), assuming that polymer solutions behave as a Newtonian fluid beyond 80 s⁻¹ shear rate.

FT-IR (*cf.* Section 3.1.1) and Raman spectra (*cf.* Section 3.1.7) of the precursors, grafted chi, and the resulting electrospun fibers were obtained. ¹³C solid-state NMR spectra were obtained with a Bruker AVANCE III HD spectrometer equipped with a 4 mm DOTY CP-MAS (cross-polarization with magic angle spinning) solids probe operating at 125.77 MHz (¹H spectral frequency at 500.23 MHz). ¹³C CP-MAS spectra were acquired at a spinning speed of 7.5 kHz, a ¹H 90° pulse of 5 μ s with a contact time of 2 ms along with a ramp pulse on the ¹H channel, and 20k accumulated scans with a recycle delay of 2s. ¹³C MAS NMR spectra were obtained with ¹H decoupling at a spinning speed of 10 kHz with 10k accumulated scans, and a recycle delay of 20s.

SEM images (*cf.* Section 3.1.5) of all samples at various magnifications were acquired. An analysis of the surface component distribution was studied using Raman spectral imaging (*cf.* Section 3.1.8) with a 12 s exposure time under a static scan mode with a spectral range of 1330-

1672 cm^{-1} and 1434-1769 cm^{-1} for the Dachí sample and its grafted form, respectively. The Z score maps were created using a standard distribution normalized spectral intensity (relative to baseline) ratio between the PEO signature (1478 cm^{-1}) and a chi related signature (1377 cm^{-1} and 1606 cm^{-1} for the original Dachí electrospun fiber and grafted Dachí electrospun fibers, respectively) to indicate the surface component distribution of electrospun fibers. The morphology of the electrospun fibers was investigated using TEM (Hitachi HT-7700 microscope) images obtained at an accelerating voltage of 100 kV. For the measurement of TEM images, a fiber sample was dispersed in aqueous ethanol solution using an ultrasonic bath, where a drop of the suspension was put onto the holey carbon-coated copper grids. Samples were air-dried and rinsed with distilled and deionized water before imaging.

An aqueous (90% D_2O /10% H_2O) dye solution was prepared, containing methylene blue (MB, 50 μM). A fixed amount (ca. 0.45 mg) of electrospun fiber was placed on an aluminum foil in a glass petri dish with quartz cover and 20 μL of MB solution was layered over the fiber. *In-situ* Raman spectra of the MB droplet in the range of 1500-2700 cm^{-1} was collected every 10 mins for 2 h to track the change of MB concentration over time using a 785 nm solid-state diode laser with a 1200 lines/mm grating system. *In-situ* Raman spectra of an MB droplet (without fiber) was layered onto aluminum foil and measured over the same period as a control sample.

6.4 Results and Discussion

As described above, modified chi was synthesized by grafting salicylic acid onto chi. Various chi/LMw PEO electrospun nanofibers were prepared. A uniform chitosan/LMw PEO electrospun fiber was successfully prepared using modified chi, and the porous chi electrospun fiber was also prepared by a unique template method. In order to understand the mechanism of the formation of such electrospun fiber, fluid properties of polymer solutions were measured by rheology. The corresponding electrospun fibers were characterized by spectroscopic methods (IR, SEM, and Raman spectroscopy), as described in the sections below.

6.4.1 Characterization of salicylic acid grafted Dachí (DachíSal)

Solid-state ^{13}C NMR spectra are displayed in **Panel I** of Figure 6.1. Compared to Dachí, a new signature with a chemical shift near 162 ppm relates to phenyl carbon (2) of salicylic acid and another signature at 149 ppm that corresponds to the phenyl carbon (1) moiety of salicylsalicylic acid. The latter signature indicates that self-reaction of salicylic acid occurred. Based on the solid-

state ^{13}C MAS NMR spectrum of DachSal-2, two additional NMR lines at 166.5 ppm and 169.1 ppm corresponds to the carbonyl group (a) and the carbonyl group (b), respectively.^{24,27} FT-IR spectra of salicylic acid grafted onto Dach are shown in **Panel II** of Figure 6.1. A new band at 1745 cm^{-1} for grafted Dach corresponds to the carbonyl groups (a) conjugated to chi *via* an ester bond.^{24,25,27} The shoulder at 1726 cm^{-1} represents carbonyl groups (b), which is a conjugated form of salicylic acid due to self-esterification. The presence of two different carbonyl groups in the FT-IR spectra is complementary to the solid-state NMR results. The FT-IR spectrum of salicylic acid is shown in Figure A6.1 of Appendix. A characteristic IR band at 1650 cm^{-1} for the carboxylic groups of salicylic acid is not observed for both DachSal-1 and -2, which suggests no free salicylic acid group in the product as there is no apparent signature for a free carboxylic group. Comparing DachSal-1 with DachSal-2, an increase of the spectral intensity of the IR band at 1745 cm^{-1} indicates that the degree of substitution for DachSal-2 is greater than that of DachSal-1. Amidation of Dach was not observed as there is no increase of the secondary amide N-H in-plane bending band near 1525 cm^{-1} .²⁸

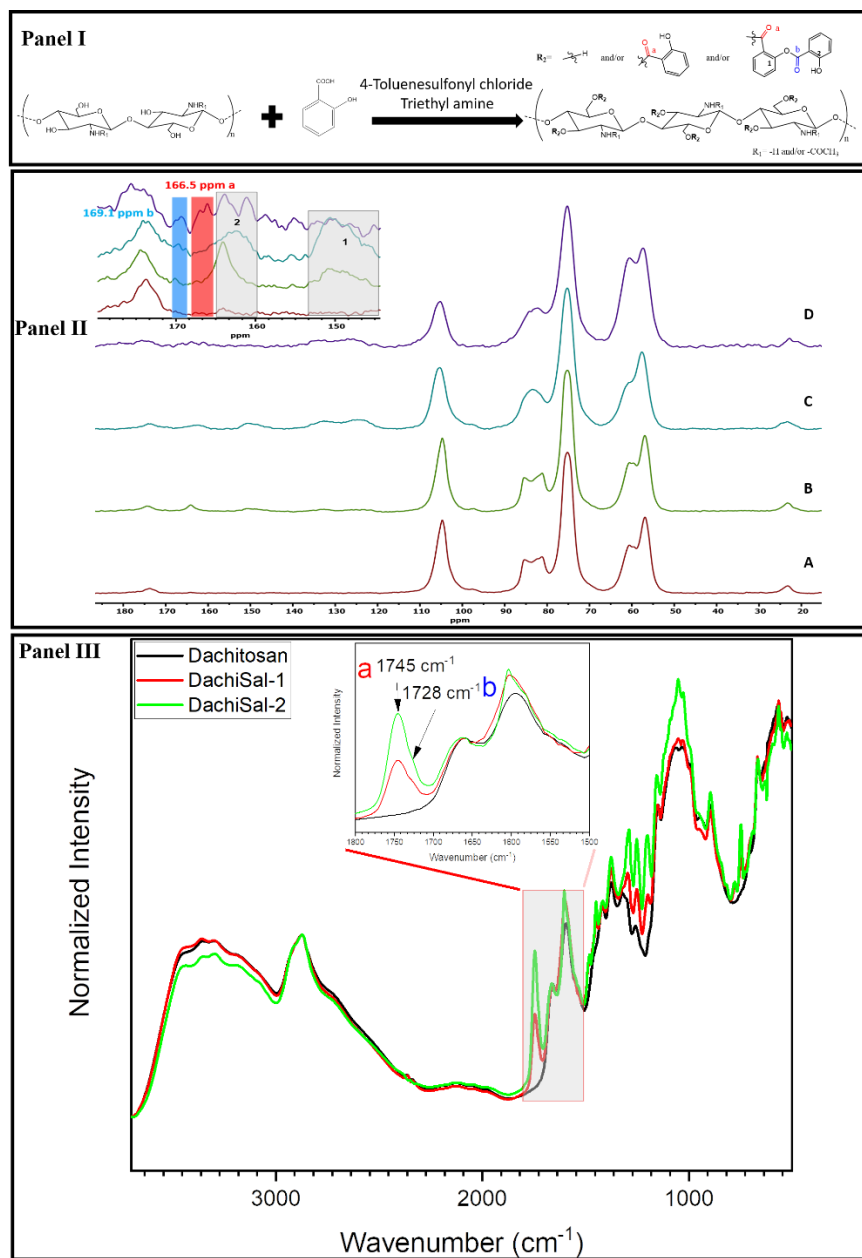


Figure 6.1. Reaction scheme for the synthesis of salicylic acid grafted chi. **Panel I:** Solid-state ^{13}C CP-MAS NMR spectra of Dachitosan (A), DachiSal-1 (B), DachiSal-2 (C), and ^{13}C MAS NMR spectrum of DachiSal-2 (D). The inset graph is an expansion of the original spectra from 145 ppm to 175 ppm. Red region and blue region indicate carbonyl group (a) and carbonyl group (b), respectively. **Panel II:** FT-IR spectra of Dachitosan, DachiSal-1, and DachiSal-2. The inset of the IR spectral region highlights 1800 to 1500 cm^{-1} spectrum.

6.4.2 SEM and surface component distribution of electrospun fibers

In order to study the effect of different levels of salicylic acid grafted onto chi and the morphology of the electrospun fibers, SEM images of Dach/PEO and grafted Dach/PEO were obtained. An estimation of the surface component distribution using Raman spectral analysis was carried out to provide complementary structural information of the chemical groups of the materials that are not accessible for typical SEM imaging results. Raman microimaging was used to gain further molecular-level insight into the materials' composition.^{9,29,30}

The morphology and surface component distribution of Dach/PEO and grafted Dach/PEO electrospun fibers and properties of the polymer solutions were studied using Raman spectral imaging of selected spectral bands, according to a previously reported method.⁹ In Figure 6.2, SEM images of Dach/PEO, DachSal-1/PEO, and DachSal-2/PEO electrospun fibers are shown in panels I, II, and III, respectively. Dach/PEO fibers contain nanofibers, beads, and films, in agreement with the morphology of chi/PEO electrospun fiber prepared using PEO with molecular weight lower than 400 kDa in the literature.^{8,31} Films were not observed in grafted Dach materials. For DachSal-1/PEO fibers, microfibers, beads, and nanofibers were observed. DachSal-2/PEO fibers, the most uniform sample, possess nanofibers and evidence of bead-like structures. The surface component distributions of the two components were studied using Raman imaging, where previous studies indicate that such spectral imaging serves as a powerful tool for the study of the component distribution of multicomponent systems.^{9,30} The data of the peak intensity (a) divided by the peak intensity (b) is assumed to follow a normal standard distribution, which is then normalized to obtain a Z score. The resulting Z score will be zero, shown as denoted by a yellow colored region on the map for the homogenous system. As the Z score deviates from zero, the system appears more heterogeneous. A positive Z score indicates a PEO rich region (white and red color), and the negative score indicates a Dach rich domain (black and green color). Thus, the Z score map shown in Figure 6.2 for panels I, II, and III, is constructed using the data to visualize the distribution of two components: chi (Dach and grafted Dach) and PEO.

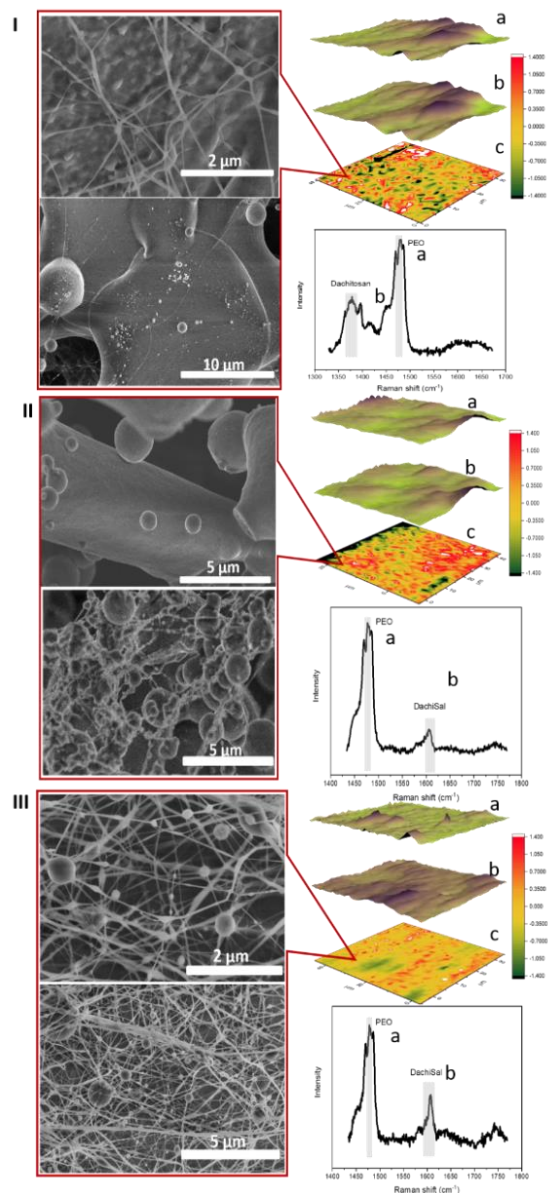


Figure 6.2. SEM images and surface distributions of different electrospun fibers: Dachi/PEO Panel (I), DachiSal-1/PEO Panel (II), and DachiSal-2/PEO Panel (III). Each panel contains the SEM and Raman images (a and b) generated by the Raman spectral intensity of the PEO peak (a) and Dachi (b), and the Z score map (c) constructed by dividing the intensity of PEO peak (a) by that of chi related peak (b). Colour scale for Z score map: white represents $z > 1.40$, red represents $0.30 < z < 1.40$, yellow represents $-0.30 < z < 0.30$, green represents $-1.40 < z < -0.30$, and black represents $z < -1.40$.

For the case of Dachi/PEO and DachiSal-1/PEO fibers, chi and PEO are not distributed homogeneously among the materials, as evidenced by a few yellow regions on the map. DachiSal-2/PEO fibers are among the most homogeneous material seen by a large area of yellow and lighter colors of red and green, as displayed on the Z score map. Overall, the morphology and component distribution of electrospun fibers depends on the relative amount of salicylic acid conjugated with Dachi.

6.4.3 Characterization of prepared polymer solutions

The viscosity of different polymer concentrations of polymer solutions as a function of shear rate was measured as shown in Figure 6.3 A-C. Dachi/PEO solution shows shear thinning behavior, while DachiSal-1/PEO and DachiSal-2/PEO solution shows yield stress behavior. Different rheological behavior of the solutions demonstrates that Dachi/PEO and grafted Dachi/PEO solution deforms differently upon the applied stress, which suggests that microstructural features of Dachi/PEO and grafted Dachi/PEO solution are drastically distinct.³² Since a minimum 80 s^{-1} shear rate of the stress is applied to the solution during the electrospinning process to drive the solution to flow continuously, the specific viscosity (η_{sp}) of the solutions at this shear rate could be used to study the interaction between chi and PEO in the solution assuming the polymer solution behaves as a Newtonian fluid beyond this shear rate. The dependence of the specific viscosity (η_{sp}) on the total polymer concentration (C), along with the slopes, is shown in Figure 6.3D. The slope of this log-log plot represents the contribution of the polymer concentration to the viscosity. It is also known as a scaling value, as described in Chapter 2.^{33,34} Typically, for polyelectrolyte solutions, $\eta_{sp} \sim C^{1-2}$ stands for the semi-dilute disentangled regime and $\eta_{sp} \sim C^{4-5}$ represents the semi-dilute entangled regime.^{34,35} For the Dachi/PEO solution, $\eta_{sp} \sim C^{3.3}$ is close to the value reported in the literature for related polyelectrolyte polymer/PEO solutions.¹³ According to the results reported by Saquing et al. for an alginate/PEO electrospun fiber system,¹³ a scaling value of this magnitude indicates that there are no molecular interactions between chi and PEO, where chain entanglements are provided mainly by PEO because the scaling value of this system approaches that of a neutral polymer in a good solvent. Because the relatively low molecular weight PEO ($M_w \approx 100 \text{ kDa}$) provides insufficient chain entanglements to produce bead free fibers, Dachi/PEO electrospun fibers contain films and beads, and the two polymer components (Dachi and PEO) of the fibers are distributed unevenly among the materials according to SEM results and

the Z score map (*cf.* Figure 6.2 Panel I). After Dachi is grafted with salicylic acid, the scaling exponent for DachiSal-1/PEO and DachiSal-2 /PEO solution changes to $\eta_{sp} \sim C^{3.4}$ and $\eta_{sp} \sim C^{7.6}$, respectively. The scaling value of DachiSal-1/PEO solution is comparable to that of Dachi/PEO solution, but the DachiSal-2/PEO solution displays a greater scaling value. This scaling value indicates that DachiSal-1/PEO solution behaves similarly to Dachi/PEO solution as the number of salicylic acid groups grafted to Dachi for DachiSal-1 is low.

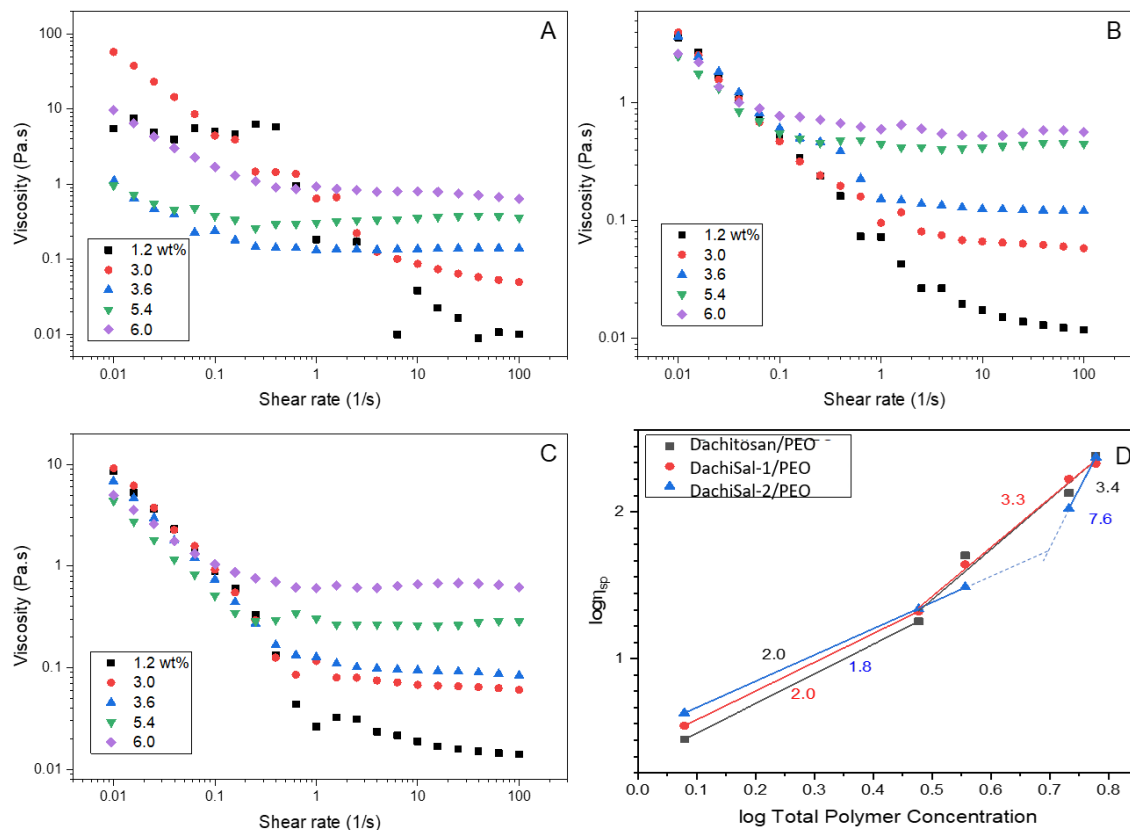


Figure 6.3. log-log plots of viscosity vs. shear rate of different total polymer concentration (1.2, 3, 3.6, 5.4, and 6 wt.%; where the ratio between chi and PEO remains at 2:1.) for various polymer solutions: Dachi/PEO (A), DachiSal-1/PEO (B), and DachiSal-2/PEO (C). Log-log Plot of specific viscosity (η_{sp}) at an 80 s^{-1} shear rate as a function of total polymer concentrations of electrospinning solutions (D). The slope, scaling value, is labeled beside the corresponding linear region.

Despite this, the appearance of microfibers instead of films in DachSal-1/PEO electrospun fibers may be due to slightly different microstructures or surface tension of the solutions. On the other hand, the solution behavior of the DachSal-2/PEO solution differs from Dach/PEO and DachSal-1/PEO solutions. The large scaling value was reported in the literature, attributed to an increase of intermolecular associations among the solutes.^{36–38} In the case of the DachSal-2/PEO solution, greater electrospinning performance was noted since there are more salicylic acid segments attached to Dach that favor the intermolecular interactions between the grafted Dach and PEO.

6.4.4 Characterization of electrospun nanofibers

To gain insight into the nature of the intermolecular interactions between Dach or grafted Dach with PEO, the FT-IR and Raman spectra of electrospun fibers for Dach and grafted Dach are shown in Figure 6.4. The IR spectra of electrospun fibers in the 1800 and 1500 cm^{-1} regions are similar to the polymer precursors prior to electrospinning. The comparable IR spectral features reveal negligible evidence of chemical change upon electrospinning of the components. The decrease of the IR spectral intensity of the signature out-of-plane bending band of the benzene ring at 750 cm^{-1} is evident for the FT-IR spectra of the electrospun fibers (Figure 6.4A), which may relate to the reduction of an out-of-plane bending motion of a benzene group after electrospinning. From the Raman spectra in Figure 6.4B, the bands located at 1038 cm^{-1} corresponding to C-O stretching for the original Dach³⁹ show a lower Raman spectral intensity than those for the grafted Dach because of the salicylic acid group of the grafted Dach.⁴⁰ Upon the formation of the PEO-blended electrospun fibers, the bands at 1038 cm^{-1} show an increase of spectral intensity due to PEO's addition. Moreover, these bands of the grafted Dach/PEO electrospun fiber display a sharper band shape than that of the original Dach/PEO electrospun fiber because there is an increased *tgg* conformation of PEO for the grafted Dach/PEO electrospun fiber, which provide the support that interactions occur between PEO and salicylic acid grafted units of Dach.⁴¹ Furthermore, the broadening of bands near 1090 cm^{-1} for the grafted Dach is also due to increased PEO's *gauche* conformation.^{41,42} The greater *gauche* conformational preference of PEO is induced by the aromatic ring's presence through hydrophobic interactions. In addition to the attenuated intensity for the out-of-plane bending band of the benzene ring in the FT-IR spectra, supramolecular interactions are inferred to occur between PEO and grafted chi, mainly through

the grafted salicylic acid groups. Pyranose ring breathing modes for chi occur near 993 cm^{-1} adopt a broader spectral appearance after blending with PEO.³⁹ The spectral broadening is inferred from changes in the dynamic motional constraint of the chi backbone. Such constraint is also supported by the shift of Dachi C-O-C bending at 1090 cm^{-1} to 1086 cm^{-1} for the original Dachi/PEO electrospun fiber and 1083 cm^{-1} for the grafted chi/PEO electrospun fiber. These results suggest that supramolecular assemblies are formed in the grafted Dachi/PEO electrospun fiber. Based on FT-IR results, the DachiSal-2/PEO system displays a more significant reduction of the intensity for the out-of-plane bending band of an aromatic ring with a higher proportion of *gauche* conformers of PEO with a more dynamic motional constraint of the chi backbone according to the Raman spectral results. It can be deduced that DachiSal-2/PEO electrospun fiber display more favourable supramolecular interactions over the DachiSal-1/PEO electrospun fiber system. Thus, supramolecular interactions play a vital role in the improved formation of the chi electrospun fibers with LMw PEO.

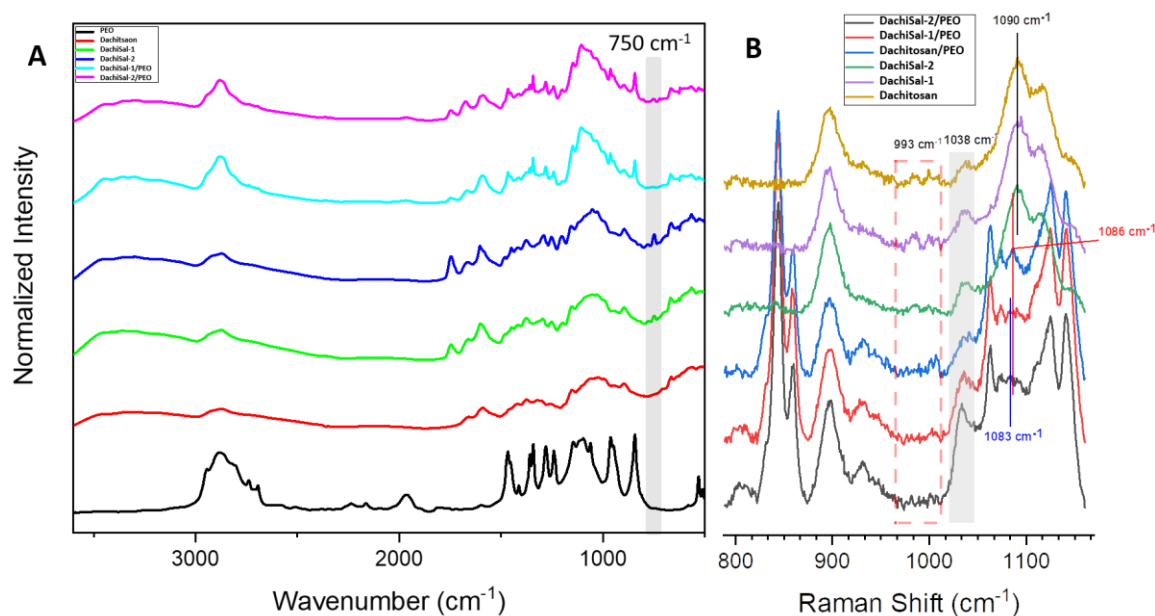


Figure 6.4. (A) FT-IR spectra of PEO, Dachi, grafted Dachi, and grafted Dachi/PEO electrospun fibers; (B) Raman spectra of Dachi, grafted Dachi, and their electrospun fibers.

6.4.5 Morphology of DachiSal-2/PEO electrospun fiber treated with physical processing

The DachiSal-2/PEO electrospun fiber was subjected to physical treatment to create porous surface features on the fiber. SEM and TEM images of electrospun fibers treated with and without physical processing are shown in Figure 6.5. In Fig. 6.5C-D, porous features can be observed on the fiber surface, confirming that LMw PEO as a sacrificial template for producing porous nanofibers is a suitable design strategy that builds upon the results presented in Chapters 4 and 5.

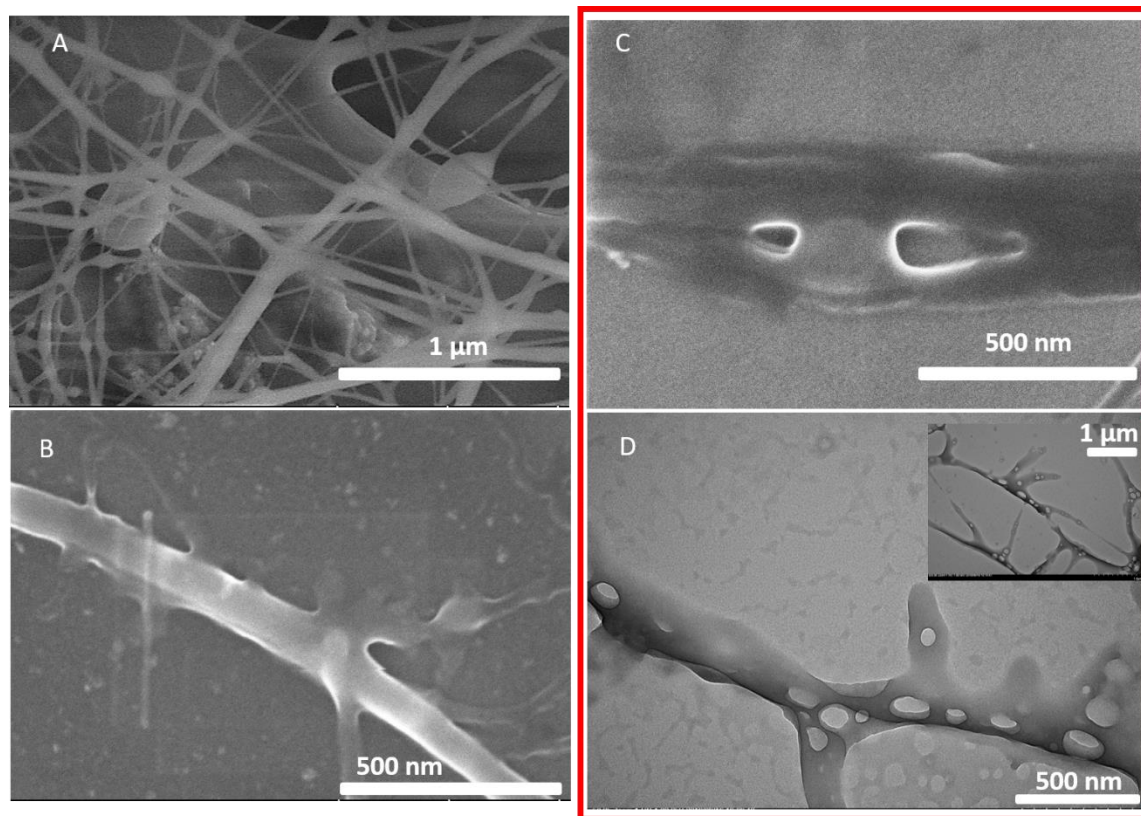


Figure 6.5. SEM images of DachiSal-2/PEO electrospun fiber after thermal treatment (A), DachiSal-2/PEO electrospun fiber **without** physical treatment after rinsing with water (B), and DachiSal-2/PEO electrospun fiber **with** physical treatment after rinsing with water (C). TEM images of DachiSal-2/PEO electrospun fiber **with** physical treatment after rinsing with water (D).

Furthermore, it also suggests that PEO with a lower molecular weight ($M_w = 100$ kDa; LMw PEO) is compartmentalized by the grafted salicylic acid as LMw PEO tends to bind with a single aromatic molecule rather than complexation with multiple aromatic molecules¹², which leads to the isolated PEO domain for the electrospun nanofiber.

6.4.6 *In-situ* MB dye uptake for various types of electrospun nanofibers

Based on the Raman spectrum of MB in 90% D₂O/10% H₂O solution, the Raman bands at 1625 cm⁻¹ and 2382 cm⁻¹ correspond to the vibrational bands of the MB dye⁴³ and D₂O⁴⁴, respectively. The intensity ratio of I_{1625}/I_{2382} is proportional to the concentration of MB in the solution, where the temporal variation of this intensity ratio is shown in Figure 6.6. The trend in dye uptake for Dachi/PEO is similar to the trend noted for the aluminum foil control, in agreement with the low adsorption properties of chi and PEO with MB.⁴⁵ Meanwhile, grafted Dachi exhibits enhanced uptake towards MB as the intensity ratios for grafted chi are much lower than onto the surface of aluminum foil (control) and Dachi, indicating that the grafted salicylic acid segments serve as the active sites for the uptake of MB. The DachiSal-1/PEO sample shows a surprisingly high uptake toward MB among the various samples, where the uptake reaches its maximum value in 40 mins, whereas desorption occurs after 80 mins. The DachiSal-1/PEO electrospun fiber has more adsorption sites as a result of attenuated interactions between PEO and the grafted chi polymer chains. For the DachiSal-2/PEO sample, it reaches a maximum uptake in 30 mins with no sign of desorption for up to 112 mins. The porous DachiSal-2 sample reaches a maximum uptake in 2 mins, which is higher than the DachiSal-2/PEO sample. The porous DachiSal-2 sample's faster uptake is attributed to the additional porous feature on the fiber surface, which provides additional binding sites for MB.

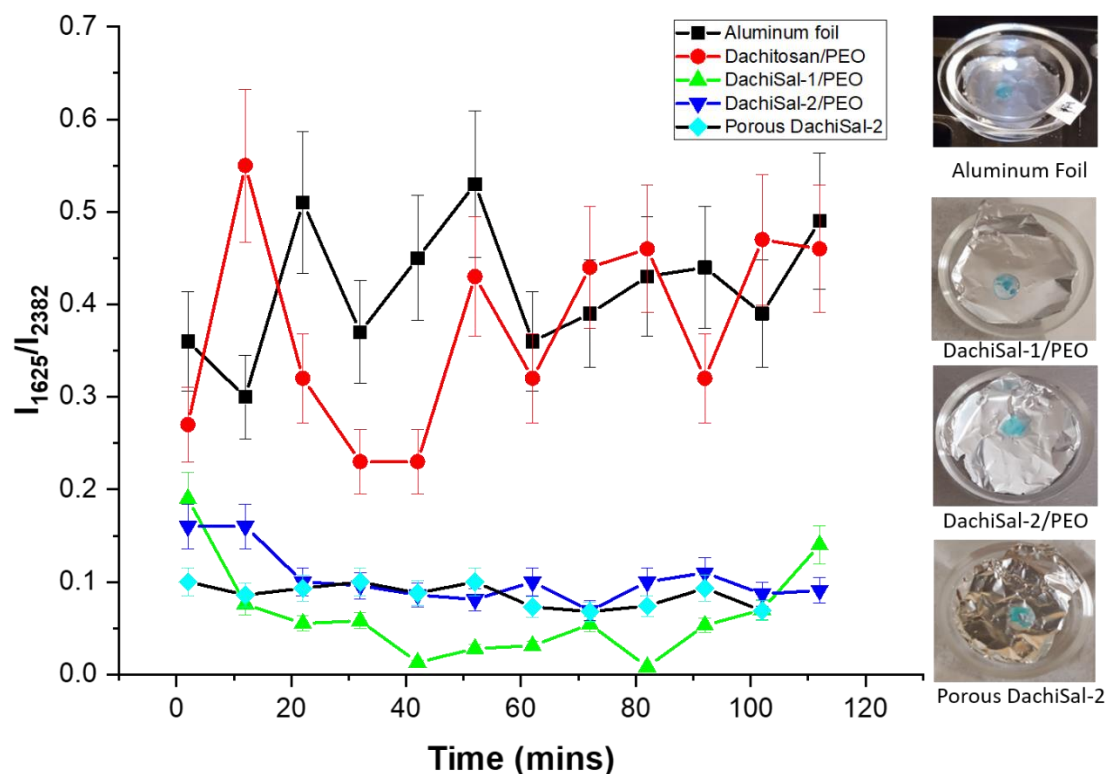


Figure 6.6. The Raman band intensity ratio variation at 1625 and 2382 cm^{-1} for various electrospun fibers imbibed in MB 90% D_2O /10% H_2O solution over time at ambient conditions.

6.5 Conclusion

In summary, the synthesis and characterization of different ratios of salicylic acid grafted Dachi was achieved. The grafted chi successfully led to the formation of electrospun nanofibers using PEO with a relatively low molecular weight ($M_w \approx 100$ kDa), in contrast to other electrospinning studies that often require PEO with a higher molecular weight above 400 kDa. An investigation of the fluid properties of Dachi/PEO solutions and the structural features of electrospun fibers reveal that a stable supramolecular assembly occurs between DachiSal and PEO that resulted in the formation of a chi electrospun nanofiber with LMw PEO. The supramolecular interaction occurs primarily between PEO and grafted salicylic acid groups of chi. A novel approach was reported, which yielded chi fiber materials with porous surface features attributed to PEO's thermal treatment and subsequent physical (solvent wash) removal of PEO as a sacrificial template. A dye uptake study with MB was monitored using *in-situ* Raman spectroscopy. The uptake results revealed that salicylic acid's addition enhanced MB uptake, where the porous

nanofibrous materials displayed notably enhanced uptake. The formation of grafted chi electrospun fibers with low molecular weight PEO ($M_w \approx 100$ kDa) according to the supramolecular chemistry approach reported herein will contribute to the development of advanced chi-based electrospun fibrous materials. The facile preparation of porous nanofibers employs PEO as a sacrificial template *via* physical processing that will contribute to a broader scope of materials design. In turn, it is envisaged that such materials will have promising potential for adsorption-desorption processes for water treatment and biomedical applications.

6.6 References

- (1) Abdel-Mohsen, A. M.; Jancar, J.; Kalina, L.; Hassan, A. F. Comparative Study of Chitosan and Silk Fibroin Staple Microfibers on Removal of Chromium (VI): Fabrication, Kinetics and Thermodynamic Studies. *Carbohydr. Polym.* **2020**, *234*, 115861. <https://doi.org/10.1016/j.carbpol.2020.115861>.
- (2) Dodero, A.; Brunengo, E.; Alloisio, M.; Sionkowska, A.; Vicini, S.; Castellano, M. Chitosan-Based Electrospun Membranes: Effects of Solution Viscosity, Coagulant and Crosslinker. *Carbohydr. Polym.* **2020**, *235*, 115976. <https://doi.org/10.1016/j.carbpol.2020.115976>.
- (3) Zhao, X.; Chen, S.; Lin, Z.; Du, C. Reactive Electrospinning of Composite Nanofibers of Carboxymethyl Chitosan Cross-Linked by Alginate Dialdehyde with the Aid of Polyethylene Oxide. *Carbohydr. Polym.* **2016**, *148*, 98–106. <https://doi.org/10.1016/j.carbpol.2016.04.051>.
- (4) Rieger, K. A.; Birch, N. P.; Schiffman, J. D. Electrospinning Chitosan/Poly(Ethylene Oxide) Solutions with Essential Oils: Correlating Solution Rheology to Nanofiber Formation. *Carbohydr. Polym.* **2016**, *139*, 131–138. <https://doi.org/10.1016/j.carbpol.2015.11.073>.
- (5) Li, D.; Xia, Y. N. Electrospinning of Nanofibers: Reinventing the Wheel? *Adv. Mater.* **2004**, *16* (14), 1151–1170. <https://doi.org/10.1002/adma.200400719>.
- (6) Ohkawa, K.; Cha, D. I.; Kim, H.; Nishida, A.; Yamamoto, H. Electrospinning of Chitosan.

- Macromol. Rapid Commun.* **2004**, 25 (18), 1600–1605.
<https://doi.org/10.1002/marc.200400253>.
- (7) Duan, B.; Dong, C. H.; Yuan, X. Y.; Yao, K. D. Electrospinning of Chitosan Solutions in Acetic Acid with Poly(Ethylene Oxide). *J. Biomater. Sci. Ed.* **2004**, 15 (6), 797–811.
<https://doi.org/10.1163/156856204774196171>.
 - (8) Klossner, R. R.; Queen, H. A.; Coughlin, A. J.; Krause, W. E. Correlation of Chitosan's Rheological Properties and Its Ability to Electrospin. *Biomacromolecules* **2008**, 9 (10), 2947–2953. <https://doi.org/10.1021/bm800738u>.
 - (9) Xue, C.; Wilson, L. D. A Structural Study of Self-Assembled Chitosan-Based Sponge Materials. *Carbohydr. Polym.* **2019**, 206, 685–693.
<https://doi.org/10.1016/j.carbpol.2018.10.111>.
 - (10) Samanta, P.; Thangapandian, V.; Singh, S.; Srivastava, R.; Nandan, B.; Liu, C. L.; Chen, H. L. Crystallization Behaviour of Poly(Ethylene Oxide) under Confinement in the Electrospun Nanofibers of Polystyrene/Poly(Ethylene Oxide) Blends. *Soft Matter* **2016**, 12 (23), 5110–5120. <https://doi.org/10.1039/c6sm00648e>.
 - (11) Zhong, G.; Wang, K.; Zhang, L.; Li, Z. M.; Fong, H.; Zhu, L. Nanodroplet Formation and Exclusive Homogenously Nucleated Crystallization in Confined Electrospun Immiscible Polymer Blend Fibers of Polystyrene and Poly(Ethylene Oxide). *Polymer (Guildf)*. **2011**, 52 (24), 5397–5402. <https://doi.org/10.1016/j.polymer.2011.09.045>.
 - (12) Lu, C.; Pelton, R. Factors Influencing the Size of PEO Complexes with a Tyrosine-Rich Polypeptide. *Langmuir* **2004**, 20 (10), 3962–3968. <https://doi.org/10.1021/la036032s>.
 - (13) Saquing, C. D.; Tang, C.; Monian, B.; Bonino, C. A.; Manasco, J. L.; Alsberg, E.; Khan, S. A. Alginate-Polyethylene Oxide Blend Nanofibers and the Role of the Carrier Polymer in Electrospinning. *Ind. Eng. Chem. Res.* **2013**, 52 (26), 8692–8704.
<https://doi.org/10.1021/ie302385b>.
 - (14) Ewaldz, E.; Brettmann, B. Molecular Interactions in Electrospinning: From Polymer Mixtures to Supramolecular Assemblies. *ACS Appl. Polym. Mater.* **2019**, 1 (3), 298–308.
<https://doi.org/10.1021/acsapm.8b00073>.

- (15) Pickelmann, J.; Plank, J. A Mechanistic Study Explaining the Synergistic Viscosity Increase Obtained from Polyethylene Oxide (PEO) and β -Naphthalene Sulfonate (BNS) in Shotcrete. *Cem. Concr. Res.* **2012**, *42* (11), 1409–1416.
<https://doi.org/10.1016/j.cemconres.2012.08.003>.
- (16) Cong, R.; Bain, A. D.; Pelton, R. An NMR Investigation of the Interaction of Polyethylene Oxide with Water-Soluble Poly(Vinyl Phenol-Co-Potassium Styrene Sulfonate). *J. Polym. Sci. Part B Polym. Phys.* **2000**, *38* (10), 1276–1284.
[https://doi.org/10.1002/\(SICI\)1099-0488\(20000515\)38:10<1276::AID-POLB20>3.0.CO;2-6](https://doi.org/10.1002/(SICI)1099-0488(20000515)38:10<1276::AID-POLB20>3.0.CO;2-6).
- (17) Stack, K. R.; Dunn, L. A.; Roberts, N. K. Study of the Interaction between Poly(Ethylene Oxide) and Phenol-Formaldehyde Resin. *Colloids and Surfaces* **1991**, *61* (C), 205–218.
[https://doi.org/10.1016/0166-6622\(91\)80310-K](https://doi.org/10.1016/0166-6622(91)80310-K).
- (18) Vane, J. R.; Botting, R. M. The Mechanism of Action of Aspirin. *Thromb. Res.* **2003**, *110* (5–6), 255–258. [https://doi.org/10.1016/S0049-3848\(03\)00379-7](https://doi.org/10.1016/S0049-3848(03)00379-7).
- (19) Guan, Y.; Li, Z.; He, F.; Huang, Y.; Song, W.; Hu, J. “On-Off” Thermoresponsive Coating Agent Containing Salicylic Acid Applied to Maize Seeds for Chilling Tolerance. *PLoS One* **2015**, *10* (3), e0120695. <https://doi.org/10.1371/journal.pone.0120695>.
- (20) Hirai, A.; Odani, H.; Nakajima, A. Determination of Degree of Deacetylation of Chitosan by Proton NMR Spectroscopy. *Polym. Bull. (Berl)*. **1991**, *26* (1), 87–94.
<https://doi.org/10.1007/BF00299352>.
- (21) Knaul, J. Z.; Kasaai, M. R.; Bui, V. T.; Creber, K. A. M. Characterization of Deacetylated Chitosan and Chitosan Molecular Weight Review. *Can. J. Chem.* **1998**, *76* (11), 1699–1706. <https://doi.org/10.1139/cjc-76-11-1699>.
- (22) de Oliveira, A. M.; Franco, T. T.; Oliveira Junior, E. N. De. Physicochemical Characterization of Thermally Treated Chitosans and Chitosans Obtained by Alkaline Deacetylation. *Int. J. Polym. Sci.* **2014**, *2014*, 1–9. <https://doi.org/10.1155/2014/853572>.
- (23) Khalafi-Nezhad, A.; Parhami, A.; Soltani Rad, M. N.; Zarea, A. Efficient Method for the Direct Preparation of Amides from Carboxylic Acids Using Tosyl Chloride under

- Solvent-Free Conditions. *Tetrahedron Lett.* **2005**, 46 (40), 6879–6882.
<https://doi.org/10.1016/j.tetlet.2005.08.021>.
- (24) Abbas, K.; Amin, M.; Hussain, M. A.; Sher, M.; Bukhari, S. N. A.; Jantan, I.; Edgar, K. J. Designing Novel Bioconjugates of Hydroxyethyl Cellulose and Salicylates for Potential Pharmaceutical and Pharmacological Applications. *Int. J. Biol. Macromol.* **2017**, 103, 441–450. <https://doi.org/10.1016/j.ijbiomac.2017.05.061>.
- (25) Hussain, M. A.; Badshah, M.; Iqbal, M. S.; Tahir, M. N.; Tremel, W.; Bhosale, S. V.; Sher, M.; Haseeb, M. T. HPMC-Salicylate Conjugates as Macromolecular Prodrugs: Design, Characterization, and Nano-Rods Formation. *J. Polym. Sci. Part A Polym. Chem.* **2009**, 47 (16), 4202–4208. <https://doi.org/10.1002/pola.23463>.
- (26) Suter, S. P.; Skalak, R. The History of Poiseuille's Law. *Annu. Rev. Fluid Mech.* **1993**, 25 (1), 1–20. <https://doi.org/10.1146/annurev.fl.25.010193.000245>.
- (27) Artamonov, A. F.; Aldabergenova, M. T.; Nigmatullina, F. S.; Dzhiembaev, B. Z. Synthesis of Saccharose Esters. *Chem. Nat. Compd.* **2000**, 36 (4), 345–348.
<https://doi.org/10.1023/A:1002876310412>.
- (28) Smith, B. C. *Infrared Spectral Interpretation : A Systematic Approach*; Boca Raton : CRC Press: Boca Raton, 1999.
- (29) Chylinska, M.; Szymanska-Chargot, M.; Zdunek, A. Imaging of Polysaccharides in the Tomato Cell Wall with Raman Microspectroscopy. *Plant Methods* **2014**, 10.
<https://doi.org/10.1186/1746-4811-10-14>.
- (30) Smith, G. P. S.; McLaughlin, A. W.; Clarkson, A. N.; Gordon, K. C.; Walker, G. F. Raman Microscopic Imaging of Electrospun Fibers Made from a Polycaprolactone and Polyethylene Oxide Blend. *Vib. Spectrosc.* **2017**, 92, 27–34.
<https://doi.org/10.1016/j.vibspec.2017.05.002>.
- (31) Desai, K.; Kit, K.; Li, J.; Zivanovic, S. Morphological and Surface Properties of Electrospun Chitosan Nanofibers. *Biomacromolecules* **2008**, 9 (3), 1000–1006.
<https://doi.org/10.1021/bm701017z>.

- (32) Nelson, A. Z.; Ewoldt, R. H. Design of Yield-Stress Fluids: A Rheology-to-Structure Inverse Problem. *Soft Matter* **2017**, *13* (41), 7578–7594.
<https://doi.org/10.1039/c7sm00758b>.
- (33) Porter, R. S.; Johnson, J. F. The Entanglement Concept in Polymer Systems. *Chem. Rev.* **1966**, *66* (1), 1–27. <https://doi.org/10.1021/cr60239a001>.
- (34) Dobrynin, A. V.; Colby, R. H.; Rubinstein, M. Scaling Theory of Polyelectrolyte Solutions. *Macromolecules* **1995**, *28* (6), 1859–1871.
<https://doi.org/10.1021/ma00110a021>.
- (35) Colby, R. H. Structure and Linear Viscoelasticity of Flexible Polymer Solutions: Comparison of Polyelectrolyte and Neutral Polymer Solutions. *Rheologica Acta*. 2010, pp 425–442. <https://doi.org/10.1007/s00397-009-0413-5>.
- (36) Gupta, D.; Jassal, M.; Agrawal, A. K. Solution Properties and Electrospinning of Poly(Galacturonic Acid) Nanofibers. *Carbohydr. Polym.* **2019**, *212* (February), 102–111.
<https://doi.org/10.1016/j.carbpol.2019.02.023>.
- (37) McKee, M. G.; Elkins, C. L.; Long, T. E. Influence of Self-Complementary Hydrogen Bonding on Solution Rheology/Electrospinning Relationships. *Polymer (Guildf)*. **2004**, *45* (26), 8705–8715. <https://doi.org/10.1016/j.polymer.2004.10.049>.
- (38) Burns, N. A.; Burroughs, M. C.; Gracz, H.; Pritchard, C. Q.; Brozena, A. H.; Willoughby, J.; Khan, S. A. Cyclodextrin Facilitated Electrospun Chitosan Nanofibers. *RSC Adv.* **2015**, *5* (10), 7131–7137. <https://doi.org/10.1039/c4ra09662b>.
- (39) Zając, A.; Hanuza, J.; Wandas, M.; Dymińska, L. Determination of N-Acetylation Degree in Chitosan Using Raman Spectroscopy. *Spectrochim. Acta Part A Mol. Biomol. Spectrosc.* **2015**, *134*, 114–120. <https://doi.org/10.1016/j.saa.2014.06.071>.
- (40) Muthu, S.; Isac Paulraj, E. Spectroscopic and Molecular Structure (Monomeric and Dimeric Structure) Investigation of 2-[(2-Hydroxyphenyl) Carbonyloxy] Benzoic Acid by DFT Method: A Combined Experimental and Theoretical Study. *J. Mol. Struct.* **2013**, *1038*, 145–162. <https://doi.org/10.1016/j.molstruc.2013.01.043>.

- (41) Maxfield, J.; Shepherd, I. W. Conformation of Poly(Ethylene Oxide) in the Solid State, Melt and Solution Measured by Raman Scattering. *Polymer (Guildf)*. **1975**, *16* (7), 505–509. [https://doi.org/10.1016/0032-3861\(75\)90008-7](https://doi.org/10.1016/0032-3861(75)90008-7).
- (42) Guo, C.; Liu, H.; Wang, J.; Chen, J. Conformational Structure of Triblock Copolymers by FT-Raman and FTIR Spectroscopy. *J. Colloid Interface Sci.* **1999**, *209* (2), 368–373. <https://doi.org/10.1006/jcis.1998.5897>.
- (43) Nicolai, S. H. A.; Rubim, J. C. Surface-Enhanced Resonance Raman (SERR) Spectra of Methylene Blue Adsorbed on a Silver Electrode. *Langmuir* **2003**, *19* (10), 4291–4294. <https://doi.org/10.1021/la034076v>.
- (44) Murphy, W. F.; Bernstein, H. J. Raman Spectra and an Assignment of the Vibrational Stretching Region of Water. *J. Phys. Chem.* **1972**, *76* (8), 1147–1152. <https://doi.org/10.1021/j100652a010>.
- (45) Dolatkhah, A.; Wilson, L. D. Magnetite/Polymer Brush Nanocomposites with Switchable Uptake Behavior Toward Methylene Blue. *ACS Appl. Mater. Interfaces* **2016**, *8* (8), 5595–5607. <https://doi.org/10.1021/acsami.5b11599>.

CHAPTER 7

Discussion, concluding remarks, and directions for future work

7.1 Integrated discussion of manuscript chapters

This section provides an overview of the thesis research findings and outlines how the objectives were addressed by the respective studies presented in the manuscript chapters (Chapter 4-6). The relation between each manuscript chapter is illustrated in Figure 7.1. As outlined in Chapter 1, the overall goal of the thesis research focuses on developing novel chi-based nonwoven micro-/nano- fibrous materials through freeze-drying and electrospinning with variable physicochemical properties and tunable surface features, along with an investigation of the formation of these materials. This overall goal was achieved by fulfilling three objectives (Objective #1, #2, and #3):

- 1) The structure of chi self-assembled sponges (nonwoven microfibrous materials) prepared *via* freeze-drying and their thermally-treated forms are investigated by a novel characterization method based on Raman spectral imaging to understand the role of the additive polymer and the interaction between chi and the additive polymer in the fiber materials (Objective #1).
- 2) The interactions leading to the formation of the chi/HP- β -CD electrospun fiber are investigated using solid-state characterization methods, including Raman spectral imaging with a suitable dye probe (Objective #2).
- 3) The structure of the chemically modified chi/LMw PEO electrospun nanofiber and its porous nanofiber prepared by utilizing an LMw PEO additive are investigated (Objective #3).

Chapter 4 relates to Objective #1. Chi-based nonwoven microfibrous composite materials have gained increasing attention because of their unique biocompatibility, biodegradability, and low toxicity comparing to other biomaterial composites.¹⁻⁷ As a result, chi-based self-assembled sponges (nonwoven fibrous composite materials) formed with other polysaccharides have found many applications in wound dressings^{2,5-7}, tissue engineering⁸, and wastewater treatment^{9,10} due to their high porosity and tunable mechanical and physicochemical properties. Freeze drying offers

a potential preparation method for designing biocompatible and multi-component sponges that contain biopolymer precursors.^{8,11} In a previous study¹², self-assembled colloidal particles with tunable physicochemical properties were formed between carboxymethyl chi (cm-chi) and sodium alginate (alg) *via* electrostatic interactions. The resulting colloidal particles can be transformed into self-assembled sponges in the presence of PEO upon freeze-drying, where the resulting composites possess tunable mechanical and physicochemical properties for diverse applications. Uncontrolled dissolution in solvent media is a key challenge associated with the utility of such chi composite materials. Thermal annealing offers a solution to address this problem by altering the water stability of the self-assembled composite materials. Conventional solid-based characterization methods (i.e., FT-IR, DSC, XRD, and SEM) are commonly used to study chi-based self-assembled microfibrillar materials. These methods pose limitations regarding the role of PEO in the solid fibrous materials and interactions among chi, alg, and PEO. FT-IR spectrum of chi overlaps with alg in 4000-400 cm^{-1} , making the interaction between them difficult to deconvolute. As for DSC, the bound water in chi and alg weakens the ability to identify interactions among chi, alg, and PEO by DSC, which was supported by Fig. 4.5 in Chapter 4.^{13,14} X-ray diffraction (XRD) provides limited structural information for chi and alg because of their amorphous nature. As well, SEM offers surface morphology of materials but no spectral information.

Therefore, there is a need to develop an alternative method to study interactions among each component for chi-based fibrous materials. Raman spectral imaging has been reported for the study of the component distribution of complex biological samples and fibrous materials.^{15–20} The use of dye probes can be employed to distinguish between chemically similar composites based on the hypothesis that dye probes interact with biopolymer components in a relatively well-defined manner, particularly where strong or directional interactions occur such as electrostatic interactions, ion-dipole interactions or hydrogen bonding for the biopolymer-dye system.^{21–23} In Chapter 4, chi-based self-assembled sponges were prepared through freeze-drying with and without annealing to compare their structural and physicochemical properties. The utility of Raman spectral imaging with a dye probe (Methylene blue solution) was reported as an effective and facile method to reveal the role of PEO in the solid fibrous materials and interactions among cm-chi, alg, and PEO for chi-based composite materials before and after thermal annealing. The

results highlight that interactions among cm-chi, alg, and PEO are strengthened *via* thermal treatment due to the melting and re-crystallization of PEO. Hypothesis #1 was addressed by this project. Moreover, the multi-functional role of PEO, such as a sacrificial template (*cf.* Fig. 4.6) and its role as a protective barrier in the composites, was evaluated by SEM and Raman spectral imaging. As a result, in Chapter 4, Raman spectral imaging with a dye probe was proven to be a powerful characterization tool to study interactions between each component for chi-based fibrous materials. As illustrated in Fig. 7.1, by changing the dye probe from MB to Rhodamine 6G, which has favorable binding towards chi²⁴ relative to HP- β -CD^{25,26}, this tool was consequently used in Chapter 5 to study the structure of chi-based electrospun fibrous materials. Furthermore, PEO can be used as a sacrificial template to construct porous surface features, which supports Hypothesis #3 leading to Chapter 6, where PEO in grafted chi/PEO electrospun fiber was used to generate pores on the fiber surface *via* physical treatment.

Chapter 5 was focused on addressing Objective #2. Chi electrospun nonwoven nanofibrous materials have been found in many fields that exploit their high surface area, as evidenced in wastewater treatment, food preservation, and biomedical devices.^{5,27-42} In this study, two chi/HP- β -CD fibers (mass ratio between chi and HP- β -CD = 2:20 and 2:50) were assembled *via* an electrospinning process that contained a mixture of chi and HP- β -CD with TFA as a solvent. Complementary thermal analysis (TGA and DSC) and spectroscopic methods (Raman and FT-IR) were used to evaluate the structure and composition of the fiber assemblies in the solid-state, in contrast to conventional characterized methods that rely on the study of materials in their solution form. Raman spectral imaging with a suitable dye probe is a useful tool to decipher the structure of complex multi-component systems, as described in Chapter 4. Therefore, the insight into the improvement of electrospun fiber formation through the chi/TFA/HP- β -CD assembly could be understood using this technique and other spectroscopic methods. This study highlights the multi-functional role of TFA as a solvent, proton donor, and electrostatically bound pendant group to chi, where the formation of a ternary supramolecular complex occurs *via* unique host-guest interactions. As a result, Hypothesis #2 was addressed. This work contributes further insight into the formation and stability of such ternary (chi + HP- β -CD + TFA) electrospun fibers. Besides, the chi-based supramolecular assembly's ability to maintain the stable jet for electrospinning supports Hypothesis #4 that Chemically modified chi and low molecular weight PEO could form

a supramolecular assembly which facilitates the electrospinning of chi/low molecular weight PEO system, leading to Chapter 6.

Chapter 6 was built upon Chapters 4 and 5, as demonstrated in Fig. 7.1, focusing on Objective #3. Chi electrospun nanofibers have been found in medical applications and food packaging despite the technical challenges in their preparation. Polymer additives like PEO are suitable for designing chi electrospun nanofibers as PEO can facilitate chi electrospun fibre formation. Chapter 4 revealed that PEO might function as a sacrificial template (*cf.* Fig. 4.6) to generate porous features on the fiber surface upon post-treatment. Therefore, chi porous electrospun nanofibrous materials could be achieved through physical processes using a relatively low molecular weight (LMw) PEO ($M_w \leq 100$ kDa) because LMw PEO could form a dispersed phase in the nanofiber due to its short polymer chain.⁴³ However, PEO with a molecular weight greater than 400 kDa was commonly employed to ensure chi electrospun fiber formation because it offers sufficient PEO-PEO chain entanglement to stabilize the electrospinning jet leading to the formation of electrospun nanofibers.^{41,44–49} As described in Chapter 5, the supramolecular assembly could offer an alternative approach to promote chi electrospun nanofiber formation using LMw PEO. In Chapter 6, chi grafted with salicylic acid was prepared to afford improved electrospun fiber formation with low molecular weight PEO, while un-modified chi did not yield electrospun fibers with Low molecular weight PEO (*cf.* Fig.6.2). The investigation of the interactions between unmodified or grafted chi with PEO revealed that supramolecular assemblies were formed between grafted chi and PEO, contributing to promoting chi electrospun fiber formation, supported by rheology studies (*cf.* Fig. 6.3) and spectroscopic studies (*cf.* Fig.6.4). Based on spectroscopic studies (*cf.* Fig.6.4), interactions between grafted chi and PEO occurred mainly at the grafted salicylic acid moiety, indicating that grafted salicylic acid moiety plays a crucial role in the electrospinning of the chi/LMw PEO system. A porous electrospun nanofibrous material was prepared successfully through physical treatment, supported by microscopic studies (*cf.* Fig. 6.5). The MB uptake results demonstrated that the porous nanofiber displayed higher uptake MB uptake than the original one (*cf.* Fig. 6.6). Hypotheses #3 and #4 were addressed by the results of this project.

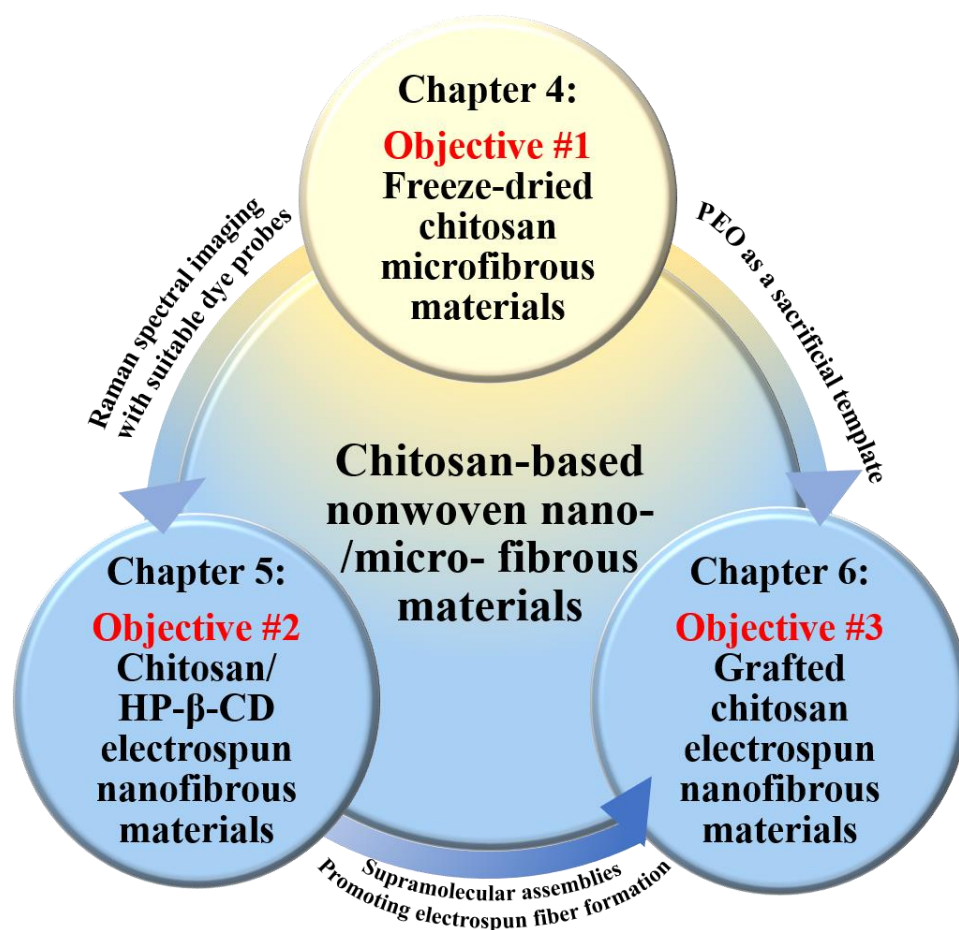


Figure 7.1. Organization of the thesis research.

7.2 Conclusion

The overall goal of the thesis research focuses on the development of novel chi-based nonwoven micro-/nano- fibrous materials through freeze-drying and electrospinning and the investigation of the insight into the formation of these materials, which contributes to the design of chi-based nonwoven fibrous materials with good water stability, distinct physicochemical properties, and tunable surface features. This overall goal was accomplished, which led to many unique findings regarding new knowledge of the design of chi-based nonwoven fibrous materials for diverse applications amenable to wastewater treatment, wound dressing, and food packaging.

In Chapter 4, self-assembled chi sponges (nonwoven microfibrinous materials) were successfully prepared by freeze-drying, and their structural features were characterized by various spectral techniques. In particular, Raman spectral imaging with a suitable dye probe was developed

to study the structure and composition of biopolymer composites before and/or after thermal annealing. Before annealing, the composite displayed a phase-separated “sandwich” structure, while the annealing of cm-chi and sodium alginate with PEO led to the strengthening of the cohesive interactions between cm-chi and alginate. Meanwhile, PEO forms *island-like* features on the biopolymer fiber surface. PEO may serve a dual function upon annealing, where it may either serve as a sacrificial template to create a porous morphology or as a protective layer to prevent water intrusion upon exposure to aqueous media. The Raman spectral methods reported herein contributed to a greater understanding of the structure-function properties of chi-based composites electrospun fibrous materials and other biopolymer composites for a wide range of emerging applications in the formulation of biomedical devices, nutraceuticals, pharmaceuticals, and cosmetics.

In Chapter 5, chi:HP- β -CD 2:20 and 2:50 fiber were produced *via* electrospinning of a mixture of HP- β -CD and chi using TFA as a solvent. The composition of chi:HP- β -CD fibers was studied using thermal analysis and complementary spectral methods. TFA was found to be a constituent in the chi:HP- β -CD fiber assembly. The heterogeneous morphology and composition of this electrospun fiber were revealed using SEM and Raman spectral imaging with a dye-based probe method described in Chapter 4. Interactions among the components were also characterized using complementary methods, such as IR and Raman spectroscopy. TFA appears to have multifunctional properties as a solvent during the electrospinning process, where it protonates chi and stabilizes host-guest interactions with HP- β -CD. Hence, the presence of lateral binding sites along the chi backbone (*cf.* Scheme 5.2) due to electrostatically bound TFA are found to play a crucial role in the effective dispersion of chi and the reduction of repulsive forces during electrospinning between chi polymer chains that favor fiber formation. There was no clear evidence of direct interactions between the glucosamine moiety of chi and HP- β -CD in the solid-state according to Raman spectral imaging with dye probes such as Rhodamine 6G. The combined complementary results herein account for the fiber formation process as the role of weak host-guest supramolecular interactions that arise from forming a facial complex due to hydrophobic effects. Moreover, such controlled-release supramolecular disassembly will contribute to the development of “smart coatings” that may utilize diverse types of chi polyelectrolyte complexes.

In Chapter 6, the synthesis and characterization of different ratios of salicylic acid grafted Dachl was achieved. The grafted chl successfully led to electrospun fibers' formation using PEO with a relatively low molecular weight ($M_w = 100$ kDa), in contrast to other electrospinning studies^{41,44-49} that often require PEO with a higher molecular weight above 400 kDa. An investigation of the fluid properties of Dachl/PEO blends and the structural features of electrospun fibers reveal that a stable supramolecular assembly occurs between DachlSal and PEO that resulted in the formation of a chl electrospun fiber with PEO possessing a lower molecular weight. The supramolecular interaction occurs primarily between PEO and grafted salicylic acid groups of chl. A novel approach was reported, which yielded chl fiber materials with porous surface features, attributed to PEO's thermal treatment and subsequent physical (solvent wash) removal of PEO as a sacrificial template. A dye uptake study with MB was monitored using *in-situ* Raman spectroscopy. The uptake results revealed that the grafting of salicylic acid's resulted in an enhanced uptake of MB, where the porous fiber materials displayed notably enhanced uptake. The formation of grafted chl electrospun fibers with low molecular weight PEO ($M_w = 100$ kDa) according to the supramolecular chemistry approach reported herein will contribute to the development of advanced chl-based electrospun fibrous materials. The facile preparation of porous nanofibers employs PEO as a sacrificial template *via* physical processing that will contribute to a broader scope of materials design. In turn, it is foreseen that such materials will have promising potential for adsorption-desorption processes for water treatment and biomedical applications.

In summary, this thesis research contributes significantly to the design of novel chl-based nonwoven micro-/nano- fibrous materials with various physicochemical properties and tunable surface features through freeze-drying and electrospinning. Uncontrolled dissolution occurs for chl-based composite materials in an aqueous environment. This challenge was addressed by thermal annealing of prepared composite materials, which is anticipated to improve the performance of chl-based composite materials in an aqueous environment. Moreover, the structure of solid chl-based fibrous materials was studied by conventional characterization methods and Raman spectral imaging with a suitable dye probe method. Chl was grafted with salicylic acid to make it electrospinnable with PEO ($M_w \leq 100$ kDa). As a result, grafted chl/LMw PEO electrospun nanofibrous materials with porous surface features were prepared by physical processes with the use of PEO ($M_w \leq 100$ kDa). The results obtained herein provided a deep

understanding of the supramolecular assembly function for the electrospun fiber formation process, leading to new material design strategies for chi-based electrospun nonwoven fibrous materials, especially for chi/low molecular weight polymer systems.

7.3 Future work

In this thesis research, various chi-based nonwoven micro-/nano- fibrous materials were prepared. These materials need to be validated for different practical applications. For example, the cytotoxicity assay is required to validate these materials for biomedical applications.⁵⁰ Also, the wound healing test *in vivo* and antimicrobial activities test of these materials is also crucial for the application in wound dressing, antibacterial filtration, and tissue engineering.⁵⁰ The potential application of the salicylic acid grafted chi/LMw PEO electrospun nanofibrous material (DachiSal/PEO) for seed coating could be explored because salicylic acid is known to improve the chilling resistance of the seed.⁵¹ This electrospun nanofibrous material can be directly applied to the seed by placing the seed on the grounded collector using the vertical configuration of the electrospinning setup instead of the horizontal one. Moreover, it was reported that chi-g-salicylic acid film was coated on the fruit to preserve fruit quality during cold storage.⁵² The fruit could be coated with DachiSal/PEO electrospun nanofibrous materials and tested for the respiration rate as an index for fruit quality during cold storage.⁵²

DachiSal/LMw PEO electrospun nanofibrous material with porous surface features was obtained with the aid of the supramolecular assembly of grafted chi and LMw PEO through physical processes. These physical processes include the thermal treatment of PEO followed by the removal of PEO. The distribution of porous features created on the fiber surface is determined by the dispersion of the PEO domain in *as-spun* fibrous materials, governed by the molecular weight of PEO's.^{43,53–58} When the supramolecular assembly involves in the formation of chi/PEO electrospun fibrous materials, lowering the molecular weight of PEO (to ~ 10 kDa) results in reducing the opportunity of the formation of the interconnected PEO domains among the chi electrospun nanofibrous materials, leading to an even distribution of the dispersed PEO phase in the materials. Therefore, it is reasonable to hypothesize that porous surface features could be distributed evenly using PEO with Mw ≈ 10 kDa. Moreover, the compound grafted onto chi has an enormous effect on the pore distribution of the final product as the complexation between the grafted compound and LMw PEO decides the allocation of the PEO domain in *as-spun* fibrous

materials.⁴³ The function of the final product relates to the properties of the grafted compound. For instance, many vital pharmaceuticals, food ingredients, and cosmetics are aromatic compounds.^{59,60} The aromatic compounds can be grafted onto chi through the method mentioned in this thesis research (*cf.* Chapter 6), the carbodiimide-based chemical coupling method, the enzyme-catalyzed grafting method, or the free-radical-mediated grafting method.⁶⁰ The final chi porous fibrous material will alternate the solubility profile of chi amenable to organic solvents and gain different functions (i.e., antioxidant, antimicrobial, anti-allergic, etc.)⁶⁰ and porosity depending on the type of grafted aromatic compounds.

Chi-based nonwoven electrospun nanofibrous materials were prepared in this thesis research. In order to develop a chi-based material with a more complicated structure, electrospinning/netting (ESN) could be applied to chi-based materials. The ESN is considered a modified electrospinning process involving splitting a small charged droplet attributed to phase separation in a high electric field. The ESN results in one step fabrication of three-dimensional (3D) nano-fiber/nets (NFN) containing conventional electrospun nanofibers as support for unique ultrafine interlinked 1D nanowires.⁶¹ The NFN has several advantages such as low packing density, small pore size, Steiner tree network geometry, and higher porosity, relative to conventional electrospun nanofibers. Because of these advantages, the NFN membranes can be used in air filtration media or face masks.⁶² The phase separation-induced splitting of small droplets occurs in the third step of the electrospinning process (*cf.* Section 2.4.2) due to the induced composition change of electrospinning formulation in this step resulting from solvent evaporation, which can be activated using solvents with a low boiling point and high dielectric constant at a high electric field.⁶¹ An example of the chi/polyamide-6 NFN membrane has been reported in the literature⁶³, but chi was not the primary component in this example. Hence, it is necessary to prepare chi-based NFN membranes using chi as the primary component to utilize chi's advantages fully. Therefore, it is hypothesized that the ESN of chi-based materials can be achieved using chemically modified chi or manipulating the mixture of solvents at high electric field strength under controlled environmental humidity. The chemically modified chi approach exploits the interaction between modified chi and additive polymer to enable the electrospinning formulation's heterogeneity. In this case, chi can be modified using polyacrylamide (PAM).⁶⁴ The electrospinning formulation can be prepared using PAM grafted chi and formic acid as formic acid is a promising solvent for the

ESN process.⁶¹ On the other hand, because conventional chi/additive polymers formulations have had some heterogeneity levels attributed to molecular interactions between chi and additive polymers, as shown in Chapter 5 and 6, the ESN of these formulations can be realized by further inducing small droplets' splitting in the third step of the electrospinning process through manipulating the mixture of solvents.

7.4 References

- (1) Albanna, M. Z.; Bou-Akl, T. H.; Blowytsky, O.; Walters, H. L.; Matthew, H. W. T. Chitosan Fibers with Improved Biological and Mechanical Properties for Tissue Engineering Applications. *J. Mech. Behav. Biomed. Mater.* **2013**, *20*, 217–226. <https://doi.org/10.1016/j.jmbbm.2012.09.012>.
- (2) Croisier, F.; Jérôme, C. Chitosan-Based Biomaterials for Tissue Engineering. *Eur. Polym. J.* **2013**, *49* (4), 780–792. <https://doi.org/10.1016/j.eurpolymj.2012.12.009>.
- (3) Elsabee, M. Z.; Naguib, H. F.; Morsi, R. E. Chitosan Based Nanofibers, Review. *Mater. Sci. Eng. C* **2012**, *32* (7), 1711–1726. <https://doi.org/10.1016/j.msec.2012.05.009>.
- (4) Knaul, J. Z.; Hudson, S. M.; Creber, K. A. M. Improved Mechanical Properties of Chitosan Fibers. *J. Appl. Polym. Sci.* **1999**, *72* (13), 1721–1732. <https://doi.org/AID-APP8>3.0.CO;2-V>.
- (5) Naseri-Nosar, M.; Ziora, Z. M. Wound Dressings from Naturally-Occurring Polymers: A Review on Homopolysaccharide-Based Composites. *Carbohydr. Polym.* **2018**, *189*, 379–398. <https://doi.org/10.1016/j.carbpol.2018.02.003>.
- (6) Rogina, A.; Rico, P.; Gallego Ferrer, G.; Ivanković, M.; Ivanković, H. Effect of in Situ Formed Hydroxyapatite on Microstructure of Freeze-Gelled Chitosan-Based Biocomposite Scaffolds. *Eur. Polym. J.* **2015**, *68*, 278–287. <https://doi.org/10.1016/J.EURPOLYMJ.2015.05.004>.
- (7) Sun, W.; Chen, G.; Wang, F.; Qin, Y.; Wang, Z.; Nie, J.; Ma, G. Polyelectrolyte-Complex Multilayer Membrane with Gradient Porous Structure Based on Natural Polymers for Wound Care. *Carbohydr. Polym.* **2018**, *181*, 183–190. <https://doi.org/10.1016/J.CARBPOL.2017.10.068>.

- (8) Jiang, C.; Wang, Z.; Zhang, X.; Zhu, X.; Nie, J.; Ma, G. Crosslinked Polyelectrolyte Complex Fiber Membrane Based on Chitosan-Sodium Alginate by Freeze-Drying. *RSC Adv.* **2014**, *40* (78), 41551–41560. <https://doi.org/10.1039/c4ra04208e>.
- (9) Rogovina, S.; Aleksanyan, K.; Vladimirov, L.; Prut, E.; Ivanushkina, N.; Berlin, A. Development of Novel Biodegradable Polysaccharide-Based Composites and Investigation of Their Structure and Properties. *J. Polym. Environ.* **2018**, *26* (4), 1727–1736. <https://doi.org/10.1007/s10924-017-1069-3>.
- (10) Xu, L.; Chen, Y.; Liu, N.; Zhang, W.; Yang, Y.; Cao, Y.; Lin, X.; Wei, Y.; Feng, L. Breathing Demulsification: A Three-Dimensional (3D) Free-Standing Superhydrophilic Sponge. *ACS Appl. Mater. Interfaces* **2015**, *7* (40), 22264–22271. <https://doi.org/10.1021/acsami.5b07530>.
- (11) Duan, G.; Jiang, S.; Jérôme, V.; Wendorff, J. H.; Fathi, A.; Uhm, J.; Altstädt, V.; Herling, M.; Breu, J.; Freitag, R.; Agarwal, S.; Greiner, A. Ultralight, Soft Polymer Sponges by Self-Assembly of Short Electrospun Fibers in Colloidal Dispersions. *Adv. Funct. Mater.* **2015**, *25* (19), 2850–2856. <https://doi.org/10.1002/adfm.201500001>.
- (12) Xue, C.; Wilson, L. D. Design and Characterization of Chitosan-Based Composite Particles with Tunable Interfacial Properties. *Carbohydr. Polym.* **2015**, *132*, 369–377. <https://doi.org/10.1016/j.carbpol.2015.06.058>.
- (13) Sakurai, K. Glass Transition Temperature of Chitosan and Miscibility of Chitosan/Poly(N-Vinyl Pyrrolidone) Blends. *Polymer (Guildf)*. **2000**, *41* (19), 7051–7056. [https://doi.org/10.1016/S0032-3861\(00\)00067-7](https://doi.org/10.1016/S0032-3861(00)00067-7).
- (14) Dong, Y.; Ruan, Y.; Wang, H.; Zhao, Y.; Bi, D. Studies on Glass Transition Temperature of Chitosan with Four Techniques. *J. Appl. Polym. Sci.* **2004**, *93* (4), 1553–1558. <https://doi.org/10.1002/app.20630>.
- (15) Smith, G. P. S.; McLaughlin, A. W.; Clarkson, A. N.; Gordon, K. C.; Walker, G. F. Raman Microscopic Imaging of Electrospun Fibers Made from a Polycaprolactone and Polyethylene Oxide Blend. *Vib. Spectrosc.* **2017**, *92*, 27–34. <https://doi.org/10.1016/j.vibspec.2017.05.002>.

- (16) Sóti, P. L.; Nagy, Z. K.; Serneels, G.; Vajna, B.; Farkas, A.; Van der Gucht, F.; Fekete, P.; Vigh, T.; Wagner, I.; Balogh, A.; Pataki, H.; Mező, G.; Marosi, G. Preparation and Comparison of Spray Dried and Electrospun Bioresorbable Drug Delivery Systems. *Eur. Polym. J.* **2015**, *68*, 671–679. <https://doi.org/10.1016/j.eurpolymj.2015.03.035>.
- (17) Nagy, Z. K.; Balogh, A.; Vajna, B.; Farkas, A.; Patyi, G.; Kramarics, Á.; Marosi, G. Comparison of Electrospun and Extruded Soluplus®-Based Solid Dosage Forms of Improved Dissolution. *J. Pharm. Sci.* **2012**, *101* (1), 322–332. <https://doi.org/10.1002/jps.22731>.
- (18) Kotzianová, A.; Řebíček, J.; Pokorný, M.; Hrbáč, J.; Velebný, V. Raman Spectroscopy Analysis of Biodegradable Electrospun Nanofibers Prepared from Polymer Blends. *Monatshefte für Chemie - Chem. Mon.* **2016**, *147* (5), 919–923. <https://doi.org/10.1007/s00706-015-1639-9>.
- (19) Büttiker, R.; Ebert, J.; Hinderling, C.; Adlhart, C. Membranes for Specific Adsorption: Immobilizing Molecularly Imprinted Polymer Microspheres Using Electrospun Nanofibers. *Chim. Int. J. Chem.* **2011**, *65* (3), 182–186. <https://doi.org/10.2533/chimia.2011.182>.
- (20) Bocklitz, T. W.; Guo, S.; Ryabchykov, O.; Vogler, N.; Popp, J. Raman Based Molecular Imaging and Analytics: A Magic Bullet for Biomedical Applications!? *Anal. Chem.* **2016**, *88* (1), 133–151. <https://doi.org/10.1021/acs.analchem.5b04665>.
- (21) Mahaninia, M. H.; Wilson, L. D. Modular Cross-Linked Chitosan Beads with Calcium Doping for Enhanced Adsorptive Uptake of Organophosphate Anions. *Ind. Eng. Chem. Res.* **2016**, *55* (45), 11706–11715. <https://doi.org/10.1021/acs.iecr.6b02814>.
- (22) Dolatkhah, A.; Wilson, L. D. Salt-Responsive Fe₃O₄ Nanocomposites and Phase Behavior in Water. *Langmuir* **2018**, *34* (1), 341–350. <https://doi.org/10.1021/acs.langmuir.7b03613>.
- (23) Dehabadi, L.; Karoyo, A. H.; Wilson, L. D. Spectroscopic and Thermodynamic Study of Biopolymer Adsorption Phenomena in Heterogeneous Solid–Liquid Systems. *ACS Omega* **2018**, *3* (11), 15370–15379. <https://doi.org/10.1021/acsomega.8b01663>.
- (24) Vanamudan, A.; Pamidimukkala, P. Chitosan, Nanoclay and Chitosan-Nanoclay

- Composite as Adsorbents for Rhodamine-6G and the Resulting Optical Properties. *Int. J. Biol. Macromol.* **2015**, *74*, 127–135. <https://doi.org/10.1016/j.ijbiomac.2014.11.009>.
- (25) Serra-Gómez, R.; Tardajos, G.; González-Benito, J.; González-Gaitano, G. Rhodamine Solid Complexes as Fluorescence Probes to Monitor the Dispersion of Cyclodextrins in Polymeric Nanocomposites. *Dye. Pigment.* **2012**, *94* (3), 427–436. <https://doi.org/10.1016/j.dyepig.2012.02.009>.
- (26) Bakkialakshmi, S.; Menaka, T. A Study of the Interaction between Rhodamine 6g and Hydroxy Propyl β -Cyclodextrin by Steady State Fluorescence. *Spectrochim. Acta - Part A Mol. Biomol. Spectrosc.* **2011**, *81* (1), 8–13. <https://doi.org/10.1016/j.saa.2011.04.082>.
- (27) Kumar, M. N. V. R.; Muzzarelli, R. A. A.; Muzzarelli, C.; Sashiwa, H.; Domb, A. J. Chitosan Chemistry and Pharmaceutical Perspectives. *Chem. Rev.* **2004**, *104* (12), 6017–6084. <https://doi.org/10.1021/cr030441b>.
- (28) Min, B.-M.; Lee, S. W.; Lim, J. N.; You, Y.; Lee, T. S.; Kang, P. H.; Park, W. H. Chitin and Chitosan Nanofibers: Electrospinning of Chitin and Deacetylation of Chitin Nanofibers. *Polymer (Guildf)*. **2004**, *45* (21), 7137–7142. <https://doi.org/10.1016/j.polymer.2004.08.048>.
- (29) Li, L.; Li, Y.; Cao, L.; Yang, C. Enhanced Chromium (VI) Adsorption Using Nanosized Chitosan Fibers Tailored by Electrospinning. *Carbohydr. Polym.* **2015**, *125*, 206–213. <https://doi.org/10.1016/j.carbpol.2015.02.037>.
- (30) Habiba, U.; Siddique, T. A.; Talebian, S.; Lee, J. J. L.; Salleh, A.; Ang, B. C.; Afifi, A. M. Effect of Deacetylation on Property of Electrospun Chitosan/PVA Nanofibrous Membrane and Removal of Methyl Orange, Fe(III) and Cr(VI) Ions. *Carbohydr. Polym.* **2017**, *177*, 32–39. <https://doi.org/10.1016/J.CARBPOL.2017.08.115>.
- (31) Yihan, W.; Minato, W. Nanofiber Fabrication Techniques and Its Applicability to Chitosan. *Prog. Chem.* **2014**, *26* (11), 1821–1831. <https://doi.org/10.7536/PC140636>.
- (32) Megelski, S.; Stephens, J. S.; Bruce Chase, D.; Rabolt, J. F. Micro- and Nanostructured Surface Morphology on Electrospun Polymer Fibers. *Macromolecules* **2002**, *35* (22), 8456–8466. <https://doi.org/10.1021/ma020444a>.

- (33) Casasola, R.; Thomas, N. L.; Trybala, A.; Georgiadou, S. Electrospun Poly Lactic Acid (PLA) Fibres: Effect of Different Solvent Systems on Fibre Morphology and Diameter. *Polymer (Guildf)*. **2014**, 55 (18), 4728–4737.
<https://doi.org/10.1016/j.polymer.2014.06.032>.
- (34) Khil, M. S.; Cha, D. I.; Kim, H. Y.; Kim, I. S.; Bhattarai, N. Electrospun Nanofibrous Polyurethane Membrane as Wound Dressing. *J. Biomed. Mater. Res. Part B-Applied Biomater*. **2003**, 67B (2), 675–679. <https://doi.org/10.1002/jbm.b.10058>.
- (35) Verma, D.; Katti, K. S.; Katti, D. R. Polyelectrolyte-Complex Nanostructured Fibrous Scaffolds for Tissue Engineering. *Mater. Sci. Eng. C* **2009**, 29 (7), 2079–2084.
<https://doi.org/10.1016/j.msec.2009.04.006>.
- (36) Li, L.; Hsieh, Y. L. Chitosan Bicomponent Nanofibers and Nanoporous Fibers. *Carbohydr. Res*. **2006**, 341 (3), 374–381. <https://doi.org/10.1016/j.carres.2005.11.028>.
- (37) Muzzarelli, R. A. A.; Mehtedi, M. El; Mattioli-Belmonte, M. Emerging Biomedical Applications of Nano-Chitins and Nano-Chitosans Obtained via Advanced Eco-Friendly Technologies from Marine Resources. *Mar. Drugs* **2014**, 12 (11), 5468–5502.
<https://doi.org/10.3390/md12115468>.
- (38) Karimian, A.; Parsian, H.; Majidinia, M.; Rahimi, M.; Mir, S. M.; Samadi Kafil, H.; Shafiei-Irannejad, V.; Kheyrollah, M.; Ostadi, H.; Yousefi, B. Nanocrystalline Cellulose: Preparation, Physicochemical Properties, and Applications in Drug Delivery Systems. *Int. J. Biol. Macromol*. **2019**, 133, 850–859. <https://doi.org/10.1016/j.ijbiomac.2019.04.117>.
- (39) Aranday-Garcia, R.; Saimoto, H.; Shirai, K.; Ifuku, S. Chitin Biological Extraction from Shrimp Wastes and Its Fibrillation for Elastic Nanofiber Sheets Preparation. *Carbohydr. Polym*. **2019**, 213, 112–120. <https://doi.org/10.1016/j.carbpol.2019.02.083>.
- (40) Jamshidifard, S.; Koushkbaghi, S.; Hosseini, S.; Rezaei, S.; Karamipour, A.; Jafari rad, A.; Irani, M. Incorporation of UiO-66-NH₂ MOF into the PAN/Chitosan Nanofibers for Adsorption and Membrane Filtration of Pb(II), Cd(II) and Cr(VI) Ions from Aqueous Solutions. *J. Hazard. Mater*. **2019**, 368, 10–20.
<https://doi.org/10.1016/j.jhazmat.2019.01.024>.

- (41) Bhattarai, N.; Edmondson, D.; Veiseh, O.; Matsen, F. A.; Zhang, M. Q. Electrospun Chitosan-Based Nanofibers and Their Cellular Compatibility. *Biomaterials* **2005**, 26 (31), 6176–6184. <https://doi.org/10.1016/j.biomaterials.2005.03.027>.
- (42) Jayakumar, R.; Prabakaran, M.; Nair, S. V; Tamura, H. Novel Chitin and Chitosan Nanofibers in Biomedical Applications. *Biotechnol. Adv.* **2010**, 28 (1), 142–150. <https://doi.org/10.1016/j.biotechadv.2009.11.001>.
- (43) Lu, C.; Pelton, R. Factors Influencing the Size of PEO Complexes with a Tyrosine-Rich Polypeptide. *Langmuir* **2004**, 20 (10), 3962–3968. <https://doi.org/10.1021/la036032s>.
- (44) Ma, G.; Liu, Y.; Peng, C.; Fang, D.; He, B.; Nie, J. Paclitaxel Loaded Electrospun Porous Nanofibers as Mat Potential Application for Chemotherapy against Prostate Cancer. *Carbohydr. Polym.* **2011**, 86 (2), 505–512. <https://doi.org/10.1016/j.carbpol.2011.04.082>.
- (45) Rieger, K. A.; Birch, N. P.; Schiffman, J. D. Electrospinning Chitosan/Poly(Ethylene Oxide) Solutions with Essential Oils: Correlating Solution Rheology to Nanofiber Formation. *Carbohydr. Polym.* **2016**, 139, 131–138. <https://doi.org/10.1016/j.carbpol.2015.11.073>.
- (46) Klossner, R. R.; Queen, H. A.; Coughlin, A. J.; Krause, W. E. Correlation of Chitosan's Rheological Properties and Its Ability to Electrospin. *Biomacromolecules* **2008**, 9 (10), 2947–2953. <https://doi.org/10.1021/bm800738u>.
- (47) Mucha, M.; Piekilna, J.; Wieczorek, A. Characterisation and Morphology of Biodegradable Chitosan / Synthetic Polymer Blends. *Macromol. Symp.* **1999**, 144 (1), 391–412. <https://doi.org/10.1002/masy.19991440137>.
- (48) Seo, H.; Matsumoto, H.; Hara, S.; Minagawa, M.; Tanioka, A.; Yako, H.; Yamagata, Y.; Inoue, K. Preparation of Polysaccharide Nanofiber Fabrics by Electrospray Deposition: Additive Effects of Poly(Ethylene Oxide). *Polym. J.* **2005**, 37 (6), 391–398. <https://doi.org/10.1295/polymj.37.391>.
- (49) Pakravan, M.; Heuzey, M.-C.; Ajji, A. A Fundamental Study of Chitosan/PEO Electrospinning. *Polymer (Guildf)*. **2011**, 52 (21), 4813–4824. <https://doi.org/10.1016/j.polymer.2011.08.034>.

- (50) Ding, F.; Deng, H.; Du, Y.; Shi, X.; Wang, Q. Emerging Chitin and Chitosan Nanofibrous Materials for Biomedical Applications. *Nanoscale* **2014**, *6* (16), 9477–9493. <https://doi.org/10.1039/C4NR02814G>.
- (51) Guan, Y.; Li, Z.; He, F.; Huang, Y.; Song, W.; Hu, J. “On-Off” Thermoresponsive Coating Agent Containing Salicylic Acid Applied to Maize Seeds for Chilling Tolerance. *PLoS One* **2015**, *10* (3), e0120695. <https://doi.org/10.1371/journal.pone.0120695>.
- (52) Zhang, Y.; Zhang, M.; Yang, H. Postharvest Chitosan-g-Salicylic Acid Application Alleviates Chilling Injury and Preserves Cucumber Fruit Quality during Cold Storage. *Food Chem.* **2015**, *174*, 558–563. <https://doi.org/10.1016/j.foodchem.2014.11.106>.
- (53) Rufino, T. D. C.; Felisberti, M. I. Confined PEO Crystallisation in Immiscible PEO/PLLA Blends. *RSC Adv.* **2016**, *6* (37), 30937–30950. <https://doi.org/10.1039/C6RA02406H>.
- (54) Samanta, P.; Thangapandian, V.; Singh, S.; Srivastava, R.; Nandan, B.; Liu, C. L.; Chen, H. L. Crystallization Behaviour of Poly(Ethylene Oxide) under Confinement in the Electrospun Nanofibers of Polystyrene/Poly(Ethylene Oxide) Blends. *Soft Matter* **2016**, *12* (23), 5110–5120. <https://doi.org/10.1039/c6sm00648e>.
- (55) Kupka, V.; Dvoráková, E.; Manakhov, A.; Michlíček, M.; Petruš, J.; Vojtová, L.; Zajíčková, L. Well-Blended PCL/PEO Electrospun Nanofibers with Functional Properties Enhanced by Plasma Processing. *Polymers (Basel)*. **2020**, *12* (6), 1403. <https://doi.org/10.3390/polym12061403>.
- (56) Zhong, G.; Wang, K.; Zhang, L.; Li, Z. M.; Fong, H.; Zhu, L. Nanodroplet Formation and Exclusive Homogenously Nucleated Crystallization in Confined Electrospun Immiscible Polymer Blend Fibers of Polystyrene and Poly(Ethylene Oxide). *Polymer (Guildf)*. **2011**, *52* (24), 5397–5402. <https://doi.org/10.1016/j.polymer.2011.09.045>.
- (57) Cong, R.; Pelton, R.; Russo, P.; Doucet, G. Factors Affecting the Size of Aqueous Poly(Vinylphenol-Co-Potassium Styrenesulfonate)/Poly(Ethylene Oxide) Complexes. *Macromolecules* **2003**, *36* (1), 204–209. <https://doi.org/10.1021/ma020965y>.
- (58) Stack, K. R.; Dunn, L. A.; Roberts, N. K. Study of the Interaction between Poly(Ethylene Oxide) and Phenol-Formaldehyde Resin. *Colloids and Surfaces* **1991**, *61* (C), 205–218.

[https://doi.org/10.1016/0166-6622\(91\)80310-K](https://doi.org/10.1016/0166-6622(91)80310-K).

- (59) SÁ, A. G. A.; Meneses, A. C. de; Araújo, P. H. H. de; Oliveira, D. de. A Review on Enzymatic Synthesis of Aromatic Esters Used as Flavor Ingredients for Food, Cosmetics and Pharmaceuticals Industries. *Trends Food Sci. Technol.* **2017**, 69, 95–105. <https://doi.org/10.1016/j.tifs.2017.09.004>.
- (60) Liu, J.; Pu, H.; Liu, S.; Kan, J.; Jin, C. Synthesis, Characterization, Bioactivity and Potential Application of Phenolic Acid Grafted Chitosan: A Review. *Carbohydr. Polym.* **2017**, 174, 999–1017. <https://doi.org/10.1016/j.carbpol.2017.07.014>.
- (61) Wang, X.; Ding, B.; Sun, G.; Wang, M.; Yu, J. Electro-Spinning/Netting: A Strategy for the Fabrication of Three-Dimensional Polymer Nano-Fiber/Nets. *Prog. Mater. Sci.* **2013**, 58 (8), 1173–1243. <https://doi.org/10.1016/j.pmatsci.2013.05.001>.
- (62) Liu, H.; Zhang, S.; Liu, L.; Yu, J.; Ding, B. A Fluffy Dual-Network Structured Nanofiber/Net Filter Enables High-Efficiency Air Filtration. *Adv. Funct. Mater.* **2019**, 29 (39), 1904108. <https://doi.org/10.1002/adfm.201904108>.
- (63) Nirmala, R.; Navamathavan, R.; El-Newehy, M. H.; Kim, H. Y. Preparation and Electrical Characterization of Polyamide-6/Chitosan Composite Nanofibers via Electrospinning. *Mater. Lett.* **2011**, 65 (3), 493–496. <https://doi.org/10.1016/j.matlet.2010.10.066>.
- (64) Lu, Y.; Shang, Y.; Huang, X.; Chen, A.; Yang, Z.; Jiang, Y.; Cai, J.; Gu, W.; Qian, X.; Yang, H.; Cheng, R. Preparation of Strong Cationic Chitosan- Graft -Polyacrylamide Flocculants and Their Flocculating Properties. *Ind. Eng. Chem. Res.* **2011**, 50 (12), 7141–7149. <https://doi.org/10.1021/ie2000665>.

8 Appendix

8.1 Supplementary information

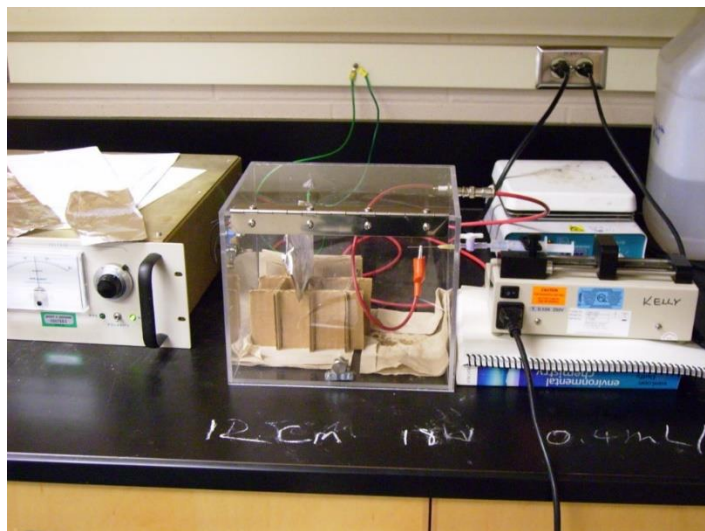


Figure A3.1. The picture of the “in-house” electrospinning apparatus.

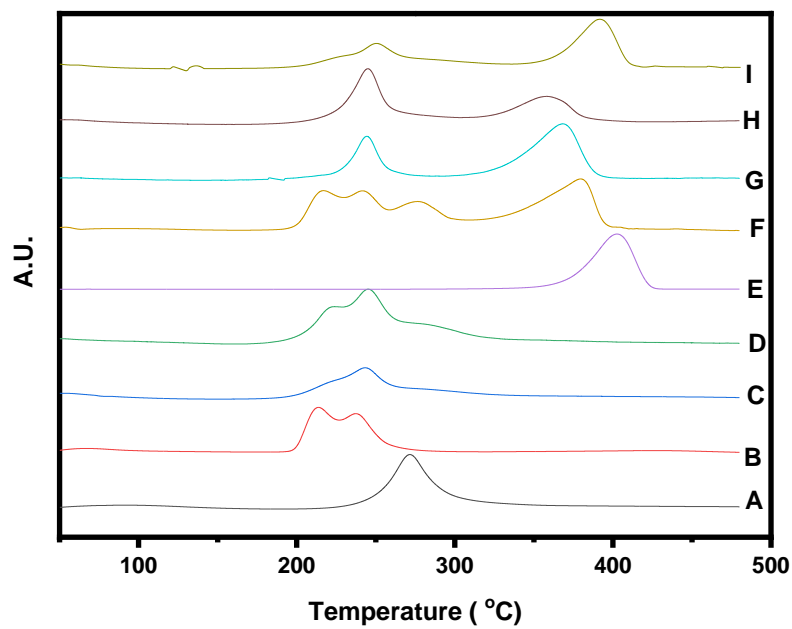


Figure A4.1. DTG plots of precursor and fiber samples. A) cm-chi, B) alg, C) S-1, D) S-2, E) PEO, F) physical mixture (cm-chi, alg, PEO), G) CP-1, H) CP-2, and I) TCP-1.

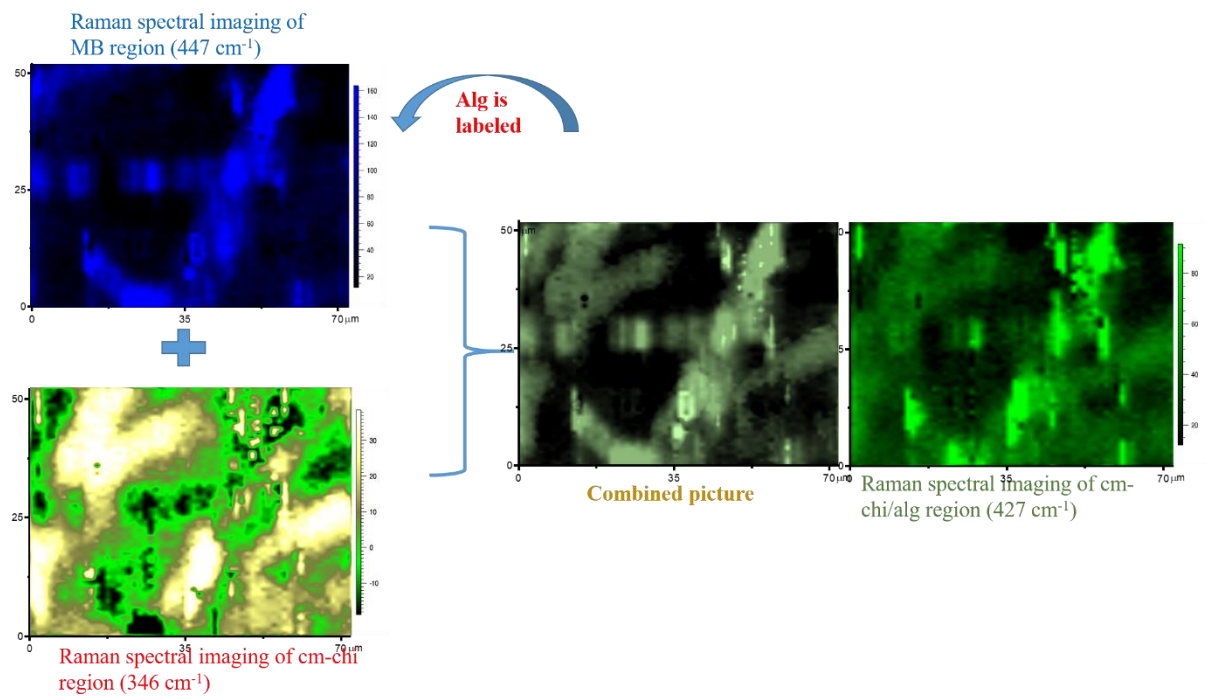


Figure A4.2. A combined additive picture of methylene blue and cm-chitosan using Image-Pro® Plus 6.0.

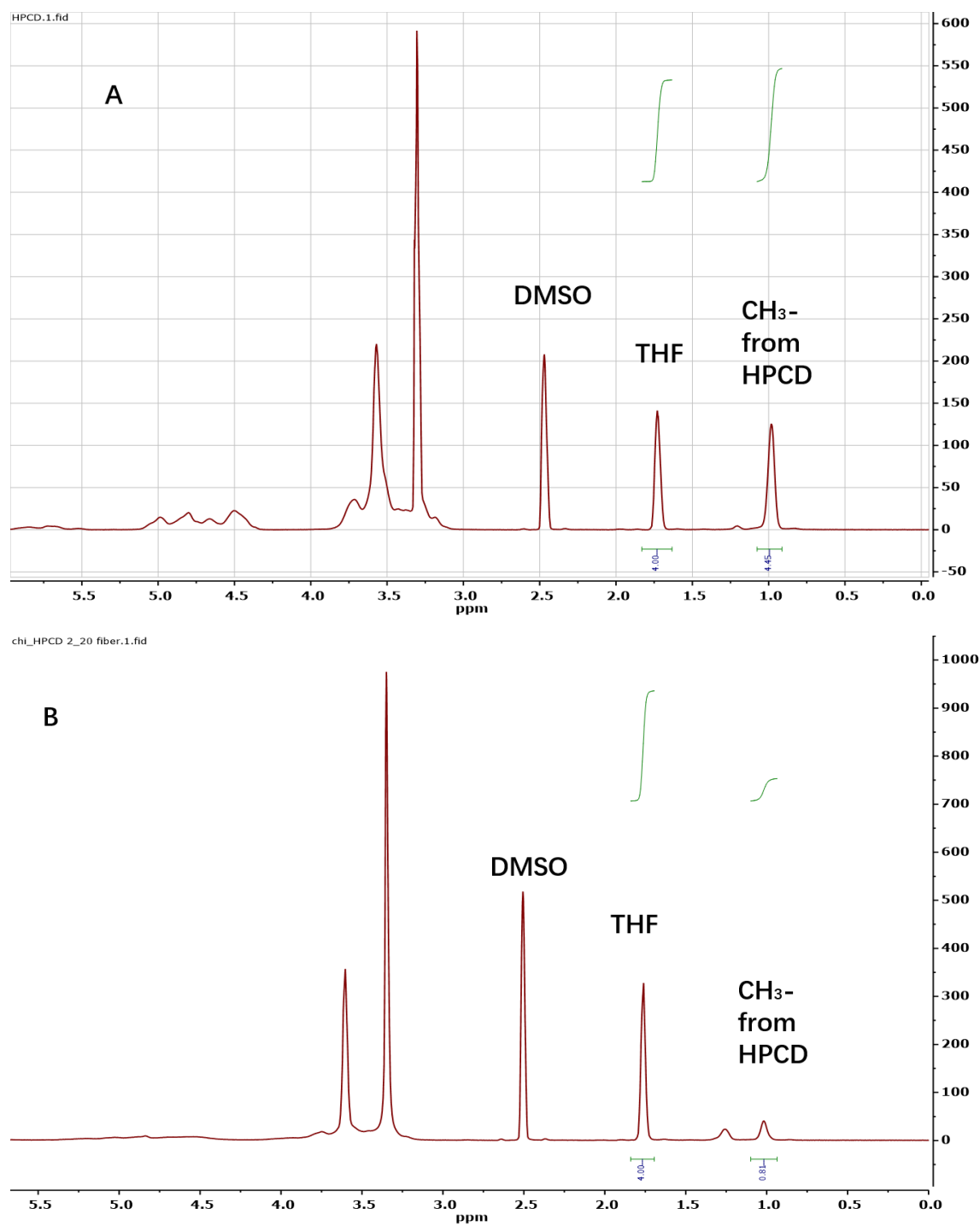


Figure A5.1. ^1H NMR spectra of chi:HP- β -CD electrospun nanofibrous materials dissolved in 1% (w/w) THF/DMSO- d_6 solution for HP- β -CD content determination. **A)** chi:HP- β -CD 2:20 fiber and **B)** chi:HP- β -CD 2:50 fiber.

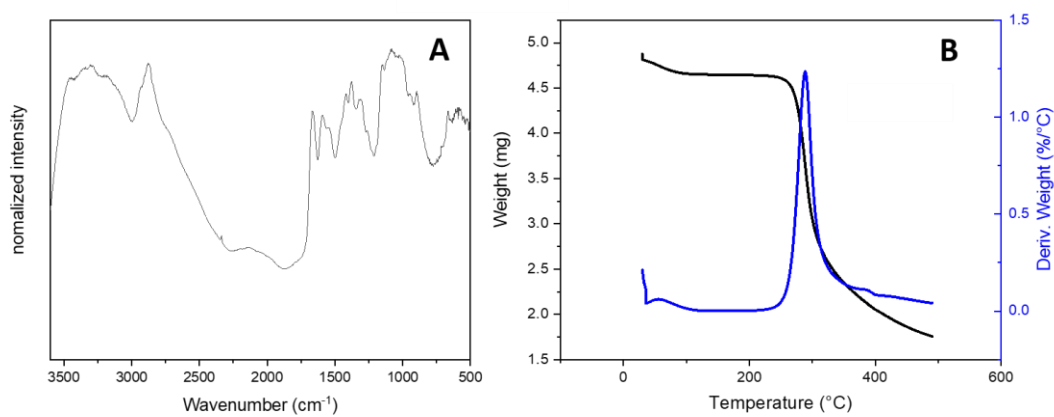


Figure A5.2. FT-IR spectrum (A) and DTG plot (B) of pristine chitosan.

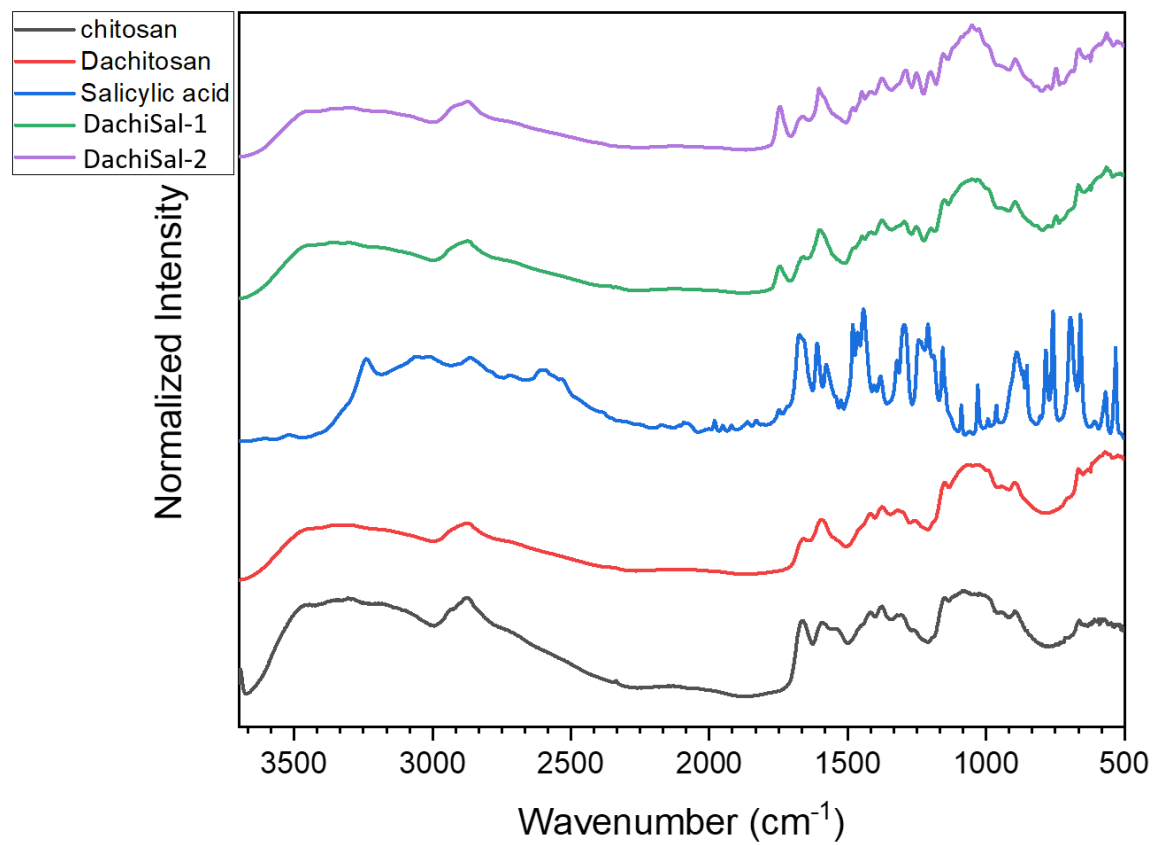


Figure A6.1. FT-IR spectra of Chitosan, Dachitsoan, Salicylic acid, DachiSal-1, and DachiSal-2.

8.2 Copyright permissions



ACS Publications
Most Trusted. Most Cited. Most Read.

Molecular Interactions in Electrospinning: From Polymer Mixtures to Supramolecular Assemblies

Author: Elena Ewaldz, Blair Brettmann

Publication: ACS Applied Polymer Materials

Publisher: American Chemical Society

Date: Mar 1, 2019

Copyright © 2019, American Chemical Society


PERMISSION/LICENSE IS GRANTED FOR YOUR ORDER AT NO CHARGE

This type of permission/license, instead of the standard Terms & Conditions, is sent to you because no fee is being charged for your order. Please note the following:

- Permission is granted for your request in both print and electronic formats, and translations.
 - If figures and/or tables were requested, they may be adapted or used in part.
 - Please print this page for your records and send a copy of it to your publisher/graduate school.
 - Appropriate credit for the requested material should be given as follows: "Reprinted (adapted) with permission from (COMPLETE REFERENCE CITATION). Copyright (YEAR) American Chemical Society." Insert appropriate information in place of the capitalized words.
 - One-time permission is granted only for the use specified in your request. No additional uses are granted (such as derivative works or other editions). For any other uses, please submit a new request.
- If credit is given to another source for the material you requested, permission must be obtained from that source.

BACK

CLOSE WINDOW



Carbohydrate Polymers

A structural study of self-assembled chitosan-based sponge materials

Author: Chen Xue, Lee D. Wilson

Publication: Carbohydrate Polymers

Publisher: Elsevier

Date: 15 February 2019

© 2018 Elsevier Ltd. All rights reserved.

Journal Author Rights

Please note that, as the author of this Elsevier article, you retain the right to include it in a thesis or dissertation, provided it is not published commercially. Permission is not required, but please ensure that you reference the journal as the original source. For more information on this and on your other retained rights, please visit: <https://www.elsevier.com/about/our-business/policies/copyright#Author-rights>

BACK

CLOSE WINDOW

Open Access

Article

A Spectroscopic Study of Solid-Phase Chitosan/Cyclodextrin-Based Electrospun Fibers

by  **Chen Xue** and  **Lee D. Wilson** * 

Department of Chemistry, University of Saskatchewan, 110 Science Place, Saskatoon, SK S7N 5C9, Canada

* Author to whom correspondence should be addressed.

Fibers **2019**, *7*(5), 48; <https://doi.org/10.3390/fib7050048>

Received: 1 April 2019 / Revised: 19 April 2019 / Accepted: 16 May 2019 / Published: 22 May 2019

(This article belongs to the Special Issue **Smart Coatings on Fibers and Textiles**)



© 2019 by the authors. Submitted for possible open access publication under the terms and conditions of the Creative Commons Attribution (CC BY) license (<http://creativecommons.org/licenses/by/4.0/>).